frontiers | Research Topics

Nematicity in iron-based superconductors

Edited by
Qisi Wang, Anna Böhmer and Laura Fanfarillo

Published in
Frontiers in Physics

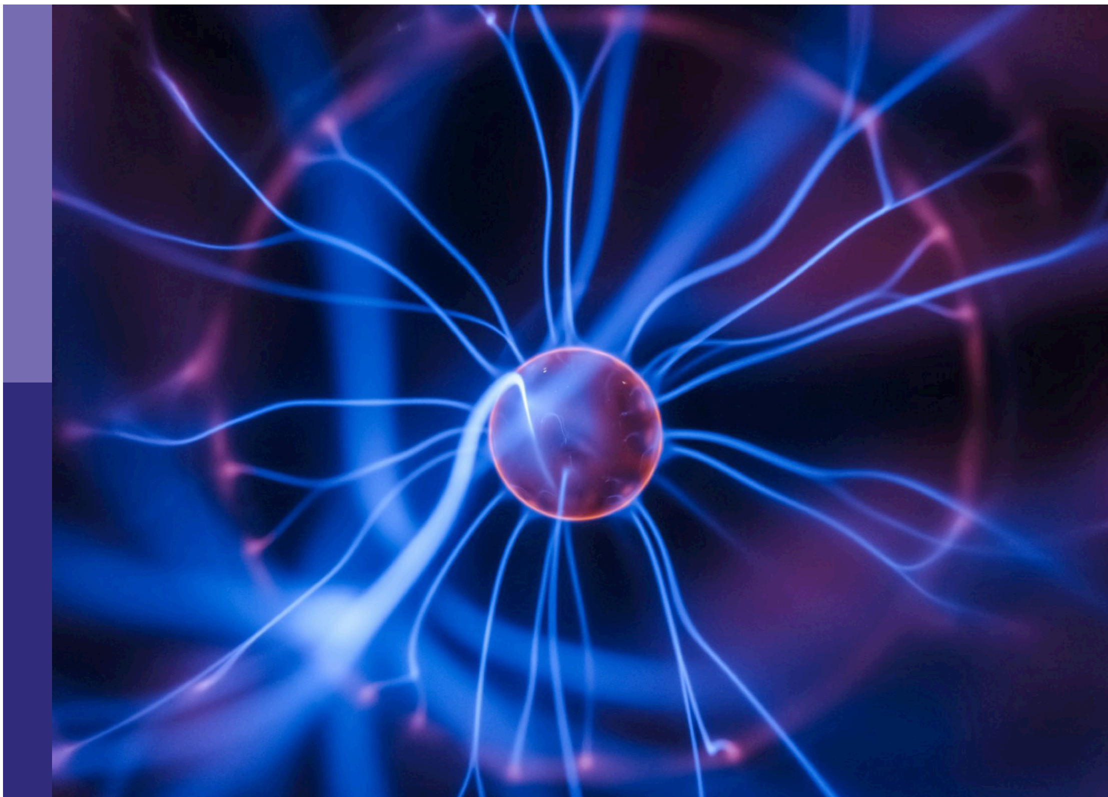

ISSN 1664-8714
ISBN 978-2-83251-470-2
DOI 10.3389/978-2-83251-470-2

About Frontiers

Frontiers is more than just an open access publisher of scholarly articles: it is a pioneering approach to the world of academia, radically improving the way scholarly research is managed. The grand vision of Frontiers is a world where all people have an equal opportunity to seek, share and generate knowledge. Frontiers provides immediate and permanent online open access to all its publications, but this alone is not enough to realize our grand goals.

Frontiers journal series

The Frontiers journal series is a multi-tier and interdisciplinary set of open-access, online journals, promising a paradigm shift from the current review, selection and dissemination processes in academic publishing. All Frontiers journals are driven by researchers for researchers; therefore, they constitute a service to the scholarly community. At the same time, the *Frontiers journal series* operates on a revolutionary invention, the tiered publishing system, initially addressing specific communities of scholars, and gradually climbing up to broader public understanding, thus serving the interests of the lay society, too.

Dedication to quality

Each Frontiers article is a landmark of the highest quality, thanks to genuinely collaborative interactions between authors and review editors, who include some of the world's best academicians. Research must be certified by peers before entering a stream of knowledge that may eventually reach the public - and shape society; therefore, Frontiers only applies the most rigorous and unbiased reviews. Frontiers revolutionizes research publishing by freely delivering the most outstanding research, evaluated with no bias from both the academic and social point of view. By applying the most advanced information technologies, Frontiers is catapulting scholarly publishing into a new generation.

What are Frontiers Research Topics?

Frontiers Research Topics are very popular trademarks of the *Frontiers journals series*: they are collections of at least ten articles, all centered on a particular subject. With their unique mix of varied contributions from Original Research to Review Articles, Frontiers Research Topics unify the most influential researchers, the latest key findings and historical advances in a hot research area.

Find out more on how to host your own Frontiers Research Topic or contribute to one as an author by contacting the Frontiers editorial office: frontiersin.org/about/contact

Nematicity in iron-based superconductors

Topic editors
Qisi Wang — University of Zurich, Switzerland
Anna Böhmer — Ruhr-University Bochum, Germany
Laura Fanfarillo — International School for Advanced Studies (SISSA), Italy

Citation
Wang, Q., Böhmer, A., Fanfarillo, L., eds. (2023). *Nematicity in iron-based superconductors*. Lausanne: Frontiers Media SA. doi: 10.3389/978-2-83251-470-2

Table of contents

04 Editorial: Nematicity in iron-based superconductors
Qisi Wang, Lara Fanfarillo and Anna E. Böhmer

07 Relationship Between Nematicity, Antiferromagnetic Fluctuations, and Superconductivity in $FeSe_{1-x}S_x$ Revealed by NMR
Khusboo Rana and Yuji Furukawa

15 Optical Fingerprints of Nematicity in Iron-Based Superconductors
Leonardo Degiorgi

29 Nematicity and Glassy Behavior Probed by Nuclear Magnetic Resonance in Iron-Based Superconductors
N. J. Curro, T. Kissikov, M. A. Tanatar, R. Prozorov, S. L. Bud'ko and P. C. Canfield

45 Elastoresistivity of Heavily Hole-Doped 122 Iron Pnictide Superconductors
Xiaochen Hong, Steffen Sykora, Federico Caglieris, Mahdi Behnami, Igor Morozov, Saicharan Aswartham, Vadim Grinenko, Kunihiro Kihou, Chul-Ho Lee, Bernd Büchner and Christian Hess

52 Theory of Spin-Excitation Anisotropy in the Nematic Phase of FeSe Obtained From RIXS Measurements
Andreas Kreisel, P. J. Hirschfeld and Brian M. Andersen

61 FeSe and the Missing Electron Pocket Problem
Luke C. Rhodes, Matthias Eschrig, Timur K. Kim and Matthew D. Watson

83 Nematic Fluctuations in the Non-Superconducting Iron Pnictide $BaFe_{1.9-x}Ni_{0.1}Cr_xAs_2$
Dongliang Gong, Ming Yi, Meng Wang, Tao Xie, Wenliang Zhang, Sergey Danilkin, Guochu Deng, Xinzhi Liu, Jitae T. Park, Kazuhiko Ikeuchi, Kazuya Kamazawa, Sung-Kwan Mo, Makoto Hashimoto, Donghui Lu, Rui Zhang, Pengcheng Dai, Robert J. Birgeneau, Shiliang Li and Huiqian Luo

95 Feedback of Non-Local d_{xy} Nematicity on the Magnetic Anisotropy in FeSe
Steffen Bötzel and Ilya M. Eremin

104 Diverse Exotic Orders and Fermiology in Fe-Based Superconductors: A Unified Mechanism for B_{1g}/B_{2g} Nematicity in FeSe/(Cs,Rb)Fe_2As_2 and Smectic Order in $BaFe_2As_2$
Seiichiro Onari and Hiroshi Kontani

frontiers | Frontiers in Physics

TYPE Editorial
PUBLISHED 27 September 2022
DOI 10.3389/fphy.2022.1038127

Editorial: Nematicity in iron-based superconductors

Qisi Wang[1]*, Lara Fanfarillo[2,3]* and Anna E. Böhmer[4,5]*

[1]Physik-Institut, Universität Zürich, Zürich, Switzerland, [2]International School for Advanced Studies SISSA/ISAS, Department of Physics, Trieste, Italy, [3]Department of Physics, University of Florida, Gainesville, FL, United States, [4]Lehrstuhl für Experimentalphysik IV, Fakultät für Physik und Astronomie, Ruhr-Universität Bochum, Bochum, Germany, [5]Institute for Quantum Materials and Technologies, Karlsruhe Institute of Technology, Karlsruhe, Germany

KEYWORDS

iron-based superconductors, nematicity, electronic anisotropy, orbital nematicity, spin nematicity, orbital ordering, nematic susceptibility, nematic fluctuations

Editorial on the Research Topic
Nematicity in iron-based superconductors

EDITED AND REVIEWED BY
Jian-Xin Zhu,
Los Alamos National Laboratory (DOE),
United States

*CORRESPONDENCE
Qisi Wang,
qisiwang@physik.uzh.ch
Lara Fanfarillo,
laura.fanfarillo@sissa.it
Anna E. Böhmer,
boehmer@physik.rub.de

SPECIALTY SECTION
This article was submitted to
Condensed Matter Physics,
a section of the journal
Frontiers in Physics

RECEIVED 06 September 2022
ACCEPTED 08 September 2022
PUBLISHED 27 September 2022

CITATION
Wang Q, Fanfarillo L and Böhmer AE (2022), Editorial: Nematicity in iron-based superconductors.
Front. Phys. 10:1038127.
doi: 10.3389/fphy.2022.1038127

In iron-based materials, nematicity is a commonly observed symmetry-breaking state that exists in proximity to superconductivity. The nematic instability is associated with a structural transition that lowers the symmetry of the lattice and characterized by both the development of anisotropy in transport and electronic properties as well as orbital-dependent splitting in the electronic bands. The variety of experimental signatures characterizing the nematic state allowed investigations with diverse experimental probes that throughout the past decade uncovered multiple surprising results. Yet, key questions regarding the origin of nematicity remain unsettled as the spin, orbital, and lattice degrees of freedom are intimately coupled [1].

The current Research Topic compiles the latest works that tackle both the origin and characterization of the nematic phase in iron-based materials. The contributions mainly focus on the analysis of doped compounds of the “122” group (e.g., $BaFe_2As_2$) including the heavily hole-doped ones, in which a new type of nematic instability has been recently reported [2], and on FeSe, that provides the unique opportunity to study the nematic phase within a wide range of temperature in the absence of long-range magnetic ordering [3]. In this way, we highlight the forefront of the research on nematicity in iron-based superconductors.

The Research Topic presents three review papers and six experimental and theoretical contributions collected from the front of original research.

Degiorgi reviews optical studies of FeSe and $Ba_{0.6}K_{0.4}Fe_2As_2$. The study of the broadband optical anisotropy in FeSe suggests that spin fluctuations together with the high-energy orbital ordering assume a dominant role in the onset of nematicity. For optimally doped $Ba_{0.6}K_{0.4}Fe_2As_2$, it is shown that the stress-induced optical anisotropy occurs only below the superconducting transition temperature. These findings demonstrate an intimate relation between spin fluctuations, orbital nematicity, and superconductivity.

Rana and Furukawa present a mini-review of their ^{77}Se nuclear magnetic resonance (NMR) studies on FeSe, when the compound is tuned by application of physical pressure, chemical pressure, or a combination of both. Indeed, FeSe exhibits a complex T-x-p phase diagram as physical pressure, p, is applied or sulfur is substituted for selenium in $FeSe_{1-x}S_x$ (chemical pressure), including magnetic order and abundant magnetic fluctuations. Rana and Furukawa find that, while antiferromagnetic fluctuations appear to enhance T_c in general, the effect is stronger in the absence of nematicity.

Rhodes et al. present a detailed review of the evolution of the Fermi surface of FeSe in the nematic phase, addressing the problematic issue of the "missing electron pocket." It is still unclear how the experimentally determined Fermi surface near the M point of the Brillouin zone evolves from having two electron pockets in the tetragonal state, to exhibiting just a single electron pocket in the nematic state [4]. In this review, Rhodes et al. collect recent angle-resolved photoemission spectroscopy (ARPES) and scanning tunneling microscopy works to analyze the orbital dependent band-shifts in the nematic phase, as well as theoretical modeling based on the inclusion of an additional nematic order parameter having "*xy*" orbital character.

Bötzel and Eremin analyze the magnetic anisotropy of FeSe using the same phenomenological model reviewed in Rhodes et al. The model combines the usual nematic order parameter based on the differentiation of the *xz* and *yz* orbitals with a non-local *xy* nematic order parameter. The interesting result is that the inclusion of the latter successfully describes not only the absence of the Y-electron pocket, but also the temperature dependence of the anisotropy on the spin susceptibility.

Onari and Kontani discuss a unified picture of nematicity for iron-based superconductors presenting a theoretical description based on a self-consistent diagrammatic approximation. The model allows for the description of several experimental signatures of nematicity both in FeSe-based superconductors and in heavily hole-doped "122"-type materials, which derive from $BaFe_2As_2$ by doping towards the end-members K/Rb/$CsFe_2As_2$.

The controversial issue of nematicity in heavily hole-doped "122" materials is also the focus of Hong et al. that discuss the Research Topic from the experimental point of view. Whereas nematic orders far from a magnetic instability have been claimed in $(Ba,Rb)Fe_2As_2$, it is still debated whether the elastoresistance of these compounds is a signature of a new nematic instability. Hong et al. present elastoresistance data for a multitude of heavily hole-doped 122-systems, which show a divergence of elastoresistance. However, they present a new interpretation based on the well-known Lifshitz transition in the system unrelated to nematicity. This work adds a new element to the interpretation of elastoresistance, an experimental quantity that has impacted heavily in the investigation of nematicity.

Curro et al. present an NMR work, on the distribution of spin fluctuations in doped pnictides and the effect of uniaxial strain and strain hysteresis. They find that the spin lattice relaxation rate is inhomogeneous, and the spatial distribution of local spin fluctuations correlates with the nematic susceptibility. Their results suggest that a nematic glass behavior is induced by quenched strain fields associated with doping atoms.

Gong et al. present a systematic study of nematic fluctuations in the non-superconducting $BaFe_{1.9-x}Ni_{0.1}Cr_xAs_2$ system combining electronic transport, ARPES, and inelastic neutron scattering measurements. By monitoring the evolution of the nematic fluctuations as a function of Cr doping, a strong correlation between the resistivity- and spin nematicity is revealed, while the orbital anisotropy behaves differently. Their results suggest the importance of the interplay between local moments and itinerant electrons for understanding the nematic fluctuations.

Kreisel et al. theoretically analyze the anisotropy of the spin excitations in FeSe, focusing on the high-energy range as the one detected by resonant inelastic x-ray scattering (RIXS) experiments. They consider an itinerant model previously used to describe the spin-excitation anisotropy as measured by neutron scattering measurements, with magnetic fluctuations included within the random phase approximation. The calculated cross section exhibits overall agreement with the data of recent RIXS experiments on FeSe [5], where a theoretical interpretation in terms of local moments was discussed. The work by Kreisel et al. proves again that nematic phenomenology presents some aspects that can be described either via an itinerant or a local spin scenario, suggesting a non-trivial role of electronic correlations in affecting the metallic state of iron-based superconductors [6].

This editorial conveys the objectives of the above nine articles that represent the latest progress in the research of nematicity in iron-based superconductors. We wish to thank all the authors and referees for their contributions and hope for more future studies on this Research Topic.

Author contributions

All authors listed have made a substantial, direct, and intellectual contribution to the work and approved it for publication.

Conflict of interest

The authors declare that the research was conducted in the absence of any commercial or financial relationships that could be construed as a potential conflict of interest.

Publisher's note

References

1. Fernandes RM, Chubukov AV, Schmalian J. What drives nematic order in iron-based superconductors? *Nat Phys* (2014) 10:97–104. doi:10.1038/nphys2877

2. Ishida K, Tsujii M, Hosoi S, Mizukami Y, Ishida S, Iyo A, et al..Novel electronic nematicity in heavily hole-doped iron pnictide superconductors. *Proc Natl Acad Sci U.S.A* (2020) 117:6424–9. doi:10.1073/pnas.1909172117

3. Böhmer AE, Kreisel A. Nematicity, magnetism and superconductivity in FeSe. *J Phys Condens Matter* (2018) 30:023001. doi:10.1088/1361-648X/aa9caa

4. Yi M, Pfau H, Zhang Y, He Y, Wu H, Chen T, et al..Nematic energy scale and the missing electron pocket in FeSe. *Phys Rev X* (2019) 9:041049. doi:10.1103/physrevx.9.041049

5. Lu X, Zhang W, Tseng Y, Liu R, Tao Z, Paris E, et al..Spin-excitation anisotropy in the nematic state of detwinned FeSe. *Nat Phys* (2022) 18:806–12. doi:10.1038/s41567-022-01603-1

6. Fanfarillo L. Go for a spin. *Nat Phys* (2022) 18:738–9. doi:10.1038/s41567-022-01624-w

frontiers in Physics

MINI REVIEW
published: 08 March 2022
doi: 10.3389/fphy.2022.849284

Relationship Between Nematicity, Antiferromagnetic Fluctuations, and Superconductivity in $FeSe_{1-x}S_x$ Revealed by NMR

Khusboo Rana and Yuji Furukawa*

Ames Laboratory, US Department of Energy, and Department of Physics and Astronomy, Iowa State University, Ames, IA, United States

The S-substituted FeSe, $FeSe_{1-x}S_x$, under pressure (p), provides a versatile platform for studying the relationship among nematicity, antiferromagnetism, and superconductivity. Here we present a short review of the recent experimental evidence showing that nematicity has a remarkable impact on the relationship between antiferromagnetic fluctuations and superconductivity. This has been revealed by several ^{77}Se nuclear magnetic resonance studies that have tracked the variability of antiferromagnetic fluctuations and superconducting transition temperature (T_c) as a function of x and p. T_c is roughly proportional to antiferromagnetic fluctuations in the presence or absence of nematic order suggesting the importance of antiferromagnetic fluctuations in the Cooper pairing mechanism in $FeSe_{1-x}S_x$. However, the antiferromagnetic fluctuations are more effective in enhancing superconductivity in the absence of nematicity as compared to when it is present. These experimental observations give renewed insights into the interrelationships between nematicity, magnetism, and superconductivity in Fe-based superconductors.

Keywords: nematicity, unconventional superconductivity, NMR, magnetic correlations, quantum materials

OPEN ACCESS

Edited by:
Anna Böhmer,
Ruhr-University Bochum, Germany

Reviewed by:
Atsushi Fujimori,
Waseda University, Japan

****Correspondence:***
Yuji Furukawa
furukawa@ameslab.gov

Specialty section:
This article was submitted to Condensed Matter Physics, a section of the journal Frontiers in Physics

Received: *05 January 2022*
Accepted: *02 February 2022*
Published: *08 March 2022*

Citation:
Rana K and Furukawa Y (2022) Relationship Between Nematicity, Antiferromagnetic Fluctuations, and Superconductivity in $FeSe_{1-x}S_x$ Revealed by NMR. Front. Phys. 10:849284. doi: 10.3389/fphy.2022.849284

1 INTRODUCTION

Suppressing the transition temperatures of long-range orders with a tuning parameter has led to the discovery of superconductivity (SC) in the associated quantum phase transition (QPT) regions of several classes of materials such as heavy-Fermion systems [1–3], itinerant ferromagnets [4, 5], high T_c cuprates and Fe-based superconductors [3, 6]. The quantum critical fluctuations of the suppressed long-range order parameter(s) could thus be responsible for the elusive Cooper pairing mechanism in those unconventional superconductors.

In most Fe-based superconductors, SC appears close to the quantum phase transitions of two long-range orders: the nematic order, which is an electronically driven structural transition from high-temperature tetragonal (C4 symmetry) to low-temperature orthorhombic (C2 symmetry), and the antiferromagnetic (AFM) order with spontaneously oriented electronic spins characterized by a wave vector [$\mathbf{q} = (\pi,0)$ or $(0,\pi)$] [3, 7–9]. In those systems, the nematic transition temperature (T_s) is at or just above the Néel temperature (T_N), and both phases are simultaneously suppressed with carrier doping and/or the application of pressure (p), leading to two QPTs originating from the nematic and the AFM states. As SC in these compounds emerges around the two QPTs, AFM and nematic phases are believed to play important roles for the appearance of SC. However, the

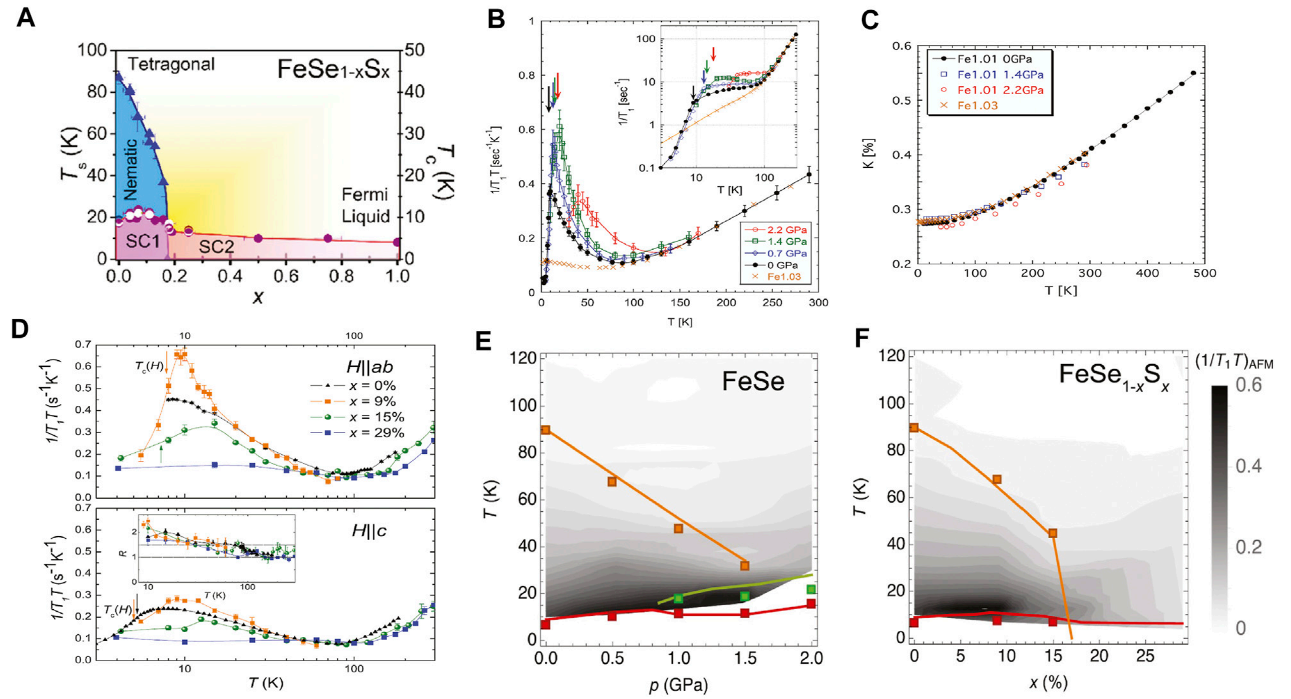

FIGURE 1 | (A) Electronic phase diagram of FeSe$_{1-x}$S$_x$ taken from Ref. [25] based on data from Refs. [26, 27]. **(B)** T dependence of $1/T_1T$ under various p in polycrystalline FeSe. The arrows show the corresponding T_c. The inset show the T dependence of $1/T_1$ under p. Reprinted with permission from T. Imai et al., Physical Review Letters 102, 177005, 2009 [17]. Copyright (2009) by the American Physical Society. **(C)** p dependence of the Knight shift K as a function of T. Reprinted with permission from Ref. [17]. Copyright (2009) by the American Physical Society. **(D)** T-dependence of $1/T_1T$ in single crystalline FeSe$_{1-x}$S$_x$ for $H \| ab$ (top) and $H \| c$ (bottom) at ambient p. The arrows show the corresponding T_c. The inset shows inset the T dependence of the ratio $R = T_{1,c}/T_{1,ab}$. Reprinted with permission from P. Wiecki *et al.*, Physical Review B 98, 020507(R), 2018 [18]. Copyright (2018) by the American Physical Society. **(E, F)** The contour plots of the amplitude of the AFM fluctuations defined as $(1/T_1T)_{AFM}$ (see text for derivation) in single crystal: FeSe under p **(E)** and FeSe$_{1-x}$S$_x$ at ambient p **(F)** taken from Ref. [18] which includes data reported in Refs. [58, 60]. The orange, red and green symbols show T_s, T_c, and T_N, respectively, determined by NMR measurements under H ~ 7.4 T [18]. The colored curves are the corresponding values from literatures [58, 60]. Reprinted with permission from Ref. [18]. Copyright (2018) by the American Physical Society.

individual contribution to SC from these two phases becomes difficult to separate due to the close proximity of the two orders [10–12].

In this sense, the sulfur-substituted FeSe system, FeSe$_{1-x}$S$_x$, provides a favorable platform for the study of the role of nematicity or antiferromagnetism on SC independently [13]. FeSe$_{1-x}$S$_x$ has the simplest of crystal structures among the Fe-based superconductors, with a quasi-two dimensional FeSe(S) layer in the *ab* plane, stacked along the *c* axis. At x = 0, FeSe undergoes a nematic transition at T_s ~ 90 K followed by a superconducting transition at T_c ~ 8.5 K, but it does not show a long range AFM order at ambient p [13–16]. This allows the study of AFM fluctuations inside the nematic order and its relationship with SC [17]. The nematic phase in FeSe can be suppressed by pressure application, with T_s decreased down to 32 K at p = 1.5 GPa [18]. T_c shows a complex multi-domed structure with p, reaching a maximum T_c ~ 37 K at p ~ 6 GPa [19–21]. At the same time, an AFM ordered state appears above p = 0.8 GPa [22, 23], and T_s merges with T_N above p = 1.7 GPa [24], limiting the range for studying the effects of nematicity on SC without AFM state.

The nematic phase in FeSe can also be suppressed with the isovalent S substitution for Se in FeSe$_{1-x}$S$_x$ as shown in **Figure 1A** taken from Ref. [25] based on data from Refs. [26, 27], where T_s decreases to zero at the critical x value, x_c ~ 0.17. As no long-range AFM order appears in FeSe$_{1-x}$S$_x$ at ambient p, one can study the variability of T_c including near a nematic QPT without an AFM order. At x_c, diverging nematic fluctuations were reported from elasto-resistivity measurements [28], and a temperature- (T-) linear behavior of the resistivity was seen under high magnetic fields (H) [29]. As shown in **Figure 1A**, T_c first increases up to 10 K around x = 0.09 making a maximum and then decreases gradually at higher x without showing any clear change in T_c around x_c [18, 26, 30]. Nevertheless, the considerable change in the size and anisotropy of the SC gap is observed at the nematic QPT in spectroscopic-imaging scanning tunneling microscopy [26, 30, 31], thermal conductivity [32], and specific heat [33] measurements, implying different SC states inside (SC1) and outside (SC2) nematic states [25]. In addition, signatures of the crossover between Bardeen-Cooper-Schrieffer and Bose-Einstein-Condensate superconductivities at the nematic QPT were recently reported by laser-excited angle-resolved photoemission spectroscopy (ARPES) measurements [34].

The nematic phase in the S-substituted FeSe system is also controlled by pressure application and an AFM state appears at higher p [35–38]. The three-dimensional T-p-x phase diagram of

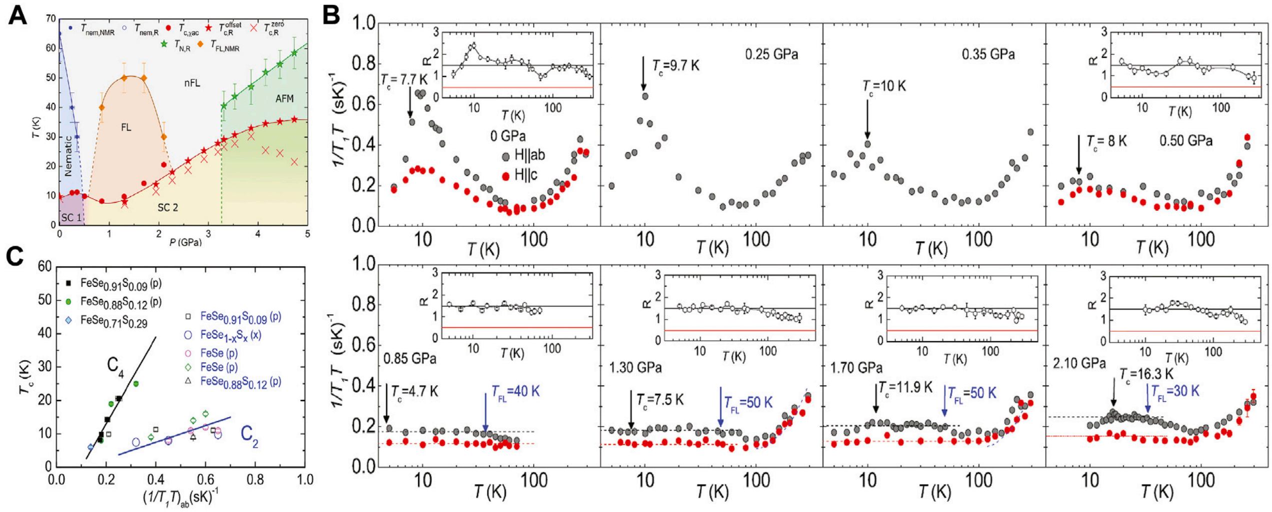

FIGURE 2 | (A) Electronic phase diagram of $FeSe_{0.91}S_{0.09}$ under pressure. Reprinted with permission from K. Rana et al., Physical Review B 101, 180503(R), 2020 [37]. Copyright (2020) by the American Physical Society. **(B)** Temperature- (T-) dependence of $1/T_1T$ in single crystalline $FeSe_{0.91}S_{0.09}$ measured at the indicated pressures under $H \| ab$ (black) and $H \| c$ (red). Black arrows indicate the superconducting transition temperatures under H = 7.4089 T parallel to the ab plane and blue arrows correspond to the Fermi liquid temperature below which $1/T_1T$ = constant is observed. The insets show the ratio, R, of $1/T_1T$ values measured for $H \| ab$ and $H \| c$ at the indicated p. The black and red lines in the insets are at 1.5 and 0.5. Reprinted with permission from Ref. [37]. Copyright (2020) by the American Physical Society. **(C)** Superconducting transition temperature (T_c) as a function of AFM fluctuations determined by the maximum of $1/T_1T$ under $H \| ab$ in $FeSe_{1-x}S_x$ under p, taken from Ref. [37] which provided the original data for x = 0.09 (open and closed black boxes). The data for x = 0 were taken from Ref. [17] (open dark green circles) and Refs. [58, 60] (open magenta circles). Values for x = 0.12 were taken from Ref. [41] (closed green circles and open triangles), and that for $FeSe_{1-x}S_x$ at ambient p (closed blue diamond and open blue circles) were taken from Ref. [18]. Black and blue lines fit the data with and without nematicity respectively. Reprinted with permission from Ref. [37]. Copyright (2020) by the American Physical Society.

$FeSe_{1-x}S_x$ up to p = 8 GPa has been reported by Matsuura et al. [35] in which the AFM ordered phase shifts to higher p with increasing x. A typical p-T phase is shown in **Figure 2A** for the case of x = 0.09 [37]. In this case, with increasing p, the nematic phase disappears around $p \sim 0.5$ GPa corresponding to a putative nematic QPT, and the AFM state appears above $p \sim 3.5$ GPa. In addition to the nematic, AFM, and SC states, Fermi liquid behaviors were reported at low temperatures in x = 0.09 (see **Figure 2A**) [37] and 0.11 [39] after the suppression of the nematic order by applying p. The Fermi liquid phase was recently attributed to the presence of a quantum griffiths phase close to the nematic QPT [40]. Similar to the T-x phase diagram of $FeSe_{1-x}S_x$, SC phase was shown to have two different states (SC1 and SC2) separated by the nematic QPT as shown in **Figure 2A**. Such two different SC states under p were also reported in x = 0.11 [39] and 0.12 [41], which is more apparent under H [41]. The presence of a series of nematic quantum phase transitions in the x-p phase diagram [35] allows the study of the correlation between T_c and AFM fluctuations in the presence and absence of the nematic order [37].

In this mini review, we show the positive correlation between AFM fluctuations and SC and the impact of nematicity on the relationship based on the nuclear magnetic resonance (NMR) studies of the $FeSe_{1-x}S_x$ system under p. After briefly introducing some basics of NMR which are used in ^{77}Se NMR studies to characterize the AFM fluctuations, we review the relationship between AFM fluctuations and SC in the presence of nematic order in FeSe under p and in $FeSe_{1-x}S_x$ at ambient p. Then, we show the studies of $FeSe_{1-x}S_x$ system under p, where we review the relationship between AFM fluctuations and SC in the absence of nematic order. Finally, we end with a summary including the current research gaps and potential future developments in the field.

2 NUCLEAR MAGNETIC RESONANCE AND ANTIFERROMAGNETIC FLUCTUATIONS

NMR is one of the powerful techniques to study the magnetic and electronic properties of materials from a microscopic point of view and has been utilized to investigate the physical properties of Fe-based superconductors. Nuclei with finite angular momentum undergo Zeeman splitting in the presence of a magnetic field at the nuclear site (H_{nuc}). The energy difference between the nearest nuclear spin levels is given as $\Delta E = \gamma_N \hbar H_{nuc}$ where γ_N is the nuclear gyromagnetic ratio. In the NMR technique, nuclei are excited from lower energy states to higher ones by applying electromagnetic wave whose energy is equal to ΔE.

The resonance frequency is determined by H_{nuc} which is a sum of the external magnetic field (H) and the hyperfine field (H_{hf}) due to the interaction between nuclei and electrons. The shift of the resonance line due to the hyperfine interaction is defined by $K = H_{hf}/H$ which is the so-called Knight shift in metals. In general, the shift K has the T-independent orbital component, K_{orb}, and T-dependent spin component, K_s, which can be expressed as $K = K_{orb} + K_s$. K_s is proportional to the static and uniform magnetic susceptibility (χ_s) with the wave vector $\mathbf{q} = 0$ and the frequency $\omega = 0$:

$$K_s \sim A_{hf}\chi_s(\mathbf{q} = 0, \omega = 0). \tag{1}$$

The T dependence of K_s gives us information of the magnetic properties of compounds at $\mathbf{q} = 0$. On the other hand, the nuclear relaxation rate ($1/T_1$) divided by T, $1/T_1T$, is sensitive to the $\mathbf{q}$-sum of the imaginary part of susceptibility ($\chi''(\mathbf{q}, \omega_N)$) at the NMR frequency ($\omega_N$) [42] and is given as

$$1\Big/T_1T \sim \gamma_N^2 k_B \sum_{\mathbf{q}} |A(\mathbf{q})|^2 \chi''(\mathbf{q}, \omega_N)\Big/\omega_N \tag{2}$$

where $A(\mathbf{q})$ is the $\mathbf{q}$-dependent hyperfine form factor. $1/T_1T$ gives us information about the total magnetic correlations at all $\mathbf{q}$ values. Therefore, one can obtain important insights about $\mathbf{q}$ dependent magnetic correlations by comparing K_s and $1/T_1T$ data.

In simple metals, K_s is related to the density of states at the Fermi energy [$\mathcal{N}(E_F)$] where $K_s = A_{hf}(g\mu_B)^2\mathcal{N}(E_F)/2$, and $1/T_1T$ is proportional to the square of $\mathcal{N}(E_F)$ as $1/T_1T = \pi\hbar\ A_{hf}^2\ (g\mu_B)^2\ \gamma_N^2\ \mathcal{N}^2(E_F)\ k_B$ [43]. In a Fermi liquid picture, the ratio $S \equiv T_1TK_s^2$ becomes a constant [42, 44] which is called the Korringa relation. In real materials, an experimentally determined value of $T_1TK_s^2$ may deviate from S due to electron correlations. Thus, the deviation parameter defined as $\alpha = S/(T_1TK_s^2)$ provides information about electron correlations in materials. When AFM fluctuations are present, $\chi''(\mathbf{q}, \omega_N)$ with $\mathbf{q} \neq 0$ is enhanced with little or no effect on K_s which probes only the $\mathbf{q} = 0$ component of χ_s. Therefore, $1/T_1T$ is enhanced much higher than K_s and α becomes greater than unity. On the other hand, $\alpha <$ unity is expected for ferromagnetic correlations.

When the Korringa relation does not hold due to strong magnetic fluctuations (non-Fermi liquid picture), the T dependence of $1/T_1T$ could be different from that of K. When strong AFM fluctuations exist in systems, the contribution to $1/T_1T$ from AFM fluctuations will be the source of the different T dependence, and the experimentally observed $1/T_1T$ is sometimes decomposed as $1/T_1T = (1/T_1T)_{AFM} + (1/T_1T)_{\mathbf{q}=0}$ [18, 45, 46]. Here $(1/T_1T)_{AFM}$ denotes the AFM contributions from $\chi(\mathbf{q} \neq 0, \omega_N)$ and $(1/T_1T)_{\mathbf{q}=0}$ represents the contributions from $\mathbf{q} = 0$ components. By assuming $(1/T_1T)_{\mathbf{q}=0} = CK_s^2$, where C is the empirically determined proportionality constant, one can extract the AFM contribution to $1/T_1T$ by subtracting $(1/T_1T)_{\mathbf{q}=0}$ from the observed $1/T_1T$, providing insights into the magnetic fluctuations.

In the case of Fe-based superconductors, Kitagawa et al. proposed that anisotropy in $1/T_1$ at the chalcogen or pnictogen sites provides more detailed information about AFM fluctuations [47]. According to them, the ratio of $1/T_1$ values measured under H parallel to c axis ($1/T_{1,c}$) and parallel to ab plane ($1/T_{1,ab}$) [$R \equiv T_{1,c}/T_{1,ab}$] can determine the dominant $\mathbf{q}$ for AFM fluctuations. In the case of isotropic AFM fluctuations, $R = 1.5$ is expected for stripe-type AFM fluctuations with $\mathbf{q} = (\pi, 0)$ or $(0, \pi)$, whereas when Néel type AFM fluctuations with $\mathbf{q} = (\pi, \pi)$ are present, $R = 0.5$. Such analysis has been extensively used in Fe-based superconductors [18, 37, 47–51] and related materials [52, 53] to characterize the AFM fluctuations in those systems.

3 ANTIFERROMAGNETIC FLUCTUATIONS AND SUPERCONDUCTIVITY WITH NEMATICITY

Soon after the discovery of the Fe-based superconductors [54, 55], ^{77}Se ($I = 1/2$, $\gamma_N/2\pi = 8.1432$ MHz) NMR studies on polycrystalline FeSe were carried out [17, 56] and the importance of AFM fluctuations for superconductivity has been pointed out. **Figure 1B** shows the T dependence of $1/T_1T$ values in FeSe under various pressures reported by Imai et al. [17]. At higher temperatures above $T \sim 100$ K, $1/T_1T$ at all pressures decreases with decreasing T. This behavior is similar to the T-dependence of K shown in **Figure 1C** where K shows a monotonic decrease when cooling from 480 to ~ 100 K. The variations in both $1/T_1T$ and K above ~ 100 K were explained in terms of spin gap formation or a peculiar band structure near the Fermi level [57]. However, upon cooling below $T \sim 100$ K, the T dependences of $1/T_1T$ and K show quite different behaviors. Although K is nearly independent of both T and p below 50 K, $1/T_1T$ shows strong enhancements at all measured pressures at low temperatures where peaks are observed at the p-dependent T_c or T_N. As described above, K is proportional to $\chi(0, 0)$ and $1/T_1T$ reflects the T dependence of $\mathbf{q}$-summed $\chi''(\mathbf{q}, \omega_N)$. Therefore, the enhancements of $1/T_1T$ at low temperatures unequivocally establish the presence of AFM fluctuations at the T region, suggesting that the AFM fluctuations are relevant to the SC in FeSe. In fact, a close relationship between the AFM fluctuations and SC has been pointed out from the p dependences of T_c and $1/T_1T$ data: the maximum of $1/T_1T$ increases along with T_c as shown in **Figure 1B** where T_cs at different p are marked by downward arrows [17]. Broad humps in $1/T_1T$ observed at temperatures much higher than their respective T_c values at $p =$ 1.4 and 2.2 GPa are due to magnetic orderings. It should be noted that, due to the occurrence of the AFM order under high pressures in FeSe, the relationship between T_c and the maximum of $1/T_1T$ can only be compared at low pressures in this system. A later single crystalline ^{77}Se NMR studies under $H\|ab$ and $H\|c$ characterized the AFM order and the AFM fluctuations at higher pressures to be of stripe type [51, 58].

A ^{77}Se NMR study of single crystalline $FeSe_{1-x}S_x$ by Wiecki *et al.* [18] at ambient p also provided clear experimental evidence of the close relationship between the AFM fluctuations and SC in this system. **Figure 1D** show the T dependence of $1/T_1T$ in $FeSe_{1-x}S_x$ for $H\|ab$ (upper) and $H\|c$ (lower), respectively, at ambient p [18], which includes the data from Ref. [58]. As in FeSe, K for all x shows monotonic decreases when lowering T from room T down to ~ 100 K, before leveling off at constant values [18] for both $H\|ab$ and $H\|c$. Although $1/T_1T$ showed a similar T dependence as K in all cases above 100 K, $1/T_1T$ shows a strong upturn below $T \sim 100$ K due to the growth of AFM fluctuations. The AFM fluctuations appear below 100 K for all samples of $x = 0$, 0.09, 0.15, and 0.29, however, the enhancement of the AFM fluctuations shows a strong x dependence. For x less than $x_c \sim 0.17$, $1/T_1T$ increases with decreasing T showing a Curie-Wiess-like behavior expected for two-dimensional AFM fluctuations from the self-consistent renormalization theory [42]. On the other hand, for $x = 0.29$ greater than x_c, a subtle upturn on cooling below $T \sim 100$ K is observed, suggesting the tiny growth of the AFM fluctuations, followed by a nearly T independent behavior below $T \sim 25$ K without showing clear Curie-Weiss-like behaviors. At all measured x values, the ratios $R \equiv T_{1,c}/T_{1,ab}$ are found to be ~ 1.5 below $T \sim 100$ K shown in the inset of the lower panel of **Figure 1D**, indicating that the AFM fluctuations are characterized to be stripe type and do not change with x.

The x-T phase diagram (**Figure 1A**) of FeSe$_{1-x}$S$_x$ at ambient p allowed Wiecki et al. to examine the correlation between AFM fluctuations and T_c, and it was shown to persist, despite the presence of a nematic QPT isolated from an AFM order. The maximum values of $1/T_1T$ first increased when x was changed from 0 to 0.09, then decreased for $x = 0.15$ and higher, similar to the x dependence of T_c shown in **Figure 1A**. **Figures 1E,F** taken from Ref. [18] are contour plots of the magnitude of AFM fluctuations determined by $1/T_1T$ data in FeSe under p (E) and in FeSe$_{1-x}$S$_x$ at ambient p (F), respectively, along with their respective phase diagrams. It can be seen that T_c is enhanced at the p or x values where AFM fluctuations are stronger. This indicates the correlation between T_c and AFM fluctuations in both cases and also demonstrates the primary importance of AFM fluctuations to SC in FeSe$_{1-x}$S$_x$. It was also pointed out that, although nematic fluctuations are most strongly enhanced near the nematic QCP at $x \sim 0.17$ in the case of FeSe$_{1-x}$S$_x$, no clear correlation with T_c was observed [18].

4 ANTIFERROMAGNETIC FLUCTUATIONS AND SUPERCONDUCTIVITY WITHOUT NEMATICITY

With the firm establishment of the correlation between AFM fluctuations and SC in FeSe$_{1-x}$S$_x$, the question then arose about the role of nematicity on the relationship. As described above, FeSe$_{1-x}$S$_x$ provides a suitable platform for the study of the role of nematicity on the relationship by changing samples as reported by Wiecki et al. [18]. The application of pressure on FeSe$_{1-x}$S$_x$ also provides a versatile opportunity to study the effect of nematicity on the relationship. This has an advantage because p is known as one of the clean tuning parameters which control the ground state without changing the composition avoiding any additional effects of S substitutions such as homogeneity by changing x. Several ^{77}Se NMR studies on single crystalline FeSe$_{1-x}$S$_x$ under pressure have been carried out [37, 38, 41, 59]. Here we show the results of NMR measurements under pressure up to 2.1 GPa on $x = 0.09$ whose p-T phase diagram is shown in **Figure 2A** reported in Ref. [37]. With p, the nematic phase is suppressed and disappears around the critical pressure $p_c \sim 0.5$ GPa, and an AFM state appears above 3 GPa with a dome-shaped Fermi-liquid phase between nematic and AFM phases. T_c shows a clear p dependence with a double dome structure with and without long-range nematicity, making the system suitable in investigating the role of nematicity on the relationship.

Figure 2B shows the T dependence of $1/T_1T$ for $x = 0.09$ under $H \| ab$ (black) and $H \| c$ (red) at several pressures, taken from the study by Rana *et al* [37]. Below $p_c = 0.5$ GPa, with decreasing T, $1/T_1T$ increases below ~70 K showing Curie-Weiss like behavior originating from two dimensional AFM fluctuations and starts to decrease around T_c (T_c for $H \| ab$ are shown by black arrows in the figures). On the other hand, above 0.5 GPa, $1/T_1T$ exhibits quite different temperature dependences in comparison with those observed at low pressures. Although $1/T_1T$ is slightly enhanced below ~70 K, indicating the existence of the AFM spin fluctuations, $1/T_1T$s are nearly constant exhibiting the so-called Korringa behavior, expected for Fermi-liquid state below the temperature (defined as T_{FL}) marked by blue arrows. Thus the results indicate that the nature of AFM fluctuations changes below and above $p_c = 0.5$ GPa in FeSe$_{0.91}$S$_{0.09}$.

Similar T dependences of $1/T_1T$ have also been reported in ^{77}Se NMR studies of FeSe$_{1-x}$S$_x$ by Kuwayama et al. [38, 41] under p up to 3.9 GPa. The authors pointed out that AFM fluctuations with different **q** vectors may be responsible for the two distinct SC domes [41]. However, Rana *et al* found that the AFM fluctuations are characterized to be stripe type and p independent by showing the fact that the ratios R are close to ~ 1.5 at low temperatures for all measured p shown in the insets of **Figure 2B**.

Then what is the difference in the nature of AFM fluctuations in the presence and absence of nematic order? The idea that nematicity changes the relationship between T_c and AFM fluctuations was proposed by Rana et al [37] and can be clearly seen in **Figure 2C** taken from that study. Here, in the x axis, the maximum values of $1/T_1T$ with $H \| ab$ were taken as a representative of the magnitude of AFM fluctuations for different values of x and p in FeSe$_{1-x}$S$_x$. The corresponding x and p dependent T_c values were plotted in the y axis. The data included for x = 0, 0.12 and 0.29 were taken from Refs. [17, 58, 60], Ref. [41] and Ref. [18], respectively, while those for $x = 0.09$ were reported by Ref. [37]. These experimental data were classified into two groups: one that includes the data points where T_c and AFM fluctuations are in the nematic order, and another that includes those measured in the absence of nematic order. The slope for the linear fitting of the data points in the absence of nematicity was higher by a factor of ~ 5 compared to the slope for the linear fitting of those in the presence of nematicity. The results indicate that, for example, T_c is less sensitive to the strength of spin fluctuations in the tetragonal phase of FeSe$_{1-x}$S$_x$ at ambient pressure for $x < 0.17$ while it is largely enhanced in the orthorhombic phase of FeSe$_{0.91}$S$_{0.09}$ above 0.5 GPa even with a small increase in AFM fluctuations. When nematicity is absent, the AFM fluctuations in this system are present at both the wave vectors $\mathbf{q} = (\pi, 0)$ and $\mathbf{q} = (0, \pi)$ due to the four-fold rotational symmetry (C4) of the tetragonal state. However, in the presence of nematicity, the rotational symmetry is reduced to two-fold rotational symmetry (C2) and the AFM fluctuations are present at only one of the wave vectors, either vector $\mathbf{q} = (\pi, 0)$ or $\mathbf{q} = (0, \pi)$ [61, 62]. Based on those results, Rana *et al.* pointed out that the AFM fluctuations with C4 symmetry are more effective in enhancing T_c for the FeSe$_{1-x}$S$_x$ system.

5 SUMMARY

We presented a brief overview of ^{77}Se NMR studies in $\mathrm{FeSe}_{1-x}\mathrm{S}_x$ at ambient pressure and under pressure, especially focusing on the role of nematicity on the relationship between superconducting transition temperature T_c and antiferromagnetic (AFM) fluctuations. It was shown that T_c has a positive relationship with AFM fluctuations, suggesting the importance of AFM fluctuations in the pairing mechanism of superconducting electrons in $\mathrm{FeSe}_{1-x}\mathrm{S}_x$. Furthermore, nematicity is found to play a central role on the positive relationship. In the absence of nematic order, T_c can be greatly enhanced by AFM fluctuations. When the nematic order is present, this enhancement decreases by a factor of ~ 5. The evidence of the impact of nematicity on the relationship between superconductivity and AFM fluctuations has emerged from various ^{77}Se NMR studies in the $\mathrm{FeSe}_{1-x}\mathrm{S}_x$ system under pressure.

Although the findings provide a renewed insight on the relationships between nematicity, magnetism, and unconventional superconductivity in Fe-based superconductors, the origin for the strong impact of nematicity on the relationship between T_c and AFM fluctuations is still an open question. Further detailed experimental as well as theoretical investigations of the underlying reason behind the impact of nematicity on the relationships between superconductivity and AFM fluctuations would bring us a step towards understanding the physical mechanism behind unconventional superconductivity.

AUTHOR CONTRIBUTIONS

All authors listed have made a substantial, direct, and intellectual contribution to the work and approved it for publication.

FUNDING

The work at Ames Laboratory was supported by the U.S. Department of Energy (DOE), Office of Basic Energy Sciences, Division of Materials Sciences and Engineering. Ames Laboratory is operated for the U.S. DOE by Iowa State University under Contract No. DE-AC02-07CH11358.

ACKNOWLEDGMENTS

The authors would like to acknowledge precious collaborations and fruitful discussions with Paul Wiecki, Anna E. Böhmer, Paul C. Canfield, Sergey L. Bud'ko, Raphael Fernandes, Raquel A. Riberio, G. G. Lesseux, Yongbin Lee, and Qing-Ping Ding.

REFERENCES

1. Curro NJ, Caldwell T, Bauer ED, Morales LA, Graf MJ, Bang Y, et al. Unconventional Superconductivity in PuCoGa$_5$. *Nature* (2005) 434:622–5. doi:10.1038/nature03428
2. Hattori T, Ihara Y, Nakai Y, Ishida K, Tada Y, Fujimoto S, et al. Superconductivity Induced by Longitudinal Ferromagnetic Fluctuations in UCoGe. *Phys Rev Lett* (2012) 108:066403. doi:10.1103/PhysRevLett.108.066403
3. Scalapino DJ. A Common Thread: the Pairing Interaction for Unconventional Superconductors. *Rev Mod Phys* (2012) 84:1383–417. doi:10.1103/RevModPhys.84.1383
4. Canfield PC, Bud'ko SL. Preserved Entropy and Fragile Magnetism. *Rep Prog Phys* (2016) 79:084506. doi:10.1088/0034-4885/79/8/084506
5. Brando M, Belitz D, Grosche FM, Kirkpatrick TR. Metallic Quantum Ferromagnets. *Rev Mod Phys* (2016) 88:025006. doi:10.1103/RevModPhys.88.025006
6. Bertel E, Menzel A. Fluctuating Charge Order: a Universal Phenomenon in Unconventional Superconductivity. *Symmetry* (2016) 8:45. doi:10.3390/sym8060045
7. Johnston DC. The Puzzle of High Temperature Superconductivity in Layered Iron Pnictides and Chalcogenides. *Adv Phys* (2010) 59:803–1061. doi:10.1080/00018732.2010.513480
8. Canfield PC, Bud'ko SL. FeAs-Based Superconductivity: A Case Study of the Effects of Transition Metal Doping on BaFe$_2$As$_2$. *Annu Rev Condens Matter Phys* (2010) 1:27–50. doi:10.1146/annurev-conmatphys-070909-104041
9. Stewart GR. Superconductivity in Iron Compounds. *Rev Mod Phys* (2011) 83:1589–652. doi:10.1103/RevModPhys.83.1589
10. Kuo H-H, Chu J-H, Palmstrom JC, Kivelson SA, Fisher IR. Ubiquitous Signatures of Nematic Quantum Criticality in Optimally Doped Fe-Based Superconductors. *Science* (2016) 352:958–62. doi:10.1126/science.aab0103
11. Lederer S, Schattner Y, Berg E, Kivelson SA. Enhancement of Superconductivity Near a Nematic Quantum Critical Point. *Phys Rev Lett* (2015) 114:097001. doi:10.1103/PhysRevLett.114.097001
12. Lederer S, Schattner Y, Berg E, Kivelson SA. Superconductivity and Non-Fermi Liquid Behavior Near a Nematic Quantum Critical Point. *Proc Natl Acad Sci USA* (2017) 114:4905–10. doi:10.1073/pnas.1620651114
13. Böhmer AE, Kreisel A. Nematicity, Magnetism and Superconductivity in FeSe. *J Phys Condens Matter* (2018) 30:023001. doi:10.1088/1361-648X/aa9caa
14. Hsu F-C, Luo J-Y, Yeh K-W, Chen T-K, Huang T-W, Wu PM, et al. Superconductivity in the PbO-type Structure α-FeSe. *Proc Natl Acad Sci* (2008) 105:14262–4. doi:10.1073/pnas.0807325105
15. McQueen TM, Williams AJ, Stephens PW, Tao J, Zhu Y, Ksenofontov V, et al. Tetragonal-to-Orthorhombic Structural Phase Transition at 90 K in the Superconductor Fe$_{1.01}$Se. *Phys Rev Lett* (2009) 103:057002. doi:10.1103/PhysRevLett.103.057002
16. Baek S-H, Efremov DV, Ok JM, Kim JS, van den Brink J, Büchner B. Orbital-driven Nematicity in FeSe. *Nat Mater* (2015) 14:210–4. doi:10.1038/nmat4138
17. Imai T, Ahilan K, Ning FL, McQueen TM, Cava RJ. Why Does Undoped FeSe Become a High-T_c Superconductor under Pressure. *Phys Rev Lett* (2009) 102:177005. doi:10.1103/PhysRevLett.102.177005
18. Wiecki P, Rana K, Böhmer AE, Lee Y, Bud'ko SL, Canfield PC, et al. Persistent Correlation between Superconductivity and Antiferromagnetic Fluctuations Near a Nematic Quantum Critical Point in FeSe$_{1-x}$S$_x$. *Phys Rev B* (2018) 98:020507. doi:10.1103/PhysRevB.98.020507
19. Mizuguchi Y, Tomioka F, Tsuda S, Yamaguchi T, Takano Y. Superconductivity at 27 K in Tetragonal FeSe under High Pressure. *Appl Phys Lett* (2008) 93:152505. doi:10.1063/1.3000616
20. Margadonna S, Takabayashi Y, Ohishi Y, Mizuguchi Y, Takano Y, Kagayama T, et al. Pressure Evolution of the Low-temperature Crystal Structure and Bonding of the Superconductor FeSe (T_c=37 K). *Phys Rev B* (2009) 80:064506. doi:10.1103/PhysRevB.80.064506
21. Medvedev S, McQueen TM, Troyan IA, Palasyuk T, Eremets MI, Cava RJ, et al. Electronic and Magnetic Phase Diagram of β-Fe$_{1.01}$Se with Superconductivity at 36.7 K under Pressure. *Nat Mater* (2009) 8:630–3. doi:10.1038/nmat2491
22. Terashima T, Kikugawa N, Kasahara S, Watashige T, Shibauchi T, Matsuda Y, et al. Pressure-induced Antiferromagnetic Transition and Phase Diagram in FeSe. *J Phys Soc Jpn* (2015) 84:063701. doi:10.7566/JPSJ.84.063701

23. Bendele M, Amato A, Conder K, Elender M, Keller H, Klauss H-H, et al. Pressure Induced Static Magnetic Order in Superconducting FeSe$_{1-x}$. *Phys Rev Lett* (2010) 104:087003. doi:10.1103/PhysRevLett.104.087003
24. Kothapalli K, Böhmer AE, Jayasekara WT, Ueland BG, Das P, Sapkota A, et al. Strong Cooperative Coupling of Pressure-induced Magnetic Order and Nematicity in FeSe. *Nat Commun* (2016) 7:12628. doi:10.1038/ncomms12728
25. Coldea AI. Electronic Nematic States Tuned by Isoelectronic Substitution in Bulk FeSe$_{1-x}$S$_x$. *Front Phys* (2021) 8:594500. doi:10.3389/fphy.2020.594500
26. Reiss P, Watson MD, Kim TK, Haghighirad AA, Woodruff DN, Bruma M, et al. Suppression of Electronic Correlations by Chemical Pressure from FeSe to FeS. *Phys Rev B* (2017) 96:121103. doi:10.1103/PhysRevB.96.121103
27. Coldea AI, Blake SF, Kasahara S, Haghighirad AA, Watson MD, Knafo W, et al. Evolution of the Low-Temperature Fermi Surface of Superconducting FeSe$_{1-x}$S$_x$ across a Nematic Phase Transition. *Npj Quant Mater* (2019) 4:2. doi:10.1038/s41535-018-0141-0
28. Hosoi S, Matsuura K, Ishida K, Wang H, Mizukami Y, Watashige T, et al. Nematic Quantum Critical Point without Magnetism in FeSe$_{1-x}$S$_x$ Superconductors. *Proc Natl Acad Sci USA* (2016) 113:8139–43. doi:10.1073/pnas.1605806113
29. Licciardello S, Buhot J, Lu J, Ayres J, Kasahara S, Matsuda Y, et al. Electrical Resistivity across a Nematic Quantum Critical Point. *Nature* (2019) 567:213–7. doi:10.1038/s41586-019-0923-y
30. Abdel-Hafiez M, Zhang Y-Y, Cao Z-Y, Duan C-G, Karapetrov G, Pudalov VM, et al. Superconducting Properties of Sulfur-doped Iron Selenide. *Phys Rev B* (2015) 91:165109. doi:10.1103/PhysRevB.91.165109
31. Watson MD, Kim TK, Haghighirad AA, Blake SF, Davies NR, Hoesch M, et al. Suppression of Orbital Ordering by Chemical Pressure in FeSe$_{1-x}$S$_x$. *Phys Rev B* (2015) 92:121108. doi:10.1103/PhysRevB.92.121108
32. Hanaguri T, Iwaya K, Kohsaka Y, Machida T, Watashige T, Kasahara S, et al. Two Distinct Superconducting Pairing States Divided by the Nematic End Point in FeSe$_{1-x}$S$_x$. *Sci Adv* (2018) 4:eaar6419. doi:10.1126/sciadv.aar6419
33. Sato Y, Kasahara S, Taniguchi T, Xing X, Kasahara Y, Tokiwa Y, et al. Abrupt Change of the Superconducting gap Structure at the Nematic Critical point in FeSe$_{1-x}$S$_x$. *Proc Natl Acad Sci USA* (2018) 115:1227–31. doi:10.1073/pnas.1717331115
34. Hashimoto T, Ota Y, Tsuzuki A, Nagashima T, Fukushima A, Kasahara S, et al. Bose-Einstein Condensation Superconductivity Induced by Disappearance of the Nematic State. *Sci Adv* (2020) 6:eabb9052. doi:10.1126/sciadv.abb9052
35. Matsuura K, Mizukami Y, Arai Y, Sugimura Y, Maejima N, Machida A, et al. Maximizing T_c by Tuning Nematicity and Magnetism in FeSe$_{1-x}$S$_x$ Superconductors. *Nat Commun* (2017) 8:1143. doi:10.1038/s41467-017-01277-x
36. Xiang L, Kaluarachchi US, Böhmer AE, Taufour V, Tanatar MA, et al. Dome of Magnetic Order inside the Nematic Phase of Sulfur-Substituted FeSe under Pressure. *Phys Rev B* (2017) 96:024511. doi:10.1103/PhysRevB.96.024511
37. Rana K, Xiang L, Wiecki P, Ribeiro RA, Lesseux GG, Böhmer AE, et al. Impact of Nematicity on the Relationship between Antiferromagnetic Fluctuations and Superconductivity in FeSe$_{0.91}$S$_{0.09}$ under Pressure. *Phys Rev B* (2020) 101:180503. doi:10.1103/PhysRevB.101.180503
38. Kuwayama T, Matsuura K, Gouchi J, Yamakawa Y, Mizukami Y, Kasahara S, et al. Pressure-induced Reconstitution of Fermi Surfaces and Spin Fluctuations in S-Substituted FeSe. *Sci Rep* (2021) 11:17265. doi:10.1038/s41598-021-96277-9
39. Reiss P, Graf D, Haghighirad AA, Knafo W, Drigo L, Bristow M, et al. Quenched Nematic Criticality and Two Superconducting Domes in an Iron-Based Superconductor. *Nat Phys* (2019) 16:89–94. doi:10.1038/s41567-019-0694-2
40. Reiss P, Graf D, Haghighirad AA, Vojta T. Signatures of a Quantum Griffiths Phase Close to an Electronic Nematic Quantum Phase Transition. *Phys Rev Lett* (2021) 127:246402. doi:10.1103/PhysRevLett.127.246402
41. Kuwayama T, Matsuura K, Mizukmami Y, Kasahara S, Matsuda Y, Shibauchi T, et al. ^{77}Se-NMR Study under Pressure on 12%-S Doped FeSe. *J Phys Soc Jpn* (2019) 88:033703. doi:10.7566/JPSJ.88.033703
42. Moriya T. The Effect of Electron-electron Interaction on the Nuclear Spin Relaxation in Metals. *J Phys Soc Jpn* (1963) 18:516–20. doi:10.1143/JPSJ.18.516
43. Slichter CP. *Principles of Magnetic Resonance*. 3rd ed. Berlin Heidelberg: Springer (1990). doi:10.1007/978-3-662-09441-9
44. Narath A, Weaver HT. Effects of Electron-electron Interactions on Nuclear Spin-Lattice Relaxation Rates and Knight Shifts in Alkali and Noble Metals. *Phys Rev* (1968) 175:373–82. doi:10.1103/PhysRev.175.373
45. Ahilan K, Ning FL, Imai T, Sefat AS, McGuire MA, Sales BC, et al. Superconductivity Near a Quantum Critical Point in Ba(Fe$_{1-x}$Co$_x$)$_2$As$_2$ *Physica C: Superconductivity its Appl* (2010) 470:S273–S275. doi:10.1016/j.physc.2009.11.124
46. Nakai Y, Iye T, Kitagawa S, Ishida K, Kasahara S, Shibauchi T, et al. Normal-state Spin Dynamics in the Iron-Pnictide Superconductors BaFe$_2$(As$_{1-x}$P$_x$)$_2$ and Ba(Fe$_{1-x}$Co$_x$)$_2$As$_2$ probed with NMR Measurements. *Phys Rev B* (2013) 87:174507. doi:10.1103/PhysRevB.87.174507
47. Kitagawa S, Nakai Y, Iye T, Ishida K, Kamihara Y, Hirano M, et al. Stripe Antiferromagnetic Correlations in LaFeAsO$_{1-x}$F$_x$ probed by ^{75}As NMR. *Phys Rev B* (2010) 81:212502. doi:10.1103/PhysRevB.81.212502
48. Kitagawa K, Katayama N, Ohgushi K, Takigawa M. Antiferromagnetism of SrFe$_2$As$_2$ Studied by Single-Crystal ^{75}As-NMR. *J Phys Soc Jpn* (2009) 78:063706. doi:10.1143/JPSJ.78.063706
49. Hirano M, Yamada Y, Saito T, Nagashima R, Konishi T, Toriyama T, et al. Potential Antiferromagnetic Fluctuations in Hole-Doped Iron-Pnictide Superconductor Ba$_{1-x}$K$_x$Fe$_2$As$_2$ Studied by ^{75}As Nuclear Magnetic Resonance Measurement. *J Phys Soc Jpn* (2012) 81:054704. doi:10.1143/JPSJ.81.054704
50. Furukawa Y, Roy B, Ran S, Bud'ko SL, Canfield PC. Suppression of Electron Correlations in the Collapsed Tetragonal Phase of CaFe$_2$As$_2$ under Ambient Pressure Demonstrated by ^{75}As NMR/NQR Measurements. *Phys Rev B* (2014) 89:121109. (R). doi:10.1103/PhysRevB.89.121109
51. Wang PS, Sun SS, Cui Y, Song WH, Li TR, Yu R, et al. Pressure Induced Stripe-Order Antiferromagnetism and First-Order Phase Transition in FeSe. *Phys Rev Lett* (2016) 117:237001. doi:10.1103/PhysRevLett.117.237001
52. Pandey A, Quirinale DG, Jayasekara W, Sapkota A, Kim MG, Dhaka RS, et al. Crystallographic, Electronic, Thermal, and Magnetic Properties of Single-crystal SrCo$_2$As$_2$. *Phys Rev B* (2013) 88:014526. doi:10.1103/PhysRevB.88.014526
53. Ding Q-P, Wiecki P, Anand VK, Sangeetha NS, Lee Y, Johnston DC, et al. Volovik Effect and Fermi-Liquid Behavior in the s-wave Superconductor CaPd$_2$As$_2$: As^{75} NMR-NQR Measurements. *Phys Rev B* (2016) 93:140502. doi:10.1103/PhysRevB.93.140502
54. Kamihara Y, Hiramatsu H, Hirano M, Kawamura R, Yanagi H, Kamiya T, et al. Iron-based Layered Superconductor: LaOFeP. *J Am Chem Soc* (2006) 128:10012–3. doi:10.1021/ja063355c
55. Kamihara Y, Watanabe T, Hirano M, Hosono H. Iron-based Layered Superconductor La[O$_{1-x}$F$_x$]FeAs (x = 0.05–0.12) with T_c = 26 K. *J Am Chem Soc* (2008) 130:3296–7. doi:10.1021/ja800073m
56. Kotegawa H, Fujita M. Magnetic Excitations in Iron Chalcogenide Superconductors. *Sci Tech Adv Mater* (2012) 13:054302. doi:10.1088/1468-6996/13/5/054302
57. Torchetti DA, Fu M, Christensen DC, Nelson KJ, Imai T, Lei HC, et al. ^{77}Se NMR Investigation of the K$_x$Fe$_{2-y}$Se$_2$ High-T_c superconductor (T_c = 33 K). *Phys Rev B* (2011) 83:104508. doi:10.1103/PhysRevB.83.104508
58. Böhmer AE, Arai T, Hardy F, Hattori T, Iye T, Wolf T, et al. Origin of the Tetragonal-To-Orthorhombic Phase Transition in FeSe: A Combined Thermodynamic and NMR Study of Nematicity. *Phys Rev Lett* (2015) 114:027001. doi:10.1103/PhysRevLett.114.02700210.1103/PhysRevLett.114.027001
59. Kuwayama T, Matsuura K, Mizukami Y, Kasahara S, Matsuda Y, Shibauchi T, et al. NMR Study under Pressure on the Iron-based Superconductor FeSe$_{1-x}$S$_x$ (x = 0.12 and 0.23): Relationship between Nematicity and AF Fluctuations. *Mod Phys Lett B* (2020) 34:2040048. doi:10.1142/S0217984920400485
60. Wiecki P, Nandi M, Böhmer AE, Bud'ko SL, Canfield PC, Furukawa Y. NMR Evidence for Static Local Nematicity and its Cooperative Interplay with Low-energy Magnetic Fluctuations in FeSe under Pressure. *Phys Rev B* (2017) 96:180502. doi:10.1103/PhysRevB.96.180502

61. Fernandes RM, Chubukov AV, Knolle J, Eremin I, Schmalian J. Preemptive Nematic Order, Pseudogap, and Orbital Order in the Iron Pnictides. *Phys Rev B* (2012) 85:024534. doi:10.1103/PhysRevB.85.024534
62. Fernandes RM, Chubukov AV, Schmalian J. What Drives Nematic Order in Iron-Based Superconductors. *Nat Phys* (2014) 10:97–104. doi:10.1038/nphys2877

Conflict of Interest: The authors declare that the research was conducted in the absence of any commercial or financial relationships that could be construed as a potential conflict of interest.

The handling editor declared a past co-authorship with the authors KR and YF.

frontiers | Frontiers in Physics

REVIEW
published: 04 April 2022
doi: 10.3389/fphy.2022.866664

Optical Fingerprints of Nematicity in Iron-Based Superconductors

Leonardo Degiorgi *

Laboratorium für Festkörperphysik, ETH—Zürich, Zürich, Switzerland

Nematicity, which refers to a phase of broken rotational but preserved translational symmetry, is underlined by the appearance of anisotropic properties and leaves remarkable fingerprints in all measurable physical quantities upon crossing the structural tetragonal-orthorhombic transition at T_s in several iron-based materials. Here, we review part of our own broadband optical investigations, addressing the impact of nematicity on the charge dynamics, as a function of temperature and of tunable applied stress, the latter acting as an external symmetry breaking field. We shall first focus our attention on FeSe, which undergoes a nematic (structural) transition without any subsequent onset of magnetic ordering below T_s. FeSe thus provides an opportunity to study nematicity without the limitations due to the reconstruction of the Fermi surface because of the spin-density-wave collective state in the orthorhombic phase, typical for several other iron-based superconductors. Our data reveal an astonishing anisotropy of the optical response in the mid-infrared-to-visible spectral range, which bears testimony of an important polarization of the underlying electronic structure in agreement with angle-resolved-photoemission-spectroscopy results. Our findings at high energy scales support models for the nematic phase resting on an orbital-ordering mechanism, supplemented by orbital selective band renormalization. The optical results at energies close to the Fermi level furthermore emphasize scenarios relying on scattering by anisotropic spin-fluctuations and shed new light on the origin of nematicity in FeSe. Moreover, the composition at which the associated Weiss temperature of the nematic susceptibility extrapolates to zero is found to be close to optimal doping (i.e., in coincidence with the largest superconducting transition temperature), boosting the debate to what extent nematic fluctuations contribute to the pairing-mechanism and generally affect the electronic structure of iron-based superconductors. The present review then offers a discussion of our optical data on the optimally hole-doped $Ba_{0.6}K_{0.4}Fe_2As_2$. We show that the stress-induced optical anisotropy in the infrared spectral range is reversible upon sweeping the applied stress and occurs only below the superconducting transition temperature. These findings demonstrate that there is a large electronic nematicity at optimal doping which extends right under the superconducting dome.

Keywords: nematicity, optical properties, electronic structure, spin fluctuations, orthorhombicity

Edited by:
Laura Fanfarillo,
International School for Advanced Studies (SISSA), Italy

Reviewed by:
Andrea Perucchi,
Elettra Sincrotrone Trieste, Italy
Jiun-Haw Chu,
University of Washington, United States

***Correspondence:**
Leonardo Degiorgi
degiorgi@solid.phys.ethz.ch

Specialty section:
This article was submitted to Condensed Matter Physics, a section of the journal Frontiers in Physics

Received: *31 January 2022*
Accepted: *16 February 2022*
Published: *04 April 2022*

Citation:
Degiorgi L (2022) Optical Fingerprints of Nematicity in Iron-Based Superconductors. Front. Phys. 10:866664. doi: 10.3389/fphy.2022.866664

INTRODUCTION

Nematicity lately arose to a key concept in solid state physics, because of its intimate relationship to the onset of superconductivity at high temperature [1–3]. It was soon recognised that this is a hallmark of iron-based superconductors, which are deemed to be unconventional and set new paradigms for superconductivity [4]. Nematicity, for which the electronic system breaks a discrete rotational symmetry of the crystal lattice without altering the existing translational symmetry, was originally brought into action in order to justify the anisotropy in the *dc* transport properties of the 122-materials $\mathrm{Ba(Fe_{1-x}Co_x)_2As_2}$ below their structural tetragonal-to-orthorhombic phase transition at T_s [5, 6]. Since the anisotropy of any measurable physical quantity is considerably larger than any reasonable expectations by solely pondering the lattice distortion, it has been conjectured that nematicity is electronic in nature. A central quantity is the nematic susceptibility in the tetragonal phase, for instance as evinced by elastoresistance measurements (i.e., measurements of the induced resistivity anisotropy due to anisotropic strain) [7, 8], which incidentally turns out to diverge in a Curie-like fashion. Such an astonishing divergence of the nematic susceptibility was also inferred by Raman [9–11] and elastic moduli [12] investigations.

In a broader perspective, electronic nematicity is not only a topic of relevance for the iron-based superconductors but its far-reaching consequences affect several cuprates and some heavy-fermion compounds, just to quote a few examples of other unconventional superconductors, which in fact provide signatures for strongly anisotropic electronic phases [13], as well.

Another basic ingredient of unconventional superconductors is the interplay of structural, magnetic and orbital order, which cannot be considered apart and disconnected from the onset of the nematic phase [4, 14–16]. Being here the focus on iron-based superconductors, it is well established that in almost all of them a structural transition at T_s coincides with or precedes a magnetic transition at T_N and the related stripe-type magnetic order is coupled to the orthorhombic lattice distortion. The anticipated anisotropy of all physical quantities implicit in the nematic phase will be also experienced, because of symmetry, by all structural, magnetic as well as orbital properties. This thus hampers the determination of the driving mechanism and microscopic origin of nematicity [16]. In this context, FeSe lately acquired a prominent role within the panorama of iron-based materials, since it harbors a tetragonal-to-orthorhombic structural phase transition at $T_s \simeq 90$ K, where the lattice breaks the $C4$ rotational symmetry, in the absence of any subsequent, ambient pressure long-range magnetic order, prior the onset of superconductivity at $T_c = 8$ K [17, 18]. Therefore, FeSe is an ideal playground for the study of nematicity, since the absence of the Fermi surface folding due to the spin-density-wave-like antiferromagnetic order allows circumventing its concomitant coupling to the lattice structural transition.

Furthermore, the divergent nematic susceptibility, as observed in the strained-dependent *dc* transport properties, is empirically established in several iron-based superconductors even up to optimally doped compositions [19]. It is then a generic property spanning the great part of the phase diagram and led to speculate about scenarios for which nematic quantum criticality could perhaps enhance the pairing interaction [16, 20, 21]. Such an opportunity is intriguing and could open novel perspectives towards the onset of superconductivity in iron-based superconductors, as it has been already envisaged for the cuprates [22, 23]. There is an ongoing theoretical debate about the relationship between superconductivity and nematicity [13]. Equally, there is still the quest to better experimentally scrutinise the influence of nematic fluctuations on the electronic properties over a large energy range and at temperatures (T) extending under the superconducting dome, which are not accessible by elastoresistive technique. This motivated us to address the hole-doped $\mathrm{Ba_{1-x}K_xFe_2As_2}$, which displays a nematic state up to $x \sim 0.3$, when the antiferromagnetic phase boundary is reached [24]. We specifically choose the optimally-doped $x = 0.4$ compound ($T_c = 38.5$ K), which is an ideal composition in order to address the impact of the nematic fluctuations and their alleged relationship to superconductivity. Indeed, the nematic order fully disappears (i.e., $T_s = 0$) at this doping.

Here, we review data of our thorough broadband optical investigations of FeSe and $\mathrm{Ba_{0.6}K_{0.4}Fe_2As_2}$, consisting in the measurement of the optical reflectivity as a function of T for samples experiencing a tunable symmetry breaking field, given by uniaxial stress. We ultimately extract the optical conductivity from the far-infrared up to the ultraviolet. This review, based on our publications in Refs. [25–27], is organised as follows: first an ample presentation of the experiment and then a thorough display of the data on both selected materials, together with their own dedicated discussion. An overall summary and a future outlook will conclude this paper.

EXPERIMENT

Any phase transition that breaks a point group symmetry naturally leads to domain formation. In the case of a ferroelastic-like tetragonal-to-orthorhombic transition, as exhibited by underdoped iron-arsenide superconductors as well as by FeSe, a spontaneous strain at low T can be oriented in one of two possible directions, and a twin domain structure forms to minimize the elastic energy [5, 6]. Therefore, a tunable applied stress acts as a conjugate field to the orthorhombic distortion and enforces an adjustable population of domains oriented along a preferential direction, effectively bypassing sample twinning below T_s. Our mechanical device for applying stress, and thus detwinning the samples, is shown in **Figure 1** [28, 29] and consists of a spring bellows, which is made of stainless steel and it is mounted at the oxygen-free Cu cold finger of the cryostat. The bellows can be extended/retracted in order to exert and release *in* − *situ* uniaxial stress (generally abbreviated by p) on the lateral side of the sample. This is undoubtedly a major technical progress, since the capability to control the symmetry breaking field grants more experimental opportunities than in the original, yet pioneering optical work based on a mechanical clamp enabling a fixed and mostly unknown amount of compressive stress [5, 30, 31].

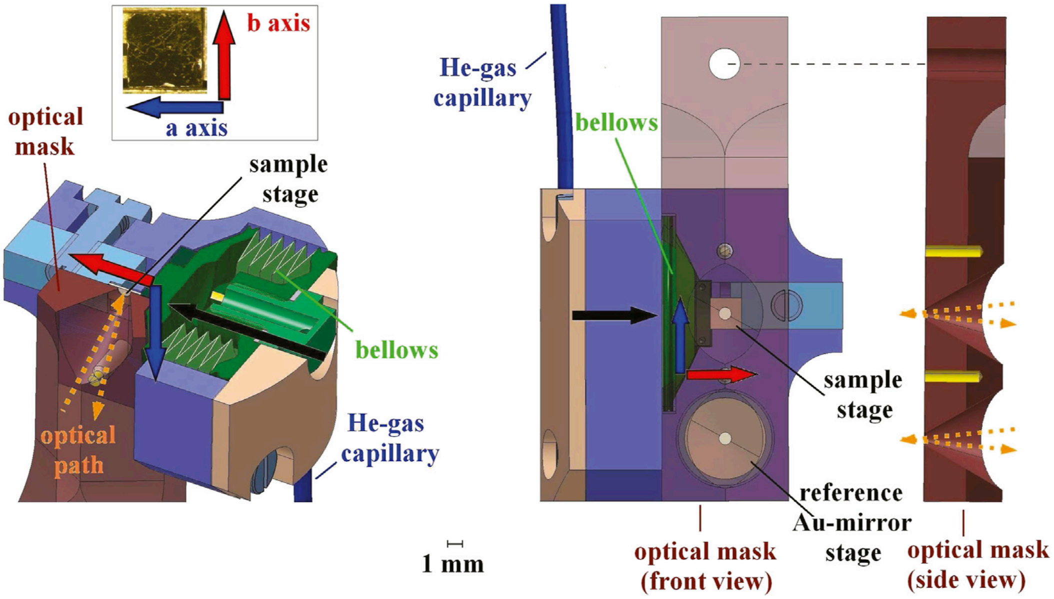

FIGURE 1 | (color online) (left) Three-dimensional schematic view of the stress device with a cross-section along the plane of the incident/reflected optical path. (right) Front view along the light path. By flushing He-gas into the spring bellows and evacuating its volume, one can exert and release stress, respectively, along the direction corresponding to the (shorter) orthorhombic *b*-axis, as indicated by the black arrow. The optical mask, placed on top of the stress device, defines equal spots of the sample and reference Au-mirror surface, which are exposed to the electromagnetic radiation polarized along the *a*- and *b*-axis (blue and red arrow, respectively). Reproduced from Ref. [29].

The stress device (**Figure 1**), with the specimens mounted into it, is then placed inside an Oxford SM 4000 cryostat coupled to a Fourier-transform infrared interferometer (Bruker Vertex 80v). This permits measurements of the frequency (ω) dependence of the reflectivity ($R(\omega)$) at nearly normal incidence [32] at different T and as a function of p in the spectral range from the far-infrared (FIR) up to the near-infrared (NIR), i.e. between 30 and 6,000 cm^{-1}. Room-temperature and stress-free data were complementary collected from NIR up to the ultra-violet (UV) range, i.e. 3200–48000 cm^{-1}. The electromagnetic radiation in all spectrometers was polarized along the a and b axes (**Figure 1**); in the following the measured reflectivity will be defined as R_a and R_b, respectively [28].

In displaying the data, we refer to the pressure of the He-gas flushed inside the volume of the bellows ($p_{bellows}$) in order to extend it: the effective stress felt by the sample (p_{sample}) depends on its size and thickness, so that $p_{bellows} = 0.1$ bar corresponds to an effective uniaxial stress of about $p_{sample} \sim 1.5$–2 MPa on our crystals. It has been widely established that an effective p of at least 10 MPa is enough to fully detwin the specimen and thus reveal the underlying symmetry-breaking [5]. The released p data are achieved upon retracting the bellows, thus by evacuating its volume (**Figure 1**). We report results obtained from zero-pressure-cooled (ZPC) 'pressure-loop' experiments: we reach the selected T without applying stress and at that fixed T we measure $R(\omega)$ at progressively increasing $p_{bellows}$ (i.e., tunable degree of detwinning) from 0 up to a material-dependent maximum pressure ranging between 0.8 and 1.2 bar. We subsequently collect $R(\omega)$ when stepwise releasing stress back to 0 bar, thus completing the p-loop.

Finally, the real part $\sigma_1(\omega)$ of the optical conductivity was obtained via the Kramers–Kronig (KK) transformation of $R(\omega)$ by applying suitable extrapolations at low and high frequencies. For the $\omega \to 0$ extrapolation, we made use of the Hagen-Rubens formula ($R(\omega) = 1 - 2\sqrt{\frac{\omega}{\sigma_{dc}}}$), inserting the *dc* conductivity values (σ_{dc}) consistent with the relative T dependence of the samples transport data, while above the upper frequency limit $R(\omega) \sim \omega^{-s}$ ($2 \leqslant s \leqslant 4$) [32].

Our original publications and their Supplemental Material [25–29] cited along this work should be consulted for more details on the experimental technique and set-up as well as samples growth.

RESULTS AND DISCUSSION

FeSe

We commence our data survey by the measured stress dependence of $R(\omega)$ in FeSe [25, 26], of which representative data in the FIR and mid-infrared (MIR) spectral range (i.e., for $\omega < 7{,}000\ \text{cm}^{-1}$) are shown in the main panel of **Figure 2A** at 10 K. The stress applied by the spring bellows of $p_{bellows} = 1.2$ bar corresponds to the situation for a fully detwinned specimen (i.e., at saturation). We can immediately recognise the overall (optical) metallicity of FeSe (inset of **Figure 2A**), identified by the increase of $R(\omega)$ below $2 \times 10^4\ \text{cm}^{-1}$ (i.e., plasma edge). The raw data explicitly convey the anisotropy of $R(\omega)$ between the two polarization directions at FIR-MIR frequencies. Such an anisotropy indeed develops from $R(\omega)$ at zero stress (see below), which shares the same trend over the whole investigated spectral range as in a previous work [33].

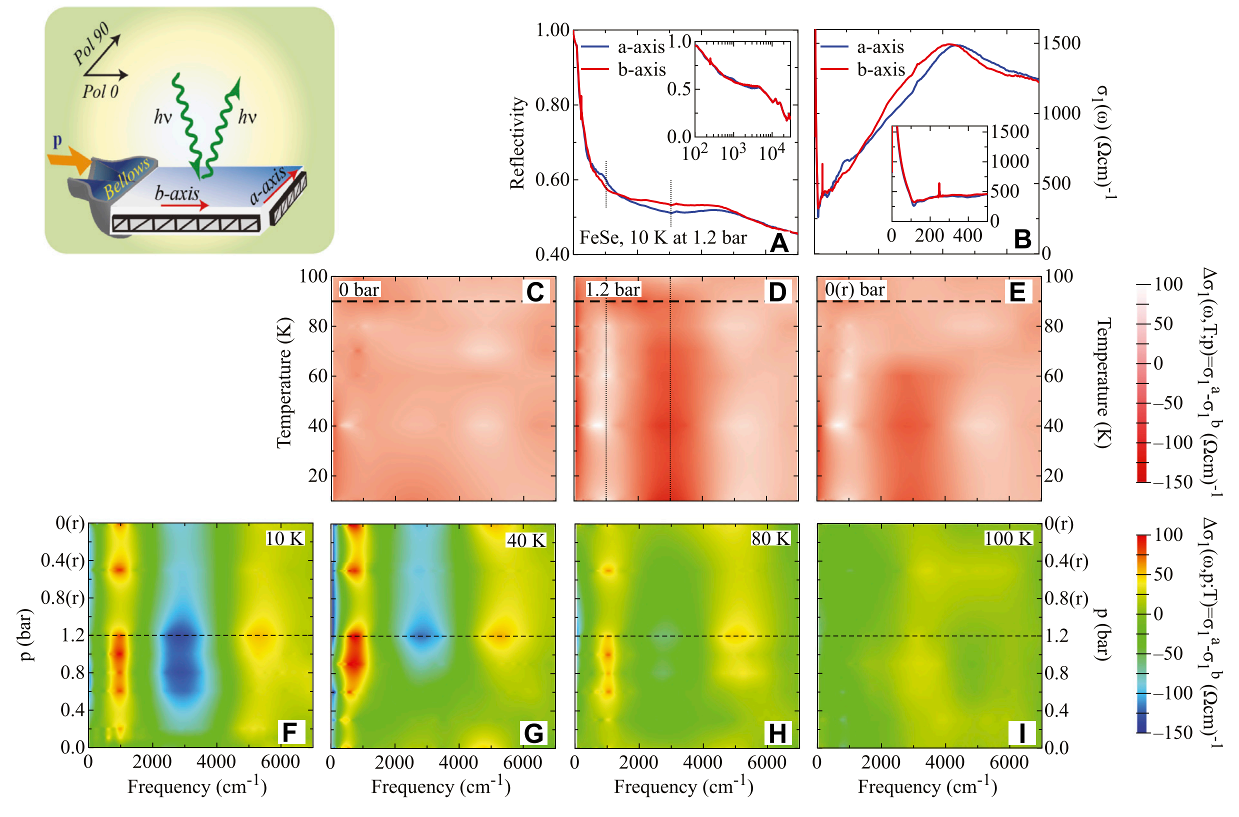

FIGURE 2 | (color online) Experimental setup as well as T and p dependence of the optical anisotropy in FeSe: The upper-left panel schematically shows a sample inside the mechanical device and emphasizes the orientation of its a- and b-axis with respect to the direction of the applied stress p. Polarized light parallel to the orthorhombic (elongated) a- and (short) b-axis (in our experimental set-up Pol 90 and Pol 0, respectively) illuminates the sample (see details in **Figure 1**). **(A)** Representative data of the optical reflectivity ($R(\omega)$) of FeSe at 10 K and 1.2 bar (i.e., at saturation) after a ZPC experiment; it emphasizes the optical anisotropy at MIR frequencies (1 eV = 8.06548 × 10^3 cm^{-1}) [25]. The inset shows $R_a(\omega)$ and $R_b(\omega)$ from the FIR up to the UV range with a logarithmic frequency scale. **(B)** Real part $\sigma_1(\omega)$ of the optical conductivity and its blow up pertinent to the FIR range (inset) at 10 K and 1.2 bar. **(C–E)** T dependence of the dichroism defined as $\Delta\sigma_1(\omega) = \sigma_1^a(\omega) - \sigma_1^b(\omega)$ at 0, 1.2 and released 0 bar after the ZPC p-loop experiment. The thick horizontal dashed line marks T_s. The thin vertical dotted lines in panels **(A)** and **(D)** mark the frequencies 1,000 and 3,000 cm^{-1}. **(F–I)** $\Delta\sigma_1(\omega)$ at selected T below and above T_s within each ZPC p-loop experiment. The thin horizontal dashed line marks p at saturation. A first-neighbor interpolation procedure is used in order to generate the color maps. Released p is denoted by "(r)". Reproduced from Ref. [26].

The polarisation dependence of $R(\omega)$ is also reflected in the excitation spectrum, represented by $\sigma_1(\omega)$, as shown at saturation in **Figure 2B**. An alternative illuminating quantity, in order to emphasise the optical anisotropy, is the so-called dichroism $\Delta\sigma_1(\omega) = \sigma_1^a(\omega) - \sigma_1^b(\omega)$, which is shown at three selected p of 0, 1.2 and released 0 bar after the p-loop experiment within the ZPC protocol in **Figures 2C–E**. The optical anisotropy is evident below T_s and is particularly well identified by the change of sign of $\Delta\sigma_1(\omega)$ around 1,000, 3,000 and 5,000 cm^{-1} at saturation. The evolution of the optical anisotropy at $T < T_s$ upon sweeping p can be equally recognised in $\Delta\sigma_1(\omega)$ at selected T within each p-loop experiment (**Figures 2F–I**). Furthermore, the anisotropy at dc (i.e., $\omega \rightarrow 0$) and for $T < T_s$ (inset of **Figure 2B**) is such that $\sigma_1^b(\omega) > \sigma_1^a(\omega)$ for fully detwinned specimens (i.e., $\Delta\sigma_1(\omega) < 0$, **Figure 2D**). This is consistent with the measured dc transport anisotropy and is reminiscent of the situation encountered in the hole-doped iron-pnictides [34].

Before going any further, we focus our attention on the hysteretic behavior of the optical anisotropy. To this goal, we shed light on the p dependence of $\Delta R_{ratio}(\omega) = (R_a(\omega)/R_b(\omega))$ - 1 at 1,000 and 3,000 cm^{-1} (dashed vertical lines in **Figure 2A**) for the ZPC p-loop measurements, shown in **Figure 3** for several representative T [25]. A clear half-hysteresis in the p dependence of ΔR_{ratio} is encountered for $T < T_s$ and at both frequencies, though with opposite sign. We claim that this startling hysteretic occurrence is likely due to twin boundary motion. A quite rapid enhancement in $|\Delta R_{ratio}|$ at low T shapes the so-called virgin curve of the hysteretic behaviour. Afterwards, the optical anisotropy starts to saturate for larger p (**Figures 3A,B,F,G**). Therefore, a relatively modest uniaxial stress of $p_{sample} \sim 6$ MPa is able to detwin the sample in the orthorhombic phase. The saturation of ΔR_{ratio} at $T \ll T_s$ presumably reflects complete detwinning of the sample, and any subsequent p dependence arises from the intrinsic response to p of the orthorhombic structure. The optical anisotropy is achieved more gradually for $T \leq T_s$ (**Figures 3C,H**), at which indeed the initial curve increases smoothly. At T_s (**Figures 3D,I**), the half-hysteresis loop has essentially collapsed and for $T \geq T_s$ (**Figures 3E,J**) the material is tetragonal and no half-hysteresis is observed so that the

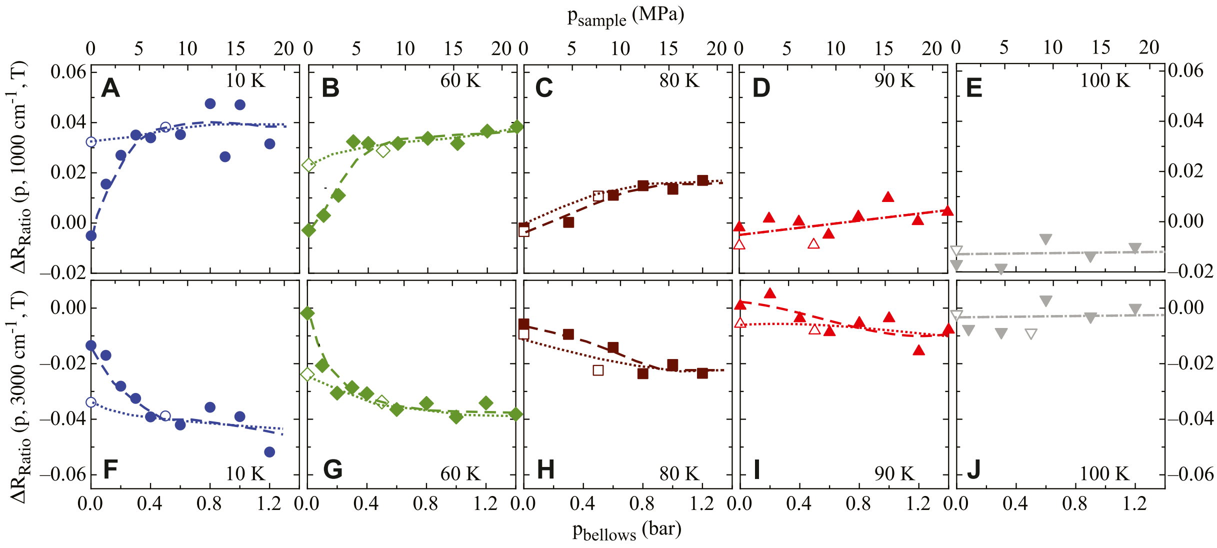

FIGURE 3 | (color online) Optical anisotropy given by ΔR_{ratio} (see text) read at **(A–E)** 1,000 and **(F–J)** 3,000 cm^{-1} (dashed vertical lines in **Figure 2A**) of FeSe as a function of applied stress p at representative T: full and open symbols denote increasing and decreasing p, respectively, for p-loop measurements following an initial ZPC protocol. Lower x-axis denotes He-gas p in the spring bellows ($p_{bellows}$) and upper x-axis the effective stress felt by the sample (p_{sample}). Dashed (increasing p) and dotted (releasing p) lines are drawn to guide the eye. Reproduced from Ref. [25].

optical anisotropy totally vanishes at 3,000 cm^{-1} and is weakly negative at 1,000 cm^{-1}.

We expect that the imbalance of the two twin orientations remains frozen in place at low T. This can be probed by the remanent optical anisotropy upon releasing p back to 0 [28]. At 10 K, the material barely shows changes in the optical anisotropy when p is released, indicating in fact that the sample remains in a near-single domain state. The intrinsic optical anisotropy of a fully detwinned but stress-free material is therefore given by ΔR_{ratio} at released $p = 0$. For increasing T, the thermally assisted domain-wall motion suppresses the anisotropy at released $p = 0$ [28]. Such a hysteretic behavior of $\Delta R_{ratio}(\omega)$ is equivalently mapped onto $\Delta\sigma_1(\omega)$, since its saturation value tends to persist at low T, while it vanishes for $T \rightarrow T_s$, upon releasing p (**Figures 2D,E** as well as **Figures 2F–I**).

Figure 4 summarizes the T dependence of ΔR_{ratio} for FeSe at 1,000 and 3,000 cm^{-1} read at fixed $p_{bellows}$ = 1.2 bar (i.e., at saturation (sat), ΔR^{sat}_{ratio}) from the p-loop experiments within the ZPC procedure (**Figure 3**), normalized by this quantity at 5 K. ΔR^{sat}_{ratio} at both energy scales undergoes a quite sharp onset at T_s and tends to flatten out below $T_s/2$. We reiterate that at 1,000 cm^{-1} $\Delta R^{sat}_{ratio} < 0$ slightly above T_s, anticipating an incipient optical anisotropy at infrared frequencies, consistent in the $\omega \rightarrow 0$ limit with the measured dc one for detwinned samples [34]. The T dependence of ΔR^{sat}_{ratio} is at variance with other experimental findings in FeSe, which attest local nematicity up to 300 K in x-ray atomic pair distribution function measurements [37] and dc transport anisotropy exhibiting a significant stress-induced tail above T_s [34]. Moreover, as shown in **Figure 4**, ΔR^{sat}_{ratio} remains constant at $T < T_c$, which is compatible with our previous results on Co-doped 122-

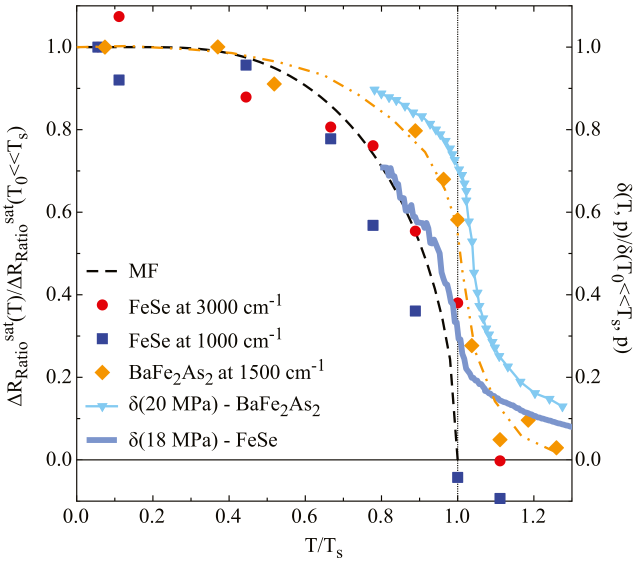

FIGURE 4 | (color online) T dependence of ΔR^{sat}_{ratio} (i.e., optical anisotropy at saturation, see text): at 1,000 and 3,000 cm^{-1} in FeSe for $p_{bellows}$ = 1.2 bar (i.e., $p_{sample} \approx$ 18.5 MPa), read from **Figure 3**. ΔR^{sat}_{ratio} is normalized by its value at T_0 = 5 K. The same quantity at 1,500 cm^{-1} for BaFe$_2$As$_2$ [28], normalized at T_0 = 10 K, is shown with dashed-double dot line as guide to the eyes. With respect to the normalized view of ΔR^{sat}_{ratio} in FeSe, it is worth reminding that as shown in **Figures 2A**, **3** $\Delta R_{ratio} > 0$ and $\Delta R_{ratio} < 0$ at 1,000 cm^{-1} and at 3,000 cm^{-1}, respectively. ΔR^{sat}_{ratio} at FeSe is compared to the T dependence of the mean-field order parameter (dashed line). The stressed-induced orthorhombicity (δ) at typical stress for fully detwinned specimens (i.e., at saturation) is reproduced from Ref. [35] for BaFe$_2$As$_2$ and estimated for FeSe [36], respectively. The T axis has been normalized by T_s ~ 90 and 135 K for FeSe and BaFe$_2$As$_2$ (vertical dotted line), respectively. Reproduced from Ref. [25].

materials [29]. Even though the impact of superconductivity on the excitation spectrum generally occurs at much lower energy scales, the high energy optical anisotropy, addressed here at $T < T_c$, indicates that the superconducting state develops within a polarized electronic structure. Similarly, the orthorhombic lattice distortion is barely affected by superconductivity in FeSe [34]. However, the most astonishing outcome from the T dependence of ΔR_{ratio} (**Figure 4**) is that the optical anisotropy at MIR energies seems to act as a proxy for a mean-field-like order parameter of nematicity [25].

When comparing FeSe (**Figure 3**) and $Ba(Fe_{1-x}Co_x)_2As_2$ [28, 29], we identify some distinct features of the hysteretic p dependence of their optical anisotropy at equivalent effectively felt uniaxial stress. First of all, the hysteretic behavior of the optical anisotropy in Co-doped $BaFe_2As_2$, while qualitatively reminiscent of FeSe, is clearly established only at frequencies below 2000 cm^{-1} with $R_a(\omega) > R_b(\omega)$ and without any sign change over the whole spectral range. Moreover the anisotropy at saturation was found to display a broad crossover through T_s (**Figure 4**), similar to the T dependence of the dc transport anisotropy for fully detwinned specimens [5] as well as of the magneto-torque signal [38] and directly comparable to the stress-induced orthorhombicity ($\delta = \frac{a-b}{a+b}$, being a and b the lattice constant of the corresponding axes) [35], replicated in **Figure 4**. This is rather different to the above-mentioned sudden onset of ΔR^{sat}_{ratio} at $T \le T_s$ in FeSe, despite its anticipated stress-induced δ above T_s (**Figure 4**) [36]. Such a distinct T dependence of the optical anisotropy across T_s between FeSe and 122-materials was also encountered in quantities from other experimental probes. For instance, the recent investigation of the linear dichroism with laser-photoemission electron microscope maps out the nematic parameter, which disappears at T_s in FeSe while it persists with a tail extending above T_s in $BaFe_2(As_{0.87}P_{0.13})_2$ [39]. To which extent the magnetic transition at T_N in the underdoped regime of 122-materials may be the dominant aspect governing these differences still remains to be figured out. It is certainly safe to conclude that, at least at the energy scales addressed here, δ in FeSe may be less strongly or not obviously bound to the electronic structure as in other iron-based superconductors.

The key role of the anisotropic electronic structure with respect to the nematic phase transition in FeSe (see Ref. [40] for the most recent, comprehensive review) is underscored by our optical data, which also highlight the central significance of the orbital degrees of freedom, affecting the band structure in an extended energy interval [41–47]. The optical anisotropy indeed occurs within the frequency range 0–6,000 cm^{-1} (**Figure 2A**), which is fairly consistent with the extent from the Fermi level of the correlated and weakly dispersing 3d iron bands [45, 48, 49]. However, there is an ongoing debate about the detailed nature of the nematic state in FeSe. Nuclear-magnetic-resonance (NMR) studies [50–52] initially promote a so-called on-site ferro-orbital ordering. Investigations of the electronic band structure in the reciprocal space force to revise the conclusions unbent from NMR, so that the purely on-site ferro-orbital order needs to be reconsidered within momentum-dependent scenarios. In fact, angle-resolved-photoemission-spectroscopy (ARPES) results [40, 45, 49, 53–61] indicate that the electronic band structure in FeSe undergoes a rather intricate momentum-dependent behavior, possibly consistent with either the bond-type ordering of the iron d_{xy}, d_{xz} and d_{yz} orbitals when crossing T_s [40, 56, 60, 62], the non-trivial energy splitting between the Γ and M point of the Brillouin zone [53, 59], leading to a band shift reversion [59], or finally the orbital-dependent Fermi-surface shrinking [45]. These scenarios demonstrate a nematicity-driven band reconstruction [33, 63], which is likely reflected in the optical anisotropy in FeSe and could account for its extension in energy and the change of sign in ΔR_{ratio}, as observed between 1,000 and 3,000 cm^{-1} (**Figures 2A**, **3**). The optical anisotropy further implies an important reshuffling of spectral weight, occurring at larger energy scales than the characteristic ones set by the critical (structural) transition temperatures. This latter observation is another manifestation of the strong orbital-selective electronic correlations in FeSe [48, 49, 64–66]. In this context, recent ARPES results [67] imply that the d_{xz} orbital has a larger quasi-particle spectral weight and a smaller spectral weight in the Hubbard band compared to the d_{yz} orbital. This may be interpreted in terms of a more coherent d_{xz} orbital than the d_{yz} orbital inside the nematic phase; a result which further highlights the importance of electronic correlations in the description of nematicity [67].

The optical conductivity allows accessing all parameters, which determine the transport properties; the scattering rate and the plasma frequency of the itinerant charge carriers. They can be extracted phenomenologically within the well-established Drude–Lorentz fit procedure [32], which we did successfully apply in the past for the 122-materials [68, 69]. By recalling that the complex optical conductivity relates to the complex dielectric function as $\tilde{\epsilon} = \epsilon_1 + i\epsilon_2 = \epsilon_\infty + 4\pi i(\sigma_1 - i\sigma_2)/\omega$, we can summarize our Drude–Lorentz fit as follows [32]:

$$\tilde{\epsilon} = \epsilon_\infty - \frac{\omega^2_{pN}}{\omega^2 + i\omega\Gamma_N} - \frac{\omega^2_{pB}}{\omega^2 + i\omega\Gamma_B} + \sum_{j=3}^{8} \frac{S^2_j}{\omega^2_{0,j} - \omega^2 - i\omega\gamma_j} \qquad (1)$$

Besides several Lorentz harmonic oscillators (h.o.) for the finite frequency excitations we consider two Drude terms, a narrow (N) and a broad (B) one, accounting for the multi-band nature of iron-based superconductors [70]. $\Gamma_{N/B}$ and $\omega_{pN/B}$ are respectively the width at half-maximum (scattering rate) and the plasma frequency ($\omega_p = \sqrt{\frac{4\pi e^2 n}{m^*}}$) of the itinerant charge carriers, with charge e, density n and effective mass m^*. The parameters for each h. o. at finite frequency are the strength (S), the center-peak frequency (ω_0) and the width (γ). In **Eq. 1**, ϵ_∞ is the optical dielectric constant (close to one for all our fits [26]). Within this phenomenological approach we simultaneously fit both $R(\omega)$ and $\sigma_1(\omega)$, achieving a good reproduction of the optical functions [26].

Here, we will argue on the Drude parameters only (for additional informations on the overall fit results, please consult Ref. [26]), since the link to the (anisotropic) dc transport properties [34] is at the center of our interest. We consider the ratio of the fit parameters between the a- and b-axis, in order to shed light on their own anisotropy. **Figure 5** then shows the anisotropy of $\Gamma^{a,b}_{N,B}$ (**Figures 5A,B**) for both Drude terms and of the total Drude weight ($SW^{a,b}_D = \omega^2_{pN} + \omega^2_{pB}$,

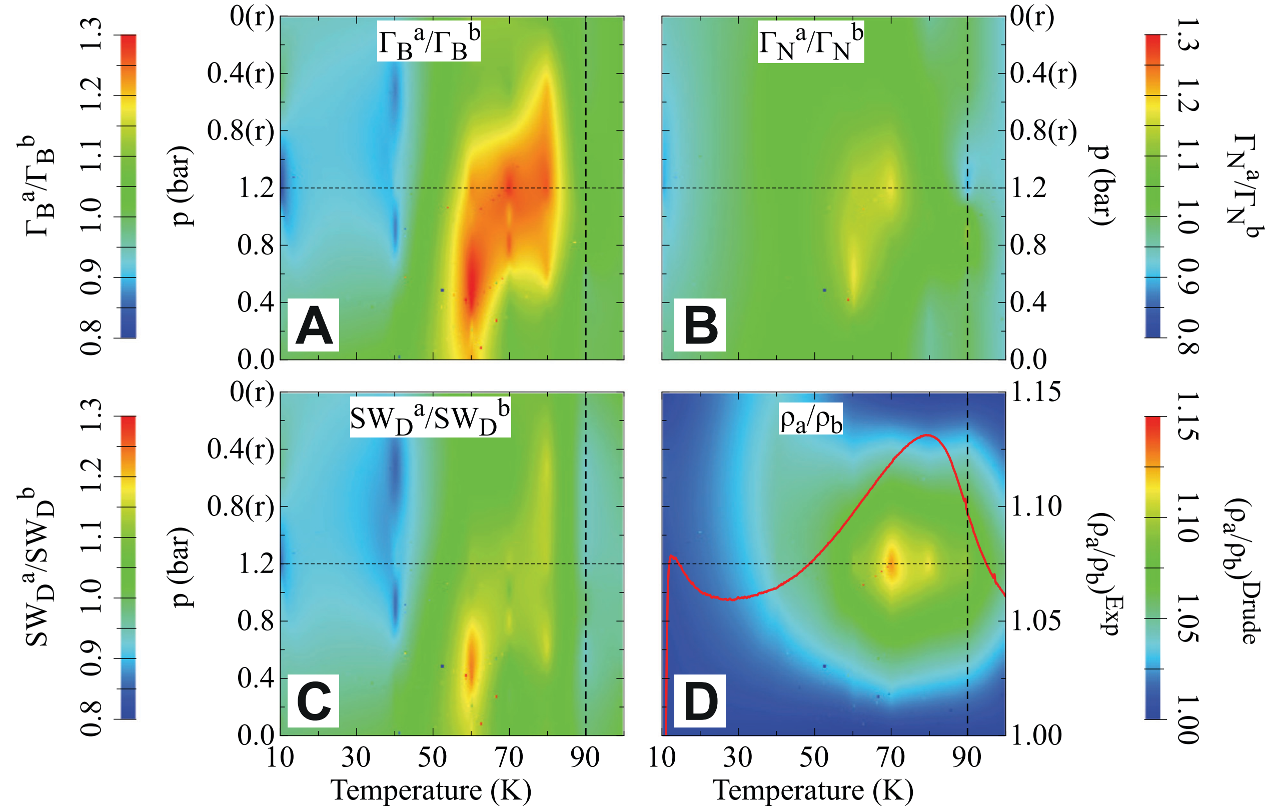

FIGURE 5 | (color online) **(A–C)** T and p dependence of the anisotropy of both scattering rates ($\Gamma^a_{N,B}/\Gamma^b_{N,B}$) for the broad (B) and narrow (N) Drude components and of the total Drude weight (SW^a_D/SW^b_D) from the phenomenological fit (**Eq. 1**) of the p-loop experiments after the ZPC protocol (see text) in FeSe. **(D)** T and p (left scale) dependence of the *dc* anisotropy (ρ_a/ρ_b) calculated within the Drude model. A first-neighbor interpolation procedure is used in order to generate the color maps. Released p is denoted by "(r)". The thick vertical dashed line marks T_s, while the thin horizontal dashed line indicates p = 1.2 bar (i.e., at saturation). The red curve in panel **(D)** corresponds to the experimental ρ_a/ρ_b (right scale) for fully detwinned specimen [34]. Reproduced from Ref. [26].

Figure 5C) as a function of T within the p-loop. The resulting anisotropy in the relevant Drude parameters develops upon progressively detwinning the specimen, particularly in the T interval between 40 and 80 K, and vanishes upon releasing p back to zero. The cut of the color maps in **Figures 5A–C** at saturation indicates that the anisotropy of all Drude quantities for fully detwinned samples is weak just above T_s, reaches its maximum value around 60–70 K and substantially drops upon further lowering T to 10 K (i.e. just above T_c). A recent approach resting upon orbital-selective spin fluctuations [45, 71, 72] can explain the emergence of the orbital ordering, as well as of the anisotropy in the scattering rate and plasma frequency. Besides being in broad qualitative agreement with our findings, those theoretical thoughts reveal the importance of the spin-orbital interplay.

The *dc* resistivity can be directly reconstructed within the Drude approach and by exploiting the corresponding parameters $(1/\rho(T) = \sigma_1(\omega = 0, T) = \frac{\omega_{pB}^2}{4\pi\Gamma_B} + \frac{\omega_{pN}^2}{4\pi\Gamma_N})$. The resulting anisotropy ρ_a/ρ_b, shown in **Figure 5D**, gets stronger upon applying p, specifically in the T interval $40\,\text{K} < T \leq T_s$. From our investigations, it turns out that both scattering rates and total Drude weight consistently cooperate in order to recover the measured *dc* anisotropy [34]. By the way, this is similar to the findings in the 122-materials [68, 69] and also provides a reliability check of our analysis (**Figure 5D**). Since the anisotropy in the scattering rate ($\Gamma_a > \Gamma_b$) does coincide with the measured *dc* anisotropy ($\rho_a > \rho_b$) [34], as expected within the Drude model (i.e., $\rho(T) \sim \Gamma$ [32]), the advanced interplay among the Drude parameters with respect to the *dc* properties is even more stringent. Conversely and interestingly enough, the anisotropy of the total Drude weight ($SW_D^a > SW_D^b$) is opposite and unexpected within the Drude model for which $\rho(T) \sim 1/\omega_p^2$ [32].

Figure 6 presents the results of our analysis from a slightly different perspective, with the aim to elaborate on possible ingredients for nematicity in FeSe. In fact, it displays the T dependence of the anisotropic Drude parameters at saturation, compared to the average *dc* resistivity [34]. It is worth remembering that the anisotropy in all Drude quantities is mostly evident around 60–70 K, consistent with the anisotropy of the *dc* transport properties for the strained sample (**Figure 5D**). Being at odds with early conclusions drawn from our optical results in 122-materials [68, 69], **Figure 6** suggests that the Drude weight has a less strong impact on the T dependence of the *dc* resistivity (**Figure 6C**) than the scattering rates for both narrow and broad Drude terms. Stated more specifically, we can

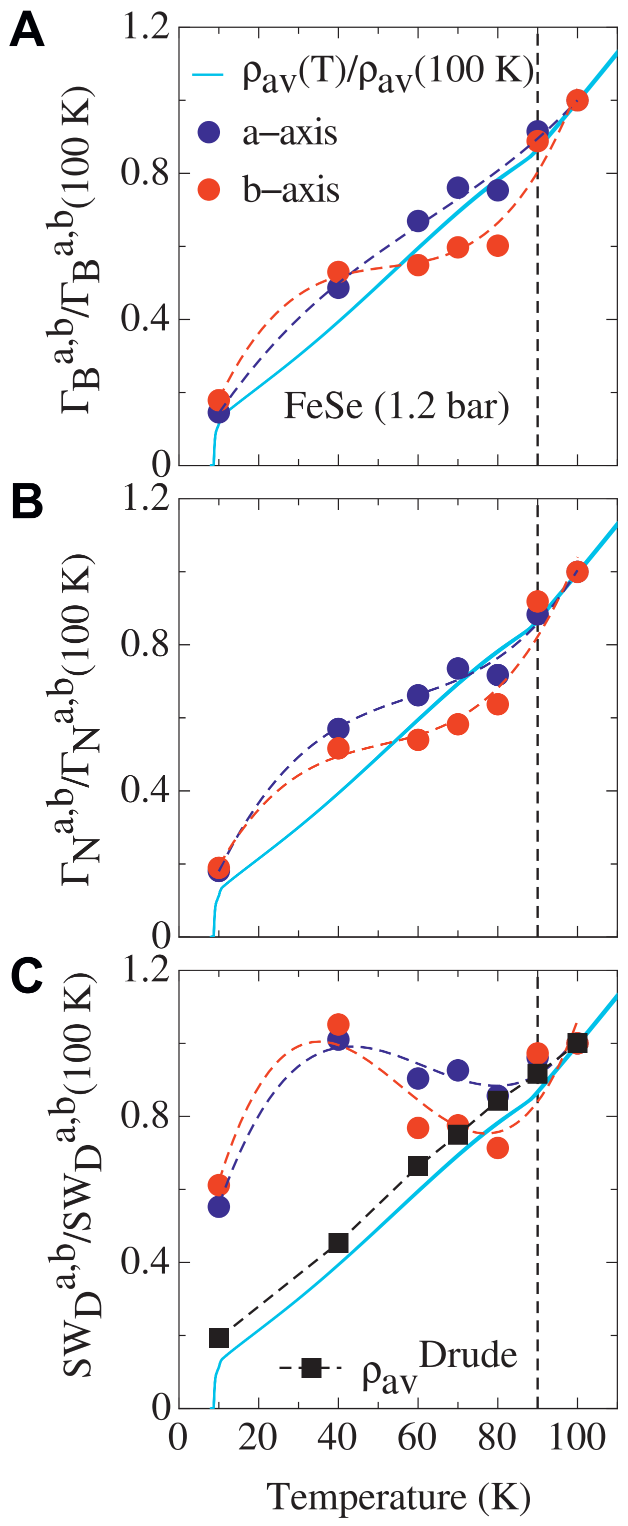

FIGURE 6 | (color online) **(A–C)** *T* dependence of the anisotropic scattering rates ($\Gamma^{a,b}_{N,B}$) for the narrow (N) and broad (B) Drude term as well as of the total Drude spectral weight $SW^{a,b}_D$ (see text), at $p = 1.2$ bar (i.e., for fully detwinned samples) along both orthorhombic *a*- and *b*-axis. The measured, average *dc* resistivity between the two axes is replicated from Ref. *(Continued)*

FIGURE 6 | [34] as comparison. Panel **(C)** also reproduces the average *dc* resistivity (ρ^{Drude}_{av}), calculated within the Drude model from the fit parameters, as alternative reliability check of our analysis. All quantities are normalized by their respective values at 100 K. The thick vertical dashed line in all panels marks T_s. Reproduced from Ref. [26].

convincingly affirm that the scattering rates closely follow the *dc* resistivity as a function of *T* (**Figures 6A,B**). Previous conjectures [73], that inelastic scattering of electrons (e.g., off magnetic fluctuations) would mainly affect the *dc* transport properties, find here a unique support, as given by the dominant role of our phenomenological Drude scattering rates.

Ideas for nematicity underpinned by magnetic interactions even when nematic order precedes the magnetic one were motivated by the frequently observed intimate coupling between structure and magnetism in iron-based materials [14, 73, 74]. Magnetic fluctuations at $T > T_N$ would then cause the tetragonal-to-orthorhombic transition in iron-pnictides (e.g., the 122-materials). Likewise, FeSe with (and despite) $T_N \sim 0$ may dissimulate the same mechanism. Interestingly, the *dc* resistivity anisotropy $\Delta\rho = \rho_a - \rho_b$ in FeSe could arise from the convolution of two functions: the order parameter of the nematic phase transition (**Figure 4**), which breaks the same symmetry as $\Delta\rho$ and therefore it is proportional to it, and a proportionality factor monotonically decreasing in *T* [34], so that an overall dome-like *T* dependence peaked at ~ 70 K (**Figure 5D**) would arise. A natural explanation for the *T* dependence of the proportionality factor derives from inelastic scattering, for instance by anisotropic magnetic excitations [34]. Indeed, the electronic scattering rates in **Figures 6A,B** exhibit such a *T* dependence. In conjunction with the nematic order parameter (**Figure 4**) the scattering rate then conspires in order to reproduce the resistivity anisotropy (**Figure 5D**). We thus speculate that the low-energy charge dynamics of FeSe is a quite direct fingerprint of a scenario for which the spin fluctuations together with the high-energy orbital ordering apparently assume a rather dominant role in connection with the onset of nematicity. Recent resonant inelastic x-ray scattering data below T_s underline a matchless strong spin-excitations anisotropy, which suggests a primarily spin-driven nematic phase transition [75]. Spin fluctuations are also an important ingredient as driving force for superconductivity [76], as advanced from recent NMR measurements [77], ARPES data [40] as well as inelastic neutron scattering investigations [78, 79].

$Ba_{0.6}K_{0.4}Fe_2As_2$

We start off this section with a comprehensive view of the collected $R(\omega)$ data within the *p*-loop experiment at 10 K (**Figures 7A,B**) [27]. The chosen *T* is well within the superconducting state and the displayed data were collected after a ZPC protocol. There is an obvious metallic behaviour of the overall $R(\omega)$ spectra along the *a*- and *b*-axis. The measured quantity along both axes approaches total reflection at finite frequencies below $\nu_g \sim 180\ \text{cm}^{-1}$, as expected at $T < T_c$ [32]. We note the great agreement of our data at $p = 0$ (averaged between the two axes) and for all *T* with those in Refs. [80–85],

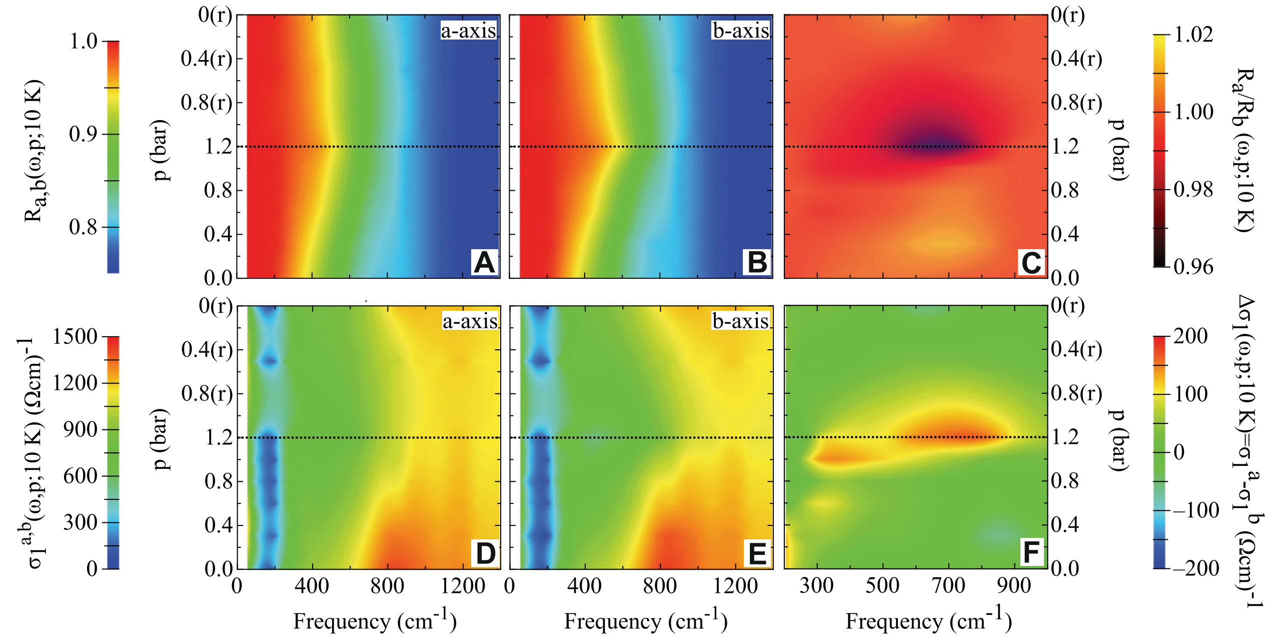

FIGURE 7 | (color online) **(A,B)** Representative data of the optical reflectivity ($R(\omega)$) of $Ba_{0.6}K_{0.4}Fe_2As_2$ at 10 K for the p-loop experiment after a ZPC protocol along the a- and b-axis (R_a and R_b, respectively, upper-left panel of **Figure 2**) in the spectral range below 1,400 cm^{-1}. **(C)** The reflectivity ratio $R_{Ratio} = R_a/R_b$. **(D,E)** Real part $\sigma_1(\omega)$ of the optical conductivity, achieved through KK transformation of the data in panels **(A,B)**. **(F)** The dichroism $\Delta\sigma_1(\omega) = \sigma_1^a(\omega) - \sigma_1^b(\omega)$ at 10 K within the p-loop experiment. Panels **(C,F)** focus the attention to the FIR energy interval 200–1,000 cm^{-1}, where the reversible optical anisotropy upon sweeping p is discovered. A first-neighbor interpolation procedure is used in order to generate the color maps. Released p is denoted by "(r)". The thick dotted line in all panels marks $p = 1.2$ bar (i.e., at saturation). Reproduced from Ref. [27].

which comprehensively address the electrodynamic response both above and below T_c in un-stressed $Ba_{1-x}K_xFe_2As_2$ samples. We encounter a reversible anisotropy of $R(\omega)$ upon sweeping p, which can be further emphasized by the calculation of the reflectivity ratio $R_{Ratio} = R_a/R_b$, shown in **Figure 7C**. In the FIR range around 600 cm^{-1}, R_{Ratio} drops below 1 (i.e., the isotropic situation) upon reaching 1.2 bar (i.e., corresponding to the saturation limit for this sample). R_{Ratio} reconverts then to unity when p is released back to zero. From the measured $R(\omega)$ we achieve $\sigma_1(\omega)$, as shown in **Figures 7D,E**, and consequently the already introduced dichroism $\Delta\sigma_1(\omega) = \sigma_1^a(\omega) - \sigma_1^b(\omega)$ (see above our discussion for the FeSe material). $\Delta\sigma_1(\omega)$ for the p-loop experiment at 10 K is depicted in **Figure 7F**. The optical anisotropy in the range between 300 and 1,000 cm^{-1} for the stressed specimen is clearly resolved and further implies an anisotropy in the spectral weight distribution at FIR frequencies [27]. It is historically well established that $\sigma_1(\omega)$ in the superconducting state allows in principle the determination of the so-called superconducting gap. This is the characteristic energy scale of the superconducting collective state and is supposed to correspond to a sharp onset of the absorption spectrum at least for s-wave like superconducting materials [32]. The drop of $\sigma_1(\omega)$ to almost zero below ν_g, as illustrated in **Figures 7D,E** as well as **Figure 8B**, is the most clear signature of the superconducting gap at 10 K for every p. We conclude that $Ba_{0.6}K_{0.4}Fe_2As_2$ is a fully gapped superconducting material. Moreover, the residual, unpaired charge carriers (i.e., activated across the gap because of the thermal pair-breaking effect) at finite T lead to the upturn of $\sigma_1(\omega)$ at frequencies towards zero [32].

So far, we could provide a clear-cut evidence for an optical anisotropy, which is p-induced in the tetragonal structure of $Ba_{0.6}K_{0.4}Fe_2As_2$ at $T = 10\ K < T_c$. The question then arises about its T dependence and its relationship to the overall phase diagram of iron-based superconductors. The quantity $\Delta R_{Ratio}(\omega_0) = \frac{R_{Ratio}(p=0,T)-R_{Ratio}(p,T)}{R_{Ratio}(p=0,T)} \times 100$ is very instrumental to this goal. It amplifies the relative change of the optical anisotropy during the p-loop experiments at each T with respect to the $p = 0$ initial situation (i.e., the isotropic limit since $R_{Ratio}(p = 0, T) \sim 1$ at all T). We made the argument that $\Delta R_{Ratio}(\omega_0)$ truly helps pointing out the variation of the optical anisotropy beyond the experimental data noise [27]. **Figure 8A** therefore pictures $\Delta R_{Ratio}(\omega_0)$ at the fixed frequency $\omega_0 = 600$ cm^{-1}, chosen because the largest anisotropy occurs at that frequency (**Figure 7C**). The nematic susceptibility in the normal state (i.e., at $T > T_c$) from elastoresistive investigation [19] images a substantial Curie-like behaviour, which is however not seen or reproduced by our own optical data above T_c. It seems that our experiment does not have enough resolution in this respect and a possible optical evidence for nematicity above T_c must be vanishingly small, if any. From our data, it follows that only upon entering the superconducting state there is a p-induced anisotropy; large enough applied p can cause a polarization dependence of the excitation spectrum. This is mostly and better seen at saturation (thick horizontal dotted line at $p = 1.2$ bar in the color map of **Figure 8A**), where an indisputable pronounced increase of the optical anisotropy is

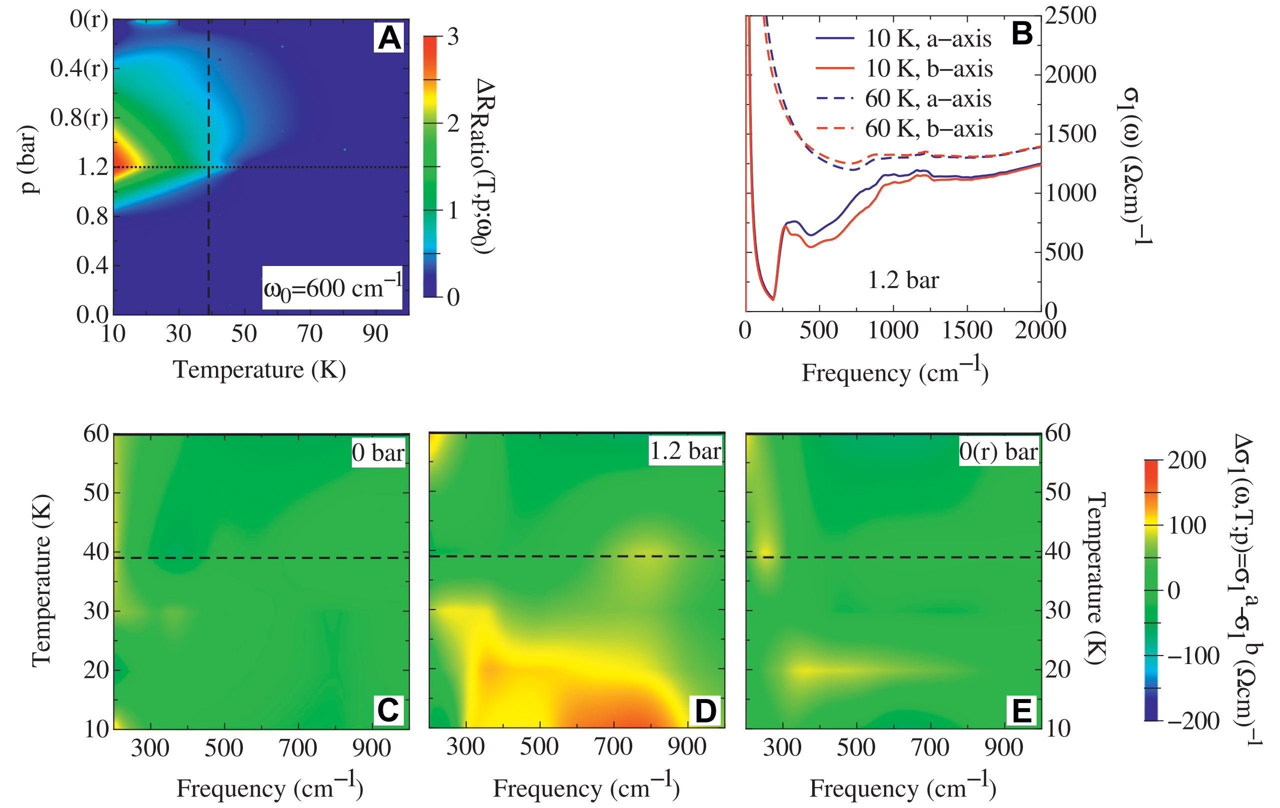

FIGURE 8 | (color online) **(A)** T dependence of the quantity ΔR_{Ratio} (ω_0) (see text) of $Ba_{0.6}K_{0.4}Fe_2As_2$ within the p-loop experiment after a ZPC protocol, which emphasizes the T evolution of the p-induced optical anisotropy. We choose $\omega_0 = 600$ cm^{-1}. The thick dotted line marks $p = 1.2$ bar (i.e., at saturation). **(B)** Measured $\sigma_1(\omega)$ at 10 K (i.e., $T < T_c$) and 60 K (i.e., $T > T_c$) for $p = 1.2$ bar along both crystallographic axes. **(C,E)** T dependence of $\Delta\sigma_1(\omega)$ at the selected p of 0, 1.2 and released 0 bar. These panels focus the attention to the FIR energy interval 200–1,000 cm^{-1}, thus emphasising the reversible optical anisotropy upon sweeping p. The thick dashed line in panels **(A)** and **(C–E)** indicates T_c. A first-neighbor interpolation procedure is used in order to generate the color maps. Released p is denoted by "(r)". Reproduced from Ref. [27].

discernible at $T < T_c$. The established hardening occurring below T_c [12] and the mild reduction at low T of the Raman susceptibilities [10] for dopings across the whole phase diagram would presage an opposite behaviour, instead of the growing of the p-induced nematicity in the superconducting state as evidenced from optics. This latter aspect calls for additional studies and it remains to be seen how this apparent controversy may be solved. Nonetheless, we stress here the T evolution of the optical anisotropy with $\Delta\sigma_1(\omega)$, shown in **Figures 8C–E**. We limit our view to the energy interval between 200 and 1,000 cm^{-1} at three selected p, which again highlight the p-induced as well as p-reversible optical anisotropy below T_c in the FIR range. This is the most important aspect of these findings, signalling the presence of electronic nematicity at T deep into the superconducting dome yet in the purely tetragonal phase and that the band structure is responding to nematic fluctuations, since here $T_s = 0$. It is worth recalling (see above, **Figure 4**) that the optical anisotropy of Co-underdoped 122-materials and FeSe persists even at $T < T_c$, and reiterating the idea that their superconductivity develops in an electronically polarized state [25, 26, 68, 69].

Our present data of $Ba_{0.6}K_{0.4}Fe_2As_2$ bear testimony to a p-induced anisotropy of the excitation spectrum, which mirrors nematicity and seems to be a generic feature in 122 iron-based superconductors [28, 29, 68, 69] even into the optimally-doped regime, similar to the *dc* transport properties [19]. We discover that the optical anisotropy in the optimally K-doped 122-compound occurs at the low FIR energy scales, relevant to the superconducting gap(s) (**Figure 7F** and **Figure 8C–E**). This is peculiar with respect to the previously investigated underdoped 122-materials and FeSe [25, 26, 28, 29, 68, 69], for which the optical anisotropy extends up to high energy scales. Our findings in $Ba_{0.6}K_{0.4}Fe_2As_2$ thus tend to exclude the involvement of bands deep into the electronic structure and potentially imply a less prominent impact of orbital ordering in the optimally doped than in the underdoped regime. Ergo, the p-induced optical anisotropy in $Ba_{0.6}K_{0.4}Fe_2As_2$ elucidates the response of the conduction bands to an external symmetry breaking field. For instance, the deployed optical response and its p dependence flag the imprint of (anisotropic) scattering, uncovering some kind of spin-orbital interplay, so that the p-induced nematicity is caused by spin fluctuations and is vestigial to stripe magnetism [16]. This would directly influence the energy scales close to the Fermi level, ultimately of relevance for the transport properties as well as superconductivity. Moreover and beyond nematicity, Raman results equally make a strong case for a pairing mechanism for superconductivity mediated by spin fluctuations [86]. In addition, a so-called differentiation of the orbital effective masses and related anisotropy, which is further enhanced by the presence of strong electronic correlations above all in hole-doped materials [46], can be alike installed by uniaxial stress, as applied here in our experiment. This impairs the optical response of the conduction bands as well and could be also reflected in an anisotropic reshuffling of spectral weight at $T < T_c$ between the superconducting collective mode and the FIR energies (**Figures 8C–E**) [87].

CONCLUSION AND OUTLOOK

We conclude this review by summarising the major outcomes of our optical studies in selected iron-based superconductors and projecting the treated topics into possible future directions.

First of all, within one single experiment we disclose all relevant ingredients (order parameter and Drude quantities, **Figures 4**, **5**), which were shown to fully determine the anisotropy in the charge dynamics as well as in the *dc* transport properties of FeSe. It is worth warning the readership that the interplay between the orbital order [25, 28, 29] and the intertwined anisotropy of the Drude parameters (**Figure 5**) cannot be neglected when addressing the complete excitation spectrum [45, 68, 69, 71]. Having said that, the inelastic scattering by magnetic fluctuations rather than the Fermi surface parameters seems to shape the nematic anisotropy in the *dc* limit (**Figure 6**). Proposals advocating a close connection between spin fluctuations, nematicity (i.e., orbital order) and superconductivity [15, 16] would be reasonably promoted by our findings, since they give ample support for the role played by magnetic interactions. In a broader context and looking ahead, it could be of interest to systematically compare our results with data collected across the whole *T* versus doping phase diagram of representative iron-based superconductors, and to exploit the broadband optical anisotropy, addressed here, in order to precisely test the impact of doping-induced disorder [88], thus expanding at finite frequencies the debate already addressed by *dc* transport investigations [89–91].

Second, the *p*-induced optical anisotropy in (optimally doped) $Ba_{0.6}K_{0.4}Fe_2As_2$ only at $T < T_c$ (**Figure 8A**) is an astonishing fingerprint that the electronic structure is extremely susceptible to symmetry breaking stress below T_c. In Ref. [87], we additionally discover that our findings (**Figure 7**) imply the presence of *p*-induced anisotropic gaps between both axes at $T \ll T_c$. Chasing the implications of the gap anisotropy with respect to the debate on the dominant pairing symmetry [86, 92, 93] goes beyond the scope of this work. Nonetheless, the unprecedented anisotropic charge dynamics deep into the superconducting dome is contingently consistent with recent observations of nematic superconductivity in compounds with similar doping [94–96] as well as in LiFeAs [97]. This is a pretty strong speculation, which needs to be challenged with *adhoc* ascertainments. As outlook, it remains to be seen whether an orbital-selective pairing, eventually supplemented by the guiding principle of spin fluctuations as proposed for FeSe [76, 98–101], may explain the anisotropy of the superconducting gap. This would also shed new light on the putative relationship between quantum critical nematic fluctuations and unconventional superconductivity [21, 22]. In this respect, interrogating the exact extent to which uniaxial stress couple to nematic fluctuations will be of paramount importance and is a task left to the future.

AUTHOR CONTRIBUTIONS

The author confirms being the sole contributor of this work and has approved it for publication.

ACKNOWLEDGMENTS

The author wishes to thank C. Mirri, M. Chinotti and A. Pal for the data collection and analysis, as reported in the original, quoted references, as well as R. Fernandes, M. Schütt, L. Benfatto, L. Fanfarillo, B. Valenzuela, E. Bascones, M. Watson, R. Lobo, A. Chubukov, P. Hirschfeld, W. Ku and D. Lu for fruitful discussions. This work was supported by the Swiss National Foundation for the Scientific Research.

REFERENCES

1. Fradkin E, Kivelson SA, Lawler MJ, Eisenstein JP, Mackenzie AP. Nematic Fermi Fluids in Condensed Matter Physics. *Annu Rev Condens Matter Phys* (2010) 1:153–78. doi:10.1146/annurev-conmatphys-070909-103925
2. Fradkin E, Kivelson SA. Electron Nematic Phases Proliferate. *Science* (2010) 327:155–6. doi:10.1126/science.1183464
3. Fradkin E, Kivelson SA. Ineluctable Complexity. *Nat Phys* (2012) 8:864–6. doi:10.1038/nphys2498
4. Fernandes RM, Coldea AI, Ding H, Fisher IR, Hirschfeld PJ, Kotliar G. Iron Pnictides and Chalcogenides: a New Paradigm for Superconductivity. *Nature* (2022) 601:35–44. doi:10.1038/s41586-021-04073-2
5. Fisher IR, Degiorgi L, Shen ZX. In-plane Electronic Anisotropy of Underdoped '122' Fe-Arsenide Superconductors Revealed by Measurements of Detwinned Single Crystals. *Rep Prog Phys* (2011) 74: 124506. doi:10.1088/0034-4885/74/12/124506
6. Tanatar MA, Kreyssig A, Nandi S, Ni N, Bud'ko SL, Canfield PC, et al. Direct Imaging of the Structural Domains in the Iron Pnictides AFe_2As_2 (A=Ca,Sr,Ba). *Phys Rev B* (2009) 79:180508. doi:10.1103/physrevb.79.180508
7. Chu J-H, Kuo H-H, Analytis JG, Fisher IR. Divergent Nematic Susceptibility in an Iron Arsenide Superconductor. *Science* (2012) 337:710–2. doi:10.1126/science.1221713
8. Kuo H-H, Shapiro MC, Riggs SC, Fisher IR. Measurement of the Elastoresistivity Coefficients of the Underdoped Iron Arsenide $Ba(Fe_{0.975}Co_{0.025})_2As_2$. *Phys Rev B* (2013) 88:085113. doi:10.1103/physrevb.88.085113
9. Gallais Y, Fernandes RM, Paul I, Chauvière L, Yang Y-X, Méasson M-A, et al. Observation of Incipient Charge Nematicity in $Ba(Fe_{1-X}Co_X)_2As_2$. *Phys Rev Lett* (2013) 111:267001. doi:10.1103/physrevlett.111.267001
10. Wu S-F, Richard P, Ding H, Wen H-H, Tan G, Wang M, et al. Superconductivity and Electronic Fluctuations in $Ba_{1-x}K_xFe_2As_2$ Studied by Raman Scattering. *Phys Rev B* (2017) 95:085125. doi:10.1103/PhysRevB.95.085125
11. Wu SF, Zhang WL, Li L, Cao HB, Kung HH, Sefat AS, et al. (2017) arXiv: 1712.06066 [cond-mat.supr-con]. Available at: https://arxiv.org/abs/1712.06066.

12. Böhmer AE, Burger P, Hardy F, Wolf T, Schweiss P, Fromknecht R, et al. Nematic Susceptibility of Hole-Doped and Electron-Doped $BaFe_2As_2$ Iron-Based Superconductors from Shear Modulus Measurements. *Phys Rev Lett* (2014) 112:047001. doi:10.1103/PhysRevLett.112.047001
13. Fradkin E, Kivelson SA, Tranquada JM. Colloquium: Theory of Intertwined Orders in High Temperature Superconductors. *Rev Mod Phys* (2015) 87: 457–82. doi:10.1103/revmodphys.87.457
14. Fernandes RM, Chubukov AV, Schmalian J. What Drives Nematic Order in Iron-Based Superconductors? *Nat Phys* (2014) 10:97–104. doi:10.1038/nphys2877
15. Glasbrenner JK, Mazin II, Jeschke HO, Hirschfeld PJ, Fernandes RM, Valentí R. Effect of Magnetic Frustration on Nematicity and Superconductivity in Iron Chalcogenides. *Nat Phys* (2015) 11:953–8. doi:10.1038/nphys3434
16. Chubukov AV, Khodas M, Fernandes RM. Magnetism, Superconductivity, and Spontaneous Orbital Order in Iron-Based Superconductors: Which Comes First and Why?. *Phys Rev X* (2016) 6:041045. doi:10.1103/physrevx.6.041045
17. Hsu F-C, Luo J-Y, Yeh K-W, Chen T-K, Huang T-W, Wu PM, et al. Superconductivity in the PbO-type Structure -FeSe. *Proc Natl Acad Sci* (2008) 105:14262–4. doi:10.1073/pnas.0807325105
18. McQueen TM, Williams AJ, Stephens PW, Tao J, Zhu Y, Ksenofontov V, et al. Tetragonal-to-Orthorhombic Structural Phase Transition at 90 K in the Superconductor $Fe_{1.01}Se$. *Phys Rev Lett* (2009) 103:057002. doi:10.1103/physrevlett.103.057002
19. Kuo H-H, Chu J-H, Palmstrom JC, Kivelson SA, Fisher IR. Ubiquitous Signatures of Nematic Quantum Criticality in Optimally Doped Fe-Based Superconductors. *Science* (2016) 352:958–62. doi:10.1126/science.aab0103
20. Metlitski MA, Mross DF, Sachdev S, Senthil T. Cooper Pairing in Non-fermi Liquids. *Phys Rev B* (2015) 91:115111. doi:10.1103/physrevb.91.115111
21. Lederer S, Schattner Y, Berg E, Kivelson SA. Enhancement of Superconductivity Near a Nematic Quantum Critical Point. *Phys Rev Lett* (2015) 114:097001. doi:10.1103/physrevlett.114.097001
22. Nie L, Tarjus G, Kivelson SA. Quenched Disorder and Vestigial Nematicity in the Pseudogap Regime of the Cuprates. *Proc Natl Acad Sci* (2014) 111:7980–5. doi:10.1073/pnas.1406019111
23. Fujita K, Kim CK, Lee I, Lee J, Hamidian MH, Firmo IA, et al. Simultaneous Transitions in Cuprate Momentum-Space Topology and Electronic Symmetry Breaking. *Science* (2014) 344:612–6. doi:10.1126/science.1248783
24. Böhmer AE, Hardy F, Wang L, Wolf T, Schweiss P, Meingast C. Superconductivity-Induced Re-Entrance of the Orthorhombic Distortion in $Ba_{1-x}K_xFe_2As_2$. *Nat Commun* (2015) 6:7911. doi:10.1038/ncomms8911
25. Chinotti M, Pal A, Degiorgi L, Böhmer AE, Canfield PC. Optical Anisotropy in the Electronic Nematic Phase of FeSe. *Phys Rev B* (2017) 96:121112. doi:10.1103/physrevb.96.121112
26. Chinotti M, Pal A, Degiorgi L, Böhmer AE, Canfield PC. Ingredients for the Electronic Nematic Phase in FeSe Revealed by its Anisotropic Optical Response. *Phys Rev B* (2018) 98:094506. doi:10.1103/physrevb.98.094506
27. Pal A, Chinotti M, Chu J-H, Kuo H-H, Fisher IR, Degiorgi L. Optical Anisotropy in Optimally Doped Iron-Based Superconductor. *Npj Quant Mater* (2019) 4:3. doi:10.1038/s41535-018-0140-1
28. Mirri C, Dusza A, Bastelberger S, Chu J-H, Kuo H-H, Fisher IR, et al. Hysteretic Behavior in the Optical Response of the Underdoped Fe-Arsenide $Ba(Fe_{1-x}Co_x)_2As_2$ in the Electronic Nematic Phase. *Phys Rev B* (2014) 89: 060501. doi:10.1103/physrevb.89.060501
29. Mirri C, Dusza A, Bastelberger S, Chu J-H, Kuo H-H, Fisher IR, et al. Nematic-driven Anisotropic Electronic Properties of Underdoped detwinned $Ba(Fe_{1-x}Co_x)_2As_2$ Revealed by Optical Spectroscopy. *Phys Rev B* (2014) 90: 155125. doi:10.1103/physrevb.90.155125
30. Dusza A, Lucarelli A, Pfuner F, Chu J-H, Fisher IR, Degiorgi L. Anisotropic Charge Dynamics in Detwinned $Ba(Fe_{1-x}Co_x)_2As_2$. *Epl* (2011) 93:37002. doi:10.1209/0295-5075/93/37002
31. Nakajima M, Liang T, Ishida S, Tomioka Y, Kihou K, Lee CH, et al. Unprecedented Anisotropic Metallic State in Undoped Iron Arsenide $BaFe_2As_2$ Revealed by Optical Spectroscopy. *Proc Natl Acad Sci* (2011) 108:12238–42. doi:10.1073/pnas.1100102108
32. Dressel M, Gruner G. *Electrodynamics of Solids*. Cambridge: Cambridge University Press (2002).
33. Wang H, Ye Z, Zhang Y, Wang N. Band Structure Reconstruction across Nematic Order in High Quality FeSe Single crystal as Revealed by Optical Spectroscopy Study. *Sci Bull* (2016) 61:1126–31. doi:10.1007/s11434-016-1102-2
34. Tanatar MA, Böhmer AE, Timmons EI, Schütt M, Drachuck G, Taufour V, et al. Origin of the Resistivity Anisotropy in the Nematic Phase of FeSe. *Phys Rev Lett* (2016) 117:127001. doi:10.1103/physrevlett.117.127001
35. Lu X, Tseng K-F, Keller T, Zhang W, Hu D, Song Y, et al. Impact of Uniaxial Pressure on Structural and Magnetic Phase Transitions in Electron-Doped Iron Pnictides. *Phys Rev B* (2016) 93:134519. doi:10.1103/physrevb.93.134519
36. The stress-induced orthorhombicity in FeSe above T_s can be reasonably estimated for effectively applied stress of about 18 MPa (i.e., at saturation) from the elastic constant and x-ray diffraction data [102, 103]. It is comparable to values measured in $BaFe_2As_2$ [35].
37. Koch RJ, Konstantinova T, Abeykoon M, Wang A, Petrovic C, Zhu Y, et al. Room Temperature Local Nematicity in FeSe Superconductor. *Phys Rev B* (2019) 100:020501. doi:10.1103/physrevb.100.020501
38. Kasahara S, Shi HJ, Hashimoto K, Tonegawa S, Mizukami Y, Shibauchi T, et al. Electronic Nematicity above the Structural and Superconducting Transition in $BaFe_2(As_{1-x}P_x)_2$. *Nature* (2012) 486:382–5. doi:10.1038/nature11178
39. Shimojima T, Motoyui Y, Taniuchi T, Bareille C, Onari S, Kontani H, et al. Discovery of Mesoscopic Nematicity Wave in Iron-Based Superconductors. *Science* (2021) 373:1122–5. doi:10.1126/science.abd6701
40. Rhodes LC, Eschrig M, Kim TK, Watson MD, (2022), and references therein, arXiv:2201.11702 [cond-mat.supr-con]. Available at: https://arxiv.org/abs/2201.11702.
41. Chen C-C, Maciejko J, Sorini AP, Moritz B, Singh RRP, Devereaux TP. Orbital Order and Spontaneous Orthorhombicity in Iron Pnictides. *Phys Rev B* (2010) 82:100504. doi:10.1103/physrevb.82.100504
42. Lee C-C, Yin W-G, Ku W. Ferro-Orbital Order and Strong Magnetic Anisotropy in the Parent Compounds of Iron-Pnictide Superconductors. *Phys Rev Lett* (2009) 103:267001. doi:10.1103/physrevlett.103.267001
43. Lv W, Krüger F, Phillips P. Orbital Ordering and Unfrustrated (π,0) Magnetism from Degenerate Double Exchange in the Iron Pnictides. *Phys Rev B* (2010) 82:045125. doi:10.1103/physrevb.82.045125
44. Daghofer M, Luo Q-L, Yu R, Yao DX, Moreo A, Dagotto E. Orbital-weight Redistribution Triggered by Spin Order in the Pnictides. *Phys Rev B* (2010) 81:180514. doi:10.1103/physrevb.81.180514
45. Fanfarillo L, Mansart J, Toulemonde P, Cercellier H, Le Fèvre P, Bertran F, et al. Orbital-dependent Fermi Surface Shrinking as a Fingerprint of Nematicity in FeSe. *Phys Rev B* (2016) 94:155138. doi:10.1103/physrevb.94.155138
46. Fanfarillo L, Giovannetti G, Capone M, Bascones E. Nematicity at the Hund's Metal Crossover in Iron Superconductors. *Phys Rev B* (2017) 95:144511. doi:10.1103/physrevb.95.144511
47. Benfatto L, Cappelluti E. Effects of the Fermi-Surface Shrinking on the Optical Sum Rule in Pnictides. *Phys Rev B* (2011) 83:104516. doi:10.1103/physrevb.83.104516
48. Watson MD, Backes S, Haghighirad AA, Hoesch M, Kim TK, Coldea AI, et al. Formation of Hubbard-Like Bands as a Fingerprint of Strong Electron-Electron Interactions in FeSe. *Phys Rev B* (2017) 95:081106. doi:10.1103/physrevb.95.081106
49. Evtushinsky DV, Aichhorn M, Sassa Y, Liu ZH, Maletz J, Wolf T, et al. (2016), arXiv:1612.02313 [cond-mat.supr-con]. Available at: https://arxiv.org/abs/1612.02313.
50. Baek S-H, Efremov DV, Ok JM, Kim JS, van den Brink J, Büchner B. Orbital-driven Nematicity in FeSe. *Nat Mater* (2015) 14:210–4. doi:10.1038/nmat4138
51. Böhmer AE, Arai T, Hardy F, Hattori T, Iye T, Wolf T, et al. Origin of the Tetragonal-to-Orthorhombic Phase Transition in FeSe: A Combined Thermodynamic and NMR Study of Nematicity. *Phys Rev Lett* (2015) 114:027001. doi:10.1103/PhysRevLett.114.027001
52. Cao RX, Hu J, Dong J, Zhang JB, Ye XS, Xu YF, et al. Observation of Orbital Ordering and Origin of the Nematic Order in FeSe. *New J Phys* (2019) 21: 103033. doi:10.1088/1367-2630/ab4927
53. Nakayama K, Miyata Y, Phan GN, Sato T, Tanabe Y, Urata T, et al. Reconstruction of Band Structure Induced by Electronic Nematicity in an

FeSe Superconductor. *Phys Rev Lett* (2014) 113:237001. doi:10.1103/physrevlett.113.237001

54. Zhang P, Qian T, Richard P, Wang XP, Miao H, Lv BQ, et al. Observation of Two Distinctdxz/dyzband Splittings in FeSe. *Phys Rev B* (2015) 91:214503. doi:10.1103/physrevb.91.214503
55. Suzuki Y, Shimojima T, Sonobe T, Nakamura A, Sakano M, Tsuji H, et al. Momentum-dependent Sign Inversion of Orbital Order in Superconducting FeSe. *Phys Rev B* (2015) 92:205117. doi:10.1103/physrevb.92.205117
56. Watson MD, Kim TK, Rhodes LC, Eschrig M, Hoesch M, Haghighirad AA, et al. Evidence for Unidirectional Nematic Bond Ordering in FeSe. *Phys Rev B* (2016) 94:201107. doi:10.1103/physrevb.94.201107
57. Fedorov A, Yaresko A, Kim TK, Kushnirenko Y, Haubold E, Wolf T, et al. Effect of Nematic Ordering on Electronic Structure of FeSe. *Sci Rep* (2016) 6:36834. doi:10.1038/srep36834
58. Pustovit YV, Kordyuk AA. Metamorphoses of Electronic Structure of FeSe-Based Superconductors (Review Article). *Low Temperature Phys* (2016) 42:995–1007. doi:10.1063/1.4969896
59. Zhang Y, Yi M, Liu Z-K, Li W, Lee JJ, Moore RG, et al. Distinctive Orbital Anisotropy Observed in the Nematic State of a FeSe Thin Film. *Phys Rev B* (2016) 94:115153. doi:10.1103/physrevb.94.115153
60. Watson MD, Haghighirad AA, Rhodes LC, Hoesch M, Kim TK. Electronic Anisotropies Revealed by Detwinned Angle-Resolved Photo-Emission Spectroscopy Measurements of FeSe. *New J Phys* (2017) 19:103021. doi:10.1088/1367-2630/aa8a04
61. Coldea AI, Watson MD. The Key Ingredients of the Electronic Structure of FeSe. *Annu Rev Condens Matter Phys* (2018) 9:125–46. doi:10.1146/annurev-conmatphys-033117-054137
62. Jiang K, Hu J, Ding H, Wang Z. Interatomic Coulomb Interaction and Electron Nematic Bond Order in FeSe. *Phys Rev B* (2016) 93:115138. doi:10.1103/physrevb.93.115138
63. Yi M, Pfau H, Zhang Y, He Y, Wu H, Chen T, et al. Nematic Energy Scale and the Missing Electron Pocket in FeSe. *Phys Rev X* (2019) 9:041049. doi:10.1103/physrevx.9.041049
64. Yu R, Zhu J-X, Si Q. Orbital Selectivity Enhanced by Nematic Order in FeSe. *Phys Rev Lett* (2018) 121:227003. doi:10.1103/physrevlett.121.227003
65. Yi M, Zhang Y, Shen Z-X, Lu D. Role of the Orbital Degree of freedom in Iron-Based Superconductors. *Npj Quant Mater* (2017) 2:57. doi:10.1038/s41535-017-0059-y
66. Huang J, Yu R, Xu Z, Zhu JX, Oh JS, Jiang Q, et al. Correlation-Driven Electronic Reconstruction in $FeTe_{1-x}Se_x$. *Communications Physics* (2022) 5 (1):29. doi:10.1038/s42005-022-00805-6
67. Pfau H, Yi M, Hashimoto M, Chen T, Dai P-C, Shen Z-X, et al. Quasiparticle Coherence in the Nematic State of FeSe. *Phys Rev B* (2021) 104:L241101. doi:10.1103/physrevb.104.l241101
68. Mirri C, Dusza A, Bastelberger S, Chinotti M, Degiorgi L, Chu J-H, et al. Origin of the Resistive Anisotropy in the Electronic Nematic Phase of $BaFe_2As_2$ Revealed by Optical Spectroscopy. *Phys Rev Lett* (2015) 115:107001. doi:10.1103/physrevlett.115.107001
69. Mirri C, Dusza A, Bastelberger S, Chinotti M, Chu J-H, Kuo H-H, et al. Electrodynamic Response in the Electronic Nematic Phase of $BaFe_2As_2$. *Phys Rev B* (2016) 93:085114. doi:10.1103/physrevb.93.085114
70. Wu D, Barišić N, Kallina P, Faridian A, Gorshunov B, Drichko N, et al. Optical Investigations of the normal and Superconducting States Reveal Two Electronic Subsystems in Iron Pnictides. *Phys Rev B* (2010) 81:100512. doi:10.1103/physrevb.81.100512
71. Fanfarillo L, Benfatto L, Valenzuela B. Orbital Mismatch Boosting Nematic Instability in Iron-Based Superconductors. *Phys Rev B* (2018) 97:121109. doi:10.1103/physrevb.97.121109
72. Fernández-Martín R, Fanfarillo L, Benfatto L, Valenzuela B. Anisotropy of the dc Conductivity Due to Orbital-Selective Spin Fluctuations in the Nematic Phase of Iron Superconductors. *Phys Rev B* (2019) 99:155117. doi:10.1103/PhysRevB.99.155117
73. Schütt M, Schmalian J, Fernandes RM. Origin of DC and AC Conductivity Anisotropy in Iron-Based Superconductors: Scattering Rate Versus Spectral Weight Effects. *Phys Rev B* (2016) 94:075111. doi:10.1103/PhysRevB.94.075111
74. Böhmer AE, Kreisel A. Nematicity, Magnetism and Superconductivity in FeSe. *J Phys Condensed Matter* (2017) 30:023001. doi:10.1088/1361-648x/aa9caa
75. Lu X, Zhang W, Tseng Y, Liu R, Tao Z, Paris E, et al. (2021), arXiv:2108.04484 [cond-mat.supr-con]. Available at: https://arxiv.org/abs/2108.04484.
76. Benfatto L, Valenzuela B, Fanfarillo L. Nematic Pairing from Orbital-Selective Spin Fluctuations in FeSe. *Npj Quant Mater* (2018) 3:56. doi:10.1038/s41535-018-0129-9
77. Baek S-H, Ok JM, Kim JS, Aswartham S, Morozov I, Chareev D, et al. Separate Tuning of Nematicity and Spin Fluctuations to Unravel the Origin of Superconductivity in FeSe. *Npj Quan Mater.* (2020) 5:8. doi:10.1038/s41535-020-0211-y
78. Wang Q, Shen Y, Pan B, Hao Y, Ma M, Zhou F, et al. Strong Interplay between Stripe Spin Fluctuations, Nematicity and Superconductivity in FeSe. *Nat Mater* (2016) 15:159–63. doi:10.1038/nmat4492
79. Chen T, Chen Y, Kreisel A, Lu X, Schneidewind A, Qiu Y, et al. Anisotropic Spin Fluctuations in Detwinned FeSe. *Nat Mater* (2019) 18:709–16. doi:10.1038/s41563-019-0369-5
80. Li G, Hu WZ, Dong J, Li Z, Zheng P, Chen GF, et al. Probing the Superconducting Energy Gap from Infrared Spectroscopy on a $Ba_{0.6}K_{0.4}Fe_2As_2$ Single Crystal with T_c=37 K. *Phys Rev Lett* (2008) 101:107004. doi:10.1103/physrevlett.101.107004
81. Charnukha A, Dolgov OV, Golubov AA, Matiks Y, Sun DL, Lin CT, et al. Eliashberg Approach to Infrared Anomalies Induced by the Superconducting State of $Ba_{0.68}K_{0.32}Fe_2As_2$ Single Crystals. *Phys Rev B* (2011) 84:174511. doi:10.1103/physrevb.84.174511
82. Charnukha A, Popovich P, Matiks Y, Sun DL, Lin CT, Yaresko AN, et al. Superconductivity-induced Optical Anomaly in an Iron Arsenide. *Nat Commun* (2011) 2:219. doi:10.1038/ncomms1223
83. Dai YM, Xu B, Shen B, Xiao H, Wen HH, Qiu XG, et al. Hidden *T*-Linear Scattering Rate in $Ba_{0.6}K_{0.4}Fe_2As_2$ Revealed by Optical Spectroscopy. *Phys Rev Lett* (2013) 111:117001. doi:10.1103/physrevlett.111.117001
84. Dai YM, Xu B, Shen B, Wen HH, Qiu XG, Lobo RPSM. Optical Conductivity of $Ba_{0.6}K_{0.4}Fe_2As_2$: The Effect of In-Plane and Out-Of-Plane Doping in the Superconducting gap. *Epl* (2013) 104:47006. doi:10.1209/0295-5075/104/47006
85. Xu B, Dai YM, Xiao H, Shen B, Wen HH, Qiu XG, et al. Infrared Probe of the gap Evolution across the Phase Diagram of $Ba_{1-x}K_xFe_2As_2$. *Phys Rev B* (2017) 96:115125. doi:10.1103/physrevb.96.115125
86. Kretzschmar F, Muschler B, Böhm T, Baum A, Hackl R, Wen H-H, et al. Raman-Scattering Detection of Nearly Degenerate s-Wave and d-Wave Pairing Channels in Iron-Based $Ba_{0.6}K_{0.4}Fe_2As_2$ and $Rb_{0.8}Fe_{1.6}Se_2$ Superconductors. *Phys Rev Lett* (2013) 110:187002. doi:10.1103/physrevlett.110.187002
87. Pal A, Chinotti M, Chu J-H, Kuo H-H, Fisher IR, Degiorgi L. Anisotropic Superconducting Gap in Optimally Doped Iron-Based Material. *J Supercond Nov Magn* (2020) 33:2313–8. doi:10.1007/s10948-019-05390-4
88. Carlson EW, Dahmen KA. Using Disorder to Detect Locally Ordered Electron Nematics via Hysteresis. *Nat Commun* (2011) 2:379. doi:10.1038/ncomms1375
89. Kuo H-H, Fisher IR. Effect of Disorder on the Resistivity Anisotropy Near the Electronic Nematic Phase Transition in Pure and Electron-Doped $BaFe_2As_2$. *Phys Rev Lett* (2014) 112:227001. doi:10.1103/physrevlett.112.227001
90. Ishida S, Nakajima M, Liang T, Kihou K, Lee CH, Iyo A, et al. Anisotropy of the In-Plane Resistivity of Underdoped $Ba(Fe_{1-x}Co_x)_2As_2$ Superconductors Induced by Impurity Scattering in the Antiferromagnetic Orthorhombic Phase. *Phys Rev Lett* (2013) 110:207001. doi:10.1103/physrevlett.110.207001
91. Nakajima M, Ishida S, Tomioka Y, Kihou K, Lee CH, Iyo A, et al. Effect of Co Doping on the In-Plane Anisotropy in the Optical Spectrum of Underdoped $Ba(Fe_{1-x}Co_x)_2As_2$. *Phys Rev Lett* (2012) 109:217003. doi:10.1103/physrevlett.109.217003
92. Christianson AD, Goremychkin EA, Osborn R, Rosenkranz S, Lumsden MD, Malliakas CD, et al. Unconventional Superconductivity in $Ba_{0.6}K_{0.4}Fe_2As_2$ from Inelastic Neutron Scattering. *Nature* (2008) 456:930–2. doi:10.1038/nature07625
93. Böhm T, Kemper AF, Moritz B, Kretzschmar F, Muschler B, Eiter H-M, et al. Balancing Act: Evidence for a Strong Subdominant *d*-Wave Pairing Channel in $Ba_{0.6}K_{0.4}Fe_2As_2$. *Phys Rev X* (2014) 4:041046. doi:10.1103/PhysRevX.4.041046

94. Li J, Pereira PJ, Yuan J, Lv Y-Y, Jiang M-P, Lu D, et al. Nematic Superconducting State in Iron Pnictide Superconductors. *Nat Commun* (2017) 8:1880. doi:10.1038/s41467-017-02016-y
95. Chen L, Han TT, Cai C, Wang ZG, Wang YD, Xin ZM, et al. Orbital-dependent Modulation of the Superconducting gap in Uniaxially Strained $Ba_{0.6}K_{0.4}Fe_2As_2$. *Phys Rev B* (2021) 104:L060502. doi:10.1103/physrevb.104.l060502
96. Dong Y, Lv Y, Xu Z, Abdel-Hafiez M, Vasiliev AN, Zhu H, et al. Observation of a Ubiquitous (π, π)-Type Nematic Superconducting Order in the Whole Superconducting Dome of Ultra-thin $BaFe_{2-x}Ni_xAs_2$ Single Crystals. *Chin Phys. Lett.* (2021) 38:097401. doi:10.1088/0256-307x/38/9/097401
97. Kushnirenko YS, Evtushinsky DV, Kim TK, Morozov I, Harnagea L, Wurmehl S, et al. Nematic Superconductivity in LiFeAs. *Phys Rev B* (2020) 102:184502. doi:10.1103/physrevb.102.184502
98. Sprau PO, Kostin A, Kreisel A, Böhmer AE, Taufour V, Canfield PC, et al. Discovery of Orbital-Selective Cooper Pairing in FeSe. *Science* (2017) 357: 75–80. doi:10.1126/science.aal1575
99. She J-H, Lawler MJ, Kim E-A. Quantum Spin Liquid Intertwining Nematic and Superconducting Order in Fese. *Phys Rev Lett* (2018) 121:237002. doi:10.1103/physrevlett.121.237002
100. Liu D, Li C, Huang J, Lei B, Wang L, Wu X, et al. Orbital Origin of Extremely Anisotropic Superconducting Gap in Nematic Phase of FeSe Superconductor. *Phys Rev X* (2018) 8:031033. doi:10.1103/physrevx.8.031033
101. Hu H, Yu R, Nica EM, Zhu J-X, Si Q. Orbital-selective Superconductivity in the Nematic Phase of FeSe. *Phys Rev B* (2018) 98:220503. doi:10.1103/physrevb.98.220503
102. Zvyagina GA, Gaydamak TN, Zhekov KR, Bilich IV, Fil VD, Chareev DA, et al. Acoustic Characteristics of FeSe Single Crystals. *EPL* (2013) 101:56005. doi:10.1209/0295-5075/101/56005
103. Kothapalli K, Boöhmer AE, Jayasekara WT, Ueland BG, Das P, Sapkota A, et al. Strong Cooperative Coupling of Pressure-Induced Magnetic Order and Nematicity in FeSe. *Nat Commun* (2016) 7:12728. doi:10.1038/ncomms12728

Conflict of Interest: The author declares that the research was conducted in the absence of any commercial or financial relationships that could be construed as a potential conflict of interest.

frontiers | Frontiers in Physics

ORIGINAL RESEARCH
published: 14 April 2022
doi: 10.3389/fphy.2022.877628

Nematicity and Glassy Behavior Probed by Nuclear Magnetic Resonance in Iron-Based Superconductors

N. J. Curro[1]*, **T. Kissikov**[1], **M. A. Tanatar**[2], **R. Prozorov**[2], **S. L. Bud'ko**[2] **and P. C. Canfield**[2]

[1]*Department of Physics and Astronomy, University of California, Davis, Davis, CA, United States,* [2]*Ames Laboratory U.S. DOE and Department of Physics and Astronomy, Iowa State University, Ames, IA, United States*

Nuclear magnetic resonance provides a wealth of information about the magnetic and nematic degrees of freedom in the iron-based superconductors. A striking observation is that the spin lattice relaxation rate is inhomogeneous with a standard deviation that correlates with the nematic susceptibility. Moreover, the spin lattice relaxation is strongly affected by uniaxial strain, and in doped samples it depends sensitively upon the history of the applied strain. These observations suggest that quenched strain fields associated with doping atoms induce a nematic glass in the iron pnictide materials.

Keywords: nuclear magnetic resonance, nematicity, uniaxial strain, glassy dynamics, spin lattice relaxation, quantum materials

Edited by:
Laura Fanfarillo,
International School for Advanced Studies (SISSA), Italy

Reviewed by:
Pietro Carretta,
University of Pavia, Italy
Kenji Ishida,
Kyoto University, Japan
Rui Zhou,
Institute of Physics (CAS), China

****Correspondence:***
N. J. Curro
njcurro@ucdavis.edu

Specialty section:
This article was submitted to Condensed Matter Physics, a section of the journal Frontiers in Physics

Received: *16 February 2022*
Accepted: *21 March 2022*
Published: *14 April 2022*

Citation:
Curro NJ, Kissikov T, Tanatar MA, Prozorov R, Bud'ko SL and Canfield PC (2022) Nematicity and Glassy Behavior Probed by Nuclear Magnetic Resonance in Iron-Based Superconductors. Front. Phys. 10:877628. doi: 10.3389/fphy.2022.877628

1 INTRODUCTION

Electronic nematic order, in which low energy electronic degrees of freedom drive a crystal to spontaneously break discrete rotational symmetry without simultaneously breaking translational symmetry, has attracted broad interest in correlated electron physics [1]. Much of this interest stems from observations that unconventional superconductivity tends to emerge in materials exhibiting competing ground states with different broken symmetries, including nematic, charge, and/or spin density wave fluctuations [2–6]. Measurements of the nematic susceptibility in the iron based superconductors indicated the presence of a putative nematic quantum critical point under the dome of superconductivity in these materials [7, 8]. These observations have suggested a connection between quantum critical nematic fluctuations and the pairing mechanism for superconductivity [9–13]. It is thus important to understand the nature of the nematic fluctuations and their relationship to the coexisting antiferromagnetism throughout the phase diagram.

Nuclear magnetic resonance (NMR) provides a wealth of information about both the magnetic and nematic degrees of freedom in the iron-based superconductors [14]. Studies under uniaxial strain offer an important new direction in thermodynamic phase space to explore the physics of nematicity. Such experiments can broadly be separated into those that probe the static properties of the magnetic and nematic order, and those that probe the dynamical properties. The latter set of experiments have yielded some important surprises, such as a change in the spin anisotropy as a function of strain [15], and the presence of dynamical inhomogeneity when the materials are doped [16]. Below we discuss how NMR probes these broken symmetries and their fluctuations, and summarize results of experiments under uniaxial strain, both in the undoped and doped materials. These observations are consistent with the emergence of a nematic glass in doped samples, possibly driven by the presence of random strain fields from quenched disorder.

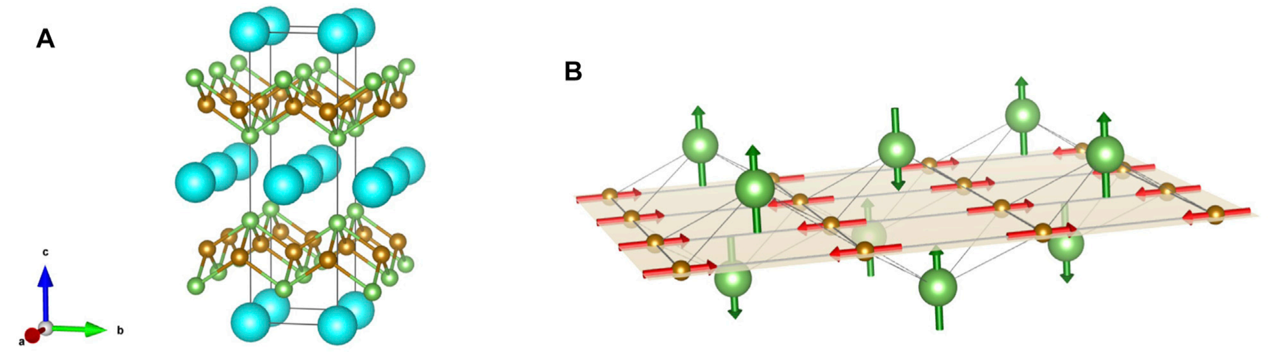

FIGURE 1 | (A) $BaFe_2As_2$ unit cell. Ba is cyan, Fe is brown and As is green. **(B)** The hyperfine field (green arrows) at the As sites in the antiferromagnetic state, with the Fe moments (red) oriented in the plane.

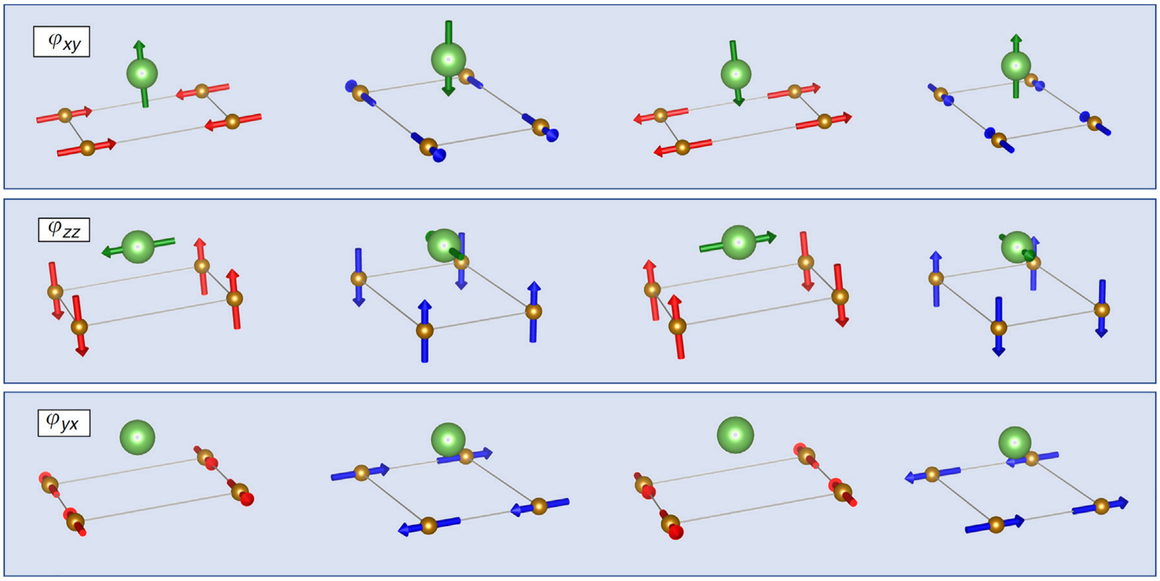

FIGURE 2 | The hyperfine field at the As site (green) for the four degenerate domains with in-plane Fe moments oriented parallel to the ordering vector (ϕ_{xy} nematic order, upper row), with *c*-axis Fe moments (ϕ_{zz} nematic order, middle row) and with in-plane moments oriented perpendicular to the ordering vector (ϕ_{yx} nematic order, bottom row). Red and blue correspond to the two different nematic domains (positive and negative strains). Within each nematic domain, there are two different antiferromagnetic configurations.

2 COUPLING TO NUCLEAR SPINS

The ^{75}As nuclei, with 100% abundance and spin $I = 3/2$, are excellent sensors of both the nematic and magnetic degrees of freedom in the iron pnictide superconductors. **Figure 1** shows the unit cell and indicates the hyperfine coupling between the As nuclei and the four nearest neighbor Fe electronic moments. The As also has a significant quadrupolar moment, $Q = 3.14 \times 10^{-29}\,\mathrm{m}^2$, which couples to the surrounding electric field gradient (EFG) [17]. The hyperfine and quadrupolar couplings enable microscopic studies of both the magnetic and nematic susceptibilities of the *electronic* degrees of freedom.

2.1 Hyperfine Interaction

The hyperfine coupling is given by:

$$\mathcal{H}_{hyp} = \sum_{i\in n.n.} \hat{\mathbf{I}}\cdot\mathbb{A}_i\cdot\hat{\mathbf{S}}_i, \tag{1}$$

where $\hat{I}_\alpha$ are the nuclear spin operators, $\hat{\mathbf{S}}_i$ are the Fe spins on the four nearest neighbors to the As nucleus, and the hyperfine coupling tensors, $\mathbb{A}_i$, have dipolar symmetry [18, 19]. In $BaFe_2As_2$, the eigenvalues of the tensor are $A_{aa} = A_{bb} = 6.6\,\mathrm{kOe}/\mu_B$, and $A_{cc} = 4.7\,\mathrm{kOe}/\mu_B$, but these values depend on details of the electronic structure and can vary between compounds. They can change as a function of pressure or doping, but the general symmetry of the $\mathbb{A}_i$ does not. The magnitude of these values are greater than those for the direct dipole interaction, which reflects the electronic hybridization between the As 4*p* and Fe 3*d* orbitals. The tensor nature of this coupling gives rise to a hyperfine field $\mathbf{H}_{hf} \parallel \mathbf{c}$ when the Fe moments lie in the *ab* plane, as illustrated in top row of **Figure 2**. Alternatively, if the Fe moments ordered parallel to **c**, then $\mathbf{H}_{hf}$ lies in the plane, as shown in the middle row of **Figure 2**.

Other magnetic orderings can be present in the pnictides, beyond the stripe-type spin density wave illustrated in **Figure 2**. In particular, the spin-vortex crystal configuration, in which the Fe spins form either loop or hedgehog structures, can be stabilized when a glide symmetry across the Fe planes is broken [20]. This type of order was recently identified in Ni-doped and Co-doped $CaKFe_4As_4$ [21]. There are two crystallographically distinct As sites in this structure, and the hyperfine field either vanishes at both sites for loop spin-vortex crystal order, or is aligned along the **c** axis for one As site and vanishes for the other As site for hedgehog spin-vortex crystal order. In this system, doping induces the latter, which was identified by NMR.

Note that when the Fe is substituted by another transition metal, the symmetry among the hyperfine couplings of the four nearest neighbors is broken, and the hyperfine field vector can acquire a component perpendicular to the **c** axis [22]. This effect contributes to inhomogeneous broadening in doped samples. In the presence of nematic order, the C_4 symmetry of the lattice is broken, and in principle $A_{aa} \neq A_{bb}$. This asymmetry has not been observed directly. In FeSe, the Knight shift tensor becomes anisotropic, with $K_{aa} \neq K_{bb}$, where $K_{\alpha\alpha} = A_{\alpha\alpha}\chi_{\alpha\alpha}$, and $\chi_{\alpha\alpha}$ is the static magnetic susceptibility [5]. However, in this case the anisotropy is believed to reflect that of the susceptibility, i.e., $\chi_{aa} \neq \chi_{bb}$ in the nematic phase, rather than an asymmetry in the hyperfine coupling [23]. Curiously, $\chi_{aa} > \chi_{bb}$ in FeSe, but $\chi_{bb} > \chi_{aa}$ in $BaFe_2As_2$, LaFeAsO, and NaFeAs [24–26], which may reflect different natures of the nematic order in these materials [27]. In particular, the nematic order parameter in the latter can be understood in terms of differential occupations between the d_{yz} and d_{xz} orbitals, whereas in the former the nematic order may involve more complex superpositions between 3*d* orbitals, giving rise to bond-centered nematic order [23, 28, 29]. The sign of the resistivity anisotropies in $BaFe_2As_2$ and FeSe match those of the magnetic anisotropies [24, 30], suggesting a common origin for the two.

2.2 Quadrupolar Interaction

For nuclei with spin $I > 1/2$, the quadrupolar coupling is given by:

$$\mathcal{H}_Q = \frac{h\nu_{zz}}{6}\left[3\hat{I}_z^2 - \hat{I}^2 + \eta\left(\hat{I}_x^2 - \hat{I}_y^2\right)\right], \tag{2}$$

where the EFG tensor is given by:

$$\nu_{\alpha\beta} = \frac{eQ}{12h}\frac{\partial^2 V}{\partial x_\alpha \partial x_\beta}, \tag{3}$$

and *V* is the electrostatic potential at the As site. This quantity is dominated by the occupation of the As 4*p* orbitals, which in turn are hybridized with the $d_{xz,yz}$-orbitals of the neighboring Fe atoms [31]. The EFG asymmetry parameter is given by:

$$\eta = \frac{\nu_{yy} - \nu_{xx}}{\nu_{xx} + \nu_{yy}}. \tag{4}$$

This quantity vanishes in the tetragonal phase because the As $4p_x$ and $4p_y$ orbitals are degenerate, hence $\nu_{xx} = \nu_{yy}$ [32]. The EFG tensor is always traceless, thus in this case it can be characterized by a single quantity, ν_{zz}. The magnitude of ν_{zz} depends on the degree of hybridization of the As $4p_z$ orbital, and is sensitive to the *c*-axis length of the unit cell [33–35] and also varies with temperature [18, 36–38].

The EFG is strongly affected by doping. Replacing the Fe by another transition metal, or replacing the As by P, will give rise to spatially-varying strain fields that will distort the electrostatic potential and alter the EFG tensor. This effect can lower the symmetry such that $\nu_{xx} \neq \nu_{yy}$, and create non-zero off-diagonal terms of the tensor. In some cases the effect is sufficiently large that separate resonances can be detected for sites that are adjacent to the substitutional site [31, 39]. This sensitivity to disorder tends to significantly broaden the NMR resonance frequencies in doped samples relative to the parent compound. In doped $Ba(Fe,Co)_2As_2$ the width of the quadrupolar satellites is dominated by a variation of η that exhibits a Curie-Weiss temperature dependence, which has been associated with the growth of nematic correlations surrounding the dopant atoms [40]. A similar effect has been observed in FeSe where the magnetic linewidth is broadened by the presence of crystal defects (there is no quadrupolar interaction for Se) [41]. In this case, the Knight shift anisotropy reflects the growth of an Edwards-Anderson order parameter of the nematicity [42].

In the presence of long range nematic order, the C_4 symmetry of the EFG tensor is broken and $\nu_{xx} \neq \nu_{yy}$ [43]. In $CaFe_2As_2$ η reaches 0.4 at low temperature, but in $BaFe_2As_2$ and $SrFe_2As_2$, η reaches 1.2 and 1.4, respectively, reflecting the fact that ν_{xx} and ν_{yy} have opposite signs [33]. Note that it is sometimes customary to define the principal axes of the EFG such that the eigenvalues $|V_{zz}| \geq |V_{yy}| \geq |V_{xx}|$, so that $0 \leq \eta \leq 1$. Here we do not follow this convention, maintaining the V_{zz} associated with the crystal *c* axis as in the tetragonal phase. This choice is the reason that $\eta > 1$, which would correspond to a confusing rotation of orientation of the principal axes under the customary definition. These changes reflect a dramatic rearrangement of the charge distribution around the As nucleus below the structural transition, despite an orthorhombicity of only approximately 1%. The EFG tensor is dominated by the occupations of the As 4*p* orbitals, which in turn are hybridized with the Fe $3d_{yz}$ and $3d_{xz}$ orbitals [31, 32]. These orbitals are degenerate in the tetragonal phase, but develop a splitting on the order of 40 meV in the nematic phase [44]. As a result, the relative occupations of the As p_x and p_y orbitals change and alter the EFG.

2.3 NMR Spectra

In order to resolve the in-plane asymmetry that emerges in the Knight shift or EFG tensors, it is important to measure the NMR spectra of carefully oriented single crystals. In an external magnetic field, the As nuclear spins experience the sum of three interactions: $\mathcal{H}_Z + \mathcal{H}_{hyp} + \mathcal{H}_Q$, where $\mathcal{H}_Z = -\gamma\hbar\hat{\mathbf{I}} \cdot \mathbf{H}_0$ is

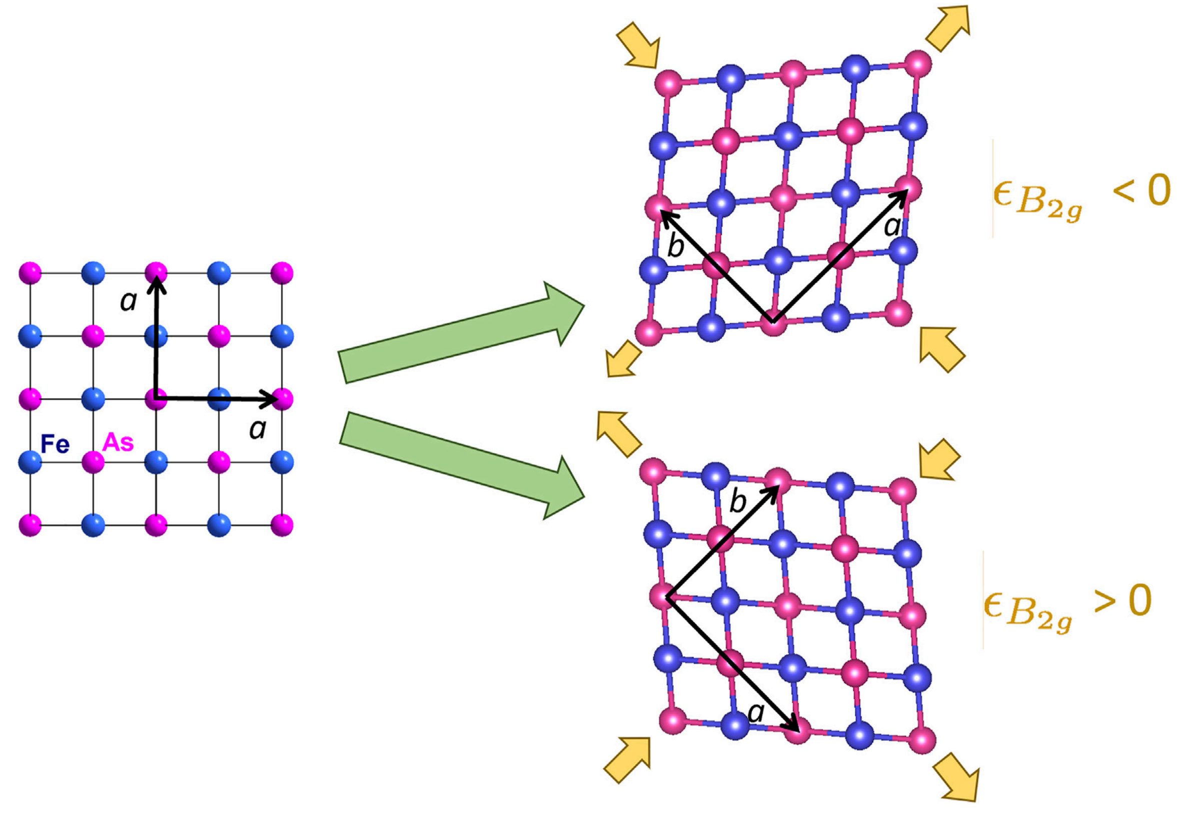

FIGURE 3 | Fe-As plane in tetragonal and orthorhombic phase of $BaFe_2As_2$. Orange arrows indicate direction of displacements giving rise to two domains with positive and negative B_{2g} strain. Strain is labeled by the unit cell of the tetragonal phase, so uniaxial strain along the $[110]_T$ direction of the tetragonal unit cell gives rise to a B_{2g} distortion.

the Zeeman interaction. The spectrum will consist of three resonances. For sufficiently large Zeeman interaction ($\gamma H_0 \gg \nu_{\alpha\alpha}$), the frequencies are given to first order by:

$$\begin{aligned} f_{sat1,2} &= \gamma H_0 \left(1 + K(\theta,\phi)\right) \pm \nu_{zz} \left(3\cos^2\theta - 1 + \eta \sin^2\theta \cos(2\phi)\right) \\ f_{cen} &= \gamma H_0 \left(1 + K(\theta,\phi)\right) + \Delta f_2(\theta,\phi) \end{aligned} \tag{5}$$

where $f_{sat1,2}$ and f_{cen} are the frequencies of the two satellites and the central transition, θ is the angle between $\mathbf{H}_0$ and $\mathbf{c}$, and ϕ is the azimuthal angle of the projection of $\mathbf{H}_0$ in the ab plane. The Knight shift is given by:

$$K(\theta,\phi) = K_{zz}\cos^2\theta + K_{xx}\sin^2\theta\cos^2\phi + K_{yy}\sin^2\theta\sin^2\phi. \tag{6}$$

The second order correction to the central transition is given by:

$$\begin{aligned} &\Delta f_2(\theta,\phi) \\ &= \frac{\nu_{zz}^2}{96\gamma H_0}\left[7\eta^2 - 18 - 6(\eta^2 - 30)\cos^2\theta - 9(18 + \eta^2)\cos^4\theta \right. \\ &\left. + 12\eta\cos(2\phi)(9\cos^4\theta - 8\cos^2\theta - 1) - 9\eta^2\cos(4\phi)\sin^4\theta\right]. \end{aligned} \tag{7}$$

Measurements of the two satellite transitions as a function of field orientation can be used to extract the Knight shift and EFG tensors.

In the tetragonal phase, there are three distinct resonances for each As in the unit cell (e.g., one As site in AFe_2As_2). However, in the nematic phase there are multiple domains in an untwinned crystal, giving rise to extra resonances. If the magnetic field is oriented in the plane, then there may be two sets of resonances associated with these two domains because the azimuthal angle, ϕ, differs for each domain, as observed in **Figure 3**. This behavior is illustrated in **Figure 4**. In general, there are five distinct transitions (six if the Knight shift is also anisotropic), but in certain directions the spectra from the two domains overlap and three resonances are recovered. Large values of $|\eta|$ cause the satellites to switch positions from below to above the central transition as the in-plane angle ϕ is rotated.

When η is non-zero the nuclear spin Hamiltonian does not commute with $\hat{I}_z$, and the eigenstates, $|i\rangle$, are superpositions of the $|I_z\rangle$ states. In such cases it may be possible to observe hidden transitions when the matrix element $\langle\psi_i|\hat{I}_\pm|\psi_j\rangle$ does not vanish. This effect can arise when $\nu_{zz} \gtrsim \gamma H$, but in almost all cases there is an internal field, H_{int}, that develops in the antiferromagnetic state that accompanies the orthorhombic distortion. Typically $\gamma H_{int} \gg \nu_{zz}$ is sufficiently large that such hidden transitions should not be evident. For $CaFe_2As_2$, however, $\nu_{zz}/\gamma H \sim 0.7$ thus it may be possible to observe these transitions for small external fields H_0 applied in the plane, as illustrated in **Figure 5**. To date no such transitions have been reported.

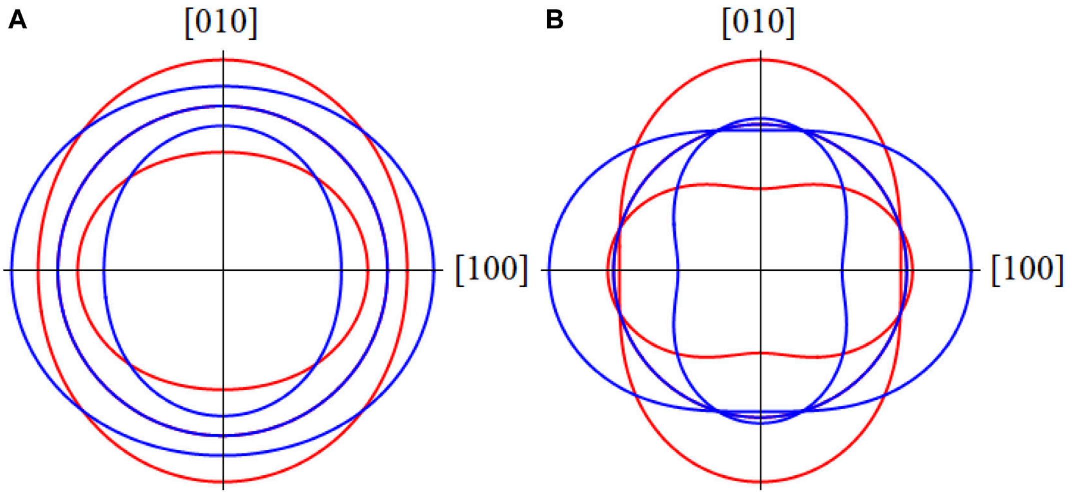

FIGURE 4 | Polar plots of the three resonance frequencies of the As for $|\eta| = 0.4$ **(A)** and for $|\eta| = 1.2$ **(B)**. Blue and red correspond to two nematic domains with $\pm\,\eta$, as a function of in-plane field direction. In this case, we assume $K_{xx} = K_{yy}$. The directions [100] and [010] correspond to the orthorhombic unit cell directions. In general, there are five distinct transitions, but for certain angles the two sets of satellites overlap. When $|\eta| > 1$, the two satellites for each domain reverse, crossing the central transition.

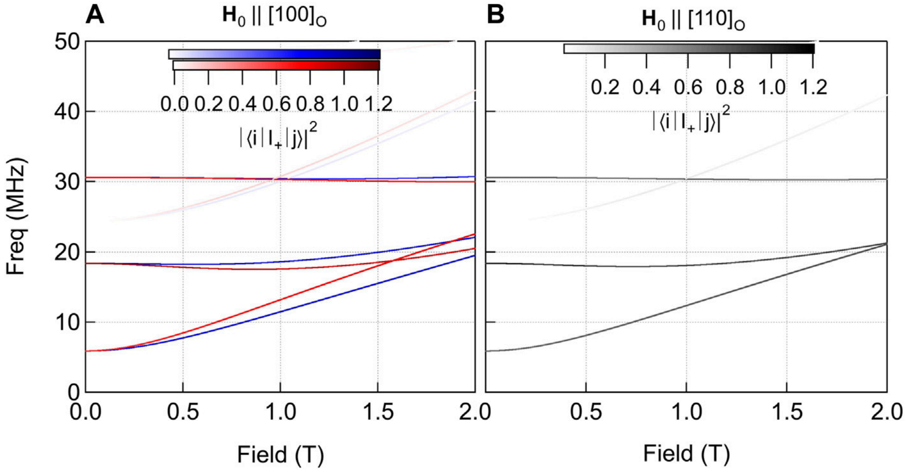

FIGURE 5 | Resonance frequencies versus applied magnetic field, $\mathbf{H}_0$, oriented either along the orthorhombic [100] **(A)** or [110] directions **(B)** assuming an internal field of 2.5 T along *c* and an EFG of $\nu_{zz} = 12.4$ MHz with $\eta = 0.4$, corresponding to the case of $CaFe_2As_2$. Red and blue correspond to the two nematic domains. The intensity of the transitions are given by the matrix elements $|\langle i|I_+|j\rangle|^2$, where *i*, *j* correspond to eigenstates of the nuclear spin Hamiltonian. Hidden transitions should be visible for certain field ranges.

2.4 Relaxation Rate

The hyperfine field, $\mathbf{H}_{hyp}$, and the EFG not only give rise to static spectral signatures, but their fluctuations can also drive relaxation of the nuclear spins. The nuclear spin energies are generally several order of magnitude smaller than the relevant electron energies, and thus the nuclear spin ensemble can easily be manipulated to have a non-equilibrium distribution among the energy levels. The nuclear spins will return to thermal equilibrium with the "lattice," or the electronic spin system, over a time scale, T_1, known as the spin-lattice relaxation time. This rate, T_1^{-1}, can be measured with high precision and is determined by the couplings described above in **Section 2.1**, **Section 2.2**. In essence, the nuclear spins act as quantum sensors that probe the noise spectra of the electronic spin and charge degrees of freedom. There are three important spectral densities that may play a role:

$$J(\omega) = \frac{\gamma^2}{2}\int_{\infty}^{\infty}[h_+, h_-]e^{i\omega\tau}d\tau \tag{8}$$

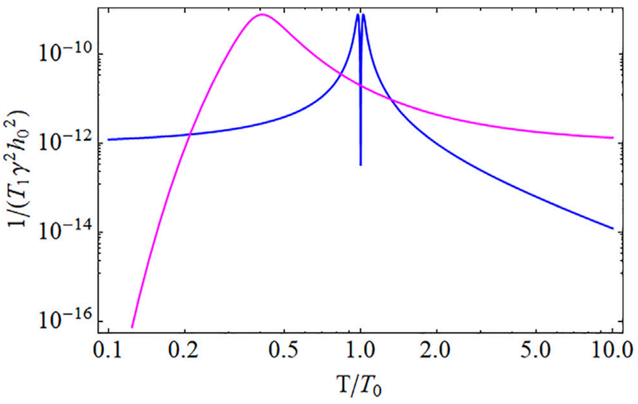

FIGURE 6 | Calculated spin lattice relaxation rate versus temperature using **Eq. 10** for two different models for the temperature dependence of the autocorrelation time, τ_c. The blue curve assumes a power law divergence: $\tau_c \propto |T - T_0|^{-2}$, appropriate for critical slowing down at a phase transition. The sharp dip around T_0 is usually not observable and there is only a single peak. The purple curve assumes an activated form: $\tau_c \propto e^{E_a/k_B T}$, where E_a is an activation energy, which is appropriate for a glassy system where the degrees of freedom gradually freeze out.

$$J^{(1,2)}(\omega) = \left(\frac{eQ}{\hbar}\right)^2 \int_{\infty}^{\infty} [V_{+1,2}, V_{-1,2}] e^{i\omega\tau} d\tau \tag{9}$$

where $[A, B] = \langle A(\tau)B(0) + B(\tau)A(0)\rangle/2$ is an ensemble average. Here $h_\pm = H_{hyp,x} \pm iH_{hyp,y}$, $V_{\pm 1} = V_{xz} \pm iV_{yz}$, and $V_{\pm 2} = (V_{xx} - V_{yy})/2 \pm iV_{xy}$ [45]. $J(\omega)$ and $J^{(1,2)}(\omega)$ are the spectral densities of the hyperfine and EFG fluctuations, respectively. The T_1^{-1} measurements probe these spectral functions at the nuclear resonance frequency, ω_N, typically on the order of 100 MHz (~ 0.4μeV). This frequency is nearly vanishing in comparison to the relevant electronic energies, typically on the order of meV. If there is only one type of fluctuation, then T_1^{-1} is directly related to the appropriate spectral density. For example, for pure magnetic fluctuations, (e.g., $V_{\pm 1,2} = 0$), then $T_1^{-1} = J(\omega_N)$, or if $h_\pm = 0$ and $V_{\pm 1} = 0$, then $T_1^{-1} = J^{(2)}(\omega_N)$, or if $h_\pm = 0$ and $V_{\pm 2} = 0$ then $T_1^{-1} = J^{(1)}(\omega_N)$. On the other hand, if multiple types of fluctuations are present, then the nuclear spin relaxation is a complex function of multiple spectral functions and it is not straightforward to disentangle the different contributions to T_1^{-1} [46–48]. It is common for the magnetic fluctuations to dominate, in which case the contribution from quadrupolar contributions can be ignored. However, as we discuss below in **Section 2.4.1**, there is a significant quadrupolar contribution to the T_1^{-1} of the As in the pnictides.

When the electronic system is close to an thermodynamic instability, critical fluctuations will slow down and may have a dramatic effect on T_1^{-1}. As an example, consider the case where the magnetic fluctuations exhibit Lorentzian autocorrelation function: $[h_+, h_-] = h_0^2 e^{-|\tau|/\tau_c}$, where τ_c is the correlation time. In this case:

$$\frac{1}{T_1} = \frac{\gamma^2 h_0^2 \tau_c}{1 + \omega_N^2 \tau_c^2}. \tag{10}$$

Usually $\omega_N \tau_c \ll 1$, but close to a phase transition where there is critical slowing down, τ_c can approach infinity as a power law. As a result, T_1^{-1} exhibits a peak at the phase transition temperature, as illustrated in **Figure 6**. This property has been exploited to investigate the critical dynamics of many correlated electron systems, especially the pnictides [39, 49].

As discussed above in **Section 2.3**, the nuclear spin eigenstates become superpositions of the I_z states for non-zero values of η. In this case, it is important to consider spectral densities other than those described in **Eqs 6**, **7** to account for fluctuations in other directions. For example, hyperfine field fluctuations, $H_{hyp,z}$, may play a role in relaxing the nuclear spins. In such cases the form of the relaxation function is more complicated, and **Eq. 8** will contain more terms.

2.4.1 Quadrupolar Relaxation From Nematic Fluctuations

Although magnetic relaxation is usually dominant, quadrupolar relaxation should also be present in the pnictides because the EFG changes dramatically at the nematic phase transition. This effect has been investigated in $BaFe_2(As_{1-x}P_x)_2$ by comparing the relaxation of the ^{75}As to ^{31}P [43]. The phosphorus isotope has spin $I = 1/2$, and does not have a quadrupolar moment. It therefore is only sensitive to magnetic fluctuations, whereas the As probes both magnetic and quadrupolar fluctuations. Importantly, both the As and the P are located in the same crystallographic site, and experience similar hyperfine interactions. In fact, the ^{75}As exhibits a higher relaxation rate, indicating the presence of a second relaxation channel that is, not probed by the ^{31}P. Moreover, the extra relaxation increases with decreasing temperature, and exhibits a peak at the nematic ordering temperature. An analysis of the extra relaxation rate suggests that the nematic susceptibility diverges below T_N for the lightly doped system, and below T_c for the optimally doped system. It was not possible to quantitatively disentangle the contributions from the magnetic and quadrupolar channels separately, primarily because the doping introduced inhomogeneous relaxation, as discussed below in **Section 4**. The three relaxation channels (one magnetic and two quadrupolar) may also be coupled to one another. For example, a nematic fluctuation can give rise spectral densities $J(\omega_N)$, $J^{(1)}(\omega_N)$, and $J^{(2)}(\omega_N)$. Nevertheless, this work provided direct proof of nematic fluctuations that diverge near the superconducting transition temperature, T_c. Theoretical work has suggested that nematic fluctuations may play a role in the superconducting pairing in these materials [9, 11].

3 RESPONSE TO UNIAXIAL STRAIN

In the iron based superconductors, the electronic nematic degrees of freedom couple to lattice strain with B_{2g} symmetry: $\varepsilon_{B2g} = (\varepsilon_{xx} - \varepsilon_{yy})/2$, where x and y are defined with respect to the tetragonal unit cell as illustrated in **Figure 3** [4]. This coupling gives rise to a linear response of the electronic nematicity to external strain on a crystal. Uniaxial strain can be applied via different techniques, however in recent years piezoelectric-based strain cells have

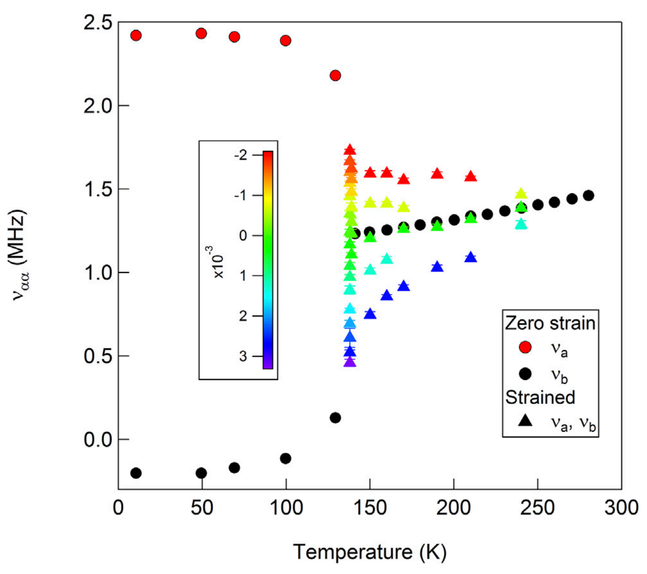

FIGURE 7 | The As EFG components, $\nu_a = \nu_{xx}$ and $\nu_b = \nu_{yy}$, as a function of temperature and uniaxial strain. The color bar indicates ε_{xx}. The circles are the measured values from [18].

demonstrated excellent properties that enable one to carefully control the level of strain even at cryogenic temperatures [50]. Even though piezoelectric actuators do not have linear response to control voltages, the strain can be controlled through feedback control algorithms for the long periods of time necessary for NMR experiments [51]. The strain is measured by a capacitive dilatometer. Note that even though the device applies a uniaxial stress, σ_0, along the x direction, the response of the crystal is not a pure uniaxial strain. Rather, the non-zero stress tensor elements become: $\varepsilon_{xx} = \sigma_0/E$ and $\varepsilon_{yy} = \varepsilon_{zz} = -\nu\sigma_0/E$, where E is the Young's modulus and ν is the Poisson's ratio of the material. This gives rise to strain in two symmetry channels:

$$\varepsilon_{B2g} = \left(\varepsilon_{xx} - \varepsilon_{yy}\right)\Big/2 = \sigma_0\frac{1+\nu}{2E} \tag{11}$$

$$\varepsilon_{A1g} = \left(\varepsilon_{xx} + \varepsilon_{yy}\right)\Big/2 = \sigma_0\frac{1-\nu}{2E}. \tag{12}$$

On the other hand, the electronic nematicity has a much stronger response to B_{2g} strain than A_{1g}, thus uniaxial stress is sufficient to probe the intrinsic B_{2g} nematic response [7].

3.1 Spectra

In $BaFe_2As_2$, uniaxial strain dramatically alters the EFG tensor and $\eta \propto \varepsilon_{xx}$, as illustrated in **Figure 7** [32]. In the absence of strain, the crystal remains tetragonal down to the nematic transition temperature T_s = 135 K, in which case the EFG tensor spontaneously develops an asymmetry such that $\nu_{xx} \neq \nu_{yy}$. However, in the presence of a finite strain field, η becomes finite above T_s. In fact, $\eta \propto \varepsilon_{xx}$ and the constant of proportionality is the nematic susceptibility. As seen in **Figure 7**, the response is largest just above T_s, where the nematic susceptibility diverges. This behavior is illustrated in **Figure 8**, which reveals that $d\eta/d\varepsilon_{xx} \approx 300$ at T_s.

Uniaxial stress has also been utilized to study the NMR spectra in LaFeAsO and FeSe [23]. In this case, compressive stress on the order of 10–20 MPa was applied by tightening a screw. A similar approach in which a crystal is suspended between the prongs of a horseshoe-shaped device was also utilized for NMR studies under tensile strain [52]. Neither approach directly measures the strain, precluding the possibility for feedback control. Moreover, differential thermal contraction may also give rise to finite strain fields even without applied stresses via the tightening screw. Nevertheless, such approaches can be used to mechanically detwin the crystal in the nematic phase [53]. If the crystal is cooled in a finite strain field, then a single nematic domain should nucleate below the transition. For a twinned crystal, there should be two sets of resonances as discussed above in **Section 2.3**. In detwinned or partially de-twinned crystals, the relative intensity changes. In FeSe, this approach enabled the identification of which resonance corresponds to which domain [23].

3.2 Relaxation Rate

The spin-lattice-relaxation rate varies strongly with uniaxial strain in $BaFe_2As_2$, as shown in **Figure 9** [15]. Strain enhances the relaxation rate and the effect is anisotropic: the enhancement is stronger for in-plane fields than for out-of-plane fields. The enhancement can be understood qualitatively by realizing that strain enhances the antiferromagnetic ordering temperature, T_N, thus for $T > T_N$, the correlation length should grow with increasing strain. The correlation time τ_c grows with increasing correlation length, thus enhancing T_1^{-1} as illustrated in **Figure 6**.

A more complete picture of the nematicity and the antiferromagnetism can be obtained by analyzing the reciprocal-space structure of the spin susceptibility tensor, $\chi_{\alpha\beta}(\mathbf{q})$. In the disordered tetragonal phase, $\chi_{xx}(\mathbf{q}) = \chi_{yy}(\mathbf{q})$, but in the presence of nematicity these components are no longer equal. In the ordered phase, the susceptibility diverges at the

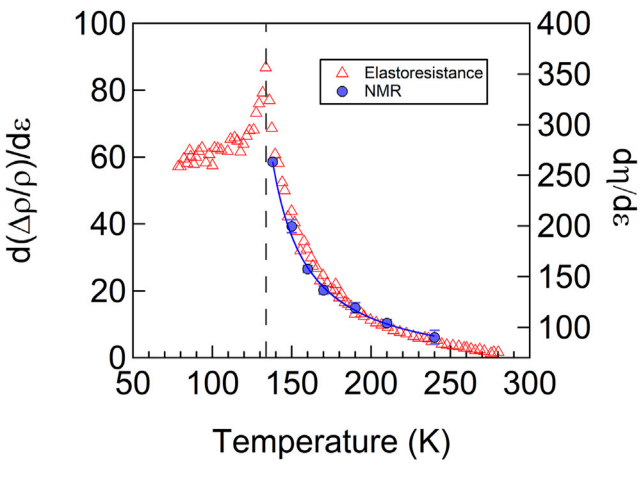

FIGURE 8 | The nematic susceptibility measured by the EFG asymmetry parameter, η and via elastoresistance measurements in $BaFe_2As_2$. The solid line is a fit to a Curie-Weiss expression. Reproduced from [32].

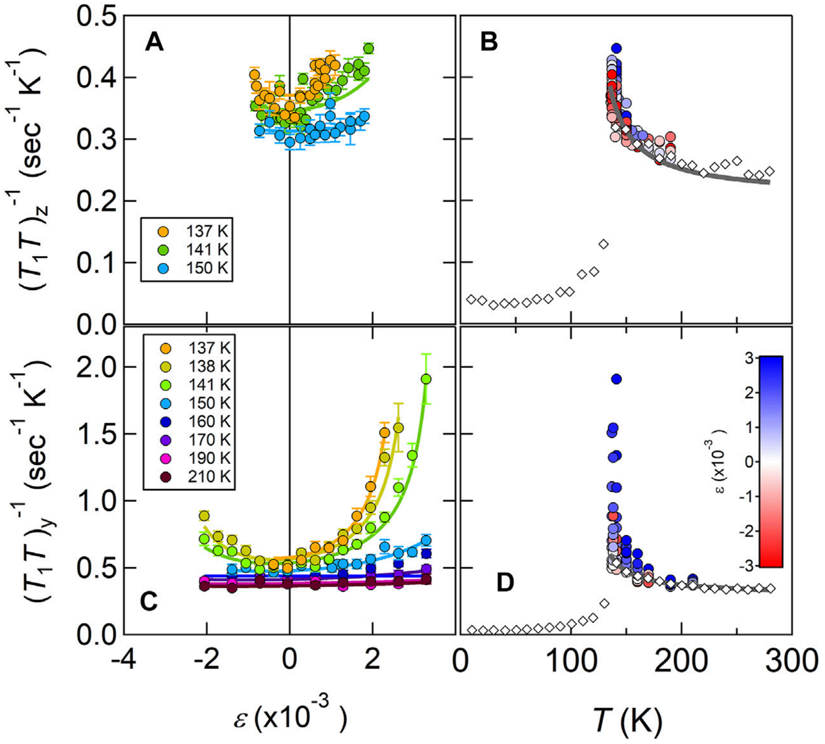

FIGURE 9 | $(T_1T)^{-1}_{y,z}$ versus strain **(A,C)** and versus temperature **(B,D)**. The solid lines are fits to the data. The y, z subscripts indicate the direction of the applied magnetic field, $\mathbf{H}_0$. Reproduced from [15].

antiferromagnetic ordering wavevectors, $\mathbf{Q}_1 = (\pi, 0)$ in one domain, and $\mathbf{Q}_2 = (0, \pi)$ in the other domain. A nematic order parameter can defined as $\phi_{\alpha\beta} = \chi^{-1}_{\alpha\alpha}(\mathbf{Q}_2) - \chi^{-1}_{\beta\beta}(\mathbf{Q}_1)$ [15]. By symmetry, the only non-vanishing components are ϕ_{xy}, ϕ_{yx} and ϕ_{zz}. In the ordered state, only ϕ_{xy} condenses, which corresponds to the spins oriented parallel to the antiferromagnetic ordering vector, as shown in the upper row of **Figure 2**. ϕ_{zz} order is illustrated in the second row of **Figure 2**. In this case, the spins are oriented along the c direction, and the hyperfine field is in-plane. Although this channel does not condense, ϕ_{zz} fluctuations are present and contribute to T_1^{-1}. ϕ_{yx} is illustrated in the bottom row, where the spins are oriented in-plane and are perpendicular to the antiferromagnetic ordering vector. For ϕ_{yx} order the hyperfine field vanishes, so T_1^{-1} is insensitive to these types of fluctuations.

The anisotropy of T_1^{-1} contains key information about these two nematic channels, ϕ_{xy} and ϕ_{zz}. The fluctuations $h_\alpha(\tau)$ of the hyperfine field that contribute to the spin-lattice-relaxation rate as described in **Eq. 10** are perpendicular to the applied field, $\mathbf{H}_0$. If $\mathbf{H}_0 \parallel \mathbf{c}$, then the in-plane fluctuations driven by ϕ_{zz} fluctuations will dominate T_1^{-1}. If $\mathbf{H}_0 \perp \mathbf{c}$, then both ϕ_{zz} and ϕ_{xy} fluctuations will contribute. As seen in **Figure 9**, T_1^{-1} measured for $\mathbf{H}_0 \perp \mathbf{c}$ has a much stronger variation with applied strain. This suggests that ϕ_{zz} fluctuations are enhanced under strain more than ϕ_{xy} fluctuations. In fact, a detailed analysis of the nematic susceptibilities, $\chi_{xy}^{nem} = \partial\phi_{xy}/\partial\varepsilon_{B2g}$ and $\chi_{zz}^{nem} = \partial\phi_{zz}/\partial\varepsilon_{B2g}$ indicates that the latter is largest, despite the fact that ϕ_{xy} condenses at zero strain [15]. These results imply that for sufficient strain, the system would order with the spins oriented along the c-axis. This interpretation was recently confirmed by polarized inelastic neutron scattering results [54].

4 GLASSY BEHAVIOR

4.1 Relaxation

Measurements of the doped pnictides under strain are challenging because the doping introduces both static and dynamic inhomogeneities. The quadrupolar linewidths of the satellites broaden significantly with doping, thus it is more difficult to discern static changes in the resonances due to strain. Measurements of the spin-lattice-relaxation rate are more straightforward and do not require sharp resonances, but doping introduces a distribution of local hyperfine fields and autocorrelation times, τ_c, so that there is no longer a homogeneous T_1^{-1} value throughout the bulk of the materials [16].

4.1.1 Stretched Relaxation

Heterogeneous spin lattice relaxation is directly manifest in the behavior of the magnetization and leads to a stretching exponent. In this case, the nuclear magnetization is described by:

$$M_z(t) = M_{eq} - \left(M_{eq} - M_0\right)e^{-(t/T_1)^{\beta}}, \tag{13}$$

where M_0 is the initial magnetization, M_{eq} is the thermal equilibrium magnetization, and $0 < \beta \leq 1$ is a stretching

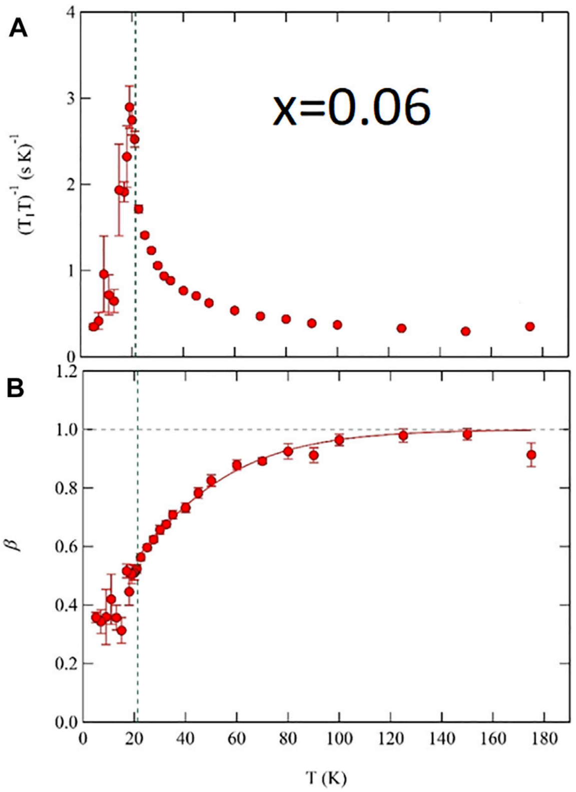

FIGURE 10 | (A) $(T_1T)^{-1}$ and **(B)** β versus temperature measured in $Ba(Fe_{1-x}Co_x)_2As_2$ with $x = 0.06$.

exponent [55]. $\beta = 1$ corresponds to homogeneous relaxation, but in several doped pnictides $\beta \sim 0.4$–0.9 depending on the doping level and temperature [16, 56–60]. A typical temperature dependence is shown in **Figure 10** for $x = 0.06$. For temperatures greater than approximately 100 K, the relaxation is homogeneous, but below this temperature β decreases from unity to approximately 0.4 at T_N. The exponent β is a measure of the width of the distribution of local relaxation rates, $\mathcal{P}(W_1)$, where W_1 is the relaxation rate. T_1^{-1}, is the median of this distribution and β is related to the logarithmic FWHM of $\mathcal{P}(W_1)$ [55]. When $\beta = 1$, the distribution is a delta function, and as β decreases the width of $\mathcal{P}(W_1)$ increases exponentially. **Figure 10** indicates that for $x = 0.06$ just above T_N the distribution of relaxation rates is at least two to three orders of magnitude in width. Additionally, the average correlation time, τ_c, does not have a power law divergence, but rather an activated or Vogel-Fulcher behavior with temperature, which tends to broaden the peak in $(T_1T)^{-1}$ with temperature, as illustrated in **Figure 6**.

4.1.2 Inverse Laplace Transform

Rather than fitting the magnetization with a stretched exponent, as in **Eq. 13**, it is possible to fit the data assuming a particular form of $\mathcal{P}(W_1)$. One such approach is via a log-normal distribution, where:

$$\mathcal{P}(W_1) = \frac{1}{W_1\sigma\sqrt{2\pi}} e^{-\left(\ln W_1 - \mu\right)^2/2\sigma^2}. \tag{14}$$

In this case the median of the distribution (T_1^{-1}) is e^{μ}, and the standard deviation is $\sigma_1 = \sqrt{e^{2\mu+\sigma^2}\left(e^{\sigma^2} - 1\right)}$ σ_1 is roughly inversely proportional to β. The relaxation in the pnictides is well-captured by this form of the distribution [16].

An alternative approach is to extract $\mathcal{P}(W_1)$ directly from the data, rather than to assume a particular form. This is known as an inverse Laplace transform (ILT), and has been utilized to investigate a range of correlated electron systems [61–63]. **Figure 11** displays representative data set with such a fit, and **Figure 12** shows the distribution versus temperature extracted using this approach in $Ba(Fe_{1-x}Co_x)_2As_2$ with $x = 0.059$. It is clear that both the median and width of this distribution change in the vicinity of T_N, and that the width approaches several orders of magnitude. The ILT approach does not make any a priori assumptions about the distribution, and may uncover features that are not captured by **Eq. 14**. On the other hand, the ILT requires time series data with high a signal-to-noise ratio, a complicated analysis algorithm, and assumptions about the smoothness of the distribution [64]. The distribution shown in **Figure 12** exhibits several structures for $T \ll T_N$ that are likely artifacts due to the poor signal to noise at these temperatures. Ultimately, the most meaningful information about the

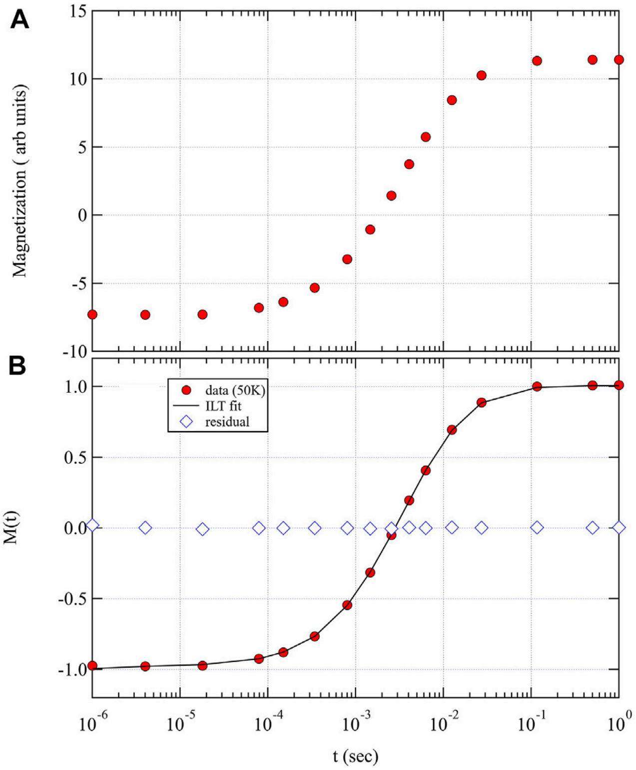

FIGURE 11 | Magnetization versus recovery time measured at 50 K in $Ba(Fe_{1-x}Co_x)_2As_2$ with $x = 0.06$. Panel **(A)** shows the raw data, and panel **(B)** shows the data after normalization such that $M(\infty) = 1$ and $M(0) = -1$. The solid line shows the fit using the ILT algorithm.

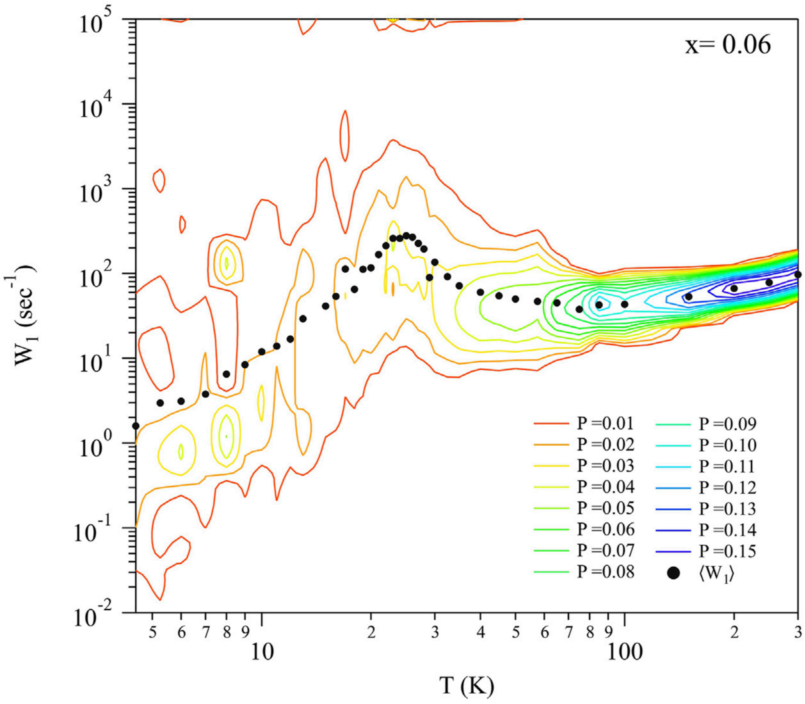

FIGURE 12 | Distribution of relaxation rates, $\mathcal{P}(W_1)$ versus temperature shown as contour lines in Ba(Fe$_{1-x}$Co$_x$)$_2$As$_2$ with x = 0.06, extracted by inverse Laplace transform. Contour lines are shown between $\mathcal{P}(W_1)$ = 0.01 to 0.15 in intervals of 0.01. The solid black circles shows the median of the distribution at teach temperature. The contributions near 10^5 sec^{-1} are artifacts introduced by normalization errors for early recovery times.

distribution appear to be the median and width, which are well-captured by the stretched exponential approach. Note that although the ^{75}As has I = 3/2 and hence a multi-exponential relaxation form even for homogeneous relaxation, the stretched exponential approach accurately captures the true distribution of relaxation rates, $\mathcal{P}(W_1)$ [64].

4.1.3 Nematicity and Dynamical Heterogeneity

Similar glassy behavior has been observed in the cuprates and been associated with stripe-glass behavior [65–73]. The cuprates, however, are doped Mott insulators, and the glassy behavior was attributed to intrinsic frustration between the competing effects of Coulomb repulsion and charge segregation [74–76]. The iron arsenides do not exhibit charge ordering and thus a different mechanism must be driving the glassy dynamics. This behavior is present for a range of doping levels, and is most pronounced near optimal doping where T_c reaches a maximum. **Figure 13** shows a phase diagram for both Cu and Co doping. Like Co, Cu introduces extra electrons but it also suppresses superconductivity [77]. The color scale indicates the standard deviation of a log-normal distribution fit, σ_1. As shown in **Figure 13**, the distribution exhibits the greatest width in the vicinity of a putative nematic quantum critical point near x ~ 0.07 if there were no superconductivity. This behavior is striking because it bears a similarity to the divergent nematic susceptibility measured by elastoresistance in these materials [7, 8]. In other words, *the width of the distribution of relaxation rates correlates with the magnitude of the nematic susceptibility.*

What is the origin of this glassy behavior, and is there a physical connection with the nematic susceptibility? A compelling hypothesis is that the dopants introduce quenched random strain fields that couple to the nematic order parameter and give rise to a distribution of local correlation times, τ_c. Local strains can nucleate different nematic domains, even in absence of long range nematic order. The result is a nematic glass, in which a distribution of local nematic domains (with different orientations) exist throughout the sample, each fluctuating with a different correlations times. These nematic fluctuations in turn drive spin fluctuations that are reflected in the distribution $\mathcal{P}(W_1)$.

Another hypothesis for the inhomogeneous dynamics is that static inhomogeneity of the EFG and Knight shift tensors induced by the dopants suppresses spin diffusion among the nuclear spins, so that they do not all relax with a common spin temperature. In principle, dipolar interactions between neighboring nuclear spins $\mathbf{I}_1$ and $\mathbf{I}_2$ may contain terms such as $\hat{I}_{1+}\hat{I}_{2-}$, which can give rise to mutual spin flips [78]. This effect could enable nuclei in regions that exhibit fast relaxation to transfer polarization with those in regions with slow relaxation, giving rise to a more homogeneous relaxation throughout the sample. If the static EFG and Knight shift tensors vary spatially, however, then mutual spin flips between neighbors would not conserve energy. In fact, spin diffusion should behave differently for a spin-1/2 versus a spin-3/2 nucleus. For the latter there are only six out of sixteen possible configurations where the two neighbors can undergo a mutual spin flip while conserving energy, whereas there are two out of four possibilities for the

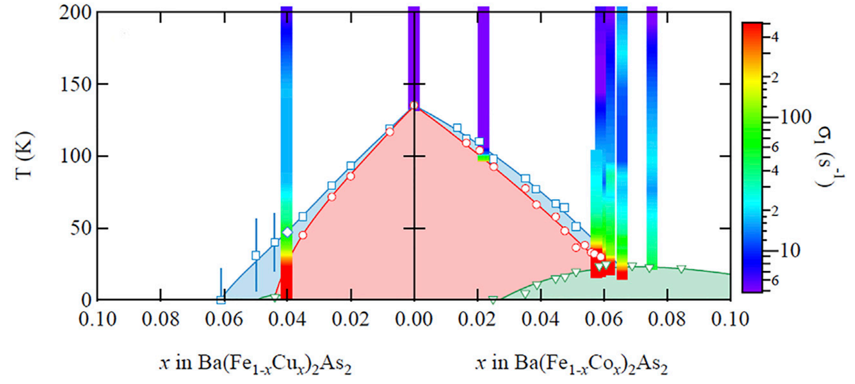

FIGURE 13 | Phase diagram of Ba(Fe$_{1-x}$Cu$_x$)$_2$As$_2$ and Ba(Fe$_{1-x}$Co$_x$)$_2$As$_2$ with the width of the distribution, σ_1 shown as the color scale. The blue diamonds represent T_s, the red circles represent T_N, and the green triangles represent T_c. Reproduced from [16].

former. Thus spin-diffusion should be suppressed for ^{75}As relative to ^{31}P, and thus one might expect β to be closer to unity for the spin-1/2 ^{31}P. In fact, both sites exhibit similar values of β at all temperatures in BaFe$_2$(As,P)$_2$ [43]. These results suggest, therefore, that spin diffusion does not play a significant role in the observed glassy dynamics.

4.1.4 Edwards-Anderson Parameter

In a recent paper, Wiecki and collaborators pointed out that the NMR linewidth of ^{77}Se in FeSe is directly proportional to the Edwards-Anderson parameter in a random-field Ising model of the nematicity [42]. Crystal defects provide local strain fields, h_i, at site i, and the enhanced nematic susceptibility gives rise to large spatial variations of local nematicity, $\phi_i(h_i)$ (we drop the distinction between ϕ_{xy}, ϕ_{yx} and ϕ_{zz} for simplicity). In this case, the Knight shift is known to vary linearly with ϕ, and the second moment of the NMR spectrum is directly proportional to the Edwards-Anderson parameter: $q_{EA} = \overline{\langle\phi^2\rangle} - \overline{\langle\phi\rangle}^2$, where the brackets indicate a thermal average and the overbar indicates an average over disorder configurations.

A similar approach can be utilized to analyze the distribution of relaxation rates, $\mathcal{P}(W_1)$. In undoped BaFe$_2$As$_2$, the spin lattice relaxation rate is a function of the nematic order parameter:

$$W_1(\phi) = W_1(0) + \alpha\phi + \cdots, \tag{15}$$

where α depends the correlation length, and is hence strongly temperature dependent [15]. In the doped system, we can model the distribution of relaxation rates by assuming a distribution of local strain fields, so that:

$$\overline{\mathcal{P}(W_1)} = \frac{1}{N}\int\prod_{j=1}^{N} dh_j p_\sigma(h_j)\sum_{i=1}^{N}\delta(W_1 - W_1(0) + \alpha\phi_i(h_i)), \tag{16}$$

where $p_\sigma(h_j)$ is the disorder distribution [42]. The second moment of $\overline{\mathcal{P}(W_1)}$ is $\sigma_1^2 = \alpha^2 q_{EA}$, thus the second moment of the distribution measures the Edwards-Anderson order parameter.

As shown in **Figure 13**, σ_1 is a strong function of temperature and doping. The magnitude of this quantity is given in part by the coefficient α, reflecting the growth of antiferromagnetic fluctuations. Note, however, that σ_1 would be zero if $q_{EA} = 0$. In other words, σ_1 is finite because the Edwards-Anderson parameter is non-zero, which indicates the presence of a nematic glass. Higher order corrections to the relationship between W_1 and strain, and the presence of other strain channels due the dopant atoms, are likely to modify the quantitative relationship between σ_1 and q_{EA}, and these issues should be addressed in future theoretical work.

4.2 Response to Strain

In principle, an *external* strain field of sufficient magnitude might overcome the local strain fields and give rise to more homogeneous relaxation. This hypothesis was tested in Ba(Fe$_{1-x}$Co$_x$)$_2$As$_2$ with $x = 0.048$ under tensile strain [52]. Although the magnitude of T_1^{-1} changed in response to the strain field, no changes were observed to the stretching exponent. This observation suggests that the intrinsic strains around the dopants exceed the homogeneous external strain, so that $\mathcal{P}(W_1)$ remains unchanged under strain. In fact, the lattice strain around Co dopants in Ba(Fe$_{1-x}$Co$_x$)$_2$As$_2$ can reach several percent [79]. The applied strain was only a fraction of a percent, thus it is not surprising that no change was observed in the width of the distribution.

4.3 Strain Hysteresis

Although the width of the $\mathcal{P}(W_1)$ does not change with externally applied strain, the median of the distribution does, and in a manner that depends on the strain history. **Figure 14** illustrates a protocol to investigate such hysteretic effects. A crystal is strain-cooled either under compressive (or tensile) strain from room temperature down to a base temperature. The spin lattice relaxation is then measured for a series of different levels of increasing (or decreasing) strain at constant temperature. The sample is then returned to room temperature (where the relaxation is homogeneous and there is no glassy behavior), and then the process is repeated under the opposite direction. For a fully linear response, the spin lattice relaxation as a function of strain should be independent of whether it was tensile-cooled or compressive-cooled.

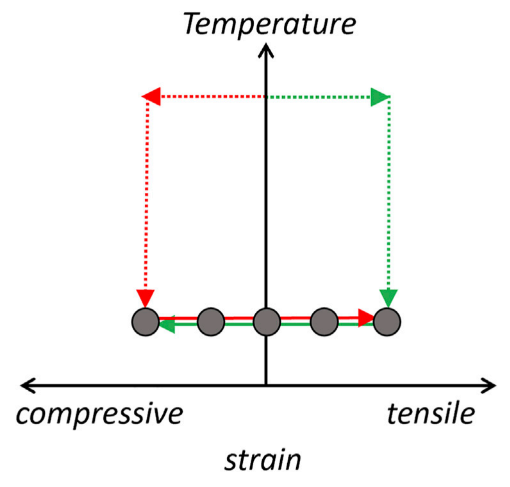

FIGURE 14 | Protocol for strain hysteresis measurements. The sample is first cooled (red arrows) in a compressive strain field from room temperature. Spin lattice relaxation measurements are then conducted at several different increasing strain levels as the displacement increases. The sample is then returned to room temperature and zero strain. Finally the sample is strain cooled under tensile strain to the same base temperature and measurements are conducted for several values of decreasing displacement. **Figure 15** compares the measured values for both protocols for various temperatures.

Figure 15 shows the results of such a study on Ba$(Fe_{1-x}Co_x)_2As_2$ for four different base temperatures for $x = 0.059$. As expected, β decreases as temperature is reduced, but remains independent of the applied strain, and is the same for both tensile- and compressive-cooling. On the other hand, the median of the distribution, T_1^{-1}, is strain-dependent and is different under the two strain conditions at low temperature.

Note that the horizontal axes in **Figure 15** are displacement, not strain. Strain is defined as $\varepsilon = (d - d_0)/L$, where d is the displacement of the capacitative dilatometer, d_0 is the equilibrium unstrained displacement, and L is the sample length. d_0 can be determined at room temperature, but thermal contractions of both the sample and the strain device make it difficult to determine d_0 under cryogenic conditions. It is best to utilize an independent measure of strain, such as the EFG tensor discussed in **Section 3.1**, to find the displacement corresponding to $\varepsilon = 0$. Such a calibration was not possible for the T_1^{-1} measurements in **Figure 15**. It is also important to note that the level of strain during the cooling part of the protocol in **Figure 14** is likely temperature-dependent, rather than constant as illustrated. Again, this is due to differential thermal contractions between the sample and the strain device. The displacement measured by the dilatometer is the quantity that is held constant.

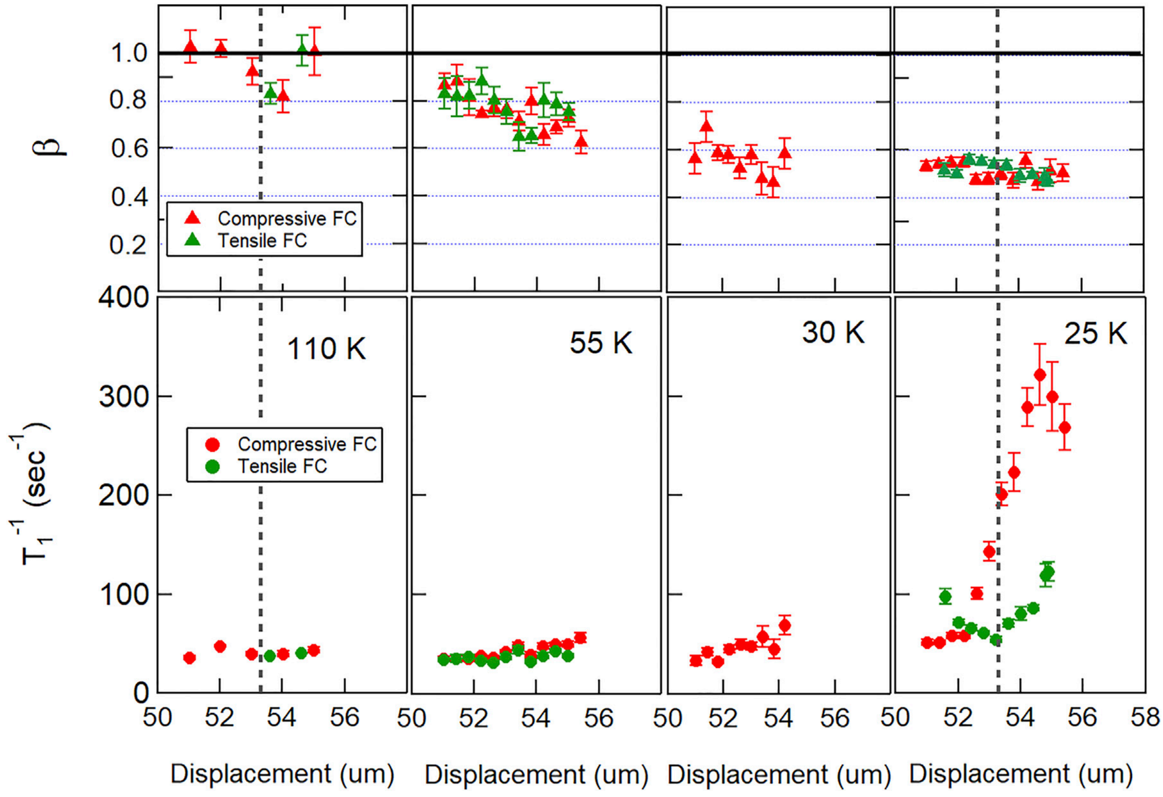

FIGURE 15 | T_1^{-1} and β versus displacement for several different temperatures in Ba$(Fe_{1-x}Co_x)_2As_2$ with $x = 0.059$. The red and green points represent data obtained during compressive field cooled and tensile field cooled protocols, as illustrated in **Figure 14**.

Despite these complications, these measurements reveal that $\mathcal{P}(W_1)$, and presumably the distribution of local nematic domains, depends on the past history of applied strain. Hysteresis is commonly observed in ordered ferromagnets, in which the static bulk magnetization is hysteretic with the applied field. If the applied field exceeds the coercive field, the magnetization will saturate, and when the applied field is reduced to zero, a remnant magnetization remains. Similar behavior should be expected in an ordered nematic without quenched disorder, in which nematic domains can reorient in an external strain field [80]. The NMR measurements described here, on the other hand, are in a nematic glass phase with quenched disorder, and probe the distribution of local correlation times of different fluctuating domains. Hysteresis has been studied in magnetic materials with quenched disorder in both the weak-disorder limit in the paramagnetic phase, as well in the strong-disorder limit in the spin glass phase [81]. The particular domain pattern is likely determined by the combination of local strains and the external strain field applied during the cool down. The fluctuation time of the domains is a complicated function of these strain fields as well as the behavior of their neighboring nematic domains. As the external strain field changes, the local correlation times change, but in such a manner that the median of the distribution of correlation times changes, but not the standard deviation. If the system were homogenous and not glassy, then the nematic domains would be mobile and there would be a single average correlation time. The presence of a distribution of correlation times that is altered by external strain provides evidence for the formation of a nematic glass, in which some domains exhibit very large correlation times, whereas others have short correlation times and may be reoriented by small external strain fields.

4.4 Theoretical Models

A quantitative theory to connect the measured distribution of the spin-lattice-relaxation rate, $\mathcal{P}(W_1)$, to the nematic domains and their dynamics in the presence of external strain, particularly in the context of the iron pnictides, is highly desirable. Although no such theory yet exists, there are important models that capture elements of the glassy behavior in these materials. Nematic ordering in the presence of random strain fields can be mapped onto the random field Ising model (RFIM) [80, 82, 83]. Detailed numerical simulations have uncovered a broad distribution of local correlation times, which agrees qualitatively with the observations of stretched relaxation in NMR experiments [16].

On the other hand, the iron pnictides exhibit both antiferromgnetism and nematicity, and there are two types of spin order for each of two possible nematic domains, as illustrated in **Figure 2**. Recently, a random Baxter-field model was proposed as an alternative to capture both the nematic and antiferromagnetic fluctuations in the presence of quenched random strain fields [84]. In this case, there are two Ising variables at each lattice site associated with the magnetic and the nematic degree of freedom. These two variables are coupled due to the next nearest neighbor coupling, J_2, in the $J_1 - J_2$ model for the iron pnictides [4]. Random strain fields couple only to the nematic degree of freedom, but the magnetic variable is also affected and consequently the system breaks up into domains of all four configurations illustrated in the top row of **Figure 2**.

5 SUMMARY AND CONCLUSION

NMR is a powerful tool to investigate nematicity in the iron based superconductors, providing microscopic insight in the local antiferromagnetic and nematic order parameters. Investigations of the NMR response to uniaxial strain in $BaFe_2As_2$ and FeSe have revealed important information about the anisotropy of the dynamical and static spin susceptibilities. In particular, the temperature dependence of the spin fluctuations under strain reflect an unusual piezomagnetic response in which the antiferromagnetically ordered spins can change their orientation direction under sufficient strain.

The doped pnictides have been less studied under strain because static and dynamical heterogeneity present in these materials render interpretation of results more difficult. Strain fields surrounding dopants create random fields that couple to the nematic order parameter, which may have a large response at low temperature. As a result, the NMR spectra broaden significantly, reflecting a distribution of static EFGs, some of which may indicate static local nematic order. More importantly, the NMR spin lattice relaxation rate reveals a broad distribution of local spin fluctuations that gradually freeze out at lower temperatures. This distribution likely reflects the correlated nematic fluctuations breaking up into spatial domains in a nematic glass. This distribution depends on the history of the strain field, but remains broad even at the highest uniaxial strain levels applied. These results suggest that quenched disorder creates large random strain fields.

Future studies on other doped materials may shed important light on the nature of the nematic glass. For example, hole doping by substituting Ba with K may introduce milder levels of local strain fields, in which case external strain might be able to induce homogeneous relaxation. Studies of static hysteretic behavior with strain in the ordered nematic phase may also shed important light on the mesoscopic physics of the domain formation, the coercive strain fields, and remnant nematicity. Unfortunately, NMR studies under strain require small crystals, and the NMR signal in doped samples tends to be suppressed due to the same glassy physics giving rise to the stretched relaxation. These effects conspire to make such experiments on doped samples particularly challenging.

DATA AVAILABILITY STATEMENT

The raw data supporting the conclusion of this article will be made available by the authors, without undue reservation.

AUTHOR CONTRIBUTIONS

TK acquired the NMR data on crystals grown and characterized by MT, RP, SB and PC, and NC conceived the experiments and wrote the manuscript.

FUNDING

Work at UC Davis was supported by the NSF under Grant No. DMR-1807889, and the UC Laboratory Fees Research Program (LFR-20-653926). Work at Ames Lab (PC, SB, RP, MT for growth and basic characterization of samples) was supported by the U.S. Department of Energy, Office of Basic Energy Science, Division of Materials Sciences and Engineering. Ames Laboratory is operated for the U.S. Department of Energy by Iowa State University under Contract No. DE-AC02-07CH11358.

ACKNOWLEDGMENTS

We thank Erica Carlson, Karin Dahmen, Stylianos Gregoriou, Lamei Nie and Rafael Fernandes for stimulating discussions.

REFERENCES

1. Fradkin E, Kivelson SA, Lawler MJ, Eisenstein JP, Mackenzie AP. Nematic Fermi Fluids in Condensed Matter Physics. *Annu Rev Condens Matter Phys* (2010) 1:153–78. doi:10.1146/annurev-conmatphys-070909-103925
2. Kivelson SA, Fradkin E, Emery VJ. Electronic Liquid-crystal Phases of a Doped Mott Insulator. *Nature* (1998) 393:550–3. doi:10.1038/31177
3. Vojta M. Lattice Symmetry Breaking in Cuprate Superconductors: Stripes, Nematics, and Superconductivity. *Adv Phys* (2009) 58:699–820. doi:10.1080/00018730903122242
4. Fernandes RM, Chubukov AV, Schmalian J. What Drives Nematic Order in Iron-Based Superconductors? *Nat Phys* (2014) 10:97–104. doi:10.1038/nphys2877
5. Baek S-H, Efremov DV, Ok JM, Kim JS, van den Brink J, Büchner B. Orbital-driven Nematicity in FeSe. *Nat Mater* (2015) 14:210–4. doi:10.1038/nmat4138
6. Comin R, Damascelli A. Resonant X-ray Scattering Studies of Charge Order in Cuprates. *Annu Rev Condens Matter Phys* (2016) 7:369–405. doi:10.1146/annurev-conmatphys-031115-011401
7. Kuo H-H, Chu J-H, Palmstrom JC, Kivelson SA, Fisher IR. Ubiquitous Signatures of Nematic Quantum Criticality in Optimally Doped Fe-Based Superconductors. *Science* (2016) 352:958–62. doi:10.1126/science.aab0103
8. Chu J-H, Kuo H-H, Analytis JG, Fisher IR. Divergent Nematic Susceptibility in an Iron Arsenide Superconductor. *Science* (2012) 337:710–2. doi:10.1126/science.1221713
9. Maier TA, Scalapino DJ. Pairing Interaction Near a Nematic Quantum Critical point of a Three-bandCuO2model. *Phys Rev B* (2014) 90:174510. doi:10.1103/PhysRevB.90.174510
10. Schattner Y, Lederer S, Kivelson SA, Berg E. Ising Nematic Quantum Critical point in a Metal: A Monte Carlo Study. *Phys Rev X* (2016) 6:031028. doi:10.1103/PhysRevX.6.031028
11. Lederer S, Schattner Y, Berg E, Kivelson SA. Superconductivity and Non-fermi Liquid Behavior Near a Nematic Quantum Critical point. *Proc Natl Acad Sci U.S.A* (2017) 114:4905–10. doi:10.1073/pnas.1620651114
12. Malinowski P, Jiang Q, Sanchez JJ, Mutch J, Liu Z, Went P. Suppression of Superconductivity by Anisotropic Strain Near a Nematic Quantum Critical point. *Nat Phys* (2020) 16:1189–93. doi:10.1038/s41567-020-0983-9
13. Lederer S, Berg E, Kim EA. Tests of Nematic-Mediated Superconductivity Applied to Ba$_{1-x}$Sr$_x$Ni$_2$As$_2$. *Phys Rev Res* (2020) 2:023122. doi:10.1103/physrevresearch.2.023122
14. Carretta P, Prando G. Iron-based Superconductors: Tales from the Nuclei. *La Rivista Del Nuovo Cimento* (2020) 43:1–43. doi:10.1007/s40766-019-0001-1
15. Kissikov T, Sarkar R, Lawson M, Bush BT, Timmons EI, Tanatar MA, et al. Uniaxial Strain Control of Spin-Polarization in Multicomponent Nematic Order of BaFe$_2$As$_2$. *Nat Commun* (2018) 9:1058. doi:10.1038/s41467-018-03377-8
16. Dioguardi AP, Lawson MM, Bush BT, Crocker J, Shirer KR, Nisson DM, et al. NMR Evidence for Inhomogeneous Glassy Behavior Driven by Nematic Fluctuations in Iron Arsenide Superconductors. *Phys Rev B* (2015) 92:165116. doi:10.1103/PhysRevB.92.165116
17. Lide D. *CRC Handbook of Chemistry and Physics, 2000-2001*. Boca Raton: CRC Press (2000).
18. Kitagawa K, Katayama N, Ohgushi K, Yoshida M, Takigawa M. Commensurate Itinerant Antiferromagnetism in BaFe$_2$As$_2$: ^{75}As-NMR Studies on a Self-Flux Grown Single crystal. *J Phys Soc Jpn* (2008) 77:114709. doi:10.1143/JPSJ.77.114709
19. Smerald A, Shannon N. Angle-resolved NMR: Quantitative Theory of ^{75}As T_1 Relaxation Rate in BaFe$_2$As$_2$. *Phys Rev B* (2011) 84:184437. doi:10.1103/PhysRevB.84.184437
20. O'Halloran J, Agterberg DF, Chen MX, Weinert M. Stabilizing the Spin Vortex crystal Phase in Two-Dimensional Iron-Based Superconductors. *Phys Rev B* (2017) 95:075104. doi:10.1103/PhysRevB.95.075104
21. Meier WR, Ding QP, Kreyssig A, Bud'ko SL, Sapkota A, Kothapalli K, et al. Hedgehog Spin-Vortex crystal Stabilized in a Hole-Doped Iron-Based Superconductor. *npj Quan Mater* (2018) 3. doi:10.1038/s41535-017-0076-x
22. Dioguardi AP, apRoberts Warren N, Shockley AC, Bud'ko SL, Ni N, Canfield PC, et al. Local Magnetic Inhomogeneities Observed via ^{75}As NMR in Ba(Fe$_{1-x}$Ni$_x$)$_2$As$_2$ with $H_0 \perp C$-axis. *J Phys Conf Ser* (2012) 344:012022. doi:10.1088/1742-6596/344/1/012022
23. Zhou R, Scherer DD, Mayaffre H, Toulemonde P, Ma M, Li Y, et al. Singular Magnetic Anisotropy in the Nematic Phase of FeSe. *npj Quan Mater* (2020) 5:93. doi:10.1038/s41535-020-00295-1
24. He M, Wang L, Ahn F, Hardy F, Wolf T, Adelmann P, et al. Dichotomy between In-Plane Magnetic Susceptibility and Resistivity Anisotropies in Extremely Strained BaFe$_2$As$_2$. *Nat Commun* (2017) 8. doi:10.1038/s41467-017-00712-3
25. Zhou R, Xing LY, Wang XC, Jin CQ, Zheng G. Orbital Order and Spin Nematicity in the Tetragonal Phase of the Electron-Doped Iron Pnictides NaFe$_{1-x}$Co$_x$As. *Phys Rev B* (2016) 93:060502. doi:10.1103/PhysRevB.93.060502
26. He M, Wang L, Hardy F, Xu L, Wolf T, Adelmann P, et al. Evidence for Short-Range Magnetic Order in the Nematic Phase of FeSe from Anisotropic In-Plane Magnetostriction and Susceptibility Measurements. *Phys Rev B* (2018) 97:104107. doi:10.1103/physrevb.97.104107
27. Jiang K, Hu J, Ding H, Wang Z. Interatomic Coulomb Interaction and Electron Nematic Bond Order in FeSe. *Phys Rev B* (2016) 93:115138. doi:10.1103/PhysRevB.93.115138
28. Christensen MH, Fernandes RM, Chubukov AV. Orbital Transmutation and the Electronic Spectrum of FeSe in the Nematic Phase. *Phys Rev Res* (2020) 2:013015. doi:10.1103/PhysRevResearch.2.013015
29. Long X, Zhang S, Wang F, Liu Z. A First-Principle Perspective on Electronic Nematicity in FeSe. *npj Quan Mater* (2020) 5. doi:10.1038/s41535-020-00253-x
30. Bartlett JM, Steppke A, Hosoi S, Noad H, Park J, Timm C, et al. Relationship between Transport Anisotropy and Nematicity in FeSe. *Phys Rev X* (2021) 11:021038. doi:10.1103/physrevx.11.021038
31. Iye T, Julien MH, Mayaffre H, Horvatić M, Berthier C, Ishida K, et al. Emergence of Orbital Nematicity in the Tetragonal Phase of BaFe$_2$(As$_{1-x}P_x$)$_2$. *J Phys Soc Jpn* (2015) 84:043705. doi:10.7566/JPSJ.84.043705
32. Kissikov T, Sarkar R, Lawson M, Bush BT, Timmons EI, Tanatar MA, et al. Local Nematic Susceptibility in Stressed BaFe$_2$As$_2$ from NMR Electric Field Gradient Measurements. *Phys Rev B* (2017) 96:241108. (R). doi:10.1103/physrevb.96.241108
33. Dioguardi AP, Crocker J, Shockley AC, apRoberts Warren N, Lin C, Shirer KR, et al. Angular Dependent ^{75}As NMR Study of the Electric Field Gradient in CaFe$_2$As$_2$. *Supercond Sci Technol* (2013) 26:025012. doi:10.1088/0953-2048/26/2/025012
34. Kawasaki S, Tabuchi T, Wang XF, Chen XH, qing Zheng G. Pressure-induced Unconventional Superconductivity Near a Quantum Critical point in CaFe$_2$As$_2$. *Supercond Sci Technol* (2010) 23:054004. doi:10.1088/0953-2048/23/5/054004

35. Ma L, Ji GF, Dai J, Saha SR, Paglione J, Yu W. Quenched Fe Moment in the Collapsed Tetragonal Phase of $Ca_{1-x}Pr_xFe_2As_2$. *Chin Phys B* (2012) 22:057401. doi:10.1088/1674-1056/22/5/057401
36. Kitagawa K, Katayama N, Ohgushi K, Takigawa M. Antiferromagnetism of $SrFe_2As_2$ Studied by Single-crystal ^{75}As-NMR. *J Phys Soc Jpn* (2009) 78:063706. doi:10.1143/JPSJ.78.063706
37. Baek SH, Curro NJ, Klimczuk T, Bauer ED, Ronning F, Thompson JD. First-order Magnetic Transition in Single-Crystalline $CaFe_2As_2$ Detected by As-75 Nuclear Magnetic Resonance. *Phys Rev B* (2009) 79. doi:10.1103/PhysRevB.79.052504
38. Baek SH, Lee H, Brown SE, Curro NJ, Bauer ED, Ronning F, et al. NMR Investigation of Superconductivity and Antiferromagnetism in $CaFe_2As_2$ under Pressure. *Phys Rev Lett* (2009) 102. doi:10.1103/PhysRevLett.102.227601
39. Ning FL, Ahilan K, Imai T, Sefat AS, McGuire MA, Sales BC, et al. Contrasting Spin Dynamics between Underdoped and Overdoped $Ba(Fe_{1-x}Co_x)_2As_2$. *Phys Rev Lett* (2010) 104:037001. doi:10.1103/PhysRevLett.104.037001
40. Toyoda M, Ichikawa A, Kobayashi Y, Sato M, Itoh M. In-plane Anisotropy of the Electric Field Gradient in $Ba(Fe_{1-x}Co_x)_2As_2$ NMR. *Phys Rev B* (2018) 97:174507. doi:10.1103/PhysRevB.97.174507
41. Wiecki P, Nandi M, Böhmer AE, Bud'ko SL, Canfield PC, Furukawa Y. NMR Evidence for Static Local Nematicity and its Cooperative Interplay with Low-Energy Magnetic Fluctuations in FeSe under Pressure. *Phys Rev B* (2017) 96:180502. doi:10.1103/PhysRevB.96.180502
42. Wiecki P, Zhou R, Julien MH, Böhmer AE, Schmalian J. Edwards-Anderson Parameter and Local Ising Nematicity in FeSe Revealed via NMR Spectral Broadening. *Phys Rev B* (2021) 104:125134. doi:10.1103/PhysRevB.104.125134
43. Dioguardi AP, Kissikov T, Lin CH, Shirer KR, Lawson MM, Grafe HJ, et al. NMR Evidence for Inhomogeneous Nematic Fluctuations in $BaFe_2(As_{1-x}P_x)_2$. *Phys Rev Lett* (2016) 116:107202. doi:10.1103/PhysRevLett.116.107202
44. Yi M, Lu DH, Moore RG, Kihou K, Lee CH, Iyo A, et al. Electronic Reconstruction through the Structural and Magnetic Transitions in Detwinned NaFeAs. *New J Phys* (2012) 14:073019. doi:10.1088/1367-2630/14/7/073019
45. Suter A, Mali M, Roos J, Brinkmann D. Mixed Magnetic and Quadrupolar Relaxation in the Presence of a Dominant Static Zeeman Hamiltonian. *J Phys Condens Matter* (1998) 10:5977. doi:10.1088/0953-8984/10/26/022
46. Suter A, Mali M, Roos J, Brinkmann D. Separation of Quadrupolar and Magnetic Contributions to Spin–Lattice Relaxation in the Case of a Single Isotope. *J Magn Reson* (2000) 143:266–73. doi:10.1006/jmre.1999.1990
47. Suter A, Mali M, Roos J, Brinkmann D. Charge Degree of freedom and the Single-Spin Fluid Model in$YBa_2Cu_4O_8$. *Phys Rev Lett* (2000) 84:4938–41. doi:10.1103/physrevlett.84.4938
48. Vinograd I, Shirer KR, Massat P, Wang Z, Kissikov T, Garcia D, et al. *Second Order Zeeman Interaction and Ferroquadrupolar Order in $TmVO_4$*. arXiv:2112.05859 (2021).
49. Nakai Y, Iye T, Kitagawa S, Ishida K, Ikeda H, Kasahara S, et al. Unconventional Superconductivity and Antiferromagnetic Quantum Critical Behavior in the Isovalent-Doped $BaFe_2(As_{1-x}P_x)_2$. *Phys Rev Lett* (2010) 105:107003. doi:10.1103/PhysRevLett.105.107003
50. Hicks CW, Barber ME, Edkins SD, Brodsky DO, Mackenzie AP. Piezoelectric-based Apparatus for Strain Tuning. *Rev Sci Instrum* (2014) 85:065003. doi:10.1063/1.4881611
51. Kissikov T, Sarkar R, Bush BT, Lawson M, Canfield PC, Curro NJ. Nuclear Magnetic Resonance Probe Head Design for Precision Strain Control. *Rev Sci Instrum* (2017) 88:103902. doi:10.1063/1.5002631
52. Kissikov T, Dioguardi AP, Timmons EI, Tanatar MA, Prozorov R, Bud'ko SL, et al. NMR Study of Nematic Spin Fluctuations in a Detwinned Single crystal of Underdoped $Ba(Fe_{2-x}Co_x)_2As_2$. *Phys Rev B* (2016) 94:165123. doi:10.1103/PhysRevB.94.165123
53. Tanatar MA, Blomberg EC, Kreyssig A, Kim MG, Ni N, Thaler A, et al. Uniaxial-strain Mechanical Detwinning of $CaFe_2As_2$ and $BaFe_2As_2$ Crystals: Optical and Transport Study. *Phys Rev B* (2010) 81:184508. doi:10.1103/PhysRevB.81.184508
54. Liu P, Klemm ML, Tian L, Lu X, Song Y, Tam DW, et al. In-plane Uniaxial Pressure-Induced Out-Of-Plane Antiferromagnetic Moment and Critical Fluctuations in $BaFe_2As_2$. *Nat Comm* (2020) 11. doi:10.1038/s41467-020-19421-5
55. Johnston DC. Stretched Exponential Relaxation Arising from a Continuous Sum of Exponential Decays. *Phys Rev B* (2006) 74:184430. doi:10.1103/PhysRevB.74.184430
56. Hammerath F, Gräfe U, Kühne T, Kühne H, Kuhns PL, Reyes AP, et al. Progressive Slowing Down of Spin Fluctuations in Underdoped $LaFeAsO_{1-x}F_x$. *Phys Rev B* (2013) 88:104503. doi:10.1103/physrevb.88.104503
57. Bossoni L, Carretta P, Halperin WP, Oh S, Reyes A, Kuhns P, et al. Evidence of Unconventional Low-Frequency Dynamics in the normal Phase of $Ba(Fe_{1-x}Rh_x)_2As_2$ Iron-Based Superconductors. *Phys Rev B* (2013) 88:100503. doi:10.1103/PhysRevB.88.100503
58. Takeda H, Imai T, Tachibana M, Gaudet J, Gaulin BD, Saparov BI, et al. Cu Substitution Effects on the Local Magnetic Properties of $Ba(Fe_{1-x}Cu_x)_2As_2$: A Site-Selective ^{75}As and ^{63}Cu NMR Study. *Phys Rev Lett* (2014) 113:117001. doi:10.1103/physrevlett.113.117001
59. Grafe HJ, Gräfe U, Dioguardi AP, Curro NJ, Aswartham S, Wurmehl S, et al. Identical Spin Fluctuations in Cu and Co Doped $BaFe_2As_2$ Independent of Doped Electrons. *Phys Rev B* (2014) 90:09451. doi:10.1103/PhysRevB.90.094519
60. Dioguardi AP, Crocker J, Shockley AC, Lin CH, Shirer KR, Nisson DM, et al. Coexistence of Cluster Spin Glass and Superconductivity in $Ba(Fe_{1-x}Co_x)_2As_2$ for $0.060 \le X \le 0.071$. *Phys Rev Lett* (2013) 111:207201. doi:10.1103/PhysRevLett.111.207201
61. Singer PM, Arsenault A, Imai T, Fujita M. NMR Investigation of the Interplay between Lattice, Charge, and Spin Dynamics in the Charge-Ordered High- T_c Cuprate $La_{1.875}Ba_{0.125}CuO_4$. *Phys Rev B* (2020) 101:174508. doi:10.1103/physrevb.101.174508
62. Arsenault A, Imai T, Singer PM, Suzuki KM, Fujita M. Magnetic Inhomogeneity in Charge-Ordered $La_{1.885}Sr_{0.115}CuO_4$ Studied by NMR. *Phys Rev B* (2020) 101:184505. doi:10.1103/physrevb.101.184505
63. Wang J, Yuan W, Singer PM, Smaha RW, He W, Wen J, et al. Emergence of Spin Singlets with Inhomogeneous Gaps in the Kagome Lattice Heisenberg Antiferromagnets Zn-Barlowite and Herbertsmithite. *Nat Phys* (2021) 17:1109–13. doi:10.1038/s41567-021-01310-3
64. Choi H, Vinograd I, Chaffey C, Curro N. Inverse Laplace Transformation Analysis of Stretched Exponential Relaxation. *J Magn Reson* (2021) 331:107050. doi:10.1016/j.jmr.2021.107050
65. Curro N, Hammel P. The Cu NMR echo Decay in Stripe Ordered $La_{1.65}Eu_{0.2}Sr_{0.15}CuO_4$. In: International Conference on Materials and Mechanisms of Superconductivity High Temperature Superconductors VI; FEB 20-25, 2000; HOUSTON, TEXAS, 341. Phys. C (2000). p. 1797–8. doi:10.1016/S0921-4534(00)01084-4
66. Curro N, Hammel P, Suh B, Hücker M, Büchner B, Ammerahl U, et al. Inhomogeneous Low Frequency Spin Dynamics in $La_{1.65}Eu_{0.2}Sr_{0.15}CuO_4$. *Phys Rev Lett* (2000) 85:642–5. doi:10.1103/PhysRevLett.85.642
67. Hunt AW, Singer PM, Cederström AF, Imai T. Glassy Slowing of Stripe Modulation in $(La,Eu,Nd)_{2-x}Sr_xCuO_4$: a ^{63}Cu and ^{139}La NQR Study Down to 350 mK. *Phys Rev B* (2001) 64:134525. doi:10.1103/PhysRevB.64.134525
68. Hunt A, Singer P, Thurber K, Imai T. ^{63}Cu NQR Measurement of Stripe Order Parameter in $La_{2-x}Sr_xCuO_4$. *Phys Rev Lett* (1999) 82:4300–3. doi:10.1103/physrevlett.82.4300
69. Julien MH, Campana A, Rigamonti A, Carretta P, Borsa F, Kuhns P, et al. Glassy Spin Freezing and NMR Wipeout Effect in the High-T_c Superconductor $La_{1.90}Sr_{0.10}CuO_4$ Critical Discussion of the Role of Stripes. *Phys Rev B* (2001) 63:144508. doi:10.1103/PhysRevB.63.144508
70. Curro NJ. Glassy Spin Dynamics in a Stripe Ordered Cuprate System. *Proc SPIE* (2004) 5469:114–24. doi:10.1117/12.537625
71. Curro N. Probing Spatial Correlations in the Inhomogeneous Glassy State of the Cuprates by Cu NMR. *J Phys Chem Sol* (2002) 63:2181–5. doi:10.1016/S0022-3697(02)00231-7
72. Mitrović VF, Julien MH, de Vaulx C, Horvatić M, Berthier C, Suzuki T, et al. Similar Glassy Features in the ^{139}La NMR Response of Pure and Disordered $La_{1.88}Sr_{0.12}CuO_4$. *Phys Rev B* (2008) 78:014504. doi:10.1103/PhysRevB.78.014504
73. Frachet M, Vinograd I, Zhou R, Benhabib S, Wu S, Mayaffre H, et al. Hidden Magnetism at the Pseudogap Critical point of a Cuprate Superconductor. *Nat Phys* (2020) 16:1064–8. doi:10.1038/s41567-020-0950-5
74. Schmalian J, Wolynes PG. Stripe Glasses: Self-Generated Randomness in a Uniformly Frustrated System. *Phys Rev Lett* (2000) 85:836–9. doi:10.1103/PhysRevLett.85.836

75. Westfahl H, Schmalian J, Wolynes PG. Self-generated Randomness, Defect Wandering, and Viscous Flow in Stripe Glasses. *Phys Rev B* (2001) 64:174203. doi:10.1103/PhysRevB.64.174203
76. Nussinov Z, Vekhter I, Balatsky AV. Nonuniform Glassy Electronic Phases from Competing Local Orders. *Phys Rev B* (2009) 79:165122. doi:10.1103/PhysRevB.79.165122
77. Canfield PC, Bud'ko SL. FeAs-based Superconductivity: A Case Study of the Effects of Transition Metal Doping on $BaFe_2As_2$. *Annu Rev Condens Matter Phys* (2010) 1:27–50. doi:10.1146/annurev-conmatphys-070909-104041
78. Slichter CP. *Principles of Nuclear Magnetic Resonance*. 3rd ed. Springer-Verlag (1992).
79. Park K, Louca D, Llobet A, Yan JQ. Evidence of Local Disorder in the Overdoped Regime of $Ba(Fe_{1-x}Co_x)_2As_2$. *Phys Rev B* (2011) 84:024512. doi:10.1103/PhysRevB.84.024512
80. Carlson EW, Dahmen KA. Using Disorder to Detect Locally Ordered Electron Nematics via Hysteresis. *Nat Commun* (2010) 2:379. doi:10.1038/ncomms1375
81. Banerjee V, Puri S. Hysteresis Effects in Spin Systems with Quenched Disorder. *Phys Rev E* (2001) 63:026106. doi:10.1103/physreve.63.026106
82. Loh CEW, Dahmen KA. Noise Predictions for STM in Systems with Local Electron Nematic Order. *Phys.Rev B* (2010) 81:224207. doi:10.1103/PhysRevB.81.224207
83. Carlson EW, Dahmen KA, Fradkin E, Kivelson SA. Hysteresis and Noise from Electronic Nematicity in High-Temperature Superconductors. *Phys Rev Lett* (2006) 96:097003. doi:10.1103/PhysRevLett.96.097003
84. Meese WJ, Vojta T, Fernandes RM. *Random-strain-induced Correlations in Materials with Intertwined Nematic and Magnetic Orders* (2021). p. 05769. arXiv:2112.

Conflict of Interest: The authors declare that the research was conducted in the absence of any commercial or financial relationships that could be construed as a potential conflict of interest.

frontiers | Frontiers in Physics

BRIEF RESEARCH REPORT
published: 20 April 2022
doi: 10.3389/fphy.2022.853717

Elastoresistivity of Heavily Hole-Doped 122 Iron Pnictide Superconductors

Xiaochen Hong[1,2]*, Steffen Sykora[2,3]*, Federico Caglieris[4,2,5]*, Mahdi Behnami[2], Igor Morozov[2,6], Saicharan Aswartham[2], Vadim Grinenko[2,7,8], Kunihiro Kihou[9], Chul-Ho Lee[9], Bernd Büchner[2,8] and Christian Hess[1,2]*

[1]Fakultät für Mathematik und Naturwissenschaften, Bergische Universität Wuppertal, Wuppertal, Germany, [2]Leibniz-Institute for Solid State and Materials Research (IFW-Dresden), Dresden, Germany, [3]Institute for Theoretical Physics and Würzburg-Dresden Cluster of Excellence ct.qmat, Technische Universität Dresden, Dresden, Germany, [4]Dipartimento di Fisica, University of Genoa, Genoa, Italy, [5]Consiglio Nazionale Delle Ricerche (CNR)-SPIN, Genova, Italy, [6]Department of Chemistry, Lomonosov Moscow State University, Moscow, Russia, [7]Tsung-Dao Lee Institute, Shanghai Jiao Tong University, Shanghai, China, [8]Institute of Solid State and Materials Physics and Würzburg-Dresden Cluster of Excellence ct.qmat, Technische Universität Dresden, Dresden, Germany, [9]National Institute of Advanced Industrial Science and Technology (AIST), Tsukuba, Japan

Edited by:
Anna Böhmer,
Ruhr-University Bochum, Germany

Reviewed by:
Konrad Jerzy Kapcia,
Adam Mickiewicz University, Poland
Marcin Matusiak,
Institute of Physics (PAN), Poland

***Correspondence:**
Xiaochen Hong
xhong@uni-wuppertal.de
Steffen Sykora
steffen.sykora@tu-dresden.de
Federico Caglieris
federico.caglieris@spin.cnr.it
Christian Hess
c.hess@uni-wuppertal.de

Specialty section:
This article was submitted to Condensed Matter Physics, a section of the journal Frontiers in Physics

Received: 12 January 2022
Accepted: 21 March 2022
Published: 20 April 2022

Citation:
Hong X, Sykora S, Caglieris F, Behnami M, Morozov I, Aswartham S, Grinenko V, Kihou K, Lee C-H, Büchner B and Hess C (2022) Elastoresistivity of Heavily Hole-Doped 122 Iron Pnictide Superconductors. Front. Phys. 10:853717. doi: 10.3389/fphy.2022.853717

Nematicity in heavily hole-doped iron pnictide superconductors remains controversial. Sizeable nematic fluctuations and even nematic orders far from magnetic instability were declared in $RbFe_2As_2$ and its sister compounds. Here, we report a systematic elastoresistance study of a series of isovalent- and electron-doped KFe_2As_2 crystals. We found divergent elastoresistance on cooling for all the crystals along their [110] direction. The amplitude of elastoresistivity diverges if K is substituted with larger ions or if the system is driven toward a Lifshitz transition. However, we conclude that none of them necessarily indicates an independent nematic critical point. Instead, the increased nematicity can be associated with another electronic criticality. In particular, we propose a mechanism for how elastoresistivity is enhanced at a Lifshitz transition.

Keywords: elastoresistance, nematicity, Lifshitz transition, iron-based superconductors, quantum criticality

1 INTRODUCTION

The “122” family, an abbreviation coined for $BaFe_2As_2$ and its substituted sister compounds, played a central role in the study of iron-based superconductors [1]. Those tetragonal $ThCr_2Si_2$-type structured compounds have the advantage that sizeable single crystals with continuous tunable doping can be prepared in a wide range, which is a crucial merit for the systematic investigation of various ordered states. Within the extended phase diagram of 122 compounds, the heavily hole-doped region, including the end-members $K/Rb/CsFe_2As_2$,, is of particular interest. The superconducting transition temperature T_c of $Ba_{1-x}K_xFe_2As_2$ peaks at optimal doping $x = 0.4$ and continuously decreases toward the overdoped (larger x) region. T_c remains finite in the end-member $x = 1$, while a change of the Fermi surface topology (Lifshitz transition) exists around $x = 0.6 \sim 0.8$ [2]. Although the T_c vs. x trend seems to be smooth across the Lifshitz transition, there are quite a lot of things happening here. Vanishing electron pockets for $x > 0.8$ destroy the basis of the interpocket scattering induced-$S\pm$ pairing symmetry which is generally believed as a feature of most iron-based superconductors. As a result, a change in the superconducting gap structure across the Lifshitz transition was observed experimentally [2–4]. Comparable pairing strength at the transition can foster a complex pairing state that breaks the time-reversal symmetry. Such an exotic state was also demonstrated to exist around the Lifshitz transition [5, 6]. Very recently, a so-called “Z_2 metal state" above T_c at the Lifshitz transition has been unveiled, with an astonishing feature of spontaneous Nernst effect [7].

Electronic nematicity, a strongly correlated electronic state of electrons breaking the underlying rotational symmetry of their lattice but preserving translation symmetry, has been a wave of research in unconventional superconductors, particularly in iron-based superconductors [8, 9]. Consistent experimental efforts have identified nematicity in all the different iron-based superconductor families [10–15], accompanied by theoretical proposals of the intimate relationship between nematicity and superconducting pairing [16–19]. However, according to the previous background, we should not simply extend what is known in the under- and optimal-doped 122s to the over-doped region. Whether nematicity exists and how it develops in this region needs independent censoring.

Indeed, nematicity in the heavily hole-doped 122 turns out to be more elusive. Heavily hole-doped 122s stand out as a featured series because of their peculiar Fermi surface topology, isostructural phase transition, and possible novel pairing symmetries [20–23]. Nematically ordered states were suggested by nuclear magnetic resonance spectroscopy and scanning tunneling microscopy on $CsFe_2As_2$ and $RbFe_2As_2$, and they were found to develop in different wave vectors other than the underdoped 122s [24, 25]. Such a nematic state far away from magnetic ordering challenges the prevailing idea that nematicity is some kind of vestigial order of magnetism [26]. An elastoresistance study further claims that a tantalizing isotropic (or XY-) nematicity is realized in the crossover region from dominating [100] nematicity in $RbFe_2As_2$ to [110] nematicity at the optimal doping [27]. However, many works pointed out that elastoresistance in K/Rb/$CsFe_2As_2$ is actually contributed by the symmetric A_{1g} channel, having little to do with the B_{1g} or B_{2g} channels which are related to nematicity [28, 29]. Overall, the debate is still on for this topic.

In this brief report, we will not touch upon the nature of the possible nematicity of K/Rb/$CsFe_2As_2$. Instead, we confirm phenomenologically the existence of elastoresistance (χ^{er}) in K/Rb/$CsFe_2As_2$ and find that its amplitude diverges exponentially with growing substituted ion size. Moreover, we present χ^{er} data on a series of $Ba_{1-x}K_xFe_2As_2$ crystals crossing the Lifshitz transition. We observe, unexpectedly, a clear enhancement of χ^{er} from both sides of the Lifshitz point. Although a presumptive nematic quantum critical point (QCP) might be of relevance, here we propose a rather more conventional explanation based on a small Fermi pocket effect. Our results add a novel phenomenon to the Lifshitz transition of the $Ba_{1-x}K_xFe_2As_2$ system and highlight another contributing factor of elastoresistance which has been almost ignored so far.

2 EXPERIMENTAL DETAILS

Single crystals of heavily hole-doped $Ba_{1-x}K_xFe_2As_2$ were grown by the self-flux method [30–32]. The actual doping level x was determined by considering their structural parameters and T_c values. Elastoresistance measurements were performed as described in Ref. s [10–12]. Thin stripe-shaped samples were glued on the surface of piezo actuators. The strain gauge were glued on the other side of the piezo actuators to monitor the real strain generated. In most cases, the samples were mounted to let the electric current flow along the polar direction of the piezo actuators (R_{xx}), along which direction the strain was measured by the gauge. For one sample ($x = 0.68$), an additional crystal was mounted at 90° rotated according to the polar direction (R_{yy}). More details are described in **Section 3.3**. The sample resistance was collected with a combination of a high-precision current source and a nanovoltage meter. Because of the very large RRR (R_{300K}/R_0) values of the samples, special care was taken to avoid a temperature drift effect, and the electric current was set in an alternating positive/negative manner to avoid artifact.

We point out that noisy and irreproducible elastoresistance results can be acquired if DuPont® 4922N silver paint is used for making contacts to the samples. On the other hand, samples contacted with EPO-TEK® H20E epoxy or directly tin-soldering gave perfectly overlapping results. Given that DuPont® 4922N silver paint is widely used for transport measurements and is indeed suitable for elastoresistance experiments of other materials (for example) the $LaFe_{1-x}Co_xAsO$ series [12], we have no idea why it does not work for heavily hole-doped $Ba_{1-x}K_xFe_2As_2$ crystals. In this work, the presented data were collected by using the H20E epoxy. To avoid sample degradation, the epoxy was cured inside an Ar-glove box. A similar silver paint contact problem of K/Rb/$CsFe_2As_2$ crystals was also noticed by another group [29].

3 RESULTS AND DISCUSSIONS

3.1 Elastoresistance Measurement

The elastoresistance measured along the [110] direction of the KFe_2As_2 single crystal is shown in **Figure 1**. The sample resistance closely followed the strain change of the piezo actuator when the voltage across the piezo actuator is tuned. As presented in **Figure 1B**, the relationship between resistance change ($\Delta R/R$) and strain ($\Delta L/L$) is linear. This fact ensures that our experiments were performed in the small strain limit. In such a case, the elastoresistance χ^{er}, defined as the ratio between $\Delta R/R$ and the strain, acts as a measurement of the nematic susceptibility [10]. It is worthwhile to note that χ^{er} in KFe_2As_2 is positive (sample under tension yields higher resistance), consistent with the previous reports [27, 28] and opposite to that of $BaFe_2As_2$ [10]. It is to be noted that sign reversal of the elastoresistance was reported to occur in the underdoped region [33].

3.2 Elastoresistance of K/Rb/$CsFe_2As_2$

We start by showing our $\chi^{er}(T)$ data measured along the [110] direction ($\chi^{er}_{[110]}$) for a set of (K/Rb/Cs)Fe_2As_2 crystals. As shown in **Figure 2**, all the $\chi^{er}_{[110]}(T)$ curves follow a divergent behavior over the whole temperature range. A Curie–Weiss (CW) fit

$$\chi^{er} = \chi_0 + \frac{\lambda/a_0}{T - T^{nem}} \tag{1}$$

can record the data. A slight deviation can be discriminated at low temperature, which is typical for elastoresistance data and is

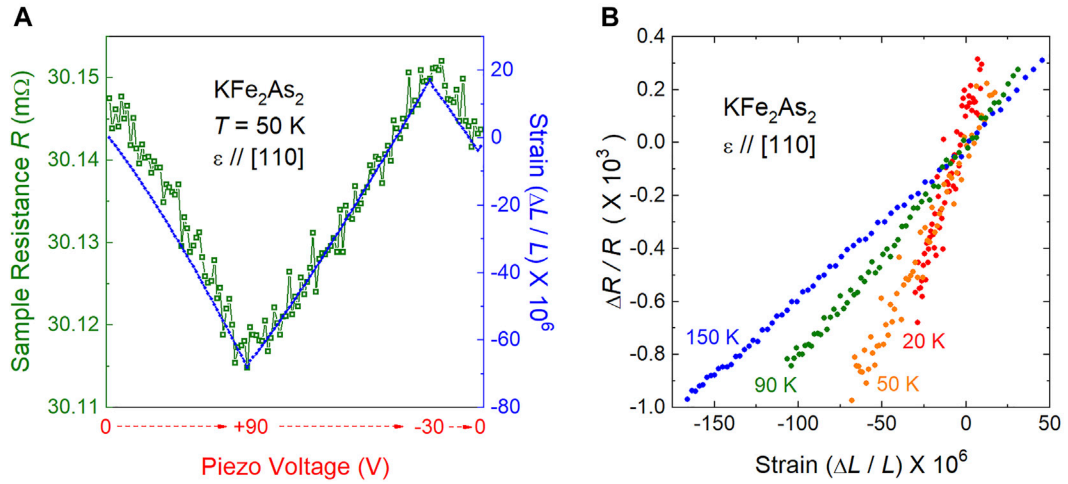

FIGURE 1 | Representative example of elastoresistance under strain for KFe_2As_2. **(A)** Resistance and strain change according to the voltage applied across the piezo actuator at a fixed temperature T = 50 K. The strain was applied along the [110] direction. **(B)** Change of resistance $\Delta R/R$ as a function of strain $\Delta L/L$ at several temperatures.

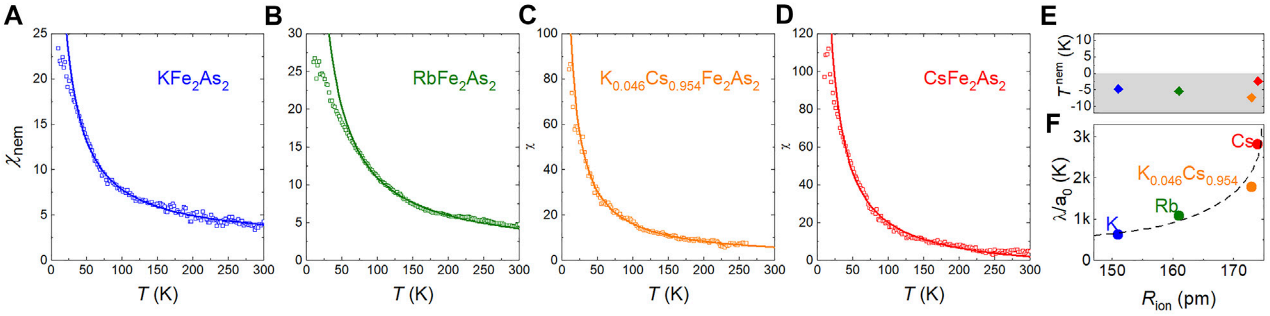

FIGURE 2 | Temperature dependence of elastoresistance $\chi^{er}_{[110]}$ for **(A)** KFe_2As_2, **(B)** $RbFe_2As_2$, **(C)** $K_{0.046}Cs_{0.095}Fe_2As_2$, and **(D)** $CsFe_2As_2$. Solid lines are CW-fit of the data (see text). The fit parameters T^{nem} and λ/a_0 are summarized in **(E,F)**, respectively. The dotted line in **(F)** is a guide to the eye.

understood as a disorder effect [13]. It is to be noted that the amplitude of the elastoresistance grows substantially from KFe_2As_2 to $CsFe_2As_2$, nearly 5-fold at 30 K. The extracted parameters from the CW fit are shown in **Figures 2E,F**. While the amplitude term shows a diverging trend, the T^{nem} of all four samples is of a very small negative value, which practically remains unchanged if experimental and fit uncertainties are taken into account, which is at odds with a possible nematic criticality in this isovalent-doping direction. The enhanced $\chi^{er}_{[110]}$ might be a result of a presumptive QCP of an unknown kind or a coherence–incoherence crossover [34–36]. These cannot be discriminated by our technique and thus are beyond the scope of this report.

3.3 Elastoresistance of Overdoped $Ba_{1-x}K_xFe_2As_2$

Next, we present a set of $\chi^{er}(T)$ data of five overdoped $Ba_{1-x}K_xFe_2As_2$ ($0.55 \le x \le 1$) across the Lifshitz point. The elastoresistance, measured only for the R_{xx} direction, as has been performed regularly in many reports [10, 12, 14], has been argued to be inconclusive for the end members (K/Rb/Cs)Fe_2As_2, as a result of the dominating A_{1g} contribution, instead of a B_{2g} (or B_{1g}) component which is related to nematicity [28, 29]. However, such complexities are ruled out by taking R_{yy} into account for calculating $\chi^{er}(T)$ for one representative example x = 0.68 (**Figure 3B**). The $\chi^{er}(T)$ curves calculated by the two different methods match well.

After checking the potential A_{1g} contribution to χ^{er} for a doping level close to the Lifshitz transition, we turn now to the data. As shown in **Figure 3**, the $\chi^{er}_{[110]}(T)$ curves of $Ba_{1-x}K_xFe_2As_2$ also follow a CW-like feature. One can see a clear dip at around 50 K in **Figure 3A** for the x = 0.55 sample. In some reports [27], such a feature was taken as a signal for a nematic order. Since no other ordering transition (structural, magnetic, and so on) has been ever reported in this doping range, we refrain from claiming an incipient nematic order solely based

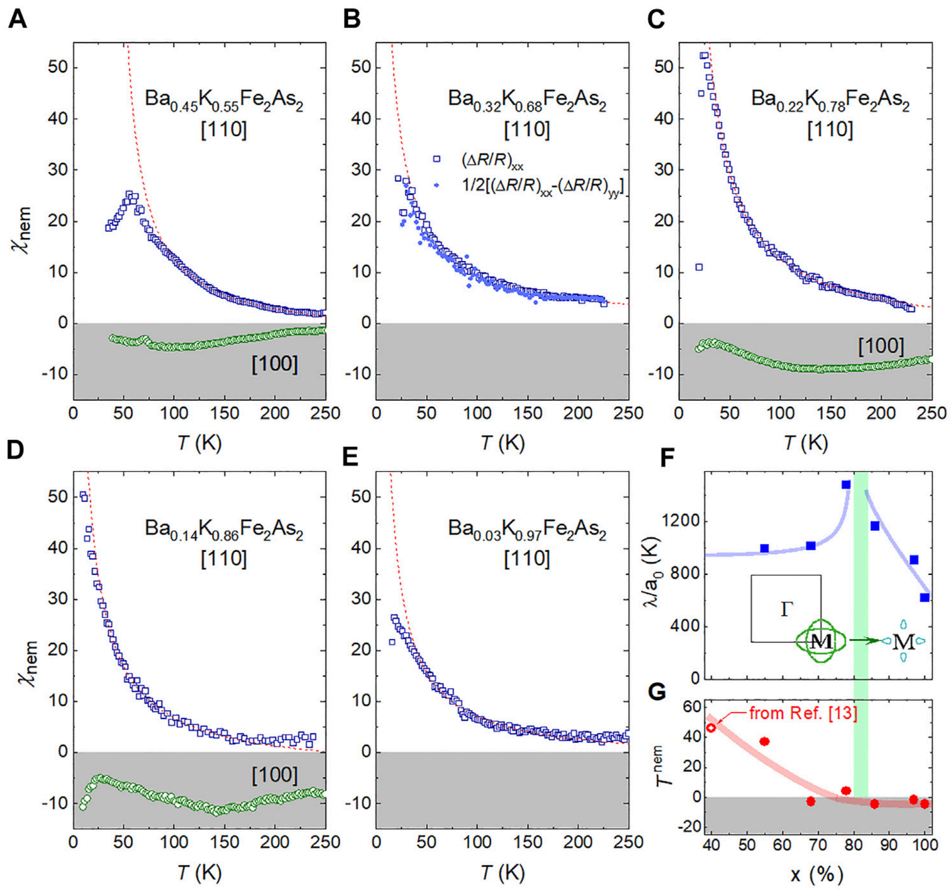

FIGURE 3 | Doping evolution of the elastoresistance in overdoped $Ba_{1-x}K_xFe_2As_2$. χ^{er} measured along the [110] direction is presented in the upper panels for $Ba_{1-x}K_xFe_2As_2$ single crystals with **(A)** $x = 0.55$, **(B)** $x = 0.68$, **(C)** $x = 0.78$, **(D)** $x = 0.86$, and **(E)** $x = 0.97$. The red dashed lines are CW-fit to the data. χ^{er} was also measured along the [100] direction for three of the samples. The data are presented in the lower panels of **(A)** and **(C,D)**. In panel **(B)**, χ^{er} extracted by using both $(\Delta R/R)_{xx}$ and $(\Delta R/R)_{yy}$ (filled light blue circles) and $(\Delta R/R)_{xx}$ (open blue squares) shows indistinguishable results. A doping dependence of the fit parameters is displayed in **(F)** λ/a_0 and **(G)** T^{nem} of the [110] $\chi^{er}_{[110]}$ data. The thick lines are a guide to the eye. A Lifshitz transition around $x = 0.8$ is highlighted by the green bar. Hole pockets around the *M* point of the Brillouin zone transform into electron lobes across the Lifshitz point [2]. T^{nem} at $x = 0.4$ is extracted from Ref. [13].

on such a feature. This might be equally well-explained by different origins. However, we also cannot exclude its possibility.

On the other hand, we measured χ^{er} along the [100] direction ($\chi^{er}_{[100]}$) for several samples. They are shown in the shaded panels of **Figure 3**. All of them are negative and small in amplitude, and none of them shows a CW-like feature. Such an observation is incompatible with the existence of B_{1g} nematicity in the heavily doped $Ba_{1-x}K_xFe_2As_2$ series, which is in sharp contrast to what is reported for the closely related $Ba_{1-x}Rb_xFe_2As_2$ series [27, 37, 38]. As a result, the so-called XY-nematicity is clearly ruled out in the $Ba_{1-x}K_xFe_2As_2$ series.

One remarkable feature, however, that can be safely concluded is that the amplitude of $\chi^{er}_{[110]}$ has a clear tendency to peak around $x = 0.8$, close to the Lifshitz transition. This becomes clearer in **Figure 3F**, where the CW fit parameters are plotted against the doping level. The question is why $\chi^{er}_{[110]}$ is increased at the Lifshitz transition? A nematic QCP is a potential explanation. However, as **Figure 3G** shows, T^{nem} drops from ~ 45 K of the $x = 0.4$ (optimal-doped) to ~ 0 K at the Lifshitz transition. Further doping does not drive T^{nem} to the more negative side within our experimental resolution. This is not typical QCP behavior. Moreover, since T_c across the Lifshitz transition is quite smooth, it seems not to be boosted by pertinent potential nematic fluctuations. Furthermore, three-point bending experiments did not show any anomaly in this doping range [39]. All these facts seem to be incompatible with the more understood nematic QCP in the electron-doped side [40]. Hence, if it is a nematic QCP, novel mechanisms need to be invoked. This motivated us to seek for alternative explanations for enhanced χ^{er} in heavily doped $Ba_{1-x}K_xFe_2As_2$. In the following section, we propose a conventional argument based on the small pocket effect, exempting from invoking a QCP to exist at the Lifshitz transition.

3.4 Theory for Enhanced Elastoresistance at the Lifshitz Transition

To study the effect of a Lifshitz transition to elastoresistance, we have calculated this quantity based on a minimal model of

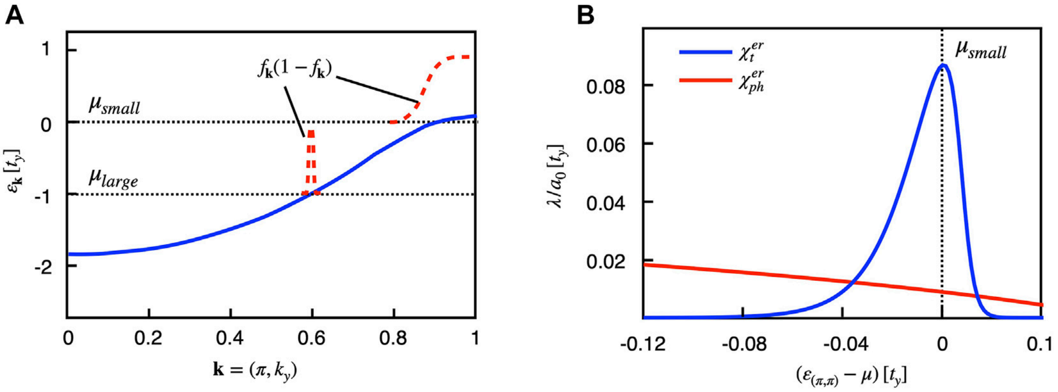

FIGURE 4 | Theoretical consideration of the elastoresisitivity. **(A)** Dispersion of the hole-like band leading to a very small hole pocket around the point (π, π) when the chemical potential μ_{small} (upper dotted line) is placed near the Lifshitz point. The range of momentum vectors contributing to the elastoresisitivity arising from the Fermi function is schematically shown by the dashed lines. A much larger hole pocket is indicated by a lower value of the chemical potential μ_{large} (lower dotted line). **(B)** Calculated parts of the elastoresistivity according to **Eq. 3**. Around the Lifshitz point μ_{small} the first-order part χ_t^{er} dominates the second-order part which is, however, the most important contribution for μ away from the Lifshitz point.

iron-based superconductors [41] with a very small Fermi surface. The corresponding dispersion which was used is shown in **Figure 4A** for the normal state along a cut (π, k_y). We considered the two orbital models in Ref. [41] with the same hopping matrix elements but having set the nematic interaction equal to a very small value. Thus, the nematic interaction accounts here only for the temperature dependence of the susceptibility according to the Curie–Weiss law. Moreover, we introduced a very small lattice distortion in the x direction which is coupled with the electron system. Using the first-order perturbation theory with respect to this coupling (linear response), we then calculated the elastoresistivity. We have considered two different cases of the coupling between distortion and electrons (strength g): (i) The conventional coupling with the local electron density (electron–phonon coupling), where we denote the corresponding response with χ_{ph}. (ii) A direct coupling of the distortion with the hopping matrix element t_x in the x direction. The corresponding response is denoted by χ_t.

$$\begin{aligned}\chi_t &\propto g \lim_{\Delta t_x\to 0}\frac{\sigma_{xx}^{-1}(t_x+\Delta t_x)-\sigma_{yy}^{-1}(t_x+\Delta t_x)}{\Delta t_x}\\ \chi_{ph} &\propto \frac{1}{N}\sum_{\mathbf{k}}\left(\frac{g}{\omega+\varepsilon_{\mathbf{k}}-\varepsilon_{\mathbf{k+q}}}\right)^2\frac{f_{\mathbf{k}}-f_{\mathbf{k+q}}}{\varepsilon_{\mathbf{k+q}}-\varepsilon_{\mathbf{k}}}.\end{aligned} \tag{2}$$

Here, t_x is the hopping matrix element in the x direction and σ_{xx}, σ_{yy} are the conductivities in the x and y directions [41]. The phonon energy ω in χ_{ph}^{er} is in general renormalized by the coupling to the electrons and becomes soft for a particular mode if the system is near a structural phase transition[42, 43]. The electron dispersion $\varepsilon_{\mathbf{k}}$ considered here is shown in **Figure 4A**. The function $f_{\mathbf{k}}$ is the Fermi distribution with respect to $\varepsilon_{\mathbf{k}}$. Thus, for most systems investigated, this term dominates χ^{er}. It is to be noted how magnetic fluctuations impact the phonons and the nematicity has been investigated [9, 16].

Figure 4B shows the two parts χ_t^{er} and χ_{ph}^{er} which were calculated separately as a function of the chemical potential μ to simulate different doping values. To compare with **Figure 3F**, we extracted the temperature behavior according to **Eq. 2** and plotted the calculated value λ/a_0 in energy units of t_y. It is seen that the first-order part χ_t^{er} dominates the second-order part only in the narrow range of μ, where the Fermi surface around (π, π) becomes very small. Thus, only when the system has very small Fermi surfaces, as in the case of $Ba_{1-x}K_xFe_2As_2$ at the Lifshitz transition, the term χ_t^{er} becomes important. However, it is also seen that if the chemical potential is chosen away from the Lifshitz point corresponding to a proper doping, the second-order part χ_{ph}^{er} is mostly important as expected.

The enhancement of χ_t^{er} in the presence of a very small Fermi surface can be explained by the existence of low-energy excitations in a relatively wide range of momentum vectors. Since the conductivities are proportional to Fermi distribution functions $f_{\mathbf{k}}$ as follows

$$\sigma_{ii} \propto \sum_{\mathbf{k}}\left(\frac{\partial\varepsilon_{\mathbf{k}}}{\partial k_i}\right)^2 f_{\mathbf{k}}(1-f_{\mathbf{k}}), \tag{3}$$

we find that at low temperature, if the Fermi surface is small, the momentum range $\mathbf{k}$, where $f_{\mathbf{k}}(1-f_{\mathbf{k}})$ is non-zero, is much larger because of the tendency of the band to rapidly change the Fermi surface topology near the Lifshitz transition (compare the red dashed lines in **Figure 4A**) than for a usual Fermi surface.

4 CONCLUSION

To summarize, we reported that a CW-like $\chi^{er}(T)$ is observed for all kinds of heavily hole-doped 122s. There is an unexpected enhancement of the elastoresistance around the Lifshitz transition. We explained it as a small Fermi pocket effect on the nematicity. We expect that our explanation of an alternative contribution to the enhanced elastoresistance other than a nematic QCP will be considered in other systems, in particular for those with small Fermi pockets.

DATA AVAILABILITY STATEMENT

The raw data supporting the conclusions of this article will be made available by the authors, without undue reservation.

AUTHOR CONTRIBUTIONS

IM, SA, VG, KK, and C-HL prepared the samples. XH, FC, and MB performed the experiments. SS proposed the theoretical model. CH and BB supervised the study. XH, SS, FC, and CH analyzed the data and wrote the manuscript with input from all authors.

FUNDING

This work has been supported by the Deutsche Forschungsgemeinschaft (DFG) through SFB 1143 (Project No. 247310070), through the Research Projects CA 1931/1-1 (FC) and SA 523/4-1 (SA). SS acknowledges funding by the Deutsche Forschungs gemeinschaft *via* the Emmy Noether Program ME4844/1-1 (project id 327807255). This project has received funding from the European Research Council (ERC) under the European Union's Horizon 2020 Research and Innovation Program (grant agreement No. 647276-MARS-ERC-2014-CoG).

ACKNOWLEDGMENTS

We would like to thank Anna Böhmer, Ian Fisher, Suguru Hosoi, Rüdiger Klingeler, Christoph Meingast, Jörg Schmalian, Christoph Wuttke, Paul Wiecki, and Liran Wang for helpful discussions. We would like to thank Christian Blum and Silvia Seiro for their technical support.

REFERENCES

1. Chen X, Dai P, Feng D, Xiang T, Zhang FC. Iron-based High Transition Temperature Superconductors. *Natl.Sci.Rev.* (2014) 1:371–95. doi:10.1093/nsr/nwu007
2. Xu N, Richard P, Shi X, van Roekeghem A, Qian T, Razzoli E. Possible Nodal Superconducting gap and Lifshitz Transition in Heavily Hole-Doped Ba_0. $_1K_{0.9}Fe_2As_2$ *Phys.Rev.B* (2013) 88:220508. doi:10.1103/PhysRevB.88.220508
3. Malaeb W, Shimojima T, Ishida Y, Okazaki K, Ota Y, Ohgushi K, et al. Abrupt Change in the Energy gap of Superconducting $Ba_{1-x}K_xFe_2As_2$ Single Crystals with Hole Doping. *Phys.Rev.B* (2012) 86:165117. doi:10.1103/PhysRevB.86.165117
4. Hong XC, Wang AF, Zhang Z, Pan J, He LP, Luo XG, et al. Doping Evolution of the Superconducting Gap Structure in Heavily Hole-Doped $Ba_{1-x}K_xFe_2As_2$: a Heat Transport Study. *Chin.Phys.Lett.* (2015) 32:127403. doi:10.1088/0256-307X/32/12/127403
5. Grinenko V, Materne P, Sarkar R, Luetkens H, Kihou K, Lee CH, et al. Superconductivity with Broken Time-Reversal Symmetry in Ion-Irradiated $Ba_{0.27}K_{0.73}Fe_2As_2$ Single Crystals. *Phys.Rev.B* (2017) 95:214511. doi:10.1103/PhysRevB.95.214511
6. Grinenko V, Sarkar R, Kihou K, Lee CH, Morozov I, Aswartham S, et al. Superconductivity with Broken Time-Reversal Symmetry inside a Superconducting *S*-Wave State. *Nat.Phys.* (2020) 16:789. doi:10.1038/s41567-020-0886-9
7. Grinenko V, Weston D, Caglieris F, Wuttke C, Hess C, Gottschall T, et al. State with Spontaneously Broken Time-Reversal Symmetry above the Superconducting Phase Transition. *Nat.Phys.* (2021) 17:1254. doi:10.1038/s41567-021-01350-9
8. Fisher IR, Degiorgi L, Shen ZX. In-plane Electronic Anisotropy of Underdoped '122' Fe-Arsenide Superconductors Revealed by Measurements of Detwinned Single Crystals. *Rep.Prog.Phys.* (2011) 74:124506. doi:10.1088/0034-4885/74/12/124506
9. Fernandes RM, Chubukov AV, Schmalian J. What Drives Nematic Order in Iron-Based Superconductors? *Nat.Phys.* (2014) 10:97. doi:10.1038/nphys2877
10. Chu JH, Kuo HH, Aanlytis JG, Fisher IR. Divergent Nematic Susceptibility in an Iron Arsenide Superconductor. *Science* (2012) 337:710. doi:10.1126/science.1221713
11. Hosoi S, Matsuura K, Ishida K, Wang H, Mizukami Y, Watashige T, et al. Nematic Quantum Critical point without Magnetism in $FeSe_{1-x}S_x$ Superconductors. *Proc.Natl.Acad.Sci.U.S.A.* (2016) 113:8139. doi:10.1073/pnas.1605806113
12. Hong XC, Caglieris F, Kappenberger R, Wurmehl S, Aswartham S, Scaravaggi F, et al. Evolution of the Nematic Susceptibility in $LaFe_{1-x}Co_xAsO$. *Phys.Rev.Lett.* (2020) 125:067001. doi:10.1103/PhysRevLett.125.067001
13. Kuo HH, Chu JH, Palmstrom JC, Kivelson SA, Fisher IR. Ubiquitous Signatures of Nematic Quantum Criticality in Optimally Doped Fe-Based Superconductors. *Science* (2016) 52:958. doi:10.1126/science.aab0103
14. Gu YH, Liu ZY, Xie T, Zhang WL, Gong DL, Hu D, et al. Unified Phase Diagram for Iron-Based Superconductors. *Phys.Rev.Lett.* (2017) 119:157001. doi:10.1103/PhysRevLett.119.157001
15. Terashima T, Matsushita Y, Yamase H, Kikugawa N, Abe H, Imai M, et al. Elastoresistance Measurements on $CaKFe_4As_4$ and $KCa_2Fe_4As_4F_2$ with the Fe Site of C_{2v} Symmetry. *Phys.RevB* (2020) 102:054511. doi:10.1103/PhysRevB.102.054511
16. Fernandes RM, Schmalian J. Manifestations of Nematic Degrees of freedom in the Magnetic, Elastic, and Superconducting Properties of the Iron Pnictides. *Supercond.Sci.Technol.* (2012) 25:084005. doi:10.1088/0953-2048/25/8/084005
17. Lederer S, Schattner Y, Berg E, Kivelson SA. Enhancement of Superconductivity Near a Nematic Quantum Critical Point. *Phys.Rev.Lett.* (2015) 114:097001. doi:10.1103/PhysRevLett.114.097001
18. Labat D, Paul I. Pairing Instability Near a Lattice-Influenced Nematic Quantum Critical point. *Phys.Rev.B* (2017) 96:195146. doi:10.1103/PhysRevB.96.195146
19. Maslov DL, Chubukov AV. Fermi Liquid Near Pomeranchuk Quantum Criticality. *Phys.Rev.B* (2010) 81:045110. doi:10.1103/PhysRevB.81.045110
20. Tafti FF, Juneau-Fecteau A, Delage M-E, René de Cotret S, Reid J-P, Wang AF, et al. Sudden Reversal in the Pressure Dependence of T_c in the Iron-Based Superconductor KFe_2As_2. *Nat.Phys.* (2013) 9:349. doi:10.1038/nphys2617
21. Wang YQ, Lu PC, Wu JJ, Liu J, Wang XC, Zhao JY, et al. Phonon Density of States of Single-crystal $SrFe_2As_2$ across the Collapsed Phase Transition at High Pressure. *Phys.Rev.B* (2016) 94:014516. doi:10.1103/PhysRevB.94.014516
22. Ptok A, Sternik M, Kapcia KJ, Piekarz P. Structural, Electronic, and Dynamical Properties of the Tetragonal and Collapsed Tetragonal Phases of KFe_2As_2. *Phys.Rev.B* (2019) 99:134103. doi:10.1103/PhysRevB.99.134103
23. Ptok A, Kapcia KJ, Cichy A, Oleś AM, Piekarz P. Magnetic Lifshitz Transition and its Consequences in Multi-Band Iron-Based Superconductors. *Sci.Rep.* (2017) 7:41979. doi:10.1038/srep41979
24. Li J, Zhao D, Wu YP, Li SJ, Song DW, Zheng LX, et al. *Reemergeing Electronic Nematicity in Heavily Hole-Doped Fe-Based Superconductors* (2016). arXiv:1611.04694.

25. Liu X, Tao R, Ren MQ, Chen W, Yao Q, Wolf T, et al. Evidence of Nematic Order and Nodal Superconducting gap along [110] Direction in $RbFe_2As_2$. *Nat.Commun.* (2019).
26. Fernandes RM, Orth PP, Schmalian J. Intertwined Vestigial Order in Quantum Materials: Nematicity and beyond. *Annu.Rev.Condens.MatterPhys.* (2019) 10: 133. doi:10.1146/annurev-conmatphys-031218-013200
27. Ishida K, Tsujii M, Hosoi S, Mizukami Y, Ishida S, Iyo A, et al. Novel Electronic Nematicity in Heavily Hole-Doped Iron Pnictide Superconductors. *Proc.Natl.Acad.Sci.U.S.A.* (2020) 117:6424. doi:10.1073/pnas.1909172117
28. Wiecki P, Haghighirad AA, Weber F, Merz M, Heid R, Böhmer AE. Dominant In-Plane Symmetric Elastoresistance in $CsFe_2As_2$. *Phys.Rev.Lett.* (2020) 125: 187001. doi:10.1103/PhysRevLett.125.187001
29. Wiecki P, Frachet M, Haghighirad AA, Wolf T, Meingast C, Heid R, et al. Emerging Symmetric Strain Response and Weakening Nematic Fluctuations in Strongly Hole-Doped Iron-Based Superconductors. *Nat.Commun.* (2021) 12:4824. doi:10.1038/s41467-021-25121-5
30. Aswartham S, Abdel-Hafiez M, Bombor D, Kumar M, Wolter AUB, Hess C, et al. Hole Doping in $BaFe_2As_2$: The Case of $Ba_{1-x}Na_xFe_2As_2$ Single Crystals. *Phys.Rev.B* (2012) 85:224520. doi:10.1103/PhysRevB.85.224520
31. Abdel-Hafiez M, Aswartham S, Wurmehl S, Grinenko V, Hess C, Drechsler S-L, et al. Specific Heat and Upper Critical fields in KFe_2As_2 Single Crystals. *Phys.Rev.B* (2012) 85:134533. doi:10.1103/PhysRevB.85.134533
32. Moroni M, Prando G, Aswartham S, Morozov I, Bukowski Z, Büchner B, et al. Charge and Nematic Orders in AFe_2As_2 (A = Rb, Cs) Superconductors. *Phys.Rev.B* (2019) 99:235147. doi:10.1103/PhysRevB.99.235147
33. Blomberg EC, Tanatar MA, Fernandes RM, Mazin II, Shen B, Wen HH, et al. Sign-reversal of the In-Plane Resistivity Anisotropy in Hole-Doped Iron Pnictides. *Nat.Commun.* (2013) 4:1914. doi:10.1038/ncomms2933
34. Eilers F, Grube K, Zocco DA, Wolf T, Merz M, Schweiss P, et al. Strain-Driven Approach to Quantum Criticality in AFe_2As_2 with A=K, Rb, and Cs. *Phys.Rev.Lett.* (2016) 116:237003. doi:10.1103/PhysRevLett.116.237003
35. Zhang ZT, Dmytriieva D, Molatta S, Wosnitza J, Khim S, Gass S, et al. Increasing Stripe-type Fluctuations in AFe_2As_2 (A=K, Rb, Cs) Superconductors Probed by ^{75}As NMR Spectroscopy. *Phys.Rev.B* (2018) 97: 115110. doi:10.1103/PhysRevB.97.115110
36. Hardy F, Böhmer AE, Aoki D, Burger P, Wolf T, Schweiss P, et al. Evidence of Strong Correlations and Coherence-Incoherence Crossover in the Iron Pnictide Superconductor KFe_2As_2. *Phys.Rev.Lett.* (2013) 111:027002. doi:10.1103/PhysRevLett.111.027002
37. Onari S, Kontani H. Origin of Diverse Nematic Orders in Fe-Based Superconductors: 45° Rotated Nematicity in AFe_2As_2 (A=Cs,Rb). *Phys.Rev.B* (2019) 100:020507. doi:10.1103/PhysRevB.100.020507
38. Borisov V, Fernandes RM, Valentí R. Evolution from B_{2g} Nematics to B_{1g} Nematics in Heavily Hole-Doped Iron-Based Superconductors. *Phys.Rev.Lett.* (2019) 123:146402. doi:10.1103/PhysRevLett.123.146402
39. Böhmer AE, Burger P, Hardy F, Wolf T, Schweiss P, Fromknecht R, et al. Nematic Susceptibility of Hole-Doped and Electron-Doped $BaFe_2As_2$ Iron-Based Superconductors from Shear Modulus Measurements. *Phys.Rev.Lett.* (2014) 112:047001. doi:10.1103/PhysRevLett.112.047001
40. Fernandes RM, VanBebber LH, Bhattacharya S, Chandra P, Keppens V, Mandrus D, et al. Effects of Nematic Fluctuations on the Elastic Properties of Iron Arsenide Superconductors. *Phys.Rev.Lett.* (2010) 105:157003. doi:10.1103/PhysRevLett.105.157003
41. Wuttke C, Caglieris F, Sykora S, Steckel F, Hong X, Ran S, et al. *Ubiquitous Enhancement of Nematic Fluctuations across the Phase Diagram of Iron Based Superconductors Probed by the Nernst Effect*. arXiv:2202.00485.
42. Sykora S, Hübsch A, Becker KW. Dominant Particle-Hole Contributions to the Phonon Dynamics in the Spinless One-Dimensional Holstein Model. *Europhys.Lett.* (2006) 76:644. doi:10.1209/epl/i2006-10327-x
43. Sykora S, Hübsch A, Becker KW. Generalized Diagonalization Scheme for many-particle Systems. *Phys.Rev.B* (2020) 102:165122. doi:10.1103/PhysRevB.102.165122

Conflict of Interest: The authors declare that the research was conducted in the absence of any commercial or financial relationships that could be construed as a potential conflict of interest.

frontiers | Frontiers in Physics

ORIGINAL RESEARCH
published: 21 April 2022
doi: 10.3389/fphy.2022.859424

Theory of Spin-Excitation Anisotropy in the Nematic Phase of FeSe Obtained From RIXS Measurements

Andreas Kreisel[1]*, *P. J. Hirschfeld*[2] *and Brian M. Andersen*[3]

[1]*Institut für Theoretische Physik, Universität Leipzig, Leipzig, Germany,* [2]*Department of Physics, University of Florida, Gainesville, FL, United States,* [3]*Niels Bohr Institute, University of Copenhagen, Copenhagen, Denmark*

Recent resonant inelastic x-ray scattering (RIXS) experiments have detected a significant high-energy spin-excitation anisotropy in the nematic phase of the enigmatic iron-based superconductor FeSe, whose origin remains controversial. We apply an itinerant model previously used to describe the spin-excitation anisotropy as measured by neutron scattering measurements, with magnetic fluctuations included within the RPA approximation. The calculated RIXS cross section exhibits overall agreement with the RIXS data, including the high energy spin-excitation anisotropy.

Keywords: RIXS (resonant inelastic X-ray scattering), condensed matter theory, nematicity, magnetic excitation, FeSe

Edited by:
Laura Fanfarillo,
International School for Advanced Studies (SISSA), Italy

Reviewed by:
Takami Tohyama,
Tokyo University of Science, Japan
Alexander F. Kemper,
North Carolina State University, United States

****Correspondence:***
Andreas Kreisel
kreisel@itp.uni-leipzig.de

Specialty section:
This article was submitted to Condensed Matter Physics, a section of the journal Frontiers in Physics

Received: *21 January 2022*
Accepted: *07 March 2022*
Published: *21 April 2022*

Citation:
Kreisel A, Hirschfeld PJ and Andersen BM (2022) Theory of Spin-Excitation Anisotropy in the Nematic Phase of FeSe Obtained From RIXS Measurements.
Front. Phys. 10:859424.
doi: 10.3389/fphy.2022.859424

1 INTRODUCTION

Identifying the dominant interaction channels, and pinpointing the correct microscopic origin of preferred electronic ordering tendencies in strongly-correlated materials, constitute a challenge to the theoretical description of materials. This is particularly relevant in systems where spin, charge, orbital, and lattice degrees of freedom all strongly couple with one another. For the iron-based superconductors, the main relevant players are spin-density waves, nematic order, and unconventional superconductivity. In this regard, iron selenide, FeSe, has played a leading role in recent years since its superconducting phase condenses directly from a nematic state without concomitant broken time-reversal symmetry breaking (magnetic order) at lower temperatures [1–3]. In addition, FeSe has been in the spotlight due to its superconducting transition temperature T_c, which is tunable by intercalation, pressure, or dimensional reduction (monolayer FeSe on STO) [3].

Since FeSe enters an orthorhombic phase below $T_n \sim 90$K it exhibits 90° rotational symmetry breaking in all measured quantities (of detwinned crystals). However, from comparisons to theoretical calculations the degree of measured rotational symmetry breaking is much too large to be ascribed solely to the bare electronic structure of the orthorhombic phase. Therefore, several theoretical works have explored the possibility of various interaction-driven feedback effects that enhance the symmetry breaking [4–10] and strongly influence the shape and orbital content of the Fermi pockets [7, 8, 11–13]. A particularly simple theoretical framework which includes such effects is the so-called orbital-selective scenario, where the low-energy self-energy is approximated by orbital-dependent, but energy- and momentum-independent, quasi-particle weight factors [6, 7, 14–19]. While this is clearly a crude simplification of the full interacting multi-orbital problem, it was shown to provide overall agreement with a series of different experiments [3].

More recently, spectroscopic probes have revealed that the Fermi surface of FeSe is exceedingly anisotropic; it appears to be missing an entire electron pocket at the Y-point of the Brillouin zone (BZ), as shown in **Figure 1** [20, 21]. This Fermi surface topology does not naturally arise from DFT band structure calculations, even with additional nematic order added to the description [3]. This

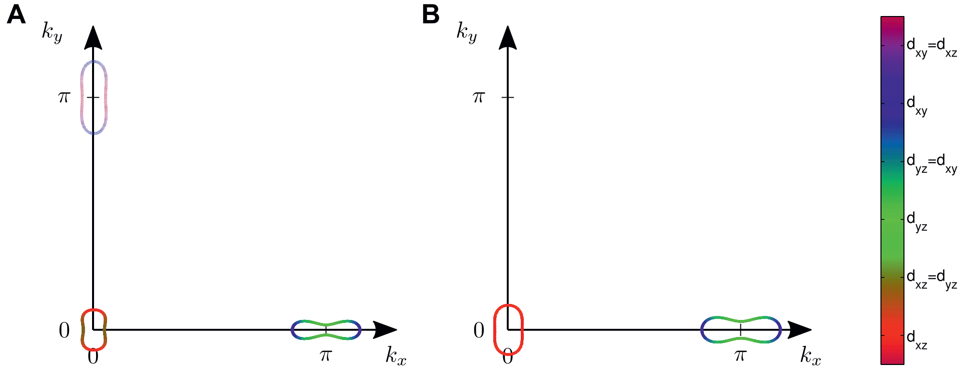

FIGURE 1 | Fermi surface of nematic FeSe with orbital content as indicated by colorbar. **(A)** Model of an electronic structure exhibiting a Fermi surface pocket at the Y point which, however, carries incoherent electronic states (sketched by fading colors) [6, 7]. Note that the model in **Eq. 1** is a three dimensional electronic structure. For the full corresponding Fermi surface we refer to **Figure 1A** of Ref. [7]. **(B)** Fermi surface of a model including d_{xy} orbital order as proposed in Ref. [27] where the Y pocket is lifted; similar topology of the Fermi surface was also discussed in [29] with a different orbital order parameter.

finding has reinvigorated the discussion of nematicity and the origin of the large electronic anisotropy in FeSe. For example, the lifting of the Y-pocket imposes new constraints on the nature of the nematic order, leading to studies of the importance of d_{xy}-orbital contributions [13, 22–27], and important inter-orbital components in the nematic order [28–30]. The latter were shown recently to arise naturally from longer-range Coulomb interactions [29]. Additionally, the possible non-existence of the Y-pocket has important consequences for superconductivity and the need for anisotropy-enhancing self-energy feedback effects. For example, as shown in Ref. [29], the highly anisotropic superconducting gap structure of FeSe follows immediately from standard spin-fluctuation mediated pairing without additional self-energy effects applied to the Fermi surface without any electron pocket at the Y-point. This conclusion, however, is mainly a direct consequence of the missing Y-pocket itself, and does not eliminate the need for self-energy feedback more generally in the theoretical description of FeSe. This is seen, for example, in theoretical modelling of the neutron response of FeSe, where a prominent momentum anisotropy seems only consistent with calculations incorporating self-energy feedback effects [29] since the possible lifting of the Y pocket alone only yields a very weak anisotropy of the susceptibility between (π, 0) and (0, π) as also presented in Ref. [27].

Therefore, further experiments probing the momentum anisotropy of detwinned FeSe are highly desirable. In this respect, Chen et al. [31] succeeded in measuring the inelastic neutron scattering response from a mosaic of single FeSe crystals glued on to $BaFe_2As_2$, detwinned at low temperatures by the single domain stripe magnetism of the (uniaxially strained) substrate $BaFe_2As_2$ material. This experiment revealed highly anisotropic low-energy ($\lesssim$ 10 meV) magnetic fluctuations in (detwinned) FeSe with the main scattering taking place near the (π, 0) position of the BZ. In the superconducting phase, a similarly momentum-anisotropic resonance peak was additionally identified [31]. These results can be explained by itinerant models that include self-energy effects that 1) suppress d_{xy} orbital contributions to the spin susceptibility predominantly near (π, π), and 2) favor (π, 0) d_{yz} over (0, π) d_{xz} orbital contributions in the nematic phase [32, 33]. Only by allowing for such orbital-selective self-energy effects can a standard RPA-like itinerant scenario be made compatible with the neutron data. We stress that this remains true irrespective of whether or not the Y-pocket is present at the Fermi surface.

Recently, the spin excitations were measured to higher energies in detwinned FeSe by RIXS measurements at the Fe-L_3 edge [34]. The RIXS energy spectra revealed clear dispersive broad spin modes. It was found that the spin-excitation anisotropy, as seen by comparing the scattering cross section along the perpendicular H and K high-symmetry directions, remains to high energies (~ 200 meV). This energy scale is substantially larger than the orbital splitting associated with the nematicity, and as pointed out in Ref. [34], the amplitude of the spin-excitation anisotropy in nematic FeSe is comparable to that obtained from the spin-wave anisotropy in the magnetically ordered stripe (π, 0) phase of $BaFe_2As_2$ [34, 35].

The RIXS results for detwinned FeSe provide new testing ground for theories of FeSe. At present the origin of nematicity and the degree of localization and correlation is still being discussed. In particular, theoretical works have both applied models based on fully localized or itinerant electrons, in order to explain the peculiar electronic ordering tendencies of FeSe [3]. Here, we compute the RIXS cross section within an itinerant RPA procedure with nematicity included in the bare band structure [6]. The applied RIXS framework is similar to that used in Ref. [36] where second order perturbation theory involving the absorption and emission process is used to calculate the RIXS intensity from the generalized spin-susceptibility. The latter is then calculated within a random phase approximation (RPA) where additional reduced coherence of the electronic structure [33] is taken into account. We find that the RIXS cross section as calculated for the fully coherent electronic structure exhibits relatively sharp modes, but remains nearly isotropic when comparing the intensity along the (π, 0) and (0, π) directions, irrespective of whether the Y pocket is present or not at the Fermi level. A strong spin-excitation anisotropy inherent in the sharp paramagnons of the itinerant system can be found if self-energy effects in the nematic state are taken into account. Furthermore, we note that this anisotropy persists to high energies much larger than the energy scale of the nematic order parameter of a few tens of *meV*, similar to the experimental findings in a recent RIXS experiment [34]. The spin-excitation anisotropy in the theoretical intensity at low energies depends sensitively on the orbital content of the Fermi surface. We discuss implications for our general understanding of magnetic fluctuations and electronic structure of FeSe by comparison to the experimentally determined RIXS data from Ref. [34].

2 MODEL AND METHOD

The following calculations are based on a tight-binding parametrization for iron-based superconductors [37] with values of the hopping parameters used earlier [6, 7, 33], that closely matches the electronic structure measured in spectroscopic probes. The Fermi surface of this band structure contains an electron Fermi pocket at the Y-point of the BZ, but its presence is largely irrelevant for the RIXS results discussed below, compare **Figure 1A** of Ref. [7] and **Figure 1** for a simplified two dimensional plot of the Fermi surface. Thus, we start from the Hamiltonian

$$H = \sum_{\mathbf{k}\sigma\ell\ell'} t_{\mathbf{k}}^{\ell\ell'} c_{\ell\sigma}^{\dagger}(\mathbf{k}) c_{\ell'\sigma}(\mathbf{k}), \tag{1}$$

where $c_{\ell\sigma}^{\dagger}(\mathbf{k})$ is the Fourier amplitude of an operator $c_{i\ell\sigma}^{\dagger}$ that creates an electron in Wannier orbital ℓ with spin $\sigma \in \{\uparrow, \downarrow\}$ and $t_{\mathbf{k}}^{\ell\ell'}$ is the Fourier transform of the hoppings connecting the Fe $3d$ orbitals $(d_{xy}, d_{x^2-y^2}, d_{xz}, d_{yz}, d_{3z^2-r^2})$. This term includes an on-site spin-orbit coupling of type $S^z L^z$, giving rise to imaginary hopping elements [38], which yield a splitting of the two hole-like bands along the Γ-Z line in the BZ. The nematic state at low temperatures is modelled by including an onsite and nearest neighbor bond order term with an energy scale of $\approx 10\,\mathrm{meV}$ [6, 33] arising from Coulomb interactions [22, 23, 29, 39]. While other types of orbital order terms have been proposed in the literature [27, 40], we do not examine these possibilities in this work.

The Bloch Hamiltonian can be diagonalized by a unitary transformation with the matrix elements $a_{\mu}^{\ell}(\mathbf{k})$, such that it reads $H = \sum_{\mathbf{k}\sigma\mu} \tilde{E}_{\mu}(\mathbf{k}) c_{\mu\sigma}^{\dagger}(\mathbf{k}) c_{\mu\sigma}(\mathbf{k})$, where $\tilde{E}_{\mu}(\mathbf{k})$ are the eigenenergies closely matching the maxima of the spectral function as deduced experimentally [6, 15, 41–44]. $c_{\mu\sigma}^{\dagger}(\mathbf{k})$ is the Fourier amplitude of electrons in band μ and momentum $\mathbf{k}$. Furthermore, we adopt an ansatz for the Green's function in orbital space incorporating correlations via quasiparticle weights Z_{ℓ} in orbital ℓ,

$$\begin{aligned}\tilde{G}_{\ell\ell'}(\mathbf{k}, \omega_n) &= \sqrt{Z_{\ell} Z_{\ell'}} \sum_{\mu} \frac{a_{\mu}^{\ell}(\mathbf{k}) a_{\mu}^{\ell'*}(\mathbf{k})}{i\omega_n - \tilde{E}_{\mu}(\mathbf{k})} \\ &= \sqrt{Z_{\ell} Z_{\ell'}} \sum_{\mu} a_{\mu}^{\ell}(\mathbf{k}) a_{\mu}^{\ell'*}(\mathbf{k}) \tilde{G}^{\mu}(\mathbf{k}, \omega_n).\end{aligned} \tag{2}$$

Here $\tilde{G}^{\mu}(\mathbf{k}, \omega_n) = [i\omega_n - \tilde{E}_{\mu}(\mathbf{k})]^{-1}$ is the coherent Green's function in band space which in the paramagnetic state is diagonal in spin space, i.e., proportional to $\delta_{\sigma,\sigma'}$. This ansatz does *not* include the actual incoherent spectral weight, and should therefore only describe the low energy properties of the electronic structure. While the quasiparticle weights are phenomenological parameters, these can also be calculated e.g., by using fluctuation exchange approach [16], or slave-boson methods or dynamical mean field theory [14, 45–50], qualitatively giving similar trends for the quasiparticle weights, but in detail yielding different band renormalizations and Fermi surfaces, i.e., exhibiting a low-energy Green's function that is not expected to describe the physical properties accurately at low energies. Here, we adopt the values $\{\sqrt{Z_l}\} = [0.2715, 0.9717, 0.4048, 0.9236, 0.5916]$ as used in previous investigations [6, 7, 33]; conclusions are robust as long as the quasiparticle weights are chosen within the range presented in Ref. [33].

To obtain two-particle responses as measured by a RIXS experiment, we adopt a standard Hubbard-Hund Hamiltonian for local interactions

$$\begin{aligned}H = U \sum_{i,\ell} n_{i\ell\uparrow} n_{i\ell\downarrow} + U' \sum_{i,\ell'<\ell} n_{i\ell} n_{i\ell'} + J \sum_{i,\ell'<\ell} \sum_{\sigma,\sigma'} c_{i\ell\sigma}^{\dagger} c_{i\ell'\sigma'}^{\dagger} c_{i\ell\sigma'} c_{i\ell'\sigma} \\ + J' \sum_{i,\ell'\neq\ell} c_{i\ell\uparrow}^{\dagger} c_{i\ell\downarrow}^{\dagger} c_{i\ell'\downarrow} c_{i\ell'\uparrow},\end{aligned} \tag{3}$$

where the parameters U, U', J, J' are given in the notation of Kuroki *et al.* [51]. Imposing spin-rotational invariance, i.e., $U' = U - 2J$, $J = J'$, there are only two parameters U and J/U left to specify the interactions which we set to values used previously [33].

Within the ansatz of **Eq. 2**, the paramagnetic orbital susceptibility is given by

$$\tilde{\chi}_{\ell_1\ell_2\ell_3\ell_4}^{0}(q) = -\sum_{k,\mu,\nu} \tilde{M}_{\ell_1\ell_2\ell_3\ell_4}^{\mu\nu}(\mathbf{k}, \mathbf{q}) \tilde{G}^{\mu}(k+q) \tilde{G}^{\nu}(k), \tag{4}$$

where we have adopted the shorthand $k \equiv (\mathbf{k}, \omega_n)$ and defined the abbreviation

$$\tilde{M}_{\ell_1\ell_2\ell_3\ell_4}^{\mu\nu}(\mathbf{k},\mathbf{q}) = \sqrt{Z_{\ell_1} Z_{\ell_2} Z_{\ell_3} Z_{\ell_4}} a_{\nu}^{\ell_4}(\mathbf{k}) a_{\nu}^{\ell_2,*}(\mathbf{k}) a_{\mu}^{\ell_1}(\mathbf{k}+\mathbf{q}) a_{\mu}^{\ell_3,*}(\mathbf{k}+\mathbf{q}).$$

After performing the internal frequency summation analytically, we calculate $\tilde{\chi}_{\ell_1\ell_2\ell_3\ell_4}^{0}$ by integrating over the full BZ, which is just the susceptibility $\chi_{\ell_1\ell_2\ell_3\ell_4}^{0}$ of a fully coherent Green's function multiplied by the quasiparticle weights

$$\tilde{\chi}_{\ell_1\ell_2\ell_3\ell_4}^{0}(\mathbf{q}, \omega) = \sqrt{Z_{\ell_1} Z_{\ell_2} Z_{\ell_3} Z_{\ell_4}}\, \chi_{\ell_1\ell_2\ell_3\ell_4}^{0}(\mathbf{q}, \omega). \tag{5}$$

Two-particle correlation functions of the interacting system with the interacting Hamiltonian of **Eq. 3** can be calculated in the random-phase approximation (RPA) by summing a subset of diagrams (see, e.g., Ref. [52]) such that the spin part of the RPA susceptibility, $\tilde{\chi}_1^{\mathrm{RPA}}$, is given by

$$\tilde{\chi}_{1\,\ell_1\ell_2\ell_3\ell_4}^{\mathrm{RPA}}(\mathbf{q}, \omega) = \left\{\tilde{\chi}^0(\mathbf{q}, \omega)\left[1 - \bar{U}^s \tilde{\chi}^0(\mathbf{q}, \omega)\right]^{-1}\right\}_{\ell_1\ell_2\ell_3\ell_4}. \tag{6}$$

The interaction matrix $\bar{U}^s$ in orbital space is composed of linear combinations of U, U', J, J'. For its detailed form, we refer to e.g., Ref. [53].

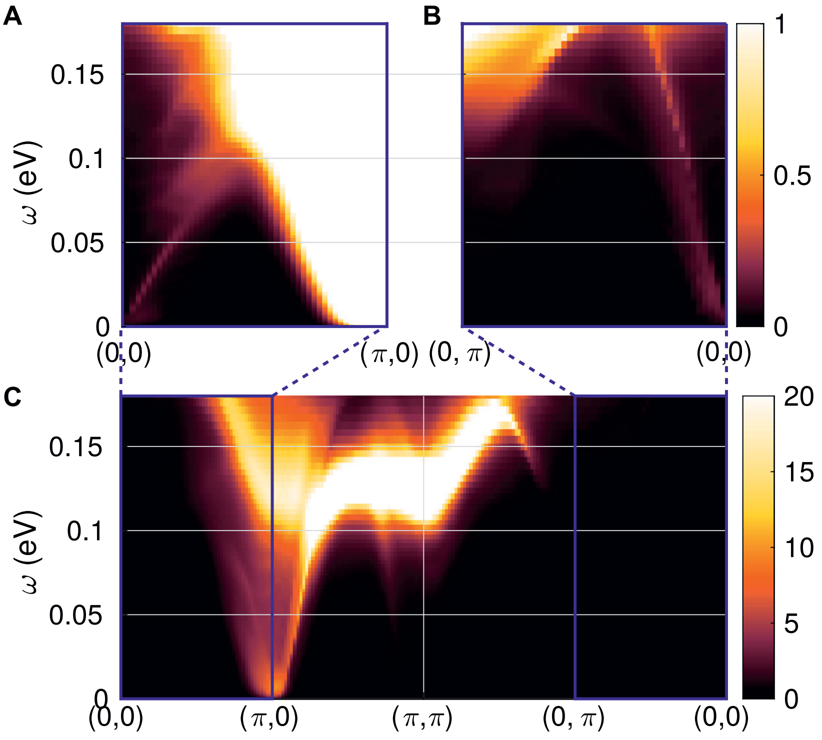

FIGURE 2 | Spin susceptibility: $-\,\mathrm{Im}\chi(\mathbf{q},\omega)$. **(A,B)** Zoom-in to the details of the spin susceptibility as calculated using the modified RPA approach for $U = 0.57$ eV and $J = U/6$, compare Figure 9C of Ref. [33]. Close to $\mathbf{q} = (0, 0)$ paramagnon modes are dispersing linearly up as seen towards the X point **(A)**, and towards the Y point **(B)**. The overall intensity close to $\mathbf{q} = (\pi, 0)$ is much larger and exhibits a dispersion with broad maximum around $\omega \geq 0.1$ eV **(C)** compared to the relatively sharp paramagnon dispersion close to $\mathbf{q} = (0, 0)$.

The total physical spin susceptibility as, for example, measured in inelastic neutron scattering experiments is then given by the sum

$$\chi(\mathbf{q},\omega) = \frac{1}{2}\sum_{\ell\ell'} \tilde{\chi}^{\mathrm{RPA}}_{1\ \ell\ell\ell'\ell'}(\mathbf{q},\omega). \tag{7}$$

For discussion purposes, and to illustrate the differences to the RIXS cross section, we present results for FeSe of this quantity in **Figure 2**. This is the same calculation as in Ref. [33], but with focus on the small $\mathbf{q}$ regions, **Figures 2A,B**.

To calculate the RIXS spectra we follow the approach presented in Ref. [36], where it is calculated as a second-order perturbation from the Kramers-Heisenberg equation in the fast-collision approximation [54]. The transition operator in the dipole approximation, $D_{\mathbf{k}} \approx \sum_{j,j_z,\ell,\sigma,\mathbf{k}'} c^{j,j_z}_{\ell,\sigma}(\boldsymbol{\varepsilon})\, c^{\dagger}_{\ell\sigma}(\mathbf{k})\, p(\mathbf{k}+\mathbf{k}')_{j,j_z} + \mathrm{H.c.}$ is written using the fermionic operator of the Fe $2p$ electrons, $p(\mathbf{k})_{j,j_z}$ for momentum $\mathbf{k}$ and total angular momentum j and z-projection j_z. The dipole transition matrix elements $c^{j\,j_z}_{\ell,\sigma}(\boldsymbol{\varepsilon}) = \langle 3d; \ell, \sigma | \boldsymbol{\varepsilon}\cdot\mathbf{r} | 2p; j, j_z\rangle$, depend on the unit vector of the polarization of the x-rays involved in the process.

Considering the Fe-L_3 edge absorption, we restrict to the intermediate $j = 3/2$ states of the $2p$ electrons, and calculate the matrix elements assuming wavefunctions with pure hydrogen-like symmetries, i.e., ignoring the deviations of the true Wannier states due to the lower crystal symmetry. The contribution from the radial integration of these wavefunctions will be just a constant (when assuming the same radial dependence for all Fe $3d$ and $2p$ orbitals) while the angular part is given by integrals of trigonometric functions on the unit sphere. Having calculated the matrix elements, one can then obtain the RIXS spectrum from the calculated orbital susceptibility as a sum over internal spin and orbital degrees of freedom via [36].

$$\begin{aligned} I_{\mathrm{RIXS}}(\mathbf{q},\omega) \propto -\,\mathrm{Im}\Bigg\{ &\sum_{\{\sigma_i\}} \sum_{\ell_1\ell_2\ell_3\ell_4} \chi^{(\sigma_1,\sigma_1')(\sigma_2,\sigma_2')}_{\ell_1\ell_2\ell_3\ell_4}(\mathbf{q},\omega) \\ &\times \Bigg[\sum_{j_z,j_z'} c^{j\,j_z}_{\ell_1,\sigma_1}(\boldsymbol{\varepsilon}_{\mathrm{o}})^{*} c^{j\,j_z}_{\ell_2,\sigma_1'}(\boldsymbol{\varepsilon}_{\mathrm{i}}) c^{j\,j_z'}_{\ell_3,\sigma_2}(\boldsymbol{\varepsilon}_{\mathrm{i}})^{*} c^{j\,j_z'}_{\ell_4,\sigma_2'}(\boldsymbol{\varepsilon}_{\mathrm{o}}) \Bigg] \Bigg\}, \end{aligned} \tag{8}$$

where $\boldsymbol{\varepsilon}_{\mathrm{i}}$ and $\boldsymbol{\varepsilon}_{\mathrm{o}}$ are the polarization vectors of the incoming and outgoing x-rays. As discussed in Ref. [36], the spin-orbit coupling allows spin-flip processes as mediated by the Clebsh-Gordan coefficients when writing the $2p$ states in the basis for the total angular momentum $j = 3/2$. However, since there is no magnetism and we ignore the transverse part of the spin-orbit coupling, the susceptibility turns out to be diagonal, $\chi^{(\sigma_1,\sigma_1')(\sigma_2,\sigma_2')}_{\ell_1\ell_2\ell_3\ell_4}(\mathbf{q},\omega) = \delta_{\sigma_1,\sigma_2}\delta_{\sigma_1',\sigma_2'}\tilde{\chi}^{\mathrm{RPA}}_{1\ \ell_1\ell_2\ell_3\ell_4}(\mathbf{q},\omega)$.

Following the experimental details given in Ref. [34], i.e., setting the scattering angle $\beta = 50°$, considering the energy

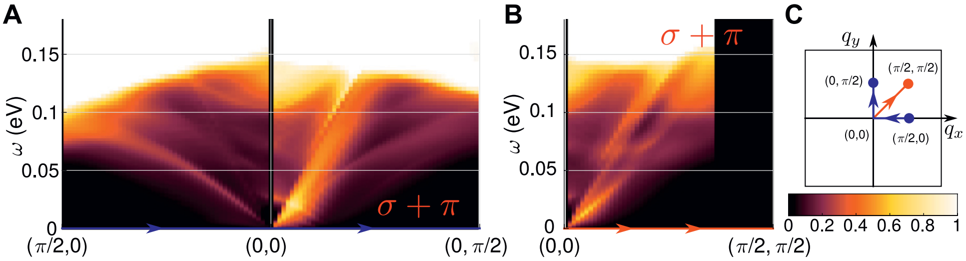

FIGURE 3 | RIXS intensity with orbital-selective quasiparticle weight reduction. The RIXS intensity (see common colorbar) at the accessible momentum transfer exhibits sharp paramagnon-like modes towards $\mathbf{q} = (\pi/2, 0)$, while towards $\mathbf{q} = (0, \pi/2)$ a broad intensity and a much weaker paramagnon mode is visible **(A)**. Along the diagonal in the BZ, there are multiple quasi-sharp paramagnon modes visible **(B)**. Calculated for $U = 0.57$ eV, $J = U/6$. Geometry of the paths along the diagonal (orange) and along the coordinate axis (blue) as shown in the other panels **(C)**.

of the resonance as $\omega_0 = 707\,eV$, we calculate the polarization vector for incoming π polarization as

$$\boldsymbol{\varepsilon}_{\mathrm{i}} = \sin\alpha\mathbf{e}_{\|} + \cos\alpha\mathbf{e}_z, \tag{9}$$

where the in plane vector is defined as $\mathbf{e}_{\|} = \mathbf{q}/q$. The polarization vectors for the two outgoing polarization directions are

$$\boldsymbol{\varepsilon}_{\mathrm{o},\sigma} = \sin(\alpha+\beta)\mathbf{e}_{\|} + \cos(\alpha+\beta)\mathbf{e}_z, \tag{10}$$

$$\boldsymbol{\varepsilon}_{\mathrm{o},\pi} = \mathbf{e}_{\perp} \tag{11}$$

with the perpendicular in – plane vector, i.e. $\mathbf{e}_{\perp}\cdot\mathbf{q} = 0$, where the angle α between wavevector $k_{\mathrm{i}} = \omega_0/(\hbar c)$ of the incoming and the outgoing k_{o} x-ray is obtained from solving the equation for momentum conservation along the surface, $q = k_{\mathrm{i}}\cos\alpha + k_{\mathrm{o}}\cos(\alpha+\beta)$ for fixed angle $\beta = 50^\circ$ and approximating $k_{\mathrm{o}} \approx k_{\mathrm{i}}$. Finally, we note that the energy resolution of the RIXS experiment in Ref. [34] is given as 80 meV. Below, we focus the theory discussion on the as-calculated (non-broadened) computed results.

3 RESULTS

For convenience, and to contrast expected intensity measured in an inelastic neutron scattering experiment and a RIXS measurement, we start by presenting the spin susceptibility as obtained from **Eq. 7** for the case with reduced coherence [33]. In **Figure 2C** the susceptibility along a high symmetry cut is presented exhibiting large intensity together with a broad dispersive feature close to $(\pi, 0)$, and, in contrast, essentially no intensity at $(0, \pi)$. At higher energies, there is also spectral weight close to (π, π). Due to the restricted momentum transfer from the photons, RIXS experiments are only able to access the momentum transfer close to $(0, 0)$. Therefore the susceptibility in these regions will contribute to the summation given in **Eq. 8**, weighted by the dipole transition matrix elements, shown in **Figure 2A,B** (note different color scale). Already at the level of the (summed) susceptibility, one can see a dispersive and relatively sharp magnetic mode emanating from $(0, 0)$ with different slopes along the q_x and q_y directions.

Next, we present our results for the RIXS intensity along high symmetry cuts as detailed in **Figure 3C**, where the sum over the perpendicular polarizations has been performed. It turns out that there is a sharp mode along $(0, 0) \to (\pi/2, 0)$ that presumably originates from the coherent small $\mathbf{q}$-scattering at the Γ-pocket, which occurs from the d_{yz} orbital component; panel **(A)**. In contrast, there is only a very broad mode along the $(0, \pi/2)$ direction also coming from scattering of the d_{yz} orbital, but at the X-pocket. Scattering contributions from the other orbital components are strongly suppressed due to a reduced quasiparticle weight $Z_\ell < 1$. Along the diagonal direction both modes are present, giving rise to two relatively sharp features; panel **(B)**. Note that the black area is due to the mentioned kinematic RIXS constraint, i.e. the respective $\mathbf{q}$-vectors cannot be reached.

We can disentangle the polarization dependence by looking at each polarization separately. As shown in **Figure 4A** the σ polarization yields a much weaker intensity along the q_x and q_y directions as compared to the π polarization, while along the diagonal both polarizations have similar structure and magnitude. One notes also that the broad feature along the q_y cut is only present in the π polarization. Indeed, there are strong effects on the anisotropy of the RIXS intensity which are mediated by orbitally selective coherence of the electronic structure, leading to the presence of a sharp mode only along the q_x direction as also detected experimentally; the broad mode along the q_y direction is, however, enhanced due to orbital selectivity. The experimental measurement of the polarization dependence might be able to disentangle scattering contributions from the Γ- and the X-pockets.

In contrast, a calculation using a fully coherent electronic structure where self-energy corrections are not taken into account, $Z_l = 1$, yields a RIXS cross section that is almost isotropic, as shown in **Figure 5A**. This result is calculated with the band structure which exhibits a Y-pocket at the Fermi level. Except for the very lowest energies $< 20\,meV$, the same conclusions remain within an electronic structure where the Y-pocket has been lifted by nematic order from nearest neighbor Coulomb interactions [29], or from including d_{xy} nematicity [27]. The reasons for this almost isotropic result are similar to the spin susceptibility discussion [7], whereby the missing Y-pocket only reduces scattering contributions at very low energies corresponding to the nematic energy scale, while interband contributions and scattering at larger energies are

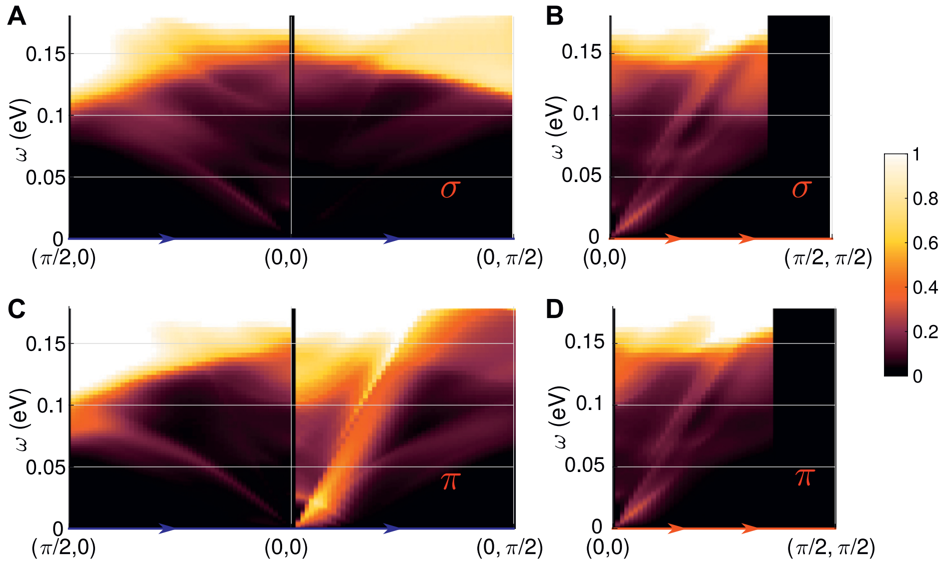

FIGURE 4 | Polarization dependence of RIXS intensity. Expected RIXS spectra decomposed in the intensities from σ **(A,B)** and π polarization of the outgoing photons **(C,D)** along the paths defined in **Figure 3B**; $U = 0.57$ eV, $J = U/6$.

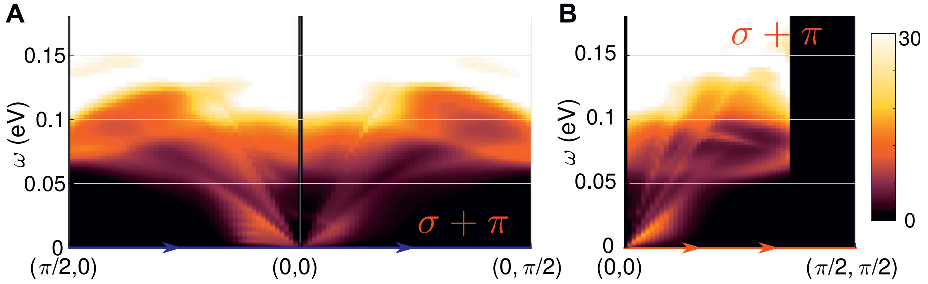

FIGURE 5 | RIXS intensity without orbital incoherence. Same as **Figure 3**, but calculated using $Z_l = 1$ and by setting $U = 0.36$ eV, $J = U/6$ as discussed in Ref. [33].

almost identical to the ones from a model with a Y-pocket present at the Fermi level.

To complete our understanding of the origin of the different spectral features in the RIXS intensity, we present in **Figure 6** a separation of the intensities in orbitally diagonal components, i.e., considering in the sum of **Eq. 8** only the terms with $\ell_1 = \ell_2 = \ell_3 = \ell_4$, panels (a-e), and extracting the off-diagonal contributions by subtracting diagonal components from the full intensity for the case of $Z_l = 1$. One clearly sees that the $d_{x^2-y^2}$ and the d_{z^2} orbitals do not contribute to the intensity in the energy range at all. The d_{xy} orbital yields an almost isotropic contribution along the q_x and the q_y cuts which, however, should be suppressed given the correlated nature of that orbital. Finally, the d_{yz} orbital contributes to a branch along q_y from scattering within the X-pocket, while the d_{xz} orbital contributes with a slightly larger intensity along the q_x direction. Again, these conclusions remain similar for models without the Y-pocket with the exception of reduced weight from the d_{xz} orbital at and below the nematic energy scale of ≈ 20 meV (not shown). **Figure 6F** demonstrates that the orbitally off-diagonal contributions are quite sizeable; we also note that different from the susceptibility extracted from inelastic neutron scattering experiments, the sum in **Eq. 8** contains elements of the susceptibility tensor with all four orbitals being different. Interestingly, the sharp dispersive mode along q_x as seen in **Figure 3A** and also **Figure 4A,C** does not originate from orbitally diagonal contributions, but rather appears as blue mode in the subtracted intensity of **Figure 6F**. Hence the orbitally off-diagonal contributions give rise to this intensity, and it is less affected by reduced coherence and therefore more visible in **Figure 3A** compared to **Figure 5A**.

Since the RIXS experiment is kinematically constrained to momentum space close to (0, 0) the dispersive modes are less affected by the particular choice of the bare interaction **Eq. 3**, i.e., no shift of intensity to lower energy is visible as the magnetic instability is approached, $U \rightarrow U_c$. This is unlike the dispersive modes close to (π, 0) or (π, π) whose bandwidth is strongly governed by the denominator in the RPA equation for the susceptibility, **Eq. 6**, i.e., the spectral position of the high

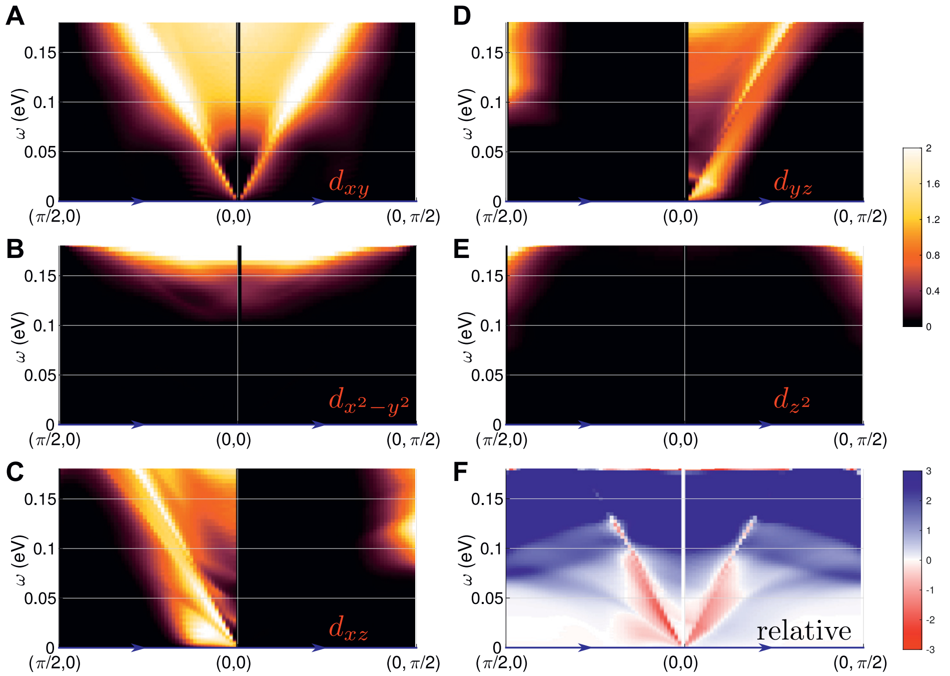

FIGURE 6 | RIXS intensity from single orbital components. Intensity calculated by setting $Z_l = 0$, except for one orbital component, where $Z_{l'} = 1$ **(A–E)**, i.e., in the sum in **Eq. 8** only the fully diagonal components of the susceptibility contribute. The off-diagonal contributions are sizeable as shown in panel **(F)** where the results of panels **(A–E)** multiplied by the number of orbitals are subtracted from the full RIXS intensity as shown in **Figure 5A**.

energy weight presented in **Figure 2C** is sensitive to the value of the bare interaction U.

In Ref. [34] the RIXS data was analyzed in terms of a phenomenological model where the RIXS spectra were fitted to a general damped harmonic oscillator model, and discussed in terms of an anisotropic Heisenberg Hamiltonian. In addition, it was concluded without explicit calculations that itinerant models are at variance with the RIXS data due to expected Landau-damped high-energy excitations. The current calculations invalidates this argumentation since we find highly dispersive magnetic excitations persisting to high energies. Indeed, the sharp dispersive mode is visibly strongest along the q_x direction, see **Figure 3A**. In general, we find a spin-excitation anisotropy with larger intensity along the q_x-directions, similar to experiments [34]. At the lowest energies, however, the current band structure produces a larger intensity in the q_y direction; a property which is not seen experimentally [34]. The reason for this discrepancy is the "boosted" d_{zy} orbital due to the particular choice of quasiparticle weight factors. This hints at more d_{xz}-orbital content present at the Fermi level than included in the present modelling.

4 SUMMARY AND CONCLUSION

We have provided a microscopic calculation of the RIXS and neutron response relevant for nematic FeSe. The model is based on itinerant electrons with additional interaction-generated self-energy effects, crudely approximated by simple energy- and momentum independent quasi-particle weight factors. This approach offers a consistent picture of spin fluctuations as detected in inelastic neutron scattering and the recent RIXS experiments, in addition to other experiments, without further tuning of parameters. Specifically, the calculations yield overall agreement with the momentum and energy structure of the low-energy modes, and their momentum anisotropy. We have also discussed quantitative discrepancies between the current calculation, and the recent RIXS measurement by Lu *et al.* [34]. The microscopic calculation allowed us to explore orbital- and band-dependence of the RIXS scattering cross section, revealing 1) an insensitivity of the RIXS spin-excitation anisotropy response to the presence or absence of a Y-pocket at the Fermi level, and 2) a sensitivity of the low-energy anisotropy to the detailed balance of d_{xz}- and d_{yx}-orbital content present on the Γ- and X-pockets of the Fermi surface.

While the RPA approach to itinerant spin excitations is expected to break down at sufficiently high energies, where exactly this occurs is not clear; the crossover to a more localized description is expected in the range of 100s of meV. Here we have shown that for intermediate energies of up to ~ 150 meV this approach appears to reproduce qualitative features, and that well-defined spin excitations are not overdamped by electron-hole scattering. Of course the theory is not complete in the sense that the quasiparticle weights are not derived properly from a self-energy, nor are vertex corrections included. Nevertheless the current framework appears to be a useful phenomenology to describe the low-energy physics of this unusual material.

DATA AVAILABILITY STATEMENT

The raw data supporting the conclusion of this article will be made available by the authors, without undue reservation.

AUTHOR CONTRIBUTIONS

AK performed the calculations, and all authors contributed to writing the manuscript.

FUNDING

BA acknowledges support from the Independent Research Fund Denmark grant number 8021-00047B. PH was supported by the U.S. Department of Energy under Grant No. DE-FG02-05ER4623.

ACKNOWLEDGMENTS

We acknowledge useful discussions with A. Kemper and X. Lu.

REFERENCES

1. Böhmer AE, Kreisel A. Nematicity, Magnetism and Superconductivity in FeSe. *J Phys Condens Matter* (2018) 30:023001. doi:10.1088/1361-648X/aa9caa
2. Coldea AI, Watson MD. The Key Ingredients of the Electronic Structure of FeSe. *Annu Rev Condens Matter Phys* (2018) 9:125–46. doi:10.1146/annurev-conmatphys-033117-054137
3. Kreisel A, Hirschfeld P, Andersen B. On the Remarkable Superconductivity of FeSe and its Close Cousins. *Symmetry* (2020) 12:1402. doi:10.3390/sym12091402
4. Fanfarillo L, Cortijo A, Valenzuela B. Spin-Orbital Interplay and Topology in the Nematic Phase of Iron Pnictides. *Phys Rev B* (2015) 91:214515. doi:10.1103/PhysRevB.91.214515
5. Mukherjee S, Kreisel A, Hirschfeld PJ, Andersen BM. Model of Electronic Structure and Superconductivity in Orbitally Ordered FeSe. *Phys Rev Lett* (2015) 115:026402. doi:10.1103/PhysRevLett.115.026402
6. Sprau PO, Kostin A, Kreisel A, Böhmer AE, Taufour V, Canfield PC, et al. Discovery of Orbital-Selective Cooper Pairing in FeSe. *Science* (2017) 357:75–80. doi:10.1126/science.aal1575
7. Kreisel A, Andersen BM, Sprau PO, Kostin A, Davis JCS, Hirschfeld PJ. Orbital Selective Pairing and gap Structures of Iron-Based Superconductors. *Phys Rev B* (2017) 95:174504. doi:10.1103/PhysRevB.95.174504
8. Benfatto L, Valenzuela B, Fanfarillo L. Nematic Pairing from Orbital-Selective Spin Fluctuations in FeSe. *Npj Quant Mater* (2018) 3:56. doi:10.1038/s41535-018-0129-9
9. Hu H, Yu R, Nica EM, Zhu J-X, Si Q. Orbital-Selective Superconductivity in the Nematic Phase of FeSe. *Phys Rev B* (2018) 98:220503. doi:10.1103/PhysRevB.98.220503
10. Bhattacharyya S, Björnson K, Zantout K, Steffensen D, Fanfarillo L, Kreisel A, et al. Nonlocal Correlations in Iron Pnictides and Chalcogenides. *Phys Rev B* (2020) 102:035109. doi:10.1103/PhysRevB.102.035109
11. Liu D, Li C, Huang J, Lei B, Wang L, Wu X, et al. Orbital Origin of Extremely Anisotropic Superconducting gap in Nematic Phase of FeSe Superconductor. *Phys Rev X* (2018) 8:031033. doi:10.1103/PhysRevX.8.031033
12. Fanfarillo L, Mansart J, Toulemonde P, Cercellier H, Le Fèvre P, Bertran F, et al. Orbital-Dependent Fermi Surface Shrinking as a Fingerprint of Nematicity in FeSe. *Phys Rev B* (2016) 94:155138. doi:10.1103/PhysRevB.94.155138
13. Christensen MH, Fernandes RM, Chubukov AV. Orbital Transmutation and the Electronic Spectrum of FeSe in the Nematic Phase. *Phys Rev Res* (2020) 2:013015. doi:10.1103/PhysRevResearch.2.013015
14. de' Medici L, Giovannetti G, Capone M. Selective Mott Physics as a Key to Iron Superconductors. *Phys Rev Lett* (2014) 112:177001. doi:10.1103/PhysRevLett.112.177001
15. Kostin A, Sprau PO, Kreisel A, Chong YX, Böhmer AE, Canfield PC, et al. Imaging Orbital-Selective Quasiparticles in the Hund's Metal State of FeSe. *Nat Mater* (2018) 17:869–74. doi:10.1038/s41563-018-0151-0
16. Björnson K, Kreisel A, Rømer AT, Andersen BM. Orbital-Dependent Self-Energy Effects and Consequences for the Superconducting gap Structure in Multiorbital Correlated Electron Systems. *Phys Rev B* (2021) 103:024508. doi:10.1103/PhysRevB.103.024508
17. Cercellier H, Rodière P, Toulemonde P, Marcenat C, Klein T. Influence of the Quasiparticle Spectral Weight in FeSe on Spectroscopic, Magnetic, and Thermodynamic Properties. *Phys Rev B* (2019) 100:104516. doi:10.1103/physrevb.100.104516
18. Biswas PK, Kreisel A, Wang Q, Adroja DT, Hillier AD, Zhao J, et al. Evidence of Nodal gap Structure in the Basal Plane of the FeSe Superconductor. *Phys Rev B* (2018) 98:180501. doi:10.1103/PhysRevB.98.180501
19. Zhou R, Scherer DD, Mayaffre H, Toulemonde P, Ma M, Li Y, et al. Singular Magnetic Anisotropy in the Nematic Phase of Fese. *Npj Quan Mater.* (2020) 5:93. doi:10.1038/s41535-020-00295-1
20. Yi M, Pfau H, Zhang Y, He Y, Wu H, Chen T, et al. Nematic Energy Scale and the Missing Electron Pocket in FeSe. *Phys Rev X* (2019) 9:041049. doi:10.1103/PhysRevX.9.041049
21. Huh SS, Seo JJ, Kim BS, Cho SH, Jung JK, Kim S, et al. Absence of Y-Pocket in 1-Fe Brillouin Zone and Reversed Orbital Occupation Imbalance in FeSe. *Commun Phys* (2020) 3:52. doi:10.1038/s42005-020-0319-1
22. Jiang K, Hu J, Ding H, Wang Z. Interatomic Coulomb Interaction and Electron Nematic Bond Order in FeSe. *Phys Rev B* (2016) 93:115138. doi:10.1103/PhysRevB.93.115138
23. Scherer DD, Jacko AC, Friedrich C, Şaşıoğlu E, Blügel S, Valentí R, et al. Interplay of Nematic and Magnetic Orders in FeSe under Pressure. *Phys Rev B* (2017) 95:094504. doi:10.1103/PhysRevB.95.094504
24. Xing R-Q, Classen L, Khodas M, Chubukov AV. Competing Instabilities, Orbital Ordering, and Splitting of Band Degeneracies from a Parquet Renormalization Group Analysis of a Four-Pocket Model for Iron-Based Superconductors: Application to FeSe. *Phys Rev B* (2017) 95:085108. doi:10.1103/PhysRevB.95.085108
25. Eugenio PM, Vafek O. Classification of Symmetry Derived Pairing at the *M* point in FeSe. *Phys Rev B* (2018) 98:014503. doi:10.1103/PhysRevB.98.014503
26. Christensen MH, Kang J, Fernandes RM. Intertwined Spin-Orbital Coupled Orders in the Iron-Based Superconductors. *Phys Rev B* (2019) 100:014512. doi:10.1103/PhysRevB.100.014512
27. Rhodes LC, Böker J, Müller MA, Eschrig M, Eremin IM. Non-Local D_{xy} Nematicity and the Missing Electron Pocket in FeSe. *Npj Quan Mater.* (2021) 6:45. doi:10.1038/s41535-021-00341-6
28. Long X, Zhang S, Wang F, Liu Z. A First-Principle Perspective on Electronic Nematicity in FeSe. *Npj Quan Mater.* (2020) 5:50. doi:10.1038/s41535-020-00253-x
29. Steffensen D, Kreisel A, Hirschfeld PJ, Andersen BM. Interorbital Nematicity and the Origin of a Single Electron Fermi Pocket in FeSe. *Phys Rev B* (2021) 103:054505. doi:10.1103/PhysRevB.103.054505
30. Yamada T, Tohyama T. Multipolar Nematic State of Nonmagnetic FeSe Based on DFT+U. *Phys Rev B* (2021) 104:L161110. doi:10.1103/PhysRevB.104.L161110
31. Chen T, Chen Y, Kreisel A, Lu X, Schneidewind A, Qiu Y, et al. Anisotropic Spin Fluctuations in Detwinned FeSe. *Nat Mater* (2019) 18:709–16. doi:10.1038/s41563-019-0369-5
32. Kreisel A, Mukherjee S, Hirschfeld PJ, Andersen BM. Spin Excitations in a Model of FeSe with Orbital Ordering. *Phys Rev B* (2015) 92:224515. doi:10.1103/PhysRevB.92.224515
33. Kreisel A, Andersen BM, Hirschfeld PJ. Itinerant Approach to Magnetic Neutron Scattering of FeSe: Effect of Orbital Selectivity. *Phys Rev B* (2018) 98:214518. doi:10.1103/PhysRevB.98.214518
34. Lu X, Zhang W, Tseng Y, Liu R, Tao Z, Paris E, et al. Spin-Excitation Anisotropy in the Nematic State of Detwinned FeSe. arXiv e-prints arXiv:2108.04484 (2021).

35. Lu X, Scherer DD, Tam DW, Zhang W, Zhang R, Luo H, et al. Spin Waves in Detwinned $BaFe_2As_2$. *Phys Rev Lett* (2018) 121:067002. doi:10.1103/PhysRevLett.121.067002
36. Kaneshita E, Tsutsui K, Tohyama T. Spin and Orbital Characters of Excitations in Iron Arsenide Superconductors Revealed by Simulated Resonant Inelastic X-ray Scattering. *Phys Rev B* (2011) 84:020511. doi:10.1103/PhysRevB.84.020511
37. Eschrig H, Koepernik K. Tight-Binding Models for the Iron-Based Superconductors. *Phys Rev B* (2009) 80:104503. doi:10.1103/PhysRevB.80.104503
38. Kreisel A, Wang Y, Maier TA, Hirschfeld PJ, Scalapino DJ. Spin Fluctuations and Superconductivity in $K_xFe_{2-y}Se_2$. *Phys Rev B* (2013) 88:094522. doi:10.1103/physrevb.88.094522
39. Wu X, Liang Y, Fan H, Hu J. Nematic Orders and Nematicity-Driven Topological Phase Transition in FeSe. ArXiv e-prints ArXiv:1603.02055 (2016).
40. Yu R, Zhu J-X, Si Q. Orbital Selectivity Enhanced by Nematic Order in FeSe. *Phys Rev Lett* (2018) 121:227003. doi:10.1103/PhysRevLett.121.227003
41. Terashima T, Kikugawa N, Kiswandhi A, Choi E-S, Brooks JS, Kasahara S, et al. Anomalous Fermi Surface in FeSe Seen by Shubnikov-De Haas Oscillation Measurements. *Phys Rev B* (2014) 90:144517. doi:10.1103/PhysRevB.90.144517
42. Audouard A, Duc F, Drigo L, Toulemonde P, Karlsson S, Strobel P, et al. Quantum Oscillations and Upper Critical Magnetic Field of the Iron-Based Superconductor FeSe. *Europhys Lett* (2015) 109:27003. doi:10.1209/0295-5075/109/27003
43. Watson MD, Kim TK, Haghighirad AA, Davies NR, McCollam A, Narayanan A, et al. Emergence of the Nematic Electronic State in FeSe. *Phys Rev B* (2015) 91:155106. doi:10.1103/PhysRevB.91.155106
44. Watson MD, Kim TK, Rhodes LC, Eschrig M, Hoesch M, Haghighirad AA, et al. Evidence for Unidirectional Nematic Bond Ordering in FeSe. *Phys Rev B* (2016) 94:201107. doi:10.1103/PhysRevB.94.201107
45. Yu R, Si Q. U(1) Slave-Spin Theory and its Application to Mott Transition in a Multiorbital Model for Iron Pnictides. *Phys Rev B* (2012) 86:085104. doi:10.1103/PhysRevB.86.085104
46. Georges A, Medici Ld., Mravlje J. Strong Correlations from Hund's Coupling. *Annu Rev Condens Matter Phys* (2013) 4:137–78. doi:10.1146/annurev-conmatphys-020911-125045
47. van Roekeghem A, Richard P, Ding H, Biermann S. Spectral Properties of Transition Metal Pnictides and Chalcogenides: Angle-Resolved Photoemission Spectroscopy and Dynamical Mean-Field Theory. *Comptes Rendus Physique* (2016) 17:140–63. doi:10.1016/j.crhy.2015.11.003
48. Yi M, Zhang Y, Shen Z-X, Lu D. Role of the Orbital Degree of freedom in Iron-Based Superconductors. *Npj Quant Mater* (2017) 2:57. doi:10.1038/s41535-017-0059-y
49. Guterding D, Backes S, Tomić M, Jeschke HO, Valentí R. Ab Initioperspective on Structural and Electronic Properties of Iron-Based Superconductors. *Phys Status Solidi B* (2017) 254:1600164. doi:10.1002/pssb.201600164
50. de' Medici L. The Physics of Correlated Insulators, Metals, and Superconductors (Modeling and Simulation). In: *Hund's Metals Explained*, 7. Juelich: Forschungszentrum Juelich (2017). p. 377–98.
51. Kuroki K, Onari S, Arita R, Usui H, Tanaka Y, Kontani H, et al. Unconventional Pairing Originating from the Disconnected Fermi Surfaces of Superconducting $LaFeAsO_{1-x}F_x$. *Phys Rev Lett* (2008) 101:087004. doi:10.1103/PhysRevLett.101.087004
52. Graser S, Maier TA, Hirschfeld PJ, Scalapino DJ. Near-Degeneracy of Several Pairing Channels in Multiorbital Models for the Fe Pnictides. *New J Phys* (2009) 11:025016. doi:10.1088/1367-2630/11/2/025016
53. Kemper AF, Maier TA, Graser S, Cheng H-P, Hirschfeld PJ, Scalapino DJ. Sensitivity of the Superconducting State and Magnetic Susceptibility to Key Aspects of Electronic Structure in Ferropnictides. *New J Phys* (2010) 12:073030. doi:10.1088/1367-2630/12/7/073030
54. Ament LJP, van Veenendaal M, Devereaux TP, Hill JP, van den Brink J. Resonant Inelastic X-ray Scattering Studies of Elementary Excitations. *Rev Mod Phys* (2011) 83:705–67. doi:10.1103/RevModPhys.83.705

Conflict of Interest: The authors declare that the research was conducted in the absence of any commercial or financial relationships that could be construed as a potential conflict of interest.

frontiers | Frontiers in Physics

REVIEW
published: 09 May 2022
doi: 10.3389/fphy.2022.859017

FeSe and the Missing Electron Pocket Problem

Luke C. Rhodes [1], Matthias Eschrig [2], Timur K. Kim [3] and Matthew D. Watson [3]*

[1]School of Physics and Astronomy, University of St. Andrews, St. Andrews, United Kingdom, [2]Institute of Physics, University of Greifswald, Greifswald, Germany, [3]Diamond Light Source, Harwell Campus, Didcot, United Kingdom

The nature and origin of electronic nematicity remains a significant challenge in our understanding of the iron-based superconductors. This is particularly evident in the iron chalcogenide, FeSe, where it is currently unclear how the experimentally determined Fermi surface near the M point evolves from having two electron pockets in the tetragonal state, to exhibiting just a single electron pocket in the nematic state. This has posed a major theoretical challenge, which has become known as the missing electron pocket problem of FeSe, and is of central importance if we wish to uncover the secrets behind nematicity and superconductivity in the wider iron-based superconductors. Here, we review the recent experimental work uncovering this nematic Fermi surface of FeSe from both ARPES and STM measurements, as well as current theoretical attempts to explain this missing electron pocket of FeSe, with a particular focus on the emerging importance of incorporating the d_{xy} orbital into theoretical descriptions of the nematic state. Furthermore, we will discuss the consequence this missing electron pocket has on the theoretical understanding of superconductivity in this system and present several remaining open questions and avenues for future research.

Keywords: FeSe, ARPES, electronic structure, superconductivity, nematicity, strong correlations, iron based superconductors

Edited by:
Anna Böhmer,
Ruhr-University Bochum, Germany

Reviewed by:
Ming Yi,
Rice University, United States
Konrad Jerzy Kapcia,
Adam Mickiewicz University, Poland

****Correspondence:***
Luke C. Rhodes
lcr23@st-andrews.ac.uk

Specialty section:
This article was submitted to Condensed Matter Physics, a section of the journal Frontiers in Physics

Received: *20 January 2022*
Accepted: *07 March 2022*
Published: *09 May 2022*

Citation:
Rhodes LC, Eschrig M, Kim TK and Watson MD (2022) FeSe and the Missing Electron Pocket Problem. Front. Phys. 10:859017. doi: 10.3389/fphy.2022.859017

1 INTRODUCTION

One of the reasons for the huge interest in FeSe over the past decade has been the sense that it holds the key to the wider understanding of the whole Fe-based superconductor family [1–3]. With its minimalistic crystal structure and alluringly simple band structure in the tetragonal phase, alongside the prevalence of high-quality single crystals, it seemed like the ideal test bed to examine in detail the themes that were emerging in the field: strong orbital-dependent correlations [4–6], spin fluctuation pairing [7, 8], and most pertinently for this review, the so-called "nematic" phase [9–11], where C_4 rotational symmetry is spontaneously broken below 90 K.

Spontaneous breaking of rotational symmetry of the underlying lattice due to electronic correlations, the signature of nematic order, is known to occur via many mechanisms, such as via a high field FFLO state, which has been proposed for various materials including FeSe [12–14]. However, whereas a clear theory for FFLO order exists, the precise microscopic origin of the zero field nematicity in FeSe is still an important open question. Part of the challenging in understanding this nematic state arises due to the formation of antiferromagnetism that often accompanies the onset of the nematic state in many systems, although not FeSe. FeSe is therefore the perfect candidate to uncover the origin of the nematic state, as well as elucidate the effect nematicity has on the superconducting properties of the iron-based superconductors.

The measurement of the momentum-dependence of the superconducting gap in FeSe, between 2016 and 2018, was a particular experimental triumph. The data from both scanning tunneling microscopy (STM) [15] and multiple angle-resolved photoemission spectroscopy (ARPES) measurements [16–20] revealed a clear conclusion: the gap structure is extremely anisotropic, and broadly follows the d_{yz} orbital weight around the Fermi surface. While a twofold-symmetric gap is of course symmetry-allowed in an orthorhombic system, the fact that such a strong anisotropy was observed implied that the nematic state must also induce a profound anistropic effect on the Fermi surface of FeSe. However due to significant uncertainty as to the correct description of the low-temperature electronic structure, multiple theoretical explanations for the anisotropic gap structure were proposed [15, 19, 21–24].

A critical question required to understand this anisotropic superconducting gap is how does the nematic state influence the low temperature Fermi surface and electronic structure of FeSe? Given that we have a second-order phase transition [25], and that the lattice distortion $\frac{|a-b|}{(a+b)}$ is only ~0.2%, the natural assumption, from an *ab-initio* perspective [26], would be that nematicity should only weakly distort the established Fermi surface of the high-temperature tetragonal phase, which ARPES measurements have shown contains two hole pockets and two electron pockets [26–33]. Yet ARPES measurements in the nematic state have revealed sizeable band shifts, of the order of 10–50 meV [33], much larger that what would be predicted from ab-initio calculations [26].

Unfortunately, the precise identification of specific parts of the band structure, the nematic energy scales and even the Fermi surface of FeSe has been complicated by the formation of orthorhombic domains upon entering the nematic state. In an orthorhombic crystal, conventional ARPES experiments measure a superposition of two perpendicularly orientated crystallographic domains, which doubles the number of bands observed in the experimental data and creates ambiguity about which bands arise from which domain. For this reason, a recent focal point of research has involved overcoming this technical challenge of orthorhombic domains, for example by applying uniaxial strain [28, 34–40] or using NanoARPES [41] or scanning tunneling microscopy [14, 15, 42, 43]. The conclusion from these measurements have been unanimous, and have revealed that within the nematic state the Fermi surface of FeSe consists of one hole pocket and one electron pocket.

This finding, however, is very surprising and presents a fundamental theoretical conundrum that is at the heart of understanding the nematic and superconducting properties of FeSe. The bands that generate the two electron pockets observed in the tetragonal state form saddle points at the high symmetry M point close to the Fermi level. It is therefore not trivial to deform or shift these saddle points to lift one of these electron pockets away from the Fermi level upon entering the nematic state. This current theoretical challenge has become known as the “missing electron pocket problem” of FeSe and resolving this problem promises deeper insight into the nematic state, and a wider understanding of superconductivity in the iron-based superconductors.

In this review we will overview the recent experimental and theoretical work uncovering the Fermi surface of FeSe in the nematic state and tackling the missing electron pocket problem. In **Section 2** we will briefly introduce the experimental electronic structure of FeSe in the tetragonal state, to use as the foundation for understanding the nematic electronic structure. In **Section 3** we will discuss the recent experimental data uncovering the electronic structure in the nematic state, in particular focusing on measurements which overcome the technical problems associated with orthorhombic crystals, including ARPES measurements under uniaxial strain, NanoARPES measurements and Scanning tunneling microscopy (STM) measurements. In **Section 4** we will review the latest theoretical attempts to resolve this missing electron pocket problem, highlighting the necessity of considering the d_{xy} orbital in the phenomenological description of the nematic state. And in **Section 5** we will discuss the consequence the updated Fermi surface has on the understanding of the superconducting properties of FeSe. A summary of the electronic structure and missing electron pocket problem of FeSe is presented in **Figure 1**.

2 ELECTRONIC STRUCTURE IN THE TETRAGONAL STATE

From both a theoretical and experimental point of view, the electronic structure of the tetragonal state is relatively well understood. Prior to the onset of nematicity at $T_s = 90$ K, FeSe exhibits tetragonal symmetry with a $P4/nmm$ crystal structure [44]. This structure consists of layers of Fe atoms, in a 2D square lattice configuration, bridged by staggered out-of-plane Se atoms, giving rise to a crystallographic unit cell containing two Fe atoms and two Se atoms. The two Fe atoms are related by a glide-mirror symmetry, which can theoretically half the number of bands and allows for an unfolding to a 1-Fe Brillouin zone used by some authors [45], but here we use the 2-Fe unit cell notation for comparison with ARPES measurements.

The low energy electronic properties are governed by the partially-filled $3d_{xz}$, $3d_{yz}$ and $3d_{xy}$ orbitals of the two Fe atoms, which in momentum space gives rise to three hole bands around the Γ point and two symmetry-protected saddle point van-Hove singularities around the M point [46] as shown in **Figure 2A**.

Of the three hole bands, two exist as a C_4 symmetric pair exhibiting predominantly d_{xz} and d_{yz} orbital weight (labelled h_1 and h_2 in **Figure 2A**) and the third is dominated by d_{xy} orbital character (h_3). h_1 and h_2 would be energy degenerate at the high symmetry point, however spin orbit coupling lifts this degeneracy [47]. As for the van-Hove singularities around the M point, one is a saddle point connecting bands of majority d_{xz} and d_{yz} weight (vH_1) and the other is a saddle point connecting two d_{xy} dominated bands (vH_2). This general structure is broadly applicable to all $P4/nmm$ Fe-based superconductors (e.g., Fe(Te,Se,S), LiFeAs, NaFeAs, LaFeAsO), with some modifications for the 122 family due to the *I*-centering of the lattice.

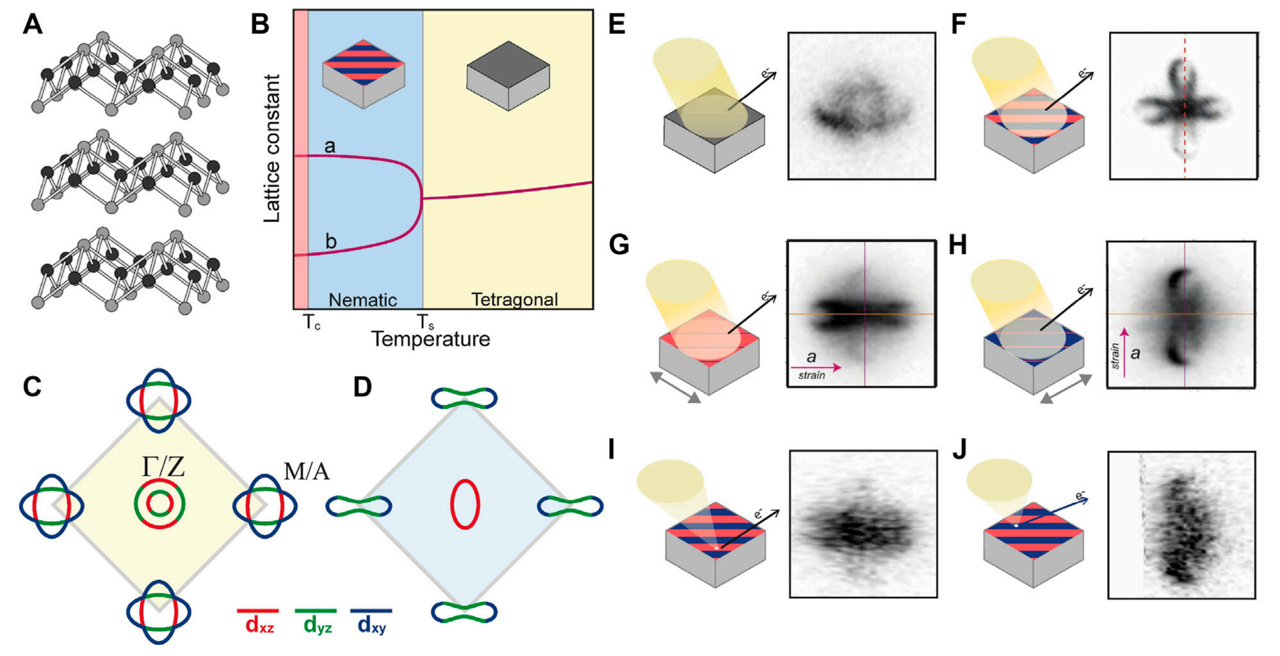

FIGURE 1 | Summary of the Fermi surface of FeSe and photoemission measurements of a single electron pocket. **(A)** Crystal structure of FeSe, Fe (black), Se (grey). **(B)** Sketch of the temperature evolution of the lattice constants in FeSe, as described in Ref. [44], highlighting the evolution from a tetragonal (dark grey surface) to orthorhombic system with differently orientated domains (red and blue striped surface). **(C)** Sketch of the experimentally determined Fermi surface of FeSe in the tetragonal state and **(D)** in the nematic state. **(E–J)** Summary of the Fermi surface of FeSe measured around the M/A point via different photoemission techniques. **(E)** Measurement in the tetragonal state (100 K, LV $h\nu = 56$ eV [32]) showing two electron pockets, **(F)** ARPES Measurement in the nematic state (10 K, LV, $h\nu = 56$ eV [32]) arising from a superposition of two orthorhombic domain orientations (red and blue regions), referred to as a "twinned" measurement. **(G,H)** ARPES measurement of a detwinned crystal in the nematic state (10 K, $h\nu = 56$ eV [34], where tensile strain is applied either along the *a* or *b* crystallographic axis and predominately probes a single domain orientation. **(I,J)** NanoARPES measurement using a photon beamspot of $< 1\ \mu m$ (30 K, $h\nu = 56$ eV [41]) in individual orthorhombic domains.

The experimentally measured Fermi surface of FeSe at 100 K (or more precisely, a map of the experimental spectral function at the chemical potential) at approximately $k_z = \pi$ is shown in **Figure 2B**, revealing a two-hole pocket and two electron pocket Fermi surface. Measurements around the center of the Brillouin zone show that both h_1 and h_2 cross the chemical potential at 100 K, as shown in **Figure 2C**. Their band maximas are separated by ~20 meV due to spin-orbit coupling [47–49]. At $k_z = 0$ these bands have a maxima at approximately $h_2 = -13\ meV$ and $h_1 = +7$ meV [48], and at $k_z = \pi$ (shown in **Figure 2C**) the bands have maxima of approximately $h_2 = +5\ meV$ and $h_1 = +30$ meV. The second smaller hole pocket of FeSe is thus only present at finite k_z, which highlights an important property of this system. Even though FeSe has a "quasi-2D" structure, i.e. the energy shift of the bands as a function of k_z is only on the order of 20 meV, this energy scale is actually on the same order of magnitude as the total Fermi energy of this system, and therefore is non-negligible in quantitative descriptions of the physical properties of FeSe. We note in passing that, due to the small Fermi energy of this system, the electronic structure is subject to substantial temperature-dependence of the chemical potential, and the appearance of the "Fermi surface" changes substantially between 100 and 300 K [50], although without any change of the symmetry.

The third d_{xy} hole band, h_3, is observed to be much flatter and cross both h_1 and h_2 at an energy of approximately −50 meV. In most ARPES data sets, this band has a much lower intensity than the h_1 and h_2 bands, which is a consequence of photoemission-based matrix element effects, which ensures the intensity of photoelectrons originating from d_{xy} states with momentum near $|\mathbf{k}| = 0$ will be suppressed [51]. Nevertheless, h_3 can be identified most clearly near where it hybridises with h_1 and h_2, and thus acquires some d_{xz} and d_{yz} orbital weight as shown in **Figure 2C**.

Near the corner of the Brillouin zone, both the d_{xy} dominated electron band, connected to vH_2, and the d_{xz}/d_{yz} electron band, connecting to vH_1, are observed to cross the Fermi level. Here the outer four-fold symmetric electron pocket is dominated by d_{xy} orbital character while the inner pocket is dominated by d_{xz} and d_{yz} orbital weight [52]. As this is a compensated system, the total Fermi volume of these electron pockets should be equal to that of the hole pockets [29].

These two sets of electron bands connect to the saddle points which have an energy of approximately $vH_1 = -20$ meV and $vH_2 = -40$ meV at the high symmetry point. The exact position of these stationary points, however, are masked by the presence of self-energy interactions which give rise to a broadening of the electronic states around the M point. This broadening is also captured in theoretical simulations involving spin and charge fluctuations [53].

The ARPES data presented in **Figure 2** is taken from our own works [29, 32], however multiple data sets are available in the literature and are all consistent with the interpretation presented here [26–28, 30, 33, 54]. Indeed, the electronic structure must be

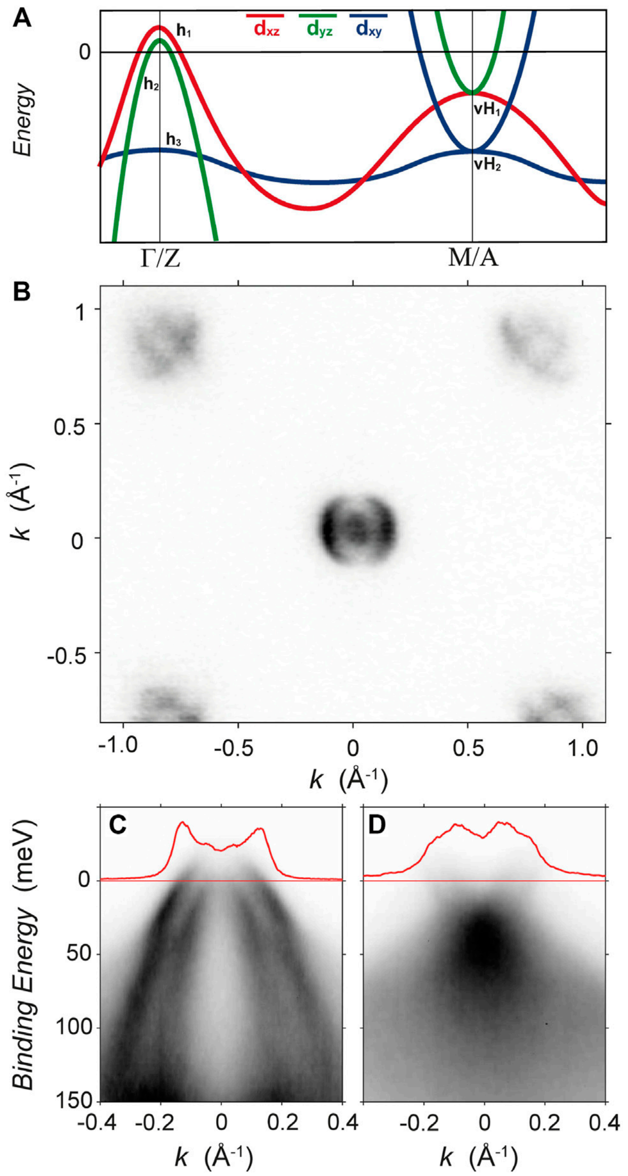

FIGURE 2 | Electronic structure in the tetragonal state of FeSe. **(A)** Sketch of the low-energy band structure of a typical *P*4/*nmm* Fe-based superconductor along the $\Gamma - M$ ($k_z = 0$) or $Z - A$ ($k_z = \pi$) high symmetry points. The colours indicate the dominant orbital character of the bands. **(B)** Fermi surface in the tetragonal state measured at 100 K close to $k_z = \pi$ ($h\nu$ = 56 eV). **(C)** Cut along the $Z - A$ direction (equivalent to $\Gamma - M$ but at $k_z = \pi$) direction for the hole bands around the Z point for the same photon energy ($h\nu$ = 56 eV). **(D)** Cut along the $Z - A$ direction for the electron bands around the A point. Figures adapted from [29, 32].

constrained by the symmetry based arguments of **Figure 2A** [46, 52, 55] and each of the bands observed in the measurements can be mapped to corresponding bands calculated from *ab-initio* techniques such as density functional theory (DFT) [26, 29, 52] of the paramagnetic tetragonal phase.

There are, however, serious quantitative issues with DFT-based calculations, which severely limit its use in describing the low energy properties of FeSe. First, DFT-based calculations overestimate the bandwidth of the Fe 3*d*-bands by a factor of ~3 [29, 56]. This is a generic finding across all Fe-based superconductors [57], and derives from the fact that electronic correlations are inadequately treated in DFT. It has been often argued that the correlation effects are orbital-dependent and particularly strong for the d_{xy} orbital [29, 57, 58]. More advanced theoretical simulations, such as DFT + DMFT [59] and QSGW + DMFT [53], have had some success in capturing the global electronic structure on the eV scale [59, 60], finding strongly incoherent spectral weight at 1–3 eV below E_F and sharp quasiparticles only in the near vicinity of E_F. However *ab-initio* efforts still usually overestimate the size of the hole and electron Fermi surfaces, which are much smaller in experiment [29, 59]. Most DFT-based simulations additionally predict that the d_{xy} hole band also crosses the Fermi level, suggesting a three hole pocket and two electron pocket Fermi surface [29, 52]. Finally, typical DFT-based calculations also suggest that a stripe or staggered-stripe antiferromagnetic ground state is the most stable configuration [57, 61], when in reality FeSe remains paramagnetic (albeit with strong antiferromagnetic fluctuations [62–64]). Current research is attempting to resolve this discrepancy from a pure *ab-initio* perspective. Wang. *et. al.* [64] were able to reproduce the band structure around the Gamma point using a polymorphus network of local structural distortions. The use of hybrid exchange correlation functionals and Hubbard-Hund correlations have recently been shown to also produce a substantial improvement on the tetragonal structure [65].

Due to the current limitations in *ab-initio* modelling however, a substantial amount of work has gone into developing quantitatively accurate tight binding models of FeSe [8, 50, 52, 66, 67]. These models bypass the limitations in our current *ab-initio* theories, allowing for an accurate, albeit phenomenological, description of the single-particle electronic structure to be defined, which we can compare with experimental measurements. Several hopping parameters sets have been developed, which have been obtained by directly comparing the numerical band dispersion with experimental ARPES data in the tetragonal state [21, 50, 66, 67]. These models have been shown to reproduce the single-particle electronic properties of tetragonal FeSe much better than conventional DFT-based approaches [50, 52, 66]. In particular these models accurately capture the small Fermi energy of FeSe, which has been shown to lead to strong chemical potential renormalising effects as a function of temperature and nematic ordering [33, 50, 68–70]. By construction, such models allow for a quantitative description of the band positions of the hole and electron bands such that a comparison of the electronic structure in the nematic state can take place.

3 EXPERIMENTAL EVIDENCE FOR A MISSING ELECTRON POCKET IN THE NEMATIC STATE

We now focus on the electronic structure in the nematic state. Here experimental measurements encounter a major challenge.

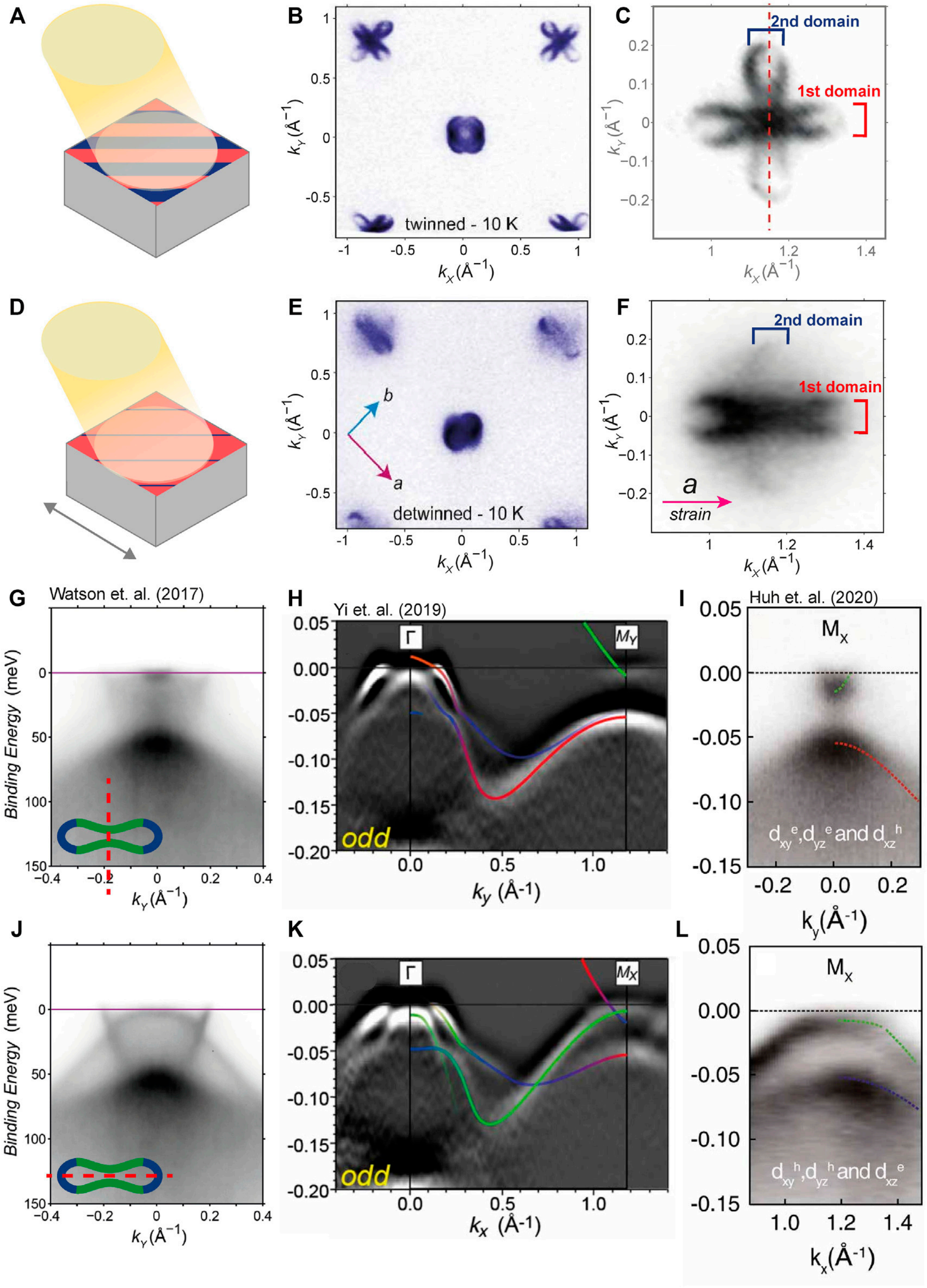

FIGURE 3 | Summary of ARPES measurements on FeSe in the nematic state. **(A)** Sketch of a photoemission setup on a twinned crystal, showing equal coverage of both red and blue orthorhombic domains. **(B)** Fermi surface measured from a measurement on a twinned crystal ($h\nu = 56$ eV). Taken from Watson *et. al.* [34] **(C)** Close up of the electron pocket near the A point from Watson *et. al.* [32] ($h\nu = 56$ eV). **(D–F)** Equivalent sketch and measurement for a detwinned crystal of FeSe, which probes a majority of orthorhombic domains aligned in one direction. **(G)** Band dispersion of a detwinned crystal centered at the electron pocket. The insert shows the band

(Continued)

FIGURE 3 | path, from Watson *et. al.* [34]. **(H)** Second derivative band dispersions of a detwinned crystal along the same path as **(G)** but extended from Z to A, taken from Yi. *et. al.* [35]. **(I)** Band dispersion of a detwinned crystal along the same path as **(G)** from Huh. *et. al.* [36]. **(J–L)** Equivalent measurements but taken along the length of the electron pocket. **(H,K)** reproduced from Ref. [35] under the Creative Commons Attribution 4.0 International License. **(I,J)** reproduced from Ref. [36] under the Creative Commons Attribution 4.0 International License.

The nematic state is accompanied by a tetragonal to orthorhombic structural transition, at which point multiple orthorhombic domains form in the crystal. It has been identified that these domains are typically on the order of 1–5 μm in size [41, 71–73], which is much smaller than the cross section of the photon beam used in most high resolution synchrotron-based ARPES measurements ($>50\mu$m [74]), as sketched in **Figure 3A**. Most of the initial photoemission data of FeSe in the nematic phase was collected on "twinned" crystals. In such measurements, the band dispersion measured along the experimental k_x axis contains contributions from domains with the orthorhombic a axis both along, or perpendicular to, this direction, i.e. one measures a superposition of the spectral function arising from both domains. This creates an apparent C_4 symmetry in the measurements even at low temperatures (in the sense that the measured spectra are invariant under 90° rotation of the sample; the as-measured spectra are not generally fourfold-symmetric due to the ARPES matrix elements [75, 76]). This can lead to ambiguity about which band arises from which domain.

3.1 ARPES Measurements on Twinned Crystals

Multiple ARPES measurements on twinned crystals of FeSe have been reported [19, 20, 26–32, 54, 68, 77] and have been extensively reviewed [1, 10, 33, 78]. We present a representative Fermi surface obtained from a twinned crystal in **Figure 3B** from Ref. [32]. The hole pockets appear as two overlapping ellipses. Meanwhile, at the corner of the Brillouin zone, measurements reveal two electron pockets, which have been pinched in to produce what looks like two overlapping "peanuts".

The challenge now lies in identifying which of these pockets, comes from which domain. The two hole pockets can be easily understood as one ellipse from each orthorhombic domain. Measurements of the band dispersion around the hole pocket reveal that the inner hole band (h_2) undergoes a Lifshitz transition as a function of temperature and resides below the Fermi level at 10 K, whilst the outer hole band (h_1) elongates into an elliptical shape. As all three hole bands can be tracked as a function of temperature from the tetragonal to nematic state, there is little ambiguity about the shape of the hole pocket Fermi surface at low temperatures. However, it is not possible to identify the orientation of the elliptical hole pocket from a single domain, i.e. to identify whether it elongates along the orthorhombic a or b axis simply from these twinned measurements.

For the electron pocket, however, the understanding was less clear, and historically several distinct band structures have been interpreted from nearly identical data sets [19, 20, 29, 30, 32]. As can be seen in **Figure 3C**, two electron pockets can be observed which look like overlapping "peanuts" in the twinned data. As the tetragonal state also exhibits two electron pockets, this may not appear that surprising. Indeed one interpretation was that the two oval shaped electron pockets in the tetragonal state simply pinched in at the sides, due to raising the binding energy of vH_1 [26, 32]. In other words, the electron pockets could retain approximate fourfold symmetry around the M point, and the pockets from each domain simply overlapped in twinned data sets [20]. However, other interpretations, particularly those attempting to understand the nematic band shifts from theoretical grounds, believed that the nematic state should have two differently shaped electron pockets [29, 30]. It was also equally plausible, experimentally at least, that only one electron pocket existed per domain [19, 28, 34]. Distinguishing between these scenarios was particularly challenging due to the broadness of the spectral weight around the M point in the tetragonal state (see **Figure 2D**), which made a precise interpretation of the temperature evolution of the two van-Hove singularities ambiguous.

3.2 ARPES Measurements on Detwinned Crystals

Compared to the measurements on twinned data, a much more preferable method to study the Fermi surface of FeSe would be to experimentally overcome the limitation imposed by these orthorhombic domains, and directly measure the electronic structure from a single crystallographic orientation. There are two strategies to overcome the twinning issue faced by ARPES measurements. Either 1) generate a sample with macroscopic ordering of the orthorhombic domains on length scales larger than the photon beam cross section, or 2) make the photon beam much smaller than the size of an orthorhombic domain. It has been known from earlier work on the 122 family of Fe-based superconductors that upon the application of "uniaxial" strain along the Fe-Fe direction, it becomes energetically favourable for a majority of the orthorhombic domains to align along that axis [79]. While the resulting domain population is unlikely to be 100% pure, measurements on strained, or "detwinned", samples, as sketched in **Figure 3D**, allows one to distinguish between the intense spectral weight arising from the majority domain and the weak spectral weight arising from the 90° rotated minority domain.

The first ARPES measurements on uniaxial strained samples of FeSe were performed in 2014 by Shimojima et. al. [28], where it was shown that the single hole pocket was elongated along the k_y axis. Later, in 2017, Watson *et. al.* [34] was additionally able to resolve the detail of the electron pockets, as shown in **Figure 3E**. These measurements on detwinned crystals confirmed that the Fermi surface consisted of one elliptical hole-pocket, as expected from interpretation of the twinned measurements, but additionally revealed only one electron-pocket around the M point. This is shown in **Figure 3F**, where the majority of the spectral weight intensity now comes from one domain, and only a weak residual intensity comes from the minority domain. Unlike in the tetragonal state, at low temperatures, the electronic band structure around the M point produces sharp quasiparticle bands, a saddle point can be observed at −5 meV, which is electron like along the minor length of the electron pocket (as shown in **Figure 3G**), but hole-like when rotated by 90° (**Figure 3J**). Additionally, along the major length of the electron pocket, a deeper electron band and saddle point at ~ − 60 meV can be observed. This gap between the upper and lower saddle points, is approximately 50 meV, and has been previously quoted as a "nematic energy scale" [29, 35, 39]. However, as we will discuss in the theoretical section below, the exact energy scale of nematic shifts and splittings is slightly more complex and requires a linear combination of order parameters of different energy scales [67].

This finding of only a single electron pocket at the Fermi level was not the expected theoretical result [66], but nevertheless Yi *et. al.* [35] and Huh *et. al.* [36] have since then reported additional measurements on detwinned crystals of FeSe, with a slightly larger degree of detwinning than what was achieved by Watson *et. al.*. These measurements further confirmed that the residual intensity observed in **Figure 3G** was due to the minority orthorhombic domain, which is nearly absent in **Figures 3H,I**. Further measurements on sulphur doped $\mathrm{FeSe}_{1-x}\mathrm{S}_x$ crystals under uniaxial strain by Cai *et. al.* [37, 38] have also reported very similar Fermi surfaces.

Polarised light analysis of the matrix elements of FeSe has also been used to identify the orbital content of the bands. If one uses Linear Vertical polarised light (LV also known as odd, or *s*-polarised light) and measures through the M point parallel to k_y as in **Figures 3G–I**, only bands with orbital character symmetric to the *yz* plane of the crystal should be detected [51]. Hence the electron-like dispersion with a very small k_F (i.e., the narrow part of the peanut-shaped pocket) is identified as having d_{yz} orbital character. Similarly, if one uses the same LV polarised light but with the sample rotated by 90°, as was performed **Figures 3J–l**), the orbital characters that will be detected will be antisymmetric with respect to the *xz* plane, which along the momentum dispersion shown in **Figures 3J–l**) is true for both the d_{yz} orbital and the d_{xy} orbital [51]. From this logic, the larger deeper electron dispersion that has a minima around − 50 meV, is attributed to d_{xy} orbital character. Equally the hole-like dispersion that has a maxima near the Fermi level and is a saddle point connecting to the electron-like dispersion in **Figures 3G–I** has been identified as having d_{yz} orbital weight. In both orientations, the most intense contribution is a broad feature located at − 60 meV. From comparison with theoretical models, this band is likely to have a mixture of d_{xz} and d_{xy} orbital character, although the precise identification remains challenging. As well as these polarisation-based arguments, one can also assign the orbital character of the bands based on comparison to DFT or tight-binding calculations, at least in the tetragonal phase.

3.3 Temperature Dependence ARPES Measurements of the Electron Pocket

So far we have only discussed the electronic structure of FeSe at either high temperature (e.g., 100 K, where two electron pockets exists) or low temperature (e.g., 10 K, where only one electron pocket exists). However, a natural question to ask is how does the electronic structure of the electron pockets evolve as a function of temperature? In principle, this data should be able to identify the mechanism responsible for the removal of an electron pocket at the Fermi level. Many temperature dependent studies on twinned samples exist (e.g., [26–32, 54, 68, 77] and reviewed e.g., by Coldea and Watson [33]), but due to the complication of orthorhombic domains as well as the broadness of the spectral weight around the M point at high temperatures, there was no obvious signature of the disappearance of an electron pocket in such data sets. To illustrate this, we present a representative temperature-dependent data set on twinned crystals, taken from Ref. [32], in **Figures 4A–D**. The evolution of these bands from twinned data has been interpreted in different ways by different groups over the years, with a key feature being the appearance of a 50 meV energy scale at the M point, emerging from a broadened "blob" at higher temperatures. Some manuscripts have claimed that the 50 meV energy scale directly corresponds to lifting of the d_{xz}/d_{yz} degeneracy [27–30], which was claimed to be consistent with earlier theoretical interpretations [9]. However other analysis [26, 32, 33] instead found an increase in the separation of the two van Hove singularities, from 20 to 50 meV, in which case the 50 meV scale is linked to nematicity but not a direct probe of $d_{xz} - d_{yz}$ splitting. However both of these interpretations would imply a ground stat Fermi surface consisting of two electron pockets, in disagreement with the experimental results.

More recently, technically challenging temperature dependent measurements on detwinned crystals have been accomplished. This highly necessary data ensures that the bands are easier to track than those taken on twinned samples. Huh *et. al.* [36] have measured the temperature dependent evolution of the detwinned ARPES measurements around the A point (**Figure 4G**), which shows the formation of clear sharp quasiparticle bands corresponding to one electron pocket, emerging from the high temperature phase with two electron pockets and much broader features. It was argued that this data was consistent with a Lifshitz transition of a second electron pocket as a function of temperature.

Yi *et. al,* [35] performed a detailed analysis of the momentum distribution curves along the major axis of the electron pocket as a function of temperature, both at the Fermi level and 10 meV above it (**Figures 4E,F**). In principle, this analysis enables the identification of any Lifshitz transitions as a function of temperature. Focusing on the data at + 10 meV in **Figure 4F**, they observe a reduction in the k_F for an inner electron band, which appears to close at around 60 K, indicating that this band becomes completely unoccupied and therefore not observed at low temperatures. This is the most compelling data so far in support of a Lifshitz transition of the electron pocket as a function of temperature.

This evidence for a Lifshitz transition has however been challenged by Cai *et. al.* [38] who reported temperature dependent Fermi surface measurements of the electron pocket for detwinned crystals of 9% sulphur-substituted FeSe, as shown in **Figure 4H**. They claim that the spectral weight of the second

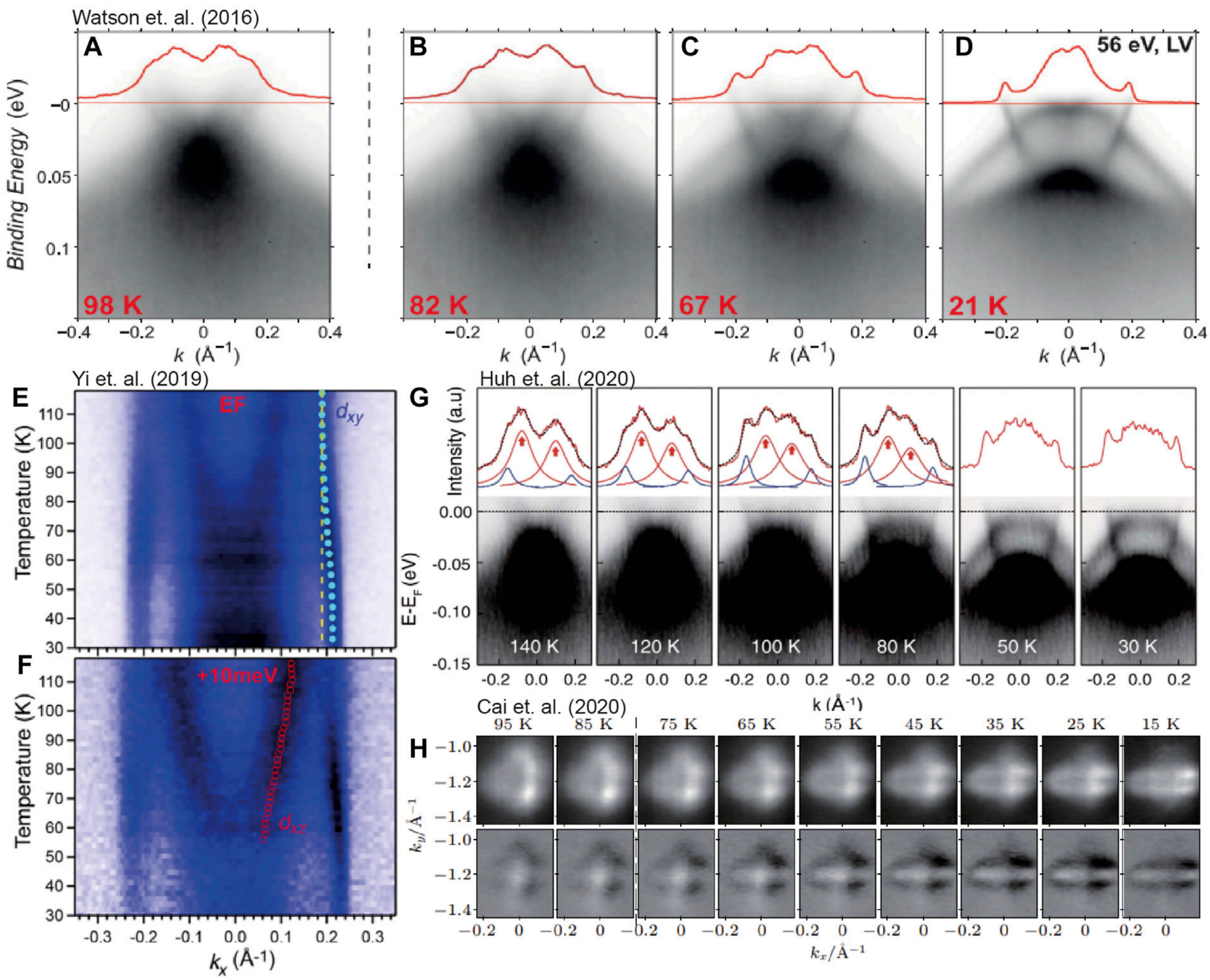

FIGURE 4 | Summary of the temperature dependent ARPES measurements of the electron pocket of FeSe **(A–D)** measurements from twinned crystals of the electron bands near the A point ($h\nu$ = 56 eV), as a function of temperature, taken from Watson *et. al.* [32]. **(E,F)** Spectral intensity at the Fermi energy **(E)** and 10 meV above the Fermi energy **(F)**, as a function of temperature on a detwinned crystal of FeSe, taken from Yi *et. al.* [35]. **(G)** Temperature dependence of the bands near the A point ($h\nu$ = 56 eV) for a detwinned crystal of FeSe, taken from Huh *et. al.* [36]. **(H)** Fermi surface maps as a function of temperature on detwinned crystals of 9% Sulphur doped FeSe, taken from Cai *et. al.* [38]. **(E,F)** reproduced from Ref. [35] under the Creative Commons Attribution 4.0 International License. **(G)** reproduced from Ref. [36] under the Creative Commons Attribution 4.0 International License. **(H)** Reproduced from Ref. [38] with permission from Chinese Physics B.

electron pocket simply decreases in intensity, rather than moving above the Fermi level. This would be indicative of a more complex, self energy evolution, rather than a single-particle Lifshitz transition.

We conclude by noting that the analysis of data, even for detwinned samples, remains challenging. The k_F magnitudes and energy separation of bands are small, challenging the resolution of ARPES instrumentation, and the spectral broadening at high temperatures and deeper energies frustrates the clear identification of the bands at around the M point. While performing the temperature-dependent measurements on detwinned samples, such measurements come with numerous complications, such as temperature-dependent domain populations and spectral contribution from the minority domain. Moreover it is known that samples with over 90% detwinning may experience changes to the underlying electronic properties [80, 81], which may be a concern if strain is altered as a function of temperature. However in our view the results obtained by Yi *et. al,* [35] make an important contribution by detecting a Lifshitz transition, which would be impossible to determine from twinned data alone, and which provides a plausible route between the two-electron Fermi surface at high temperature and the one-electron pocket Fermi surface in the ground state.

3.4 NanoARPES

There are experimental complications with performing ARPES measurements on uniaxially strained crystals, which may leave doubt as to the validity of the conclusions presented above. First, it is hard to fully exclude if the application of uniaxial strain has actually perturbed the underlying electronic structure of the crystal you are measuring. For example in the tetragonal

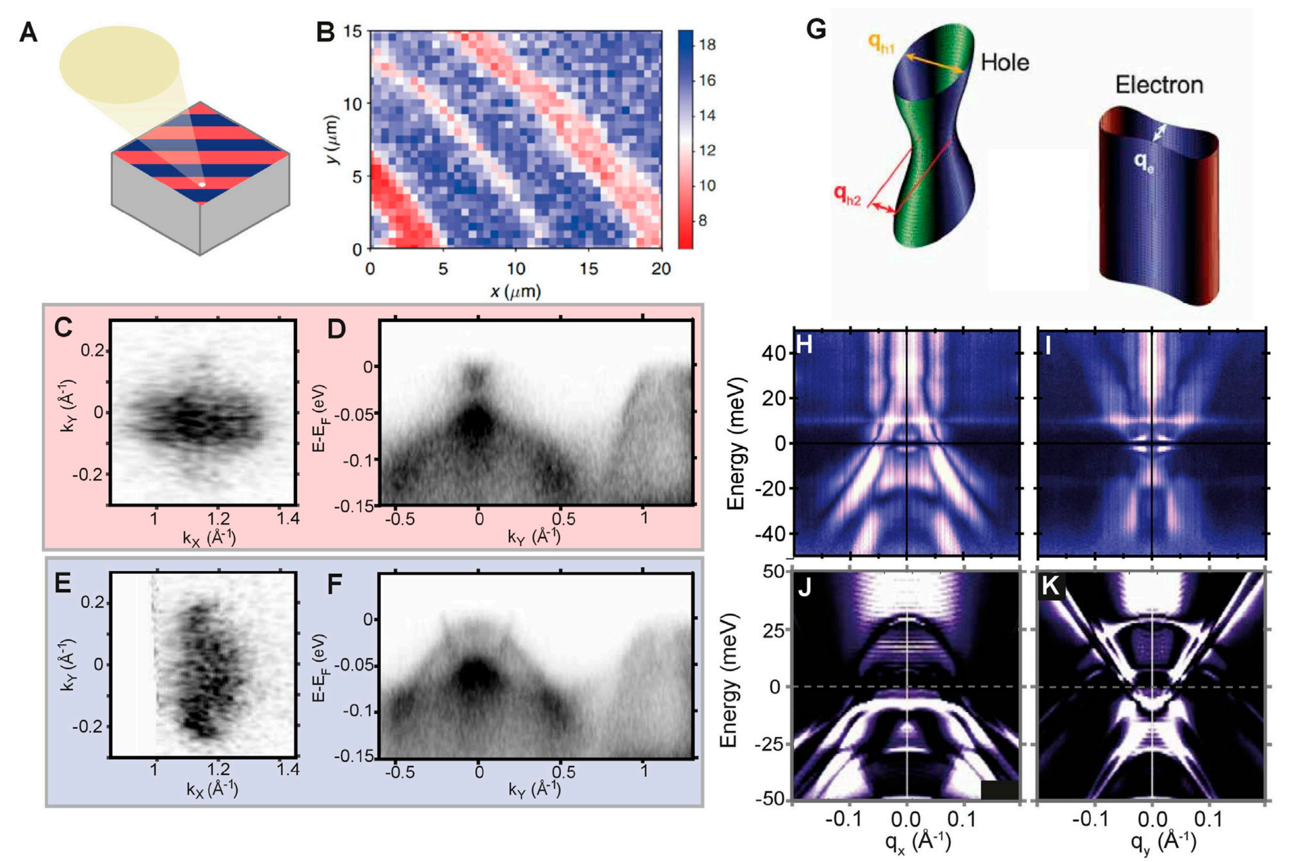

FIGURE 5 | Electronic structure within a single domain without the application of uniaxial strain. **(A)** Sketch of a NanoARPES measurement, where the beam is focused to have a cross section < 1μm. **(B)** Experimental spatial map of FeSe where the colour corresponds to the orthorhombic domains of FeSe, reproduced from Ref. [41]. **(C,D)** Fermi surface around the electron pocket ($h\nu$ = 56 eV, 30 K) and $A_y - Z$ cut taken within a single orthorhombic domain [41]. **(E,F)** Fermi surface around the electron pocket and $A_y - Z$ cut taken in an adjacent orthorhombic domain [41]. **(G)** Sketch of the Fermi surface scattering vectors inferred from STM measurements, as suggested by Ref. [42]. **(H,I)** STM measurements of the QPI scattering dispersions as a function of energy along the q_x and q_y high symmetry axes respectively, reproduced from Ref. [42]. **(J,K)** Simulated QPI scattering dispersion from a model of FeSe which described the band structure shown in **Figure 3**, from Ref. [82]. **(G–I)** are reproduced under the Creative Commons Attribution 4.0 International License.

material Sr_2RuO_4, uniaxial strain on the order of 1% shifts the position of the vHs by nearly 20 meV [83]. In order to fully support the conclusions from these ARPES measurements on detwinned crystals, complementary techniques must be employed and their results compared. To this end, nanoARPES has also been performed on crystals of FeSe. In these technically demanding measurements, the photon beam is focused to sub-micrometer spatial resolution using a focusing optic close to the sample [84]. The reduction of the spot size comes at the cost of dramatically reducing the photon flux, and thus the energy and angular resolutions are typically relaxed (compared to the earlier high-resolution results presented) in order to have a reasonable signal of photoelectrons. Nevertheless, the technique has been improved over the past 10 years to allow for energy resolution better than 20 meV [85]. This sub-micrometer spot size is smaller than a single orthorhombic domain, allowing for a spatial map of the sample from which the two orthorhombic domains can be distinguished by analysing their differing ARPES spectra, shown as red and blue stripes in **Figures 5A,B**. Measurements of the Fermi surface and band dispersion around the electron pocket in both domains (**Figures 5C–F**) reveal an electronic structure totally consistent with that extracted from the ARPES measurements under uniaxial strain. In summary, the nanoARPES results fully support the conclusion of a Fermi surface in the nematic state consisting of a single hole pocket and a single electron pocket.

3.5 STM Measurements

An entirely independent method to study the momentum resolved electronic structure within a single domain is to use scanning tunneling microscopy (STM). STM utilises quantum tunnelling, between the surface of a material and an atomically sharp tip, to study the electronic structure on the sub-nanometer scale. Information about the electronic structure can then be extracted in two ways. The first is by studying the differential conductance (dI/dV) to obtain a quantity proportional to the local density of states of the system. The second is to measure quasiparticle interference (QPI), to measure the perturbations to the local density of states generated by the presence of defects such as impurities or atomic vacancies. The wavelength associated with this perturbation contains direct information about the allowed momentum dependent scattering vectors associated with an electronic structure at a constant energy via $\mathbf{q} = \mathbf{k} - \mathbf{k}'$.

Multiple STM measurements have been reported for FeSe, and information regarding the nematic [14, 15, 43] and superconducting state [14, 15, 42, 86] have been determined, tetragonal state information has also been obtained from studies of isoelectronic sulphur doped crystals [42]. These measurements all contain a plethora of information regarding the local structure of the surface of FeSe, as well as information on defects [87, 88]. Here, however, we focus on what the STM measurements can tell us about the low energy electronic structure in the nematic state, and whether this is consistent with the ARPES measurements discussed above. Although measuring QPI is an indirect method to measuring the electronic structure of a material, it is particularly powerful in determining band minimas and maximas, especially above the Fermi level, as well identifying whether bands have hole or electron scattering characteristics within a certain energy range.

The scattering vector vs. energy dispersion along the q_x and q_y directions, taken from Ref. [42], are presented in **Figures 5H,I**. In agreement with other data sets [14, 43], several hole-like scattering vectors can be observed predominately along the q_x axis, with a narrower hole-like dispersion along the q_y direction. Also along the q_y axis, one very clear electron-like scattering vector can be detected, which has a minima at ∼ − 5 meV, and has been identified as a scattering vector that connects the d_{yz} parts of the electron pocket in FeSe (**Figure 5G**) [14, 42, 43, 82]. No corresponding electron-like dispersion can be observed along the q_x direction, which should be the case in a two electron pocket scenario where all bands scatter equally. This was therefore interpreted as further evidence, from an independent technique to ARPES, that the Fermi surface of FeSe only consists of one hole pocket and one electron pocket, as sketched in **Figure 5G**.

We note that due to the indirect nature of QPI measurements, there is a degree of interpretation and uncertainty about the assignment of the electronic states and often it is necessary to directly simulate the QPI dispersion from a theoretical assumption of the electronic structure and compare the agreement. Due to the intrinsic broadness of the experimentally measured scattering vectors, this can lead to differing conclusions based on initial assumptions. For example, Kostin *et. al.* [43], assuming that two electron pockets must be present at the Fermi level, interpreted a weak spectral feature as evidence for a second electron pocket, with a greatly reduced scattering intensity. Whereas Rhodes *et. al.* [82], assuming that only one electron pocket was present at the Fermi level, interpreted this weak feature as an artifact of the Feenstra function, used in the experimental processing [89]. Importantly however, both theoretical simulations agree that a Fermi surface consisting of one hole pocket and two electron pockets can not independently reproduce the observed data without some additional form of anisotropy, which implies that ARPES and STM are probing the same underlying electronic structure. We present the numerical simulations from Ref. [82] in **Figures 5J,K**.

As an aside, it is interesting to note that the hole band maxima in 5(h) extends to + 25 meV [42]. It is known from ARPES that only one hole-like scattering vector at this energy can exist, and specifically must be generated by the $k_z = \pi$ states [33]. This reveals that QPI measurements are sensitive to states with different k_z. From arguments about the group velocity of electrons scattering off of defects [90, 91], and the short range nature of quantum tunneling, it actually implies that QPI measurements will exhibit a k_z-selectivity rule [82], such that all stationary points along the k_z axis will contribute to scattering vectors that will be detected by STM measurements, this has recently been realised in the fully 3D system, PbS [92].

3.6 Points of Contention

While we have so far presented a unified picture of the electronic structure of FeSe and have focused on points where broad agreement is found in the recent literature, historically there have been many points of disagreement surrounding the identification of bands and the nature of the Fermi surface, and there remain some points of contention.

Regarding the hole pockets, an outlying report is a recent claim from laser-ARPES measurements that there is additional splitting, most prominently resulting in two hole pockets at the Fermi level instead of one [93]. The implication is that the Kramer's degeneracy of the bands is lifted, i.e., that either time-reversal or inversion symmetry is broken. However, it is worth noting that at low photon energies used the k_z is not well-defined as the final states are not free electron-like, and the two Fermi contours identified appear to be fairly close to the known Fermi contours at $k_z = 0$ and $k_z = \pi$. Moreover, synchrotron-ARPES measurements with equally high energy resolution and better angular resolution (due to better definition of k_z) do not identify any additional splitting either in the Γ or Z planes [19], and neither has any comparable splitting been observed for the electron pockets. Finally, there is no supporting evidence for time-reversal symmetry breaking from other techniques. Thus it remains our view that the Kramer's degeneracy holds for all states and that there is only one hole pocket crossing EF, which is significantly warped along the k_z axis.

Regarding the electron pockets, while several groups have now coalesced around the one electron pocket scenario, it has previously been claimed that the ARPES data on twinned crystals is consistent with four features in the EDC at the M point [26] such that there are two electron pockets per domain, with each domain contributing a pair of crossed peanuts with slightly differing shapes [20]. This scenario is perhaps the most natural, as it is based on DFT predictions, and comes down to somewhat technical questions of whether asymmetric lineshapes at the M point contain one or two peaks, and whether the proposed small splittings can be resolved. Some of this groups data on twinned samples does indeed seem to show a splitting, which at face value would support their scenario. However, neither our group nor other groups have observed these claimed features and peak splittings in comparable data on twinned samples. Moreover, the detwinned data shows a

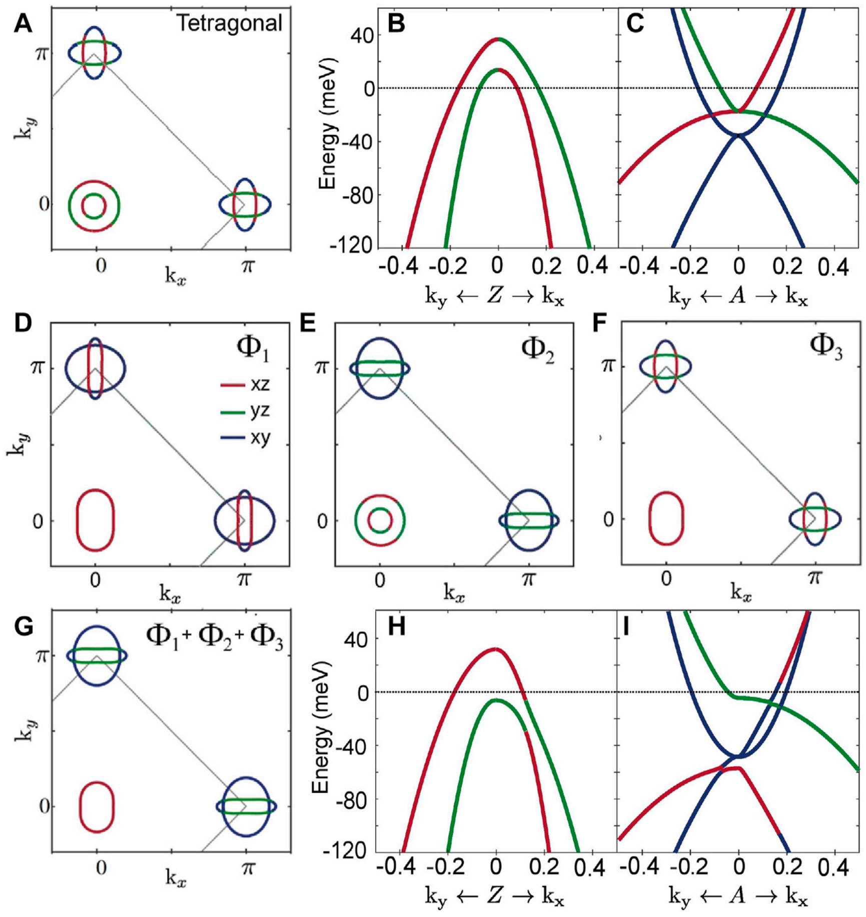

FIGURE 6 | Limitations of d_{xz}/d_{yz} nematic ordering and origin of the missing electron pocket problem. **(A,B,C)** Fermi surface and band dispersions around the Z and A point, for a tetragonal state model of the electronic structure from Ref. [67] in quantitative agreement with ARPES measurements. **(D,E,F)** The individual effect of the three symmetry breaking $d_{xz/yz}$ nematic order terms on the Fermi surface of the tetragonal state model. **(D)** Ferro orbital order (Φ_1 = 26 meV) **(E)** d-wave bond order (Φ_2 = −26 meV) **(F)** Extended s-wave bond order (Φ_3 = 15 meV). **(G,H,I)** Fermi surface and band dispersions around the Z and A point, using a combination of Φ_1, Φ_2 and Φ_3 as is often used in the literature. No matter what linear combination of these order parameters are used, a Fermi surface in agreement with the experimental data can not be produced.

complete absence of any spectral weight aside from the peanut along the *a* direction, in multiple experimental geometries, which cannot easily be explained away by matrix element effects in ARPES (and similarly in QPI). We encourage all groups to continue to push for higher resolution data which could finally settle the controversy, especially on detwinned samples.

4 THEORETICAL EXPLANATIONS FOR THE MISSING ELECTRON POCKET

As we have discussed, the low energy electronic structure of the tetragonal state of FeSe can be qualitatively understood just from symmetry based arguments regarding the crystal structure and the d_{xz}, d_{yz} and d_{xy} orbitals of the Fe atoms. This band structure can be explained both from the framework of tight-binding modelling [8, 50, 52, 66] as well as DFT-based simulations. All of this implies that, although a true quantitative explanation describing the renormalisation of the band structure from correlation effects may be missing, our understanding of the single-particle physics is complete.

Within the nematic state, however, this is not the case. Following the previous logic, it would be assumed that the orthorhombic distortion produces a negligible change to the electronic structure, such that two hole pockets and two electron pockets should be present in the nematic state, which as the experimental data has revealed is clearly not the case. It is for this reason that the nematic state is believed to be of electronic or magnetic origin, yet the microscopic details still remain unclear. To address this, there has been a great deal of focus on trying to model how the nematic state evolves the electronic structure of a tetragonal-based model of FeSe, such as that shown in **Figures 6A–C** originally presented in Ref. [67]. Specifically, theoretical research has attempted to develop a nematic order parameter which.

- Lowers the symmetry from C_4 to C_2 whilst still preserving mirror symmetry.
- Generates an elliptical hole pocket dominated by d_{xz} orbital weight.
- Removes one of the two electron pockets from the Fermi surface.

Historically, the first attempt to describe such a mechanism assumed that the C_4 symmetry breaking was governed by a lifting of the energy degeneracy of the d_{xz} and d_{yz} orbitals [94].

$$\Phi_1\left(n_{xz} - n_{yz}\right), \tag{1}$$

where $n_{xz/yz} = c^{\dagger}_{A,xz/yz} c_{A,xz/yz} + c^{\dagger}_{B,xz/yz} c_{B,xz/yz}$ is the number operator for the *xz* or *yz* orbital respectively on atom *A* and *B* in a two atom unit cell model of FeSe, and Φ_1 is a scalar value used to describe the magnitude of the nematic order, which can in principle be fit to experiment.

This term, referred to in the literature as ferro-orbital ordering, is the simplest form of C_4 symmetry breaking possible in this system. It acts in a momentum independent fashion to raise the binding energy of the d_{xz} bands and lower the binding energy of the d_{yz} band, similar to a Jahn-teller distortion [95]. In this scenario, the electronic structure would evolve to produce a Fermi surface as shown in **Figure 6D**, which despite producing the correct elliptical hole pocket, does not generate the one-electron-pocket Fermi surface determined from experiment.

Following the train of thought that the phenomenology of the nematic state may be captured by a degeneracy breaking of the d_{xz} and d_{yz} states, it was also noted that there are two additional B_{1g} symmetry breaking terms that can be defined and are equally valid in the nematic state [55, 66].

$$\Phi_2\left(n'_{xz} + n'_{yz}\right)\left(\cos(k_x) - \cos\left(k_y\right)\right) \tag{2}$$

$$\Phi_3\left(n'_{xz} - n'_{yz}\right)\left(\cos(k_x) + \cos\left(k_y\right)\right) \tag{3}$$

Here, $n'_{xz/yz} = c^{\dagger}_{A,xz/yz} c_{B,xz/yz} + c^{\dagger}_{B,xz/yz} c_{A,xz/yz}$ describes a hopping from an *xz* or *yz* orbital on atom *A* (*B*) to a *xz* or *yz* orbital on atom *B* (*A*). These two terms, referred to as d-wave nematic bond order (Φ_2) and extended-s wave bond order (Φ_3) respectively, in combination with the ferro orbital order (Φ_1) are the only possible nematic order parameters that can be defined for the d_{xz} and d_{yz} orbitals up to nearest neighbour hopping [55], and have been extensively used in previous theoretical descriptions of the nematic state of FeSe [15, 18, 19, 23, 24, 32, 43, 82, 96–104]. The individual consequences of these order parameters are shown in **Figures 6E,F**.

However, despite this vast amount of literature assuming these three d_{xz}/d_{yz} nematic order parameters as the starting point for theoretical analysis, there lies one big problem. No matter what values of Φ_1, Φ_2 and Φ_3 are chosen, a Fermi surface consisting of one hole pocket and a single electron pocket can not be produced, at least not starting from a quantitatively accurate ARPES-based model of FeSe in the tetragonal state [67]. The best attempts to describe the ARPES data within this limitation result in a Fermi surface consisting of the correct elliptical hole pocket, a first electron pocket, of correct shape and size, and a second large electron pocket, dominated by d_{xy} orbital character, as shown in **Figures 6G–I**.

There is no experimental evidence for this large second electron pocket in the nematic state, and this discrepancy between theory and experiment has posed a major challenge for our theoretical understanding of nematicity. This is the central origin of the missing electron pocket problem. It has now become clear that a theory of nematicity only involving the physics captured in **Eqs 1–3**, i.e., nematicity derived solely from d_{xz} and d_{yz} orbital ordering, is insufficient to reproduce our experimental measurements, and additional explanations for this discrepancy have had to be developed.

4.1 Orbital Selective Quasiparticle Weights

The earliest attempt to explain this discrepancy came from attempts to understand local spin fluctuations in tetragonal FeSe, such as those incorporated by DFT + dynamic mean field theory (DMFT). Within this framework it has been shown that the self-consistently determined quasiparticle weight (*Z*) of the d_{xy} orbital was significantly smaller than the quasiparticle weight of the $d_{xz/yz}$ orbitals [53, 57, 105], approximately half. As the spectral function intensity measured by ARPES is directly proportional to the quasiparticle weight, the contribution of d_{xy} dominated bands should be significantly reduced, compared to the d_{xz} and d_{yz} dominated bands in ARPES measurements. It was thus argued that ARPES measurements may not be able to observe the d_{xy} orbital, and thus would not detect the second d_{xy} dominated electron pocket in the nematic state, e.g., in Ref. [100], shown in **Figures 7A,B**.

This argument, however, is not supported by experimental measurements. Both in the tetragonal and nematic state, bands of d_{xy} orbital character have been identified, particularly around the M point [33]. And although it is true that the d_{xy} orbital appears to exhibit a larger effective mass renormalisation than the d_{xz} and d_{yz} orbitals [29], this extra renormalisation appears to not be enough to mask d_{xy} spectral weight from ARPES-based measurements.

A similar, more phenomenological, approach was later employed by Kreisel *et. al.* [21] and popularised by Sprau *et. al.* [15]. Here the values of the nematic order parameters ($\Phi_1 - \Phi_3$) were adjusted such that two similar shaped electron pockets were generated (**Figure 7D**), one dominated by d_{xz} orbital weight and one dominated by d_{yz} orbital weight, with the tips retaining significant d_{xy} orbital character. Specifically, starting from an ARPES-based tetragonal model of FeSe [21] values of Φ_1 = 9.6 meV, $\Phi_2 = -$ 8.9 meV and Φ_3 = 0 meV were used. It was then assumed that the nematic state could exhibit a significant reduction in the d_{xz} quasiparticle weight compared to the d_{yz} weight and, following the same argument as before, hidden from ARPES measurements of the spectral function. This is shown in **Figure 7E**. Following this logic, Sprau *et. al.* attempted to determine which values of *Z* by fitting them to experimental measurements of the angular dependence of the superconducting gap (discussed in **Section 5**) and the quasiparticle weight values chosen were Z_{xy} = 0.1 Z_{xz} = 0.2 and Z_{yz} = 0.8, which in a later

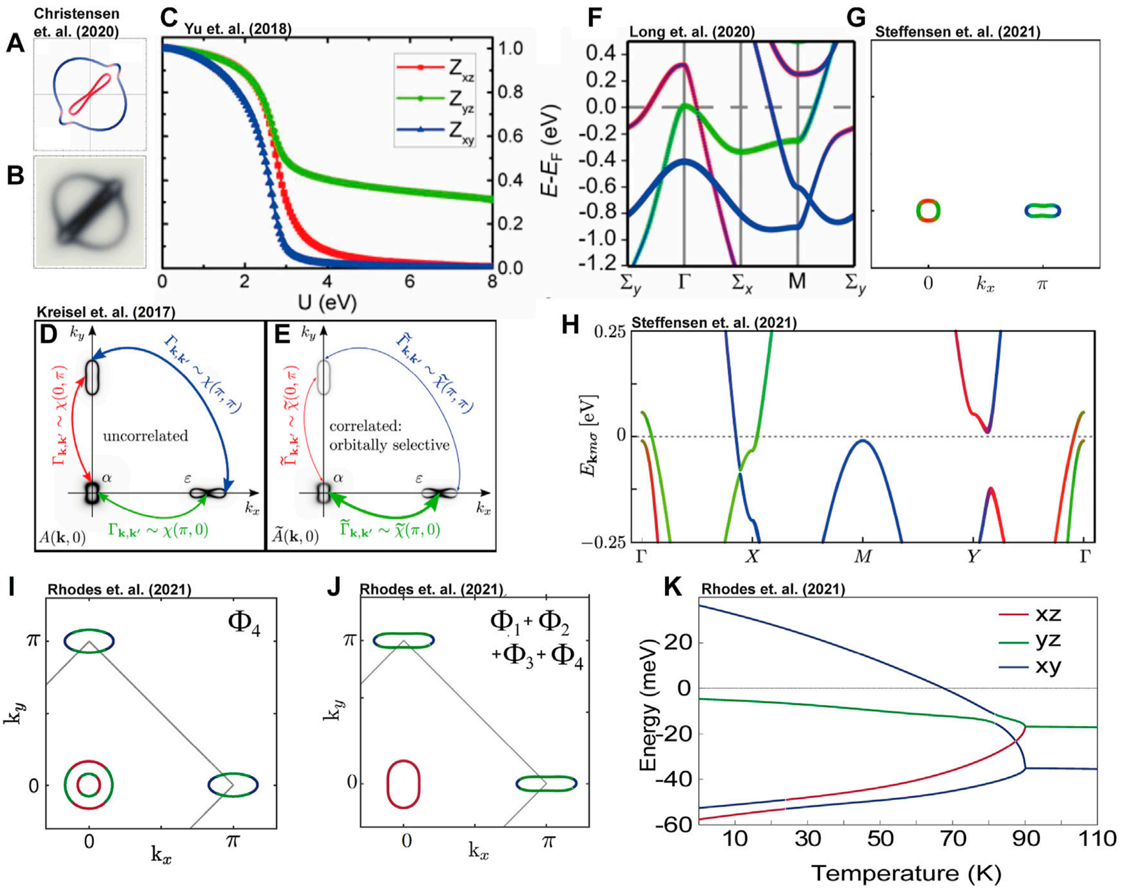

FIGURE 7 | Theoretical attempts to resolve the missing electron pocket problem. **(A)** Fermi surface of the electron pockets in the nematic state proposed by Christensen *et. al.* [100]. The spectral function is argued to have an increased decoherence of d_{xy} weight, which is argued would not be observed by experiment and is simulated in **(B)**. **(C)** Slave-spin calculations from Yu *et. al.* [24], revealing the possibility of highly anisotropic quasiparticle weights with local Coulomb repulsion. **(D,E)** Spectral function of the 1-Fe unit cell tight binding model from Kreisel *et. al.* [21], with and without orbital-selective quasiparticle weights, highlighting the possible suppression of the second electron pocket via incoherent d_{xz} and d_{xy} spectral weight. **(F)** Band dispersion of FeSe obtained from a DFT + U calculation with symmetry preconditioned wavefunctions from Long *et. al.* [106], highlighting the band hybridisation obtained if an E-type nematic order parameter is considered. **(G)** Fermi surface of the 1-Fe unit cell model from Steffensen *et. al.* [108] taking into account a self consistently obtained E-type nematic order parameter. **(H)** Band dispersion from the model used by Steffensen *et. al.* [108] showing a band hybridisation of the d_{xz} (red) and d_{xy} (blue) bands around the Y point (1-Fe unit cell), gapping out the second electron pocket. **(I)** Fermi surface obtained from the 2-Fe unit cell tetragonal model from **Figure 6A** assuming dominant d_{xy} nematic ordering, as suggested by Rhodes *et. al.* [67]. **(J)** Equivalent Fermi surface including all four symmetry allowed nematic order parameters of FeSe and a symmetry allowed Hartree shift. **(K)** Mean-field temperature evolution of the electronic states at the high symmetry M point, highlighting a Lifshitz transition of the d_{xy} band and removal of the second electron pocket as proposed by Rhodes. *et. al.* [67]. **(A,B)** Reproduced from Ref. [100] under the Creative Commons Attribution 4.0 International License. **(C)** Reproduced from Ref. [24] with permission from the American Physical Society. **(D,E)** Reproduced from Ref. [21] with permission from the American Physical Society. **(F)** Reproduced from Ref. [106] under the Creative Commons Attribution 4.0 International License.

study was refined to $Z_{xy} = 0.073$, $Z_{xz} = 0.16$ and $Z_{yz} = 0.86$ [43]. In order to reproduce experimental data, it was also necessary to strongly suppress the quasiparticle weight of the d_{xy} orbital, which as a consequence effectively fully suppressed one of the two electron pockets at the Fermi level. Slave-spin calculations, starting from a DFT-based tight binding model and varying the contributions of $\Phi_1 - \Phi_3$ have also been performed and found that similar anisotropic ratios of the quasiparticle weights can be obtained [24], as shown in **Figure 7C**. A review of the slave-spin approach can be found in Ref. [98].

This formalism of "orbital selective quasiparticle weights", i.e., suppressing the contribution of electronic states with d_{xz} and d_{xy} orbital character in the nematic state, has received the most traction out of the potential theories of the missing electron pocket of FeSe. It has been claimed to be in agreement with STM and QPI measurements of the electronic structure [43], the superconducting gap properties [15], the spin susceptibility measured by inelastic neutron scattering [63], μSR measurements of spin relaxations [102] and thermodynamic based-measurements [99]. A recent review on the topic can be found in Ref. [1].

In our view, however, the success of this approach is due to accurately generating a Fermi surface of FeSe that has the correct one hole pocket and one electron pocket structure, and not necessarily due to the underlying assumptions behind the ansatz of highly anisotropic quasiparticle weights. Indeed, a change in spectral weight, on the order of magnitude as proposed by this theory, is something that should be directly observable with ARPES based measurements. In the tetragonal state, the quasiparticle weight of the d_{xz} and d_{yz} orbitals must be equivalent by symmetry, and thus, under this assumption, there would be a strong sudden suppression of the d_{xz} dominated bands upon entering the nematic state. This is not what is observed in experimental measurements, bands of d_{xz} dominated weight are detected at all temperatures within the nematic state, with no obvious reduction to the spectral intensity [17–20, 30, 40]. It is also not clear how this interpretation would account for the observed band shifts as shown in **Figure 4E** [35], and **Figure 4G** [36]. Additionally, alternate explanations of the STM data and superconducting gap data, that do not rely on the assumption of orbital-selective quasiparticle weights, have been presented [19, 22, 42, 82].

4.2 E-Type Order Parameters

More recent attempts to explain the missing electron pocket have gone back to studying the single-particle physics of FeSe. A recent DFT + U calculation by Long *et. al.* [106], involving symmetry preconditioned wavefunctions, found a lower energy configuration of FeSe by breaking the *E* symmetry via a multipole nematic order, as shown in **Figure 7F**. This has been further studied by Yamada *et. al.* [107]. This symmetry breaking essentially generates a tetragonal to monolclinic distortion by generating an overlap between a d_{xy} orbital and either d_{xz} or d_{yz} orbital, which as a bi-product also breaks C_4 symmetry. This consequentially generates a hybridisation between the d_{xy} dominated electron band and either the d_{xz} or d_{yz} dominated electron band and was shown to produce a one-electron pocket Fermi surface within a certain parameter regime.

A stable E-type nematic order parameter was equally identified, within a tight-binding framework using parameters extracted from LDA-based calculations, by Steffensen *et. al.* [108]. Here it was shown that including nearest-neighbour Coloumbic repulsion, the self consistently calculated mean-field nematic order parameter that had the largest magnitude was an inter-orbital term hybridising the d_{xz} and d_{xy} orbitals (or d_{yz} and d_{xy}). This order parameter was equally able to generate a one-electron pocket Fermi surface, via a similar hybridisation mechanism as the DFT-based calculation as shown in **Figures 7G,H**.

This appears to suggest that long-range Coulomb repulsion can stabilise a C_4 symmetry breaking ground state in FeSe. However, in this scenario, the *E*-type order parameter would also reduce the crystal symmetry of FeSe from tetragonal to monoclinic. Currently, the experimental evidence suggesting a tetragonal to monoclinic structural distortion in FeSe is lacking. However, upon $>85\%$ Te doping of the Se sites, a tetragonal to monoclinic transition has been realised [109]. This could hint that the known monoclinic structure of FeTe is actually stabilised by electron interactions [110], however whether this mechanism can describe the physics of FeSe will require further experimental investigation.

4.3 Non-Local d_{xy} Nematic Order Parameter

When considering the relevant d_{xz}, d_{yz} and d_{xy} orbitals of tetragonal FeSe within a tight binding framework, there are only four order parameters that can be defined which break the B_{1g} rotational symmetry of the material within a single unit cell. The first three, described in **Eqs 1–3**, involve breaking the degeneracy of the d_{xz} and d_{yz} orbitals. However, a fourth equally valid order parameter involving the d_{xy} orbital can also be defined as,

$$\Phi_4\left(n'_{xy}\right)\left(\cos\left(k_x\right) - \cos\left(k_y\right)\right). \tag{4}$$

This term acts as a hopping anisotropy for nearest neighbour d_{xy} orbitals, in a similar manner as **Eq. 2** for the d_{xz} and d_{yz} orbitals. It was initially defined by Fernandes *et. al.* [55], however in subsequent works it was assumed that this d_{xy} nematic term would be much smaller, or negligible, compared to **Eqs 1–3** [55]. Renormalisation group theory [111–113] additionally found, that whilst **Eq. 4** was symmetry allowed, nematic symmetry breaking only had stable RG flow in either the d_{xz}/d_{yz} channel or the d_{xy} channel, implying that finite $\Phi_1 - \Phi_3$ and Φ_4 would not both be present simultaneously [111]. However a weakly unstable trajectory suggested that this may not be the case [112].

In Ref. [67] Rhodes *et. al.* looked at the qualitative effect Φ_4 has on the electronic structure. They showed that a one-electron pocket Fermi surface could be generated from a ARPES-based tight binding model of FeSe solely using the Φ_4 term, as shown in **Figure 7I**. It was shown that Φ_4 has the effect of breaking the degeneracy of the d_{xy} vHs (vH_2 in **Figure 2A**), which if made large enough (~50 meV) would induce a Lifshitz transition of the d_{xy} band, and thus reduce the total number of electron pockets crossing the Fermi level to one. This is shown in **Figure 7K**. In combination with Φ_1 to Φ_3, the addition of Φ_4 made it possible to generate a Fermi surface in agreement with the ARPES measurements, as shown in **Figure 7J**. One recent study has also found this ordering to be consistent with specific heat measurements [114], and a second independent study has found that this order parameter can explain the dc resistivity anisotropy within the framework of elastic scattering at low temperatures [115].

However, in order to get quantitative agreement with the Fermi surface and low-energy electronic structure using **Eqs 1–4**, it was observed that the splitting of the d_{xy} van-Hove singularity must be asymmetric. Specifically, ARPES measurements as a function of temperature find that the lower part of the d_{xy} vHs around the M point remains approximately at the same energy [30, 32, 35]. This is not captured by the Φ_4 term that assumes a symmetric splitting of the bands. To account for this, Rhodes *et. al.* [67] included a d_{xy}-specific Hartree shift, a constant energy shift of the d_{xy} orbital at the *M* point, that although allowed by symmetry, did not have an obvious origin. Additionally, in order to generate a Lifshitz transition of the electron pocket, and obtain quantitative agreement with experimental data as a function of temperature both d_{xy} terms, Φ_4 and the Hartree shift, had to be significantly larger than the d_{xz}/d_{yz} terms ($\Phi_1 - \Phi_3$). Specifically, in order to reproduce the ARPES measurements $\Phi_1 + \Phi_3 = 15$ meV, $\Phi_1 + \Phi_2 = -26$ meV and $\Phi_4 = \Delta_{Hartree} = 45$ meV [67]. It is also worth noting that the mean-field analysis by Steffensen *et. al.* [108] equally found that the Φ_4 nematic order parameter should be finite, but found it to be of approximately equal magnitude as Φ_1-Φ_3 rather than twice as large, as suggested by Rhodes *et. al.* [67].

4.4 Importance of the d_{xy} Orbital in Theories of Nematicity

Each theory proposed to describe the low-energy electronic structure of the nematic state of FeSe has it is relative strengths and weaknesses. Nevertheless a common theme in these different attempts has begun to emerge. In all methods used to theoretically remove an electron pocket from the Fermi level, it has been necessary to modify the d_{xy} orbital in some way. Whether that's suppressing its contribution via quasiparticle weights, gapping out the d_{xy} band via hybridisation, or rigidly shifting the d_{xy} band above the Fermi level. What we can gleam from this analysis therefore, is that we should view the nematic state in a new light, not originating from a specific orbital ordering mechanism of d_{xz} and d_{yz} states, but rather as a symmetry breaking phenomena which couples to every orbital at the Fermi level. Further theoretical investigations are required in order to elucidate the origin of the nematic state. The importance of the d_{xy} orbital has also been recently noted from NMR measurements [116] and angular dependent magnetoresistance [117].

5 CONSEQUENCES FOR THE SUPERCONDUCTING GAP SYMMETRY

One of the most striking properties of FeSe is it is highly tuneable superconducting transition temperature, ranging from 8 K in bulk crystals [44], 36.7 K under pressure [118], and up to 65 K when a monolayer is placed on $SrTiO_3$ [119], and hence the nature of superconductivity in FeSe is an important question that attracted a lot of attention.

From an experimental point of view, the momentum dependence of the superconducting gap of bulk FeSe, has been extensively determined from ARPES [16–20], STM [15, 42, 86], Specific heat [120, 121] and muSR measurements [102], with surprisingly near unanimous agreement as to the angular dependence of the gap structure around both the hole and electron pocket. This achievement provided the perfect opportunity to directly compare theories of superconductivity with experimental measurements.

In this section, we will review the experimental data of the momentum dependence of the superconducting gap, particularly from ARPES measurements, and discuss the theoretical consequence the updated Fermi surface topology has on the theoretical understanding of superconductivity in FeSe.

5.1 Experimental Measurements of the Superconducting Gap

The key findings from the multiple ARPES and QPI measurements are presented in **Figure 8**. For the gap situated on the hole pocket, a highly two-fold anisotropic momentum dependence of the gap was measured, as shown from QPI analysis by Sprau *et. al.* in **Figure 8A**. The angular dependence of the hole pocket using ARPES was first reported in 2016 by Xu *et. al.* [16] on 7% sulphur doped FeSe measured at 6.3 K, as shown in **Figure 8F**. It was found that the angular dependence at both $k_z = 0$ (using a photon energy of $h\nu = 37$ eV) and $k_z = \pi$ ($h\nu = 21$ eV) produced near identical momentum distributions. This sulphur doped system has a very similar electronic structure to undoped FeSe, albeit with a slightly reduced nematic transition temperature [122] and slightly higher superconducting transition temperature (9.8 K [16]). Later, in 2018, Liu *et. al.* [18] and Hashimoto *et. al.* [17] used laser ARPES, with $h\nu = 6.994$ eV, on FeSe at 1.6 K and observed the same highly anistropic angular dependence of the gap at the hole pocket, as shown in **Figures 8B,C**. By using such a low photon energy and temperature these authors ensured the greatest possible energy resolution for resolving the gap of the hole pocket. However the trade-off here is that information about states with large angular momentum, e.g., the electron pockets, as well as the k_z-dependence of the hole pocket, can not be obtained. Kushnirenko *et. al.* [20], as well as Rhodes *et. al.* [19], were able to resolve the three dimensional gap structure of both the hole and electron pockets using synchrotron radiation, as shown in **Figures 8D,E**. In these manuscripts, it was again confirmed that the gap structure of the hole pocket at both $k_z = 0$ and $k_z = \pi$ exhibited the same highly anisotropic two-fold angular dependence of the gap as determined in the Sulphur doped sample of Xu. *et. al.* [16]. Kushnirenko *et. al.* claimed that the superconducting gap that was larger at $k_z = \pi$ and smaller at $k_z = 0$, however Rhodes *et. al.* suggested the opposite: the gap was observed to be larger at $k_z = 0$ and smaller at $k_z = \pi$. We note that in order to reach the $k_z = 0$ hole pocket, a higher photon energy of 37 eV is required, which makes the measurement of the gap at the Γ point exceedingly challenging, and the measurements are at the cutting edge of what is currently achievable by synchrotron-based ARPES measurements.

Hashimoto *et. al.* additionally claimed that the gap structure produced a different behaviour with and without the presence of uniaxial strain. Without strain, they observed a cos (8θ) behaviour [17], which when accidentally detwinned *via* uniaxial strain, yielded a gap structure that is consistent with the other measurements. So far this cos (8θ) dependence of the gap has not been reproduced.

As for the electron pocket, the angular dependence of the gap from QPI measurements is presented in **Figure 8G**. Revealing a particularly constant gap magnitude across the length of the ellipse, which quickly decays towards zero at the tips of the pocket. This is where the orbital character of the pocket transforms from predominantly d_{yz} weight to d_{xy} weight. ARPES measurements by Kushnirenko *et. al* [20], and Rhodes *et. al.* [19], were also able to resolve the angular dependence of the superconducting gap at the electron pocket. ARPES measurements along the minor length of the electron pocket, above and below T_c, are shown in **Figures 8H,I**. Thanks to the orbital sensitivity of ARPES-based measurements, Rhodes *et. al.* found a direct correlation between the intensity of d_{yz} orbital weight and the size of the superconducting gap, establishing a direct link between orbital character and gap magnitude (**Figure 7J**). Kushnirenko *et. al.* [20] also observed that the rate that the gap decreased as a function of momentum was slightly different for intermediate k_z values (**Figure 8K**).

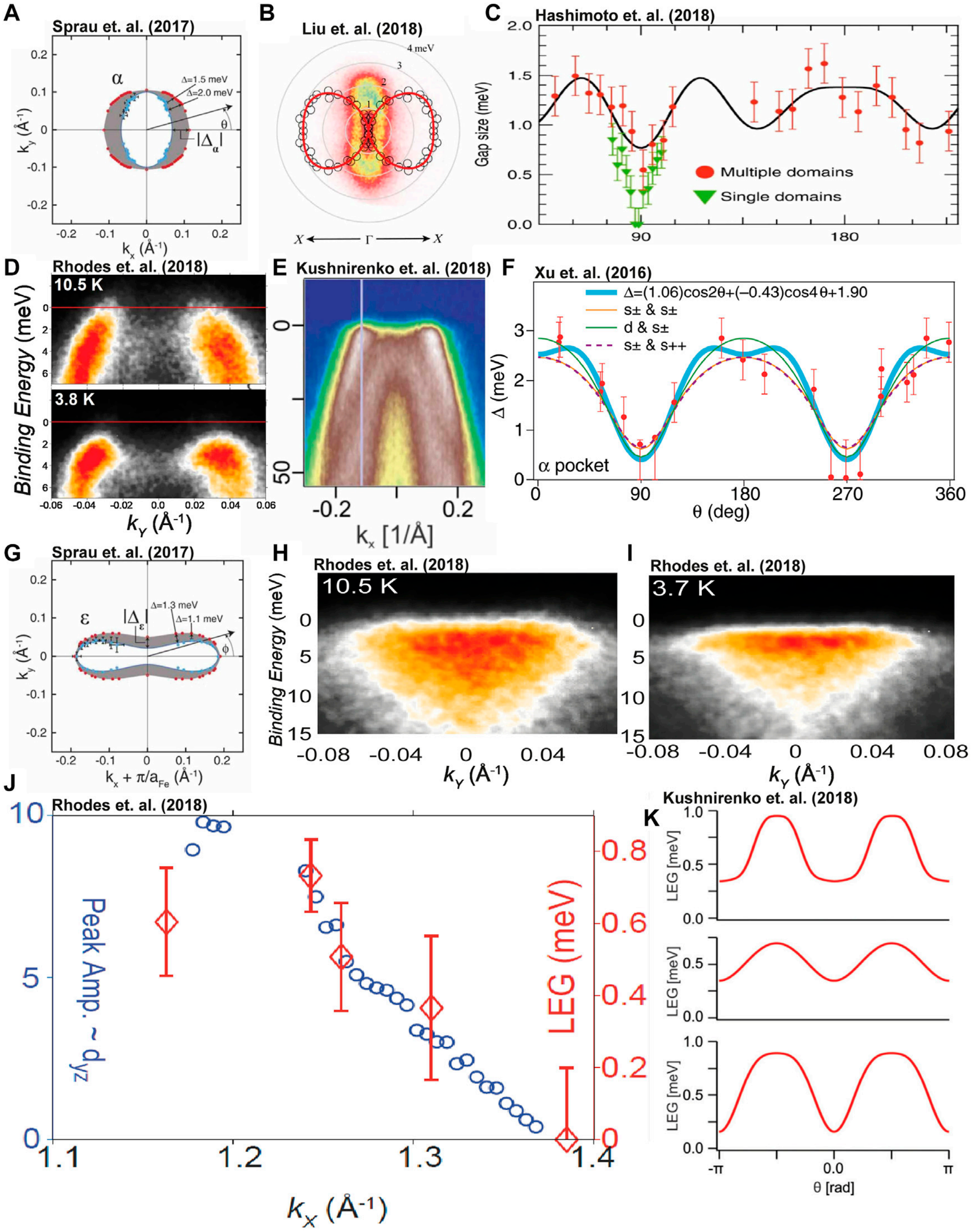

FIGURE 8 | Experimental measurements of the superconducting gap of FeSe. **(A)** Angular dependence of the gap around the hole pocket as extracted from BQPI measurements from Sprau *et. al.* [15]. **(B)** Angular dependence of the gap around the hole pocket as extracted from Laser ARPES measurements from Liu et. al [18]. **(C)** Angular dependence of the gap around the hole pocket from Hashimoto *et. al.* [17]. Red dots are data from a twinned sample, whereas green data was measured on an accidentally strained sample. **(D)** Band dispersion of the $k_z = 0$ hole band ($h\nu = 37$ eV) from Rhodes *et. al.* [19] taken along the direction where the hole band gap is largest, above and below T_c. **(E)** Equivalent band dispersion of the $k_z = \pi$ hole band ($h\nu = 21$ eV) below T_c from Kushnirenko *et. al.* [20]. **(F)** Angular dependence of the hole band of $FeSe_{0.93}S_{0.07}$ from Xu *et. al.* [16], showing equivalent momentum dependence as the undoped sample. **(G)** Angular dependence of the gap around the electron pocket as extracted from BQPI measurements from Sprau *et. al.* [15]. **(H,I)** Band dispersion along the minor length of the electron pocket above and below T_c, along the high symmetry axis from Rhodes *et. al.* [19]. **(J)** Comparison of the gap magnitude (Leading Edge Gap - LEG) and the intensity of the spectral weight from Linear Vertical polarised light as a function of k_x, which is directly correlated to the amplitude of d_{yz} orbital weight. The gap is observed to decrease with decreasing d_{yz} weight. Taken

(Continued)

FIGURE 8 | from Rhodes *et. al.* [19]. **(K)** Sketch of the angular dependence of the electron pocket at $k_z = 0$ (bottom) $k_z = \frac{\pi}{2}$ (middle) and $k_z = \pi$ (top) from Kushirenko *et. al.* [20]. **(A,G)** Reproduced from Ref. [15] with permission from the AAAS. **(B)** Reproduced from Ref. [18] under the Creative Commons Attribution 4.0 International License. **(C)** b) Reproduced from Ref. [17] under the Creative Commons Attribution 4.0 International License. **(F)** Reproduced from Ref. [16] with permission from the American Physical Society. **(E,K)** Reproduced from Ref. [20] with permission from the American Physical Society.

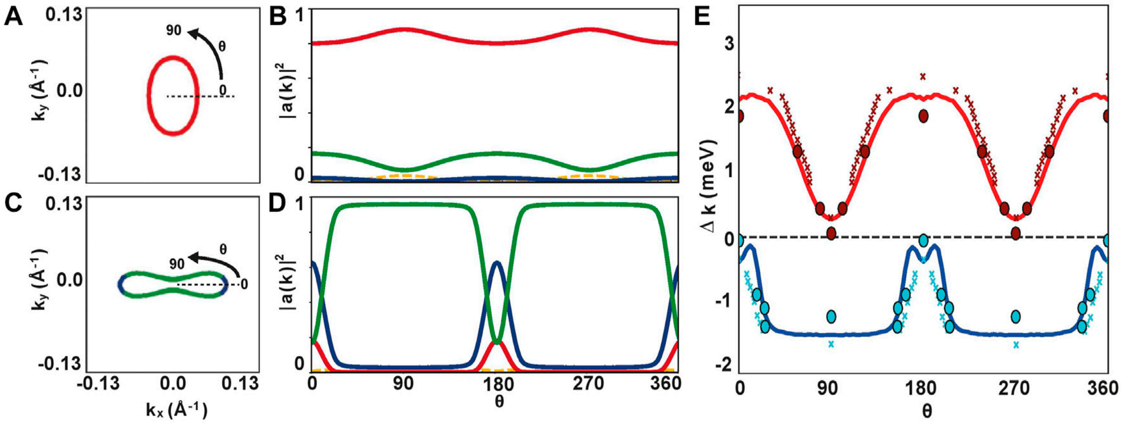

FIGURE 9 | Theoretical simulation of the momentum dependence of the superconducting gap from Rhodes *et. al.* [19]. Here, a Fermi surface consisting of one hole pocket a single electron pocket were considered and a spin fluctuation pairing mechanism was assumed. **(A,B)** Fermi surface of the hole pocket and angular dependence of the orbital content of the hole pocket. **(C,D)** Fermi surface of the one electron pocket and angular dependence of the orbital content of the electron pocket. The colour labels are red d_{xz}, green d_{yz} and blue d_{xy}. **(E)** Simulated angular dependence of the superconducting gap for the hole pocket (red) and electron pocket (blue), revealing a direct correlation with the d_{yz} weight shown in **(B)** and **(D)**. The crosses and dots are experimental data extracted from STM [15] and ARPES [19] measurements respectively.

This extremely aniostropic gap structure for both the hole and electron pocket raises a question as to whether FeSe is a nodal or nodeless superconductor, which could have a profound effect on our understanding of the gap symmetry in this system. For example, neglecting the electron pocket, it was argued by Hashimoto *et. al.* that a nodal gap structure of the hole pocket would be consistent with p-wave superconductivity [17] (This is not consistent once the gap structure of the electron pocket is additionally taken into account). It is not possible to clearly distinguish between a nodal gap or a very small gap in ARPES measurements, due to the limitations of energy resolution arising from thermal broadening and the choice of photon energy. Alternate techniques, such as STM and specific heat measurements, do have sufficient energy and thermal resolution to tackle this issue, but here STM measurements of the density of states by Sprau *et. al.* [15] suggest a fully gapped, nodeless, superconducting ground state, whereas specific heat measurements have argued that the measured data is consistent with a nodal superconducting gap [120]. It is still unclear whether FeSe exhibits nodes or very small superconducting gaps, however as we will discuss below, theoretical arguments appear to suggest that if any nodes do exist, they would be accidental in nature.

5.2 Theoretical Understanding of the Superconducting Gap

The most striking result from the experimentally determined gap structure of FeSe, is the clear realisation that the size of the superconducting gap at the Fermi level is correlated with the magnitude of d_{yz} orbital weight. This tells us that the superconducting pairing mechanism is sensitive to orbital character, and is evidence for superconductivity mediated by Coulomb interactions, such as via a spin-fluctuation mechanism of superconductivity.

Although the idea that spin fluctuations govern the Cooper pairing in the iron-based superconductors, was originally proposed back when superconductivity in these materials were first discovered [7], the evidence for this has often been inferred from gap symmetry arguments, such as a sign-changing $s^{\pm}$ order parameter [15], or from the general argument that FeSe is close to a magnetic instability. FeSe, being such a clean system, has enabled a direct comparison between theoretical simulations and experimental data.

Indeed many theoretical simulations of the angular dependence of the superconducting gap in FeSe have been performed [15, 19, 21–24, 67, 108]. However, as the formation of Cooper pairs are directly sensitive to the states at the Fermi level, the starting model used to describe FeSe is very important. Numerical simulations have shown that models of FeSe which do not account for the missing electron pocket of the nematic state, i.e. a model Fermi surface which describes two electron pockets around the M point, can not reproduce the experimentally observed gap structure [15, 19, 22, 23].

Initially, this was a confusing result, but with hindsight it is not that surprising. The presence of an extra electron pocket in the simulations would naturally influence the superconducting pairing. Due to the local nature of Coulomb repulsion, the pairing between electrons in real space will be largest for electrons located on the same atom in the same orbital. It follows from this argument, that the pairing of electrons in momentum space would be favoured if a spin scattering process occurs which couples electronic states of the same orbital character. In the nematic state of FeSe, spin-fluctuations are strongest when connecting the hole and electron pocket [63, 123, 124]. In a one-electron pocket scenario, the only common orbital content between the two pockets are the d_{yz} orbital weight, as shown in **Figures 9A–D**, and thus this would dominate the superconducting gap magnitude. This would not be the case in a two-electron pocket scenario, where scattering with d_{xz} electrons between the hole and electron pocket would also contribute.

It has now been shown that irregardless of the theoretical mechanism employed to remove this second electron pocket from the superconducting calculation, whether that's orbital selective quasiparticle weights [15, 21, 24], orbital selective spin fluctuations [22], E-type nematic ordering [108], a non-local d_{xy} nematic order parameter [67] or simply ignoring it from simulations of the superconducting pairing outright [19] (as shown in **Figure 9**), the correct momentum dependence of the gap structure can be naturally captured assuming weak-coupling spin fluctuation mediated pairing.

This is a remarkable finding, not only does it further support the theory of spin-fluctuation mediated superconductivity in the iron-based superconductors, but it provides another independent piece of evidence for a single electron pocket around the M point in the nematic state of FeSe. This result highlights the incredible importance of correctly accounting for the missing electron pocket in the nematic state, as without it we can not begin to understand the superconducting properties of this material.

6 DISCUSSION

This review has been wholly focused on what at first glance might appear to be an esoteric point of discussion, namely, the characterisation and modelling of the Fermi surface of FeSe in the nematic state. However, we propose that after the hundreds of papers and many years of debate and controversy on the subject, that there are very important conclusions to be drawn, which have wider implications for our understanding of both nematic ordering and superconductivity across the wider family of Fe-based superconductors.

The first conclusions surround nematic ordering, where the results establish.

- That nematic ordering affects all bands at the Fermi level, with the d_{xy} derived bands playing as significant a role as the d_{xz} and d_{yz} derived bands.
- That nematic order manifests in the band structure through a combination of all allowed symmetry-breaking terms, primarily anisotropic hopping terms, and cannot be exclusively treated by on-site orbital ordering.
- That nematic ordering does not cause a minor perturbation of the electronic structure, but can lift an entire electron pocket away from the Fermi level.

We believe that these conclusions should be widely applicable across other Fe-based superconductors. While these conclusions do not yet constitute a self-consistent microscopic mechanism of nematic order, they do present strong constraints to any proposed microscopic models.

The second set of conclusions relate to the superconductivity:

- The superconducting gap of FeSe is remarkably anisotropic.
- The fact that the gap follows the d_{yz} orbital character is strong experimental evidence that the pairing mechanism is sensitive to local orbital degrees of freedom, i.e., for spin-fluctuation pairing.
- The superconducting gap of FeSe can be naturally reproduced by spin-fluctuation calculations assuming only one electron pocket at the Fermi level.

There has long been a consensus that the superconductivity in the Fe-based systems is mediated by spin-fluctuation pairing, but we argue that FeSe provides some of the most direct experimental support for this. As long as one starts with the one-electron pocket Fermi surface, the further details of the calculation are not critical, because in this scenario the only orbital component which is present on both the hole and electron pockets is the d_{yz} character, and so this channel dominates the structure of the gap. The success of this result justifies the use of similar spin-fluctuation pairing calculations on other Fe-based superconductors, although we emphasize the importance of starting with an experimentally accurate Fermi surface.

Importantly this insight has only been unlocked once we understand that the true Fermi surface of FeSe consists of one hole pocket and a single electron pocket, rather than one hole pocket and two electron pockets as was initially believed. However, despite us emphasizing how the one electron pocket scenario is key to the understanding of the unusual properties of FeSe, we believe it is still an open question as to what mechanism really drives this modification of the electronic structure. The models of describing the electronic structure in the nematic state have grown more accurate and more sophisticated, yet there is a lack of intuition about what is the real driving force for the evolution of the electronic structure that we observe. In our opinion it remains a delicate and important open question, but solving it in the case of FeSe could unlock a wider understanding of nematicity in the iron-based superconductors.

Additionally, whilst the experimental challenge imposed by measuring the electronic structure of orthorhombic crystals has always been present, the focus on an answer to the origin of nematicity in FeSe has particularly emphasised the continued development of detwinning methods in ARPES [28, 34–40, 85, 125], as well as showcasing the potential of NanoARPES for strongly correlated materials with local domain structures [67, 85].

The anisotropic Fermi surface of the nematic state also has important consequences for the understanding of the spin excitation spectrum of FeSe, which has also been shown to be highly anisotropic [63], revealing a dominant scattering vector at (π, 0) in the nematic state but not (0, π). From an itinerant magnetism perspective, this can be intuitively understood, the only allowed scattering vectors at the Fermi level are the one hole pocket and one electron pocket, seperated by (0, π), thus the imaginary part of the spin susceptibility should also be highly anisotropic [67, 97, 108]. This has so far mainly been discussed within the weak coupling-RPA approximation for the spin fluctuation, within the concext of orbital selective quasiparticle weights [97, 126], however it would be interesting to explore how well this weak coupling calculations agrees with the inelastic neutron scattering data applied the other descriptions of the missing electron pocket.

7 OUTLOOK AND CONCLUSION

With an outlook to the future, there are still multiple open questions regarding the missing electron pocket problem, nematicity and superconductivity in FeSe. Firstly, can we experimentally identify the exact conditions when one of the electron pockets in the tetragaonal state appears or disappears from the Fermi level? So far, this has remained slightly ambiguous, with some experiments claiming a gradual disappearance of the electron pocket [37] and others claiming a Lifshitz transition around 70 K [35, 36, 67].

Another open question is how the missing electron pocket scenario can be reconciled with the QPI measurements as a function of sulphur doping [42] or Tellurium doping [2], each providing an isoelectronic tuning parameter to control the evolution of the Fermi surface. The systematic evolution of the Fermi surface has been studied by Quantum Oscillations [127], however due to the tiny size of the Fermi energy in this system, the unambiguous assignment of the quantum oscillation frequencies is challenging [67]. Equally, twinned ARPES measurements on sulphur doped FeSe have already been performed [54, 77], as well as several studies on detwinned crystals for 9% sulphur doping [37, 38]. So far it is unclear when the missing electron pocket reappears, and so further measurements of detwinned $FeSe_{1-x}S_x$ are desirable, although by 18% the system is tetragonal once more and two electron pockets are certainly observed [77].

Finally, an important avenue of research is how does the momentum-dependence of the superconducting gap change as nematicity is supressed, e.g., as a function of sulphur doping. The momentum dependence of the superconducting gap for undoped FeSe has now been extensively characterised, and theoretical predictions of how the gap should evolve as nematicity is suppressed have been proposed [67]. This much needed experimental data would again place important constraints on our theories of nematicity and superconductivity in these systems.

As the study of the Fe-based superconductors has matured since they exploded onto the scene in 2008, the emphasis has shifted from basic characterisation of a wide variety of superconducting families, to detailed examination of particular cases. FeSe has been the subject of particularly focused attention, and the effort has been worthwhile, with two remarkable results emerging: the one electron pocket Fermi surface, and the highly anisotropic superconducting gap structure. We have argued that these two, taken together, provide strong evidence for spin-fluctuation pairing in FeSe, which is presumably applicable to the wider family of Fe-based superconductors. However, the extent to which the one electron pocket phenomenology may be applicable to the nematic phase of other material systems is a large open question; as well as $FeSe_{1-x}S_x$ and $FeSe_{1-x}Te_x$, we propose NaFeAs [125] as a candidate worthy of re-examination. Thus as this review of FeSe concludes, we propose it is time to take the experimental and theoretical tools developed for case of FeSe, and apply them with renewed vigour to the wider field of Fe-based superconductors.

AUTHOR CONTRIBUTIONS

All authors listed have made a substantial, direct, and intellectual contribution to the work and approved it for publication.

FUNDING

LR acknowledges funding from the royal commission for the exhibition for the 1851.

REFERENCES

1. Kreisel A, Hirschfeld P, Andersen B. On the Remarkable Superconductivity of FeSe and its Close Cousins. *Symmetry* (2020) 12(9):1402. doi:10.3390/sym12091402
2. Shibauchi T, Hanaguri T, Matsuda Y. Exotic Superconducting States in FeSe-Based Materials. *J Phys Soc Jpn* (2020) 89(10):102002. doi:10.7566/jpsj.89.102002
3. Fernandes RM, Coldea AI, Ding H, Fisher IR, Hirschfeld PJ, Kotliar G. Iron Pnictides and Chalcogenides: a New Paradigm for Superconductivity. *Nature* (2022) 601(7891):35–44. doi:10.1038/s41586-021-04073-2
4. Georges A, de' Medici L., Mravlje J. Strong Correlations from Hund's Coupling. *Annu Rev Condens Matter Phys* (2013) 4(1):137–78. doi:10.1146/annurev-conmatphys-020911-125045
5. de' Medici L, Giovannetti G, Capone M. Selective Mott Physics as a Key to Iron Superconductors. *Phys Rev Lett* (2014) 112:177001. doi:10.1103/physrevlett.112.177001
6. Lanatà N, Strand HUR, Giovannetti G, Hellsing B, de' Medici L, Capone M. Orbital Selectivity in Hund's Metals: The Iron Chalcogenides. *Phys Rev B* (2013) 87:045122. doi:10.1103/physrevb.87.045122
7. Mazin II, Singh DJ, Johannes MD, Du MH. Unconventional Superconductivity with a Sign Reversal in the Order Parameter of $LaFeAsO_{1-x}F_x$. *Phys Rev Lett* (2008) 101:057003. doi:10.1103/physrevlett.101.057003
8. Graser S, Maier TA, Hirschfeld PJ, Scalapino DJ. Near-degeneracy of Several Pairing Channels in Multiorbital Models for the Fe Pnictides. *New J Phys* (2009) 11:025016. doi:10.1088/1367-2630/11/2/025016

9. Fernandes RM, Chubukov AV, Schmalian J. What Drives Nematic Order in Iron-Based Superconductors? *Nat Phys* (2014) 10(2):97–104. doi:10.1038/nphys2877
10. Böhmer AE, Kreisel A. Nematicity, Magnetism and Superconductivity in FeSe. *J Phys Condens Matter* (2017) 30(2):023001. doi:10.1088/1361-648x/aa9caa
11. Coldea AI. Electronic Nematic States Tuned by Isoelectronic Substitution in Bulk $FeSe_{1-x}S_x$. *Front Phys* (2021) 8:528. doi:10.3389/fphy.2020.594500
12. Ptok A, Kapcia KJ, Piekarz P, Oleś AM. The ab-initio Study of Unconventional Superconductivity in $CeCoIn_5$ and FeSe. *New J Phys* (2017) 19(6):063039. doi:10.1088/1367-2630/aa6d9d
13. Kasahara S, Sato Y, Licciardello S, Čulo M, Arsenijević S, Ottenbros T, et al. Evidence for an Fulde-Ferrell-Larkin-Ovchinnikov State with Segmented Vortices in the BCS-BEC Crossover Superconductor FeSe. *Phys Rev Lett* (2020) 124:107001. doi:10.1103/physrevlett.124.107001
14. Kasahara S, Watashige T, Hanaguri T, Kohsaka Y, Yamashita T, Shimoyama Y, et al. Field-induced Superconducting Phase of FeSe in the BCS-BEC Cross-Over. *Proc Natl Acad Sci U.S.A* (2014) 111(46):16309–13. doi:10.1073/pnas.1413477111
15. Sprau PO, Kostin A, Kreisel A, Böhmer AE, Taufour V, Canfield PC, et al. Discovery of Orbital-Selective Cooper Pairing in FeSe. *Science* (2017) 357:75–80. doi:10.1126/science.aal1575
16. Xu HC, Niu XH, Xu DF, Jiang J, Yao Q, Chen QY, et al. Highly Anisotropic and Twofold Symmetric Superconducting Gap in Nematically Ordered $FeSe_{0.93}S_{0.07}$. *Phys Rev Lett* (2016) 117:157003. doi:10.1103/physrevlett.117.157003
17. Hashimoto T, Ota Y, Yamamoto HQ, Suzuki Y, Shimojima T, Watanabe S, et al. Superconducting gap Anisotropy Sensitive to Nematic Domains in FeSe. *Nat Commun* (2018) 9(1):282. doi:10.1038/s41467-017-02739-y
18. Liu D, Li C, Huang J, Lei B, Wang L, Wu X, et al. Orbital Origin of Extremely Anisotropic Superconducting Gap in Nematic Phase of FeSe Superconductor. *Phys Rev X* (2018) 8:031033. doi:10.1103/physrevx.8.031033
19. Rhodes LC, Watson MD, Haghighirad AA, Evtushinsky DV, Eschrig M, Kim TK. Scaling of the Superconducting gap with Orbital Character in FeSe. *Phys Rev B* (2018) 98(18):180503. doi:10.1103/physrevb.98.180503
20. Kushnirenko YS, Fedorov AV, Haubold E, Thirupathaiah S, Wolf T, Aswartham S, et al. Three-dimensional Superconducting gap in FeSe from Angle-Resolved Photoemission Spectroscopy. *Phys Rev B* (2018) 97:180501. doi:10.1103/physrevb.97.180501
21. Kreisel A, Andersen BM, Sprau PO, Kostin A, Davis JCS, Hirschfeld PJ. Orbital Selective Pairing and gap Structures of Iron-Based Superconductors. *Phys Rev B* (2017) 95:174504. doi:10.1103/physrevb.95.174504
22. Benfatto L, Valenzuela B, Fanfarillo L. Nematic Pairing from Orbital-Selective Spin Fluctuations in FeSe. *Npj Quant Mater* (2018) 3(1):56. doi:10.1038/s41535-018-0129-9
23. Kang J, Fernandes RM, Chubukov A. Superconductivity in FeSe: The Role of Nematic Order. *Phys Rev Lett* (2018) 120:267001. doi:10.1103/physrevlett.120.267001
24. Yu R, Zhu J-X, Si Q. Orbital Selectivity Enhanced by Nematic Order in FeSe. *Phys Rev Lett* (2018) 121:227003. doi:10.1103/physrevlett.121.227003
25. Böhmer AE, Hardy F, Eilers F, Ernst D, Adelmann P, Schweiss P, et al. Lack of Coupling between Superconductivity and Orthorhombic Distortion in Stoichiometric Single-Crystalline FeSe. *Phys Rev B* (2013) 87:180505. doi:10.1103/physrevb.87.180505
26. Fedorov A, Yaresko A, Kim TK, Kushnirenko Y, Haubold E, Wolf T, et al. Effect of Nematic Ordering on Electronic Structure of FeSe. *Sci Rep* (2016) 6:36834. doi:10.1038/srep36834
27. Nakayama K, Miyata Y, Phan GN, Sato T, Tanabe Y, Urata T, et al. Reconstruction of Band Structure Induced by Electronic Nematicity in an FeSe Superconductor. *Phys Rev Lett* (2014) 113:237001. doi:10.1103/physrevlett.113.237001
28. Shimojima T, Suzuki Y, Sonobe T, Nakamura A, Sakano M, Omachi J, et al. Lifting Of xz/yz Orbital Degeneracy at the Structural Transition in Detwinned FeSe. *Phys Rev B* (2014) 90:121111. doi:10.1103/physrevb.90.121111
29. Watson MD, Kim TK, Haghighirad AA, Davies NR, McCollam A, Narayanan A, et al. Emergence of the Nematic Electronic State in FeSe. *Phys Rev B* (2015) 91:155106. doi:10.1103/physrevb.91.155106
30. Fanfarillo L, Mansart J, Toulemonde P, Cercellier H, Le Fèvre P, Bertran F, et al. Orbital-dependent Fermi Surface Shrinking as a Fingerprint of Nematicity in FeSe. *Phys Rev B* (2016) 94:155138. doi:10.1103/physrevb.94.155138
31. Maletz J, Zabolotnyy VB, Evtushinsky DV, Thirupathaiah S, Wolter AUB, Harnagea L, et al. Unusual Band Renormalization in the Simplest Iron-Based Superconductor $FeSe_{1-x}$. *Phys Rev B* (2014) 89:220506. doi:10.1103/physrevb.89.220506
32. Watson MD, Kim TK, Rhodes LC, Eschrig M, Hoesch M, Haghighirad AA, et al. Evidence for Unidirectional Nematic Bond Ordering in FeSe. *Phys Rev B* (2016) 94:201107. doi:10.1103/physrevb.94.201107
33. Coldea AI, Watson MD. The Key Ingredients of the Electronic Structure of FeSe. *Annu Rev Condens Matter Phys* (2018) 9(1):125–46. doi:10.1146/annurev-conmatphys-033117-054137
34. Watson MD, Haghighirad AA, Rhodes LC, Hoesch M, Kim TK. Electronic Anisotropies Revealed by Detwinned Angle-Resolved Photo-Emission Spectroscopy Measurements of FeSe. *New J Phys* (2017) 19:103021. doi:10.1088/1367-2630/aa8a04
35. Yi M, Pfau H, Zhang Y, He Y, Wu H, Chen T, et al. Nematic Energy Scale and the Missing Electron Pocket in FeSe. *Phys Rev X* (2019) 9:041049. doi:10.1103/physrevx.9.041049
36. Huh SS, Seo JJ, Kim BS, Cho SH, Jung JK, Kim S, et al. Absence of Y-Pocket in 1-Fe Brillouin Zone and Reversed Orbital Occupation Imbalance in FeSe. *Commun Phys* (2020) 3:52. doi:10.1038/s42005-020-0319-1
37. Cai C, Han TT, Wang ZG, Chen L, Wang YD, Xin ZM, et al. Momentum-resolved Measurement of Electronic Nematic Susceptibility in the $FeSe_{0.9}S_{0.1}$ Superconductor. *Phys Rev B* (2020) 101:180501. doi:10.1103/physrevb.101.180501
38. Cai C, Han TT, Wang ZG, Chen L, Wang YD, Xin ZM, et al. Anomalous Spectral Weight Transfer in the Nematic State of Iron-Selenide Superconductor. *Chin Phys. B* (2020) 29:077401. doi:10.1088/1674-1056/ab90ec
39. Pfau H, Chen SD, Yi M, Hashimoto M, Rotundu CR, Palmstrom JC, et al. Momentum Dependence of the Nematic Order Parameter in Iron-Based Superconductors. *Phys Rev Lett* (2019) 123:066402. doi:10.1103/PhysRevLett.123.066402
40. Pfau H, Yi M, Hashimoto M, Chen T, Dai P-C, Shen Z-X, et al. Quasiparticle Coherence in the Nematic State of FeSe. *Phys Rev B* (2021) 104:L241101. doi:10.1103/physrevb.104.l241101
41. Rhodes LC, Watson MD, Haghighirad AA, Evtushinsky DV, Kim TK. Revealing the Single Electron Pocket of FeSe in a Single Orthorhombic Domain. *Phys Rev B* (2020) 101:235128. doi:10.1103/physrevb.101.235128
42. Hanaguri T, Iwaya K, Kohsaka Y, Machida T, Watashige T, Kasahara S, et al. Two Distinct Superconducting Pairing States Divided by the Nematic End point in $FeSe_{1-x}S_x$. *Sci Adv* (2018) 4(5):eaar6419. doi:10.1126/sciadv.aar6419
43. Kostin A, Sprau PO, Kreisel A, Chong YX, Böhmer AE, Canfield PC, et al. Imaging Orbital-Selective Quasiparticles in the Hund's Metal State of FeSe. *Nat Mater* (2018) 17:869–74. doi:10.1038/s41563-018-0151-0
44. Margadonna S, Takabayashi Y, McDonald MT, Kasperkiewicz K, Mizuguchi Y, Takano Y, et al. Crystal Structure of the New $FeSe_{1-x}$ Superconductor. *Chem Commun (Camb)* (2008) 4(8):5607–9. doi:10.1039/b813076k
45. Andersen OK, Boeri L. On the Multi-Orbital Band Structure and Itinerant Magnetism of Iron-Based Superconductors. *Annalen der Physik* (2011) 523(1-2):8–50. doi:10.1002/andp.201000149
46. Eugenio PM, Vafek O. Classification of Symmetry Derived Pairing at the *M* point in FeSe. *Phys Rev B* (2018) 98:014503. doi:10.1103/physrevb.98.014503
47. Borisenko SV, Evtushinsky DV, Liu Z-H, Morozov I, Kappenberger R, Wurmehl S, et al. Direct Observation of Spin-Orbit Coupling in Iron-Based Superconductors. *Nat Phys* (2016) 12(4):311–7. doi:10.1038/nphys3594
48. Watson MD, Haghighirad AA, Takita H, Mansuer W, Iwasawa H, Schwier EF, et al. Shifts and Splittings of the Hole Bands in the Nematic Phase of FeSe. *J Phys Soc Jpn* (2017) 86(5):053703. doi:10.7566/jpsj.86.053703
49. Day RP, Levy G, Michiardi M, Zwartsenberg B, Zonno M, Ji F, et al. Influence of Spin-Orbit Coupling in Iron-Based Superconductors. *Phys Rev Lett* (2018) 121:076401. doi:10.1103/PhysRevLett.121.076401

50. Rhodes LC, Watson MD, Haghighirad AA, Eschrig M, Kim TK. Strongly Enhanced Temperature Dependence of the Chemical Potential in FeSe. *Phys Rev B* (2017) 95:195111. doi:10.1103/physrevb.95.195111
51. Zhang Y, He C, Ye ZR, Jiang J, Chen F, Xu M, et al. Symmetry Breaking via Orbital-dependent Reconstruction of Electronic Structure in Detwinned NaFeAs. *Phys Rev B* (2012) 85:085121. doi:10.1103/physrevb.85.085121
52. Eschrig H, Koepernik K. Tight-binding Models for the Iron-Based Superconductors. *Phys Rev B* (2009) 80(10):104503. doi:10.1103/physrevb.80.104503
53. Acharya S, Pashov D, Jamet F, van Schilfgaarde M. Electronic Origin of Tc in Bulk and Monolayer FeSe. *Symmetry* (2021) 13(2):169. doi:10.3390/sym13020169
54. Watson MD, Kim TK, Haghighirad AA, Blake SF, Davies NR, Hoesch M, et al. Suppression of Orbital Ordering by Chemical Pressure in $FeSe_{1-x}S_x$. *Phys Rev B* (2015) 92:121108. doi:10.1103/physrevb.92.121108
55. Fernandes RM, Vafek O. Distinguishing Spin-Orbit Coupling and Nematic Order in the Electronic Spectrum of Iron-Based Superconductors. *Phys Rev B* (2014) 90:214514. doi:10.1103/physrevb.90.214514
56. Yi M, Zhang Y, Shen Z-X, Lu D. Role of the Orbital Degree of freedom in Iron-Based Superconductors. *Npj Quant Mater* (2017) 2(1):57. doi:10.1038/s41535-017-0059-y
57. Yin ZP, Haule K, Kotliar G. Kinetic Frustration and the Nature of the Magnetic and Paramagnetic States in Iron Pnictides and Iron Chalcogenides. *Nat Mater* (2011) 10(12):932–5. doi:10.1038/nmat3120
58. Yi M, Liu Z-K, Zhang Y, Yu R, Zhu J-X, Lee JJ, et al. Observation of Universal strong Orbital-dependent Correlation Effects in Iron Chalcogenides. *Nat Commun* (2015) 6(1):7777. doi:10.1038/ncomms8777
59. Watson MD, Backes S, Haghighirad AA, Hoesch M, Kim TK, Coldea AI, et al. Formation of Hubbard-like Bands as a Fingerprint of strong Electron-Electron Interactions in FeSe. *Phys Rev B* (2017) 95:081106. doi:10.1103/physrevb.95.081106
60. Evtushinsky DV, Aichhorn M, Sassa Y, Liu Z-H, Maletz J, Wolf T, et al. Direct Observation of Dispersive Lower Hubbard Band in Iron-Based Superconductor FeSe (2017). *arXiv:1612.02313*.
61. Glasbrenner JK, Mazin II, Jeschke HO, Hirschfeld PJ, Fernandes RM, Valentí R. Effect of Magnetic Frustration on Nematicity and Superconductivity in Iron Chalcogenides. *Nat Phys* (2015) 11(11):953–8. doi:10.1038/nphys3434
62. He M, Wang L, Hardy F, Xu L, Wolf T, Adelmann P, et al. Evidence for Short-Range Magnetic Order in the Nematic Phase of FeSe from Anisotropic In-Plane Magnetostriction and Susceptibility Measurements. *Phys Rev B* (2018) 97:104107. doi:10.1103/physrevb.97.104107
63. Chen T, Chen Y, Kreisel A, Lu X, Schneidewind A, Qiu Y, et al. Anisotropic Spin Fluctuations in Detwinned FeSe. *Nat Mater* (2019) 18(7):709–16. doi:10.1038/s41563-019-0369-5
64. Wang Z, Zhao X-G, Koch R, Billinge SJL, Zunger A. Understanding Electronic Peculiarities in Tetragonal FeSe as Local Structural Symmetry Breaking. *Phys Rev B* (2020) 102:235121. doi:10.1103/physrevb.102.235121
65. Gorni T, Villar Arribi P, Casula M, de' Medici L. Accurate Modeling of FeSe with Screened Fock Exchange and Hund Metal Correlations. *Phys Rev B* (2021) 104:014507. doi:10.1103/physrevb.104.014507
66. Mukherjee S, Kreisel A, Hirschfeld PJ, Andersen BM. Model of Electronic Structure and Superconductivity in Orbitally Ordered FeSe. *Phys Rev Lett* (2015) 115(2):026402. doi:10.1103/PhysRevLett.115.026402
67. Rhodes LC, Böker J, Müller MA, Eschrig M, Eremin IM. Non-local d_{xy} Nematicity and the Missing Electron Pocket in FeSe. *Npj Quan Mater.* (2021) 6(1):45. doi:10.1038/s41535-021-00341-6
68. Kushnirenko YS, Kordyuk AA, Fedorov AV, Haubold E, Wolf T, Büchner B, et al. Anomalous Temperature Evolution of the Electronic Structure of FeSe. *Phys Rev B* (2017) 96:100504. doi:10.1103/physrevb.96.100504
69. Pustovit YV, Bezguba VV, Kordyuk AA. Temperature Dependence of the Electronic Structure of FeSe. *Metallofiz Noveishie Tekhnol* (2017) 39:709–18. doi:10.15407/mfint.39.06.0709
70. Pustovit YV, Brouet V, Chareev DA, Kordyuk AA. Temperature Evolution of Charge Carrier Density in the Centre of the Brillouin Zone of Fe(Se,Te) Superconductor. *Metallofiz Noveishie Tekhnol* (2018) 40:139–46. doi:10.15407/mfint.40.02.0139
71. Schwier EF, Takita H, Mansur W, Ino A, Hoesch M, Watson MD, et al. Applications for Ultimate Spatial Resolution in LASER Based μ - ARPES: A FeSe Case Study. *AIP Conf Proc* (2019) 2054(1):040017. doi:10.1063/1.5084618
72. Shimojima T, Motoyui Y, Taniuchi T, Bareille C, Onari S, Kontani H, et al. Discovery of Mesoscopic Nematicity Wave in Iron-Based Superconductors. *Science* (2021) 373(6559):1122–5. doi:10.1126/science.abd6701
73. Tanatar MA, Böhmer AE, Timmons EI, Schütt M, Drachuck G, Taufour V, et al. Origin of the Resistivity Anisotropy in the Nematic Phase of FeSe. *Phys Rev Lett* (2016) 117:127001. doi:10.1103/physrevlett.117.127001
74. Hoesch M, Kim TK, Dudin P, Wang H, Scott S, Harris P, et al. A Facility for the Analysis of the Electronic Structures of Solids and Their Surfaces by Synchrotron Radiation Photoelectron Spectroscopy. *Rev Sci Instrum* (2017) 88:013106. doi:10.1063/1.4973562
75. Brouet V, Fuglsang Jensen M, Lin P-H, Taleb-Ibrahimi A, Le Fèvre P, Bertran F, et al. Impact of the Two Fe Unit Cell on the Electronic Structure Measured by ARPES in Iron Pnictides. *Phys Rev B* (2012) 86:075123. doi:10.1103/physrevb.86.075123
76. Day RP, Zwartsenberg B, Elfimov IS, Damascelli A. Computational Framework chinook for Angle-Resolved Photoemission Spectroscopy. *npj Quan Mater* (2019) 4(1):54. doi:10.1038/s41535-019-0194-8
77. Reiss P, Watson MD, Kim TK, Haghighirad AA, Woodruff DN, Bruma M, et al. Suppression of Electronic Correlations by Chemical Pressure from FeSe to FeS. *Phys Rev B* (2017) 96:121103. doi:10.1103/physrevb.96.121103
78. Pustovit YV, Kordyuk AA. Metamorphoses of Electronic Structure of FeSe-Based Superconductors. *Low Temperature Phys* (2016) 42(11):995–1007. doi:10.1063/1.4969896
79. Fisher IR, Degiorgi L, Shen ZX. In-plane Electronic Anisotropy of Underdoped '122' Fe-Arsenide Superconductors Revealed by Measurements of Detwinned Single Crystals. *Rep Prog Phys* (2011) 74(12):124506. doi:10.1088/0034-4885/74/12/124506
80. Bartlett JM, Steppke A, Hosoi S, Noad H, Park J, Timm C, et al. Relationship between Transport Anisotropy and Nematicity in FeSe. *Phys Rev X* (2021) 11:021038. doi:10.1103/physrevx.11.021038
81. Ghini M, Bristow M, Prentice JCA, Sutherland S, Sanna S, Haghighirad AA, et al. Strain Tuning of Nematicity and Superconductivity in Single Crystals of FeSe. *Phys Rev B* (2021) 103:205139. doi:10.1103/physrevb.103.205139
82. Rhodes LC, Watson MD, Kim TK, Eschrig M. K_z Selective Scattering within Quasiparticle Interference Measurements of FeSe. *Phys Rev Lett* (2019) 123:216404. doi:10.1103/physrevlett.123.216404
83. Sunko V, Abarca Morales E, Marković I, Barber ME, Milosavljević D, Mazzola F, et al. Direct Observation of a Uniaxial Stress-Driven Lifshitz Transition in Sr_2RuO_4. *npj Quan Mater* (2019) 4(1):46. doi:10.1038/s41535-019-0185-9
84. Iwasawa H. High-resolution Angle-Resolved Photoemission Spectroscopy and Microscopy. *Electron Struct* (2020) 2(4):043001. doi:10.1088/2516-1075/abb379
85. Watson MD, Dudin P, Rhodes LC, Evtushinsky DV, Iwasawa H, Aswartham S, et al. Probing the Reconstructed Fermi Surface of Antiferromagnetic $BaFe_2As_2$ in One Domain. *npj Quan Mater* (2019) 4(1):36. doi:10.1038/s41535-019-0174-z
86. Jiao L, Huang C-L, Rößler S, Koz C, Rößler UK, Schwarz U, et al. Superconducting gap Structure of FeSe. *Scientific Rep* (2017) 7(1):44024. doi:10.1038/srep44024
87. Choubey P, Berlijn T, Kreisel A, Cao C, Hirschfeld PJ. Visualization of Atomic-Scale Phenomena in Superconductors: Application to FeSe. *Phys Rev B* (2014) 90:134520. doi:10.1103/physrevb.90.134520
88. Bu K, Wang B, Zhang W, Fei Y, Zheng Y, Ai F, et al. Study of Intrinsic Defect States of FeSe with Scanning Tunneling Microscopy. *Phys Rev B* (2019) 100:155127. doi:10.1103/physrevb.100.155127
89. Macdonald AJ, Tremblay-Johnston Y-S, Grothe S, Chi S, Dosanjh P, Johnston S, et al. Dispersing Artifacts in FT-STS: a Comparison of Set point Effects across Acquisition Modes. *Nanotechnology* (2016) 27(41):414004. doi:10.1088/0957-4484/27/41/414004
90. Weismann A, Wenderoth M, Lounis S, Zahn P, Quaas N, Ulbrich RG, et al. Seeing the Fermi Surface in Real Space by Nanoscale Electron Focusing. *Science* (2009) 323(5918):1190–3. doi:10.1126/science.1168738
91. Lounis S, Zahn P, Weismann A, Wenderoth M, Ulbrich RG, Mertig I, et al. Theory of Real Space Imaging of Fermi Surface Parts. *Phys Rev B* (2011) 83:035427. doi:10.1103/physrevb.83.035427

92. Marques CA, Bahramy MS, Trainer C, Marković I, Watson MD, Mazzola F, et al. Tomographic Mapping of the Hidden Dimension in Quasi-Particle Interference. *Nat Comm* (2021) 12(1):6739. doi:10.1038/s41467-021-27082-1
93. Li C, Wu X, Wang L, Liu D, Cai Y, Wang Y, et al. Spectroscopic Evidence for an Additional Symmetry Breaking in the Nematic State of FeSe Superconductor. *Phys Rev X* (2020) 10:031033. doi:10.1103/physrevx.10.031033
94. Lee C-C, Yin W-G, Ku W. Ferro-Orbital Order and Strong Magnetic Anisotropy in the Parent Compounds of Iron-Pnictide Superconductors. *Phys Rev Lett* (2009) 103:267001. doi:10.1103/physrevlett.103.267001
95. Pradhan B, Parida PK, Sahoo S. Superconductivity and Jahn-Teller Distortion in S±-Wave Iron-Based Superconductors. *Braz J Phys* (2021) 51(3):393–400. doi:10.1007/s13538-020-00827-x
96. Kreisel A, Mukherjee S, Hirschfeld PJ, Andersen BM. Spin Excitations in a Model of FeSe with Orbital Ordering. *Phys Rev B* (2015) 92:224515. doi:10.1103/physrevb.92.224515
97. Kreisel A, Andersen BM, Hirschfeld PJ. Itinerant Approach to Magnetic Neutron Scattering of FeSe: Effect of Orbital Selectivity. *Phys Rev B* (2018) 98:214518. doi:10.1103/physrevb.98.214518
98. Yu R, Hu H, Nica EM, Zhu J-X, Si Q. Orbital Selectivity in Electron Correlations and Superconducting Pairing of Iron-Based Superconductors. *Front Phys* (2021) 9(92). doi:10.3389/fphy.2021.578347
99. Cercellier H, Rodière P, Toulemonde P, Marcenat C, Klein T. Influence of the Quasiparticle Spectral Weight in FeSe on Spectroscopic, Magnetic, and Thermodynamic Properties. *Phys Rev B* (2019) 100:104516. doi:10.1103/physrevb.100.104516
100. Christensen MH, Fernandes RM, Chubukov AV. Orbital Transmutation and the Electronic Spectrum of FeSe in the Nematic Phase. *Phys Rev Res* (2020) 2:013015. doi:10.1103/physrevresearch.2.013015
101. Jiang K, Hu J, Ding H, Wang Z. Interatomic Coulomb Interaction and Electron Nematic Bond Order in FeSe. *Phys Rev B* (2016) 93(11):115138. doi:10.1103/physrevb.93.115138
102. Biswas PK, Kreisel A, Wang Q, Adroja DT, Hillier AD, Zhao J, et al. Evidence of Nodal gap Structure in the Basal Plane of the FeSe Superconductor. *Phys Rev B* (2018) 98:180501. doi:10.1103/physrevb.98.180501
103. Xing R-Q, Classen L, Chubukov AV. Orbital Order in FeSe: The Case for Vertex Renormalization. *Phys Rev B* (2018) 98:041108. doi:10.1103/physrevb.98.041108
104. Kang J, Chubukov AV, Fernandes RM. Time-reversal Symmetry-Breaking Nematic Superconductivity in FeSe. *Phys Rev B* (2018) 98:064508. doi:10.1103/physrevb.98.064508
105. Mandal S, Zhang P, Ismail-Beigi S, Haule K. How Correlated Is the FeSe/SrTiO$_3$ System? *Phys Rev Lett* (2017) 119:067004. doi:10.1103/PhysRevLett.119.067004
106. Long X, Zhang S, Wang F, Liu Z. A First-Principle Perspective on Electronic Nematicity in FeSe. *npj Quan Mater* (2020) 5(1):50. doi:10.1038/s41535-020-00253-x
107. Yamada T, Tohyama T. Multipolar Nematic State of Nonmagnetic FeSe Based on DFT + U. *Phys Rev B* (2021) 104:L161110. doi:10.1103/physrevb.104.l161110
108. Steffensen D, Kreisel A, Hirschfeld PJ, Andersen BM. Interorbital Nematicity and the Origin of a Single Electron Fermi Pocket in FeSe. *Phys Rev B* (2021) 103:054505. doi:10.1103/physrevb.103.054505
109. Rodriguez EE, Stock C, Zajdel P, Krycka KL, Majkrzak CF, Zavalij P, et al. Magnetic-crystallographic Phase Diagram of the Superconducting Parent Compound Fe$_{1+x}$Te. *Phys Rev B* (2011) 84:064403. doi:10.1103/physrevb.84.064403
110. Trainer C, Yim C-M, Heil C, Giustino F, Croitori D, Tsurkan V, et al. Manipulating Surface Magnetic Order in Iron telluride. *Sci Adv* (2019) 5(3):eaav3478. doi:10.1126/sciadv.aav3478
111. Chubukov AV, Khodas M, Fernandes RM. Magnetism, Superconductivity, and Spontaneous Orbital Order in Iron-Based Superconductors: Which Comes First and Why? *Phys Rev X* (2016) 6:041045. doi:10.1103/physrevx.6.041045
112. Xing R-Q, Classen L, Khodas M, Chubukov AV. Competing Instabilities, Orbital Ordering, and Splitting of Band Degeneracies from a Parquet Renormalization Group Analysis of a Four-Pocket Model for Iron-Based Superconductors: Application to FeSe. *Phys Rev B* (2017) 95:085108. doi:10.1103/physrevb.95.085108
113. Classen L, Xing R-Q, Khodas M, Chubukov AV. Interplay between Magnetism, Superconductivity, and Orbital Order in 5-Pocket Model for Iron-Based Superconductors: Parquet Renormalization Group Study. *Phys Rev Lett* (2017) 118:037001. doi:10.1103/PhysRevLett.118.037001
114. Islam KR, Böker J, Eremin IM, Chubukov AV. Specific Heat and gap Structure of a Nematic Superconductor: Application to FeSe. *Phys Rev B* (2021) 104:094522. doi:10.1103/physrevb.104.094522
115. Marciani M, Benfatto L. Resistivity Anisotropy from Multiorbital Boltzmann Equation in Nematic FeSe. (2022). *arXiv:2202.12070*.
116. Li J, Lei B, Zhao D, Nie LP, Song DW, Zheng LX, et al. Spin-Orbital-Intertwined Nematic State in FeSe. *Phys Rev X* (2020) 10:011034. doi:10.1103/physrevx.10.011034
117. Liu S, Yuan J, Ma S, Lu Z, Zhang Y, Ma M, et al. Magnetic-Field-Induced Spin Nematicity in FeSe$_{1-x}S_x$ and FeSe$_{1-y}$Te$_y$ Superconductor Systems. *Chin Phys. Lett.* (2021) 38:087401. doi:10.1088/0256-307x/38/8/087401
118. Medvedev S, McQueen TM, Troyan IA, Palasyuk T, Eremets MI, Cava RJ, et al. Electronic and Magnetic Phase Diagram of β-Fe$_{1.01}$Se with Superconductivity at 36.7K under Pressure. *Nat Mater* (2009) 8(8):630–3. doi:10.1038/nmat2491
119. Huang D, Hoffman JE. Monolayer FeSe on SrTiO$_3$. *Annu Rev Condens Matter Phys* (2017) 8(1):311–36. doi:10.1146/annurev-conmatphys-031016-025242
120. Hardy F, He M, Wang L, Wolf T, Schweiss P, Merz M, et al. Calorimetric Evidence of Nodal Gaps in the Nematic Superconductor FeSe. *Phys Rev B* (2019) 99:035157. doi:10.1103/physrevb.99.035157
121. Sun Y, Kittaka S, Nakamura S, Sakakibara T, Irie K, Nomoto T, et al. Gap Structure of FeSe Determined by Angle-Resolved Specific Heat Measurements in Applied Rotating Magnetic Field. *Phys Rev B* (2017) 96:220505. doi:10.1103/physrevb.96.220505
122. Matsuura K, Mizukami Y, Arai Y, Sugimura Y, Maejima N, Machida A, et al. Maximizing Tc by Tuning Nematicity and Magnetism in FeSe$_{1-x}S_x$ Superconductors. *Nat Commun* (2017) 8(1):1143. doi:10.1038/s41467-017-01277-x
123. Wang Q, Shen Y, Pan B, Zhang X, Ikeuchi K, Iida K, et al. Magnetic Ground State of FeSe. *Nat Comm* (2016) 7(1):12182. doi:10.1038/ncomms12182
124. Wang Q, Shen Y, Pan B, Hao Y, Ma M, Zhou F, et al. Strong Interplay between Stripe Spin Fluctuations, Nematicity and Superconductivity in FeSe. *Nat Mater* (2016) 15(2):159–63. doi:10.1038/nmat4492
125. Watson MD, Aswartham S, Rhodes LC, Parrett B, Iwasawa H, Hoesch M, et al. Three-dimensional Electronic Structure of the Nematic and Antiferromagnetic Phases of NaFeAs from Detwinned Angle-Resolved Photoemission Spectroscopy. *Phys Rev B* (2018) 97:035134. doi:10.1103/physrevb.97.035134
126. Chen T, Yi M, Dai P. Electronic and Magnetic Anisotropies in FeSe Family of Iron-Based Superconductors. *Front Phys* (2020) 8:314. doi:10.3389/fphy.2020.00314
127. Coldea AI, Blake SF, Kasahara S, Haghighirad AA, Watson MD, Knafo W, et al. Evolution of the Low-Temperature Fermi Surface of Superconducting FeSe$_{1-x}S_x$ across a Nematic Phase Transition. *npj Quan Mater* (2019) 4(1):2. doi:10.1038/s41535-018-0141-0

Conflict of Interest: The authors declare that the research was conducted in the absence of any commercial or financial relationships that could be construed as a potential conflict of interest.

frontiers | Frontiers in Physics

ORIGINAL RESEARCH
published: 13 June 2022
doi: 10.3389/fphy.2022.886459

Edited by:
Ivar Martin,
Argonne National Laboratory (DOE),
United States

Reviewed by:
Andreas Kreisel,
Leipzig University, Germany
Yao Shen,
Brookhaven National Laboratory
(DOE), United States

***Correspondence:**
Huiqian Luo
hqluo@iphy.ac.cn

†Present addresses:
Dongliang Gong,
Department of Physics and
Astronomy, University of Tennessee,
Knoxville, Tennessee, United States
Tao Xie,
Neutron Scattering Division, Oak
Ridge National Laboratory, Oak Ridge,
Tennessee, United States
Wenliang Zhang,
Photon Science Division, Swiss Light
Source, Paul Scherrer Institut, Villigen
PSI, Switzerland

Specialty section:
This article was submitted to
Condensed Matter Physics,
a section of the journal
Frontiers in Physics

Received: 28 February 2022
Accepted: 12 April 2022
Published: 13 June 2022

Citation:
Gong D, Yi M, Wang M, Xie T,
Zhang W, Danilkin S, Deng G, Liu X,
Park JT, Ikeuchi K, Kamazawa K,
Mo S-K Hashimoto M, Lu D, Zhang R,
Dai P, Birgeneau RJ, Li S and Luo H
(2022) Nematic Fluctuations in the
Non-Superconducting Iron Pnictide
$BaFe_{1.9-x}Ni_{0.1}Cr_xAs_2$.
Front. Phys. 10:886459.
doi: 10.3389/fphy.2022.886459

Nematic Fluctuations in the Non-Superconducting Iron Pnictide $BaFe_{1.9-x}Ni_{0.1}Cr_xAs_2$

*Dongliang Gong[1,2†], Ming Yi[3,4], Meng Wang[5], Tao Xie[1,2†], Wenliang Zhang[1,2†], Sergey Danilkin[6], Guochu Deng[6], Xinzhi Liu[5], Jitae T. Park[7], Kazuhiko Ikeuchi[8], Kazuya Kamazawa[8], Sung-Kwan Mo[9], Makoto Hashimoto[10], Donghui Lu[10], Rui Zhang[11], Pengcheng Dai[11], Robert J. Birgeneau[4,12,13], Shiliang Li[1,2,14] and Huiqian Luo[1,14]**

[1]Beijing National Laboratory for Condensed Matter Physics, Institute of Physics, Chinese Academy of Sciences, Beijing, China, [2]School of Physical Sciences, University of Chinese Academy of Sciences, Beijing, China, [3]Department of Physics and Astronomy, Rice University, Houston, TX, United States, [4]Department of Physics, University of California, Berkeley, Berkeley, CA, United States, [5]School of Physics, Sun Yat-Sen University, Guangzhou, China, [6]Australian Centre for Neutron Scattering, Australian Nuclear Science and Technology Organisation, Lucas Heights, NSW, Australia, [7]Heinz Maier-Leibnitz Zentrum (MLZ), Technische Universität München, Garching, Germany, [8]Neutron Science and Technology Center, Comprehensive Research Organization for Science and Society, Tokai, Japan, [9]Lawrence Berkeley National Laboratory, Berkeley, CA, United States, [10]Stanford Synchrotron Radiation Lightsource, SLAC National Accelerator Laboratory, Menlo Park, CA, United States, [11]Department of Physics and Astronomy, Rice Center for Quantum Materials, Rice University, Houston, TX, United States, [12]Materials Science Division, Lawrence Berkeley National Laboratory, Berkeley, CA, United States, [13]Department of Materials Science and Engineering, University of California, Berkeley, Berkeley, CA, United States, [14]Songshan Lake Materials Laboratory, Dongguan, China

The main driven force of the electronic nematic phase in iron-based superconductors is still under debate. Here, we report a comprehensive study on the nematic fluctuations in a non-superconducting iron pnictide system $BaFe_{1.9-x}Ni_{0.1}Cr_xAs_2$ by electronic transport, angle-resolved photoemission spectroscopy (ARPES), and inelastic neutron scattering (INS) measurements. Previous neutron diffraction and transport measurements suggested that the collinear antiferromagnetism persists to $x = 0.8$, with similar Néel temperature T_N and structural transition temperature T_s around 32 K, but the charge carriers change from electron type to hole type around $x = 0.5$. In this study, we have found that the in-plane resistivity anisotropy also highly depends on the Cr dopings and the type of charge carriers. While ARPES measurements suggest possibly weak orbital anisotropy onset near T_s for both $x = 0.05$ and $x = 0.5$ compounds, INS experiments reveal clearly different onset temperatures of low-energy spin excitation anisotropy, which is likely related to the energy scale of spin nematicity. These results suggest that the interplay between the local spins on Fe atoms and the itinerant electrons on Fermi surfaces is crucial to the nematic fluctuations of iron pnictides, where the orbital degree of freedom may behave differently from the spin degree of freedom, and the transport properties are intimately related to the spin dynamics.

Keywords: iron-based superconductors, electronic nematic phase, nematic fluctuations, resistivity, spin excitations, orbital ordering, neutron scattering

1 INTRODUCTION

Electronic nematic phase breaks the rotational symmetry but preserves the translational symmetry of the underlying lattice in correlated materials [1–4]. In iron-based superconductors, the nematic order associated with a tetragonal-to-orthorhombic structural transition at temperature T_s acts as a precursor of the magnetic order below T_N and the superconducting state below T_c [5–10]. The nematic fluctuations can be described by the electronic nematic susceptibility, which is defined as the susceptibility of electronic anisotropy to the uniaxial in-plane strain [11]. Divergent nematic susceptibility upon approaching T_s from high temperature is revealed by the elastoresistance and elastic moduli measurements, suggesting nematic fluctuations well above T_s [12–16]. The nematic fluctuations commonly exist in iron-based superconductors and are even present in compounds with tetragonal crystal symmetry without any static nematic order [17]. Accumulating evidence suggests that the optimal superconductivity with maximum T_c usually occurs near a nematic quantum critical point where the nematic fluctuations are the strongest [18–29]. However, the charge, spin, and orbital degrees of freedom are always intertwined in the presence of nematic fluctuations [30–39], giving a twofold rotational (C_2) symmetry in many physical properties [5–11, 40–44] including anisotropic in-plane electronic resistivity and optical conductivity [45–51], lifting of degeneracy between d_{xz}/d_{yz} orbitals [52–58], anisotropic spin excitations at low energies [59–63], phonon-energy split in lattice dynamics [64, 65], and splitting of the Knight shift [66, 67]. In addition, it has been proposed that the local anisotropic impurity scattering of chemical dopants likely induces the twofold symmetry in the transport properties [68–70]. Such complex cases make it is difficult to clarify the main driven force of nematic phase by a single experimental probe.

Our previous works suggest that the Cr substitution is an effective way both to suppress the superconductivity and to tune the magnetism in iron-based superconductors [27, 71–73]. Specifically, in the $BaFe_{1.9-x}Ni_{0.1}Cr_xAs_2$ system, by continuously doping Cr to the optimally superconducting compound $BaFe_{1.9}Ni_{0.1}As_2$ with $T_c = 20$ K, the superconductivity is quickly suppressed above $x = 0.05$, but the magnetic transition temperature T_N and the structural transition temperature T_s remain between 30 and 35 K as shown by neutron diffraction results on naturally twinned samples (**Figure 1A**). Moreover, the effective moment m is significantly enhanced first and then suppressed for dopings higher than $x = 0.5$, where the charge carriers change from electron type to hole type as shown by the sign of Hall and Seebeck coefficients [73]. These make $BaFe_{1.9-x}Ni_{0.1}Cr_xAs_2$ a rare example to separately tune the magnetically ordered temperature T_N by the local spin interactions and the magnetically ordered strength by the scattering of itinerant electrons on Fermi surfaces, respectively. The extra holes introduced by Cr substitutions compensate the electron doping thus may drive those non-superconducting compounds to a half-filled Mott insulator similar to the parent compounds of cuprate and nickelate superconductors [74–79]. It would be interesting to monitor the evolution of the nematic fluctuations starting from a metallic state toward to a localized insulating state [79–81], especially on the detwinned samples (**Figure 1B**).

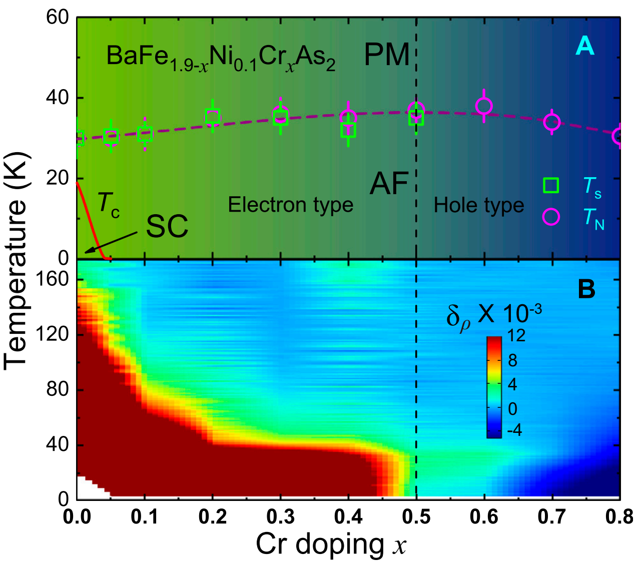

FIGURE 1 | (Color online) Phase diagram and in-plane resistivity anisotropy of $BaFe_{1.9-x}Ni_{0.1}Cr_xAs_2$. **(A)** The PM, AF, and SC mark the region of paramagnetic, antiferromagnetic, and superconducting phases defined by T_s, T_N, and T_c, respectively. Here, T_s and T_N were measured by neutron diffraction in our previous work on the naturally twinned samples [73]. **(B)** The gradient color maps the in-plane resistivity anisotropy δ_ρ measured on detwinned samples. The vertical dashed line divides the regions for electron-type and hole-type charge carriers as determined by the sign of Hall and Seebeck coefficients [73].

In this paper, we further report a multi-probe study on the nematic fluctuations in the non-superconducting compounds $BaFe_{1.9-x}Ni_{0.1}Cr_xAs_2$ ($x = 0.05 \sim 0.8$) by electronic transport, angle-resolved photoemission spectroscopy (ARPES), and inelastic neutron scattering (INS) measurements. The in-plane resistivity anisotropy measured in the detwinned samples under uniaxial pressure shows a strong dependence on the Cr content with a clear sign change above $x = 0.6$. By focusing on two compounds with $x = 0.05$ and 0.5, ARPES measurements suggest possible band shifts induced by orbital anisotropy near T_s/T_N for both dopings, but INS experiments reveal clearly different behaviors on the spin nematicity. The onset temperature of low-energy spin excitation anisotropy between $Q = (1, 0, 1)$ and $Q = (0, 1, 1)$ for $x = 0.05$ is about 110 K, but for $x = 0.5$, it is much lower, only about 35 K near the magnetic transition. Such temperature dependence of spin nematicity is consistent with the results of in-plane resistivity anisotropy. At high energies, the spin nematicity for $x = 0.05$ extends to about 120 meV, much larger than the case for $x = 0.5$ (about 40 meV), suggesting a possible linear correlation between the highest energy scale and the onset temperature of spin nematicity. Therefore, the nematic behaviors in iron pnictides are highly related to the interplay between local moments and itinerant electrons. While the C_2-type anisotropies in spin excitations and in-plane resistivity are strongly correlated with each other [60], the orbital anisotropy induced band splitting may behave differently as affected by the complex Fermi surface topology [82–91].

2 EXPERIMENT DETAILS

High-quality single crystals of $BaFe_{1.9-x}Ni_{0.1}Cr_xAs_2$ were grown by the self-flux method [71–73, 92–95]; the characterization results of our sample can be found in previous reports [71, 73]. The crystalline directions of our sample were determined by an X-ray Laue camera (*Photonic Sciences*) in the backscattering mode with incident beam along the $c-$ axis. After that, the crystals were cut into rectangle shapes (typical sizes: 1 mm × 2 mm) by a wire saw under the directions $[1, 0, 0] \times [0, 1, 0]$ in orthorhombic lattice notation ($a = b = 5.6$ Å). By applying a uniaxial pressure around 10 MPa, the crystal can be fully detwinned at low temperature, where the direction of pressure was defined as the b direction, and the pressure-free direction was defined as the a direction [60–63, 96–99]. The in-plane resistivity ($\rho_{a,b}$) was measured by the standard four-probe method with the Physical Property Measurement System (PPMS) from Quantum Design. To compare the temperature dependence of resistivity at different directions, we normalized the resistivity $\rho_{a,b}(T)$ data at 150 K for each sample. The in-plane resistivity anisotropy was defined by $\delta_\rho = (\rho_b - \rho_a)/(\rho_b + \rho_a)$ same as other literature [45–47].

ARPES experiments were performed at beamline 10.0.1 of the Advanced Light Source and beamline 5-4 of the Stanford Synchrotron Radiation Light source with R4000 electron analyzers. The angular resolution was 0.3°, and the total energy resolution was 15 meV. All samples were cleaved *in-situ* at 10 K and measured in ultra-high vacuum with a base pressure lower than 4×10^{-11} Torr. We note that we used twinned samples without uniaxial pressure for the ARPES experiments. INS experiments were carried out at two thermal triple-axis spectrometers: PUMA at Heinz Maier-Leibnitz Zentrum (MLZ) [100], Germany, and TAIPAN at the Australian Centre for Neutron Scattering (ACNS) [101], ANSTO, Australia. The wave vector **Q** at (q_x, q_y, q_z) was defined as $(H, K, L) = (q_x a/2\pi, q_y b/2\pi, q_z c/2\pi)$ in reciprocal lattice units (r.l.u.) using the orthorhombic lattice parameters $a \approx b = 5.6$ Å and $c \approx 13$ Å. All measurements were done with fixed final energy $E_f = 14.8$ meV, and a double focusing monochromator and analyzer using pyrolytic graphite crystals. To gain a better signal-noise ratio, eight pieces of rectangularly cut crystals (typical sizes: 7 mm × 8 mm × 0.5 mm) were assembled in a detwinned device made by aluminum and springy gaskets [60–63]. To reach both $Q = (1, 0, 1)$ and $Q = (0, 1, 1)$, the sample holder was designed to easily rotate by 90°, thus the scattering plane can switch from $[H, 0, 0] \times [0, 0, L]$ to $[0, K, 0] \times [0, 0, L]$. The total mass of the crystals used in INS experiments was about 2 g from each sample set of $x = 0.05$ and $x = 0.5$. Time-of-flight neutron scattering experiments were carried out on the same sample sets at 4SEASONS spectrometer (BL-01) at J-PARC [102, 103], Tokai, Japan, with multiple incident energies $E_i = 250, 73, 34, 20$ meV, k_i parallel to the c axis, and chopper frequency $f = 250$ Hz. The data were only corrected by the efficiency of detectors from the incoherent scattering of vanadium with white beam. As we were comparing two samples with similar mass under the same measured conditions at the same spectrometer, it was not necessary to do the vanadium normalization with mono-beam. The data were analyzed by the Utsusemi and MSlice software packages [104, 105].

3 RESULTS AND DISCUSSIONS

We first present the resistivity results in **Figures 1-3**. Apparently, the in-plane resistivity anisotropy show a strong dependence on the Cr doping level. In the Cr free sample $BaFe_{1.9}Ni_{0.1}As_2$, the difference between ρ_a and ρ_b presents above the superconducting transition temperature $T_c = 20$ K, where ρ_a is metallic and ρ_b is semiconducting-like with an upturn at low temperature (namely, $\rho_a < \rho_b$) (**Figure 2A**). The superconductivity is completely suppressed at $x = 0.05$, and there is a dramatic difference between ρ_a and ρ_b with an anisotropy δ_ρ persisting to about $T = 110$ K (**Figure 2B**). By further increasing Cr doping, both ρ_a and ρ_b become semiconducting-like even insulating-like above $x = 0.1$, and the resistivity anisotropy gets weaker and weaker, until it nearly disappears at $x = 0.5$ and 0.6 compounds (**Figure 2C–H**). For those high doping compounds $x = 0.7$ and 0.8, it seems that δ_ρ changes sign with $\rho_a > \rho_b$ at low temperatures (**Figure 2I,J**). To clearly compare the resistivity anisotropy upon Cr doping, we plot δ_ρ as gradient color mapping in **Figure 1B** and show its detailed temperature dependence in **Figure 3**. Interestingly, the sign of δ_ρ is also related to the type of charge carriers. δ_ρ keeps strong and positive in the electron-type compounds but changes to negative and weak ($<1\%$) in the hole-type compounds (**Figure 1B** and **Figure 3B**). This is consistent with the results in the electron doped $BaFe_{2-x}(Ni, Co)_xAs_2$ and the hole doped $Ba_{1-x}K_xFe_2As_2$, $Ca_{1-x}Na_xFe_2As_2$, and $BaFe_{2-x}Cr_xAs_2$ systems [45–48, 106–109]. However, in those cases, the onset temperature of δ_ρ decreases with the structural transition temperature T_s when increasing the doping level from the non-superconducting parent compounds to optimally doped superconducting compounds. Here, in the $BaFe_{1.9-x}Ni_{0.1}Cr_xAs_2$ system, both T_N and T_s are actually within the range $32 \sim 35$ K for all probed dopings [73], but the onset temperature of δ_ρ still extends to high temperatures, and it is then strongly suppressed by Cr doping (**Figure 3A**). In those hole-type compounds, δ_ρ shows a peak feature (for $x = 0.5$ and 0.6) or a kink (for $x = 0.7$ and 0.8) responding to the magnetic and structural transitions (**Figure 3B**). The non-monotonic behavior of δ_ρ may come from the competition between the scattering from hole bands and electron bands, and similar behaviors were observed in the nematic susceptiblity of the Cr doped $BaFe_2(As_{1-x}P_x)_2$ system [27].

Next, we focus on the electronic structure and the spin excitations in two typical dopings $x = 0.05$ with $T_N = 32$ K and $x = 0.5$ with $T_N = 35$ K. The Fermi surface topology and band structure measured by ARPES on naturally twinned samples are shown in **Figure 4**. From the Fermi surface mapping in **Figure 4A,B**, we can find typical hole pockets

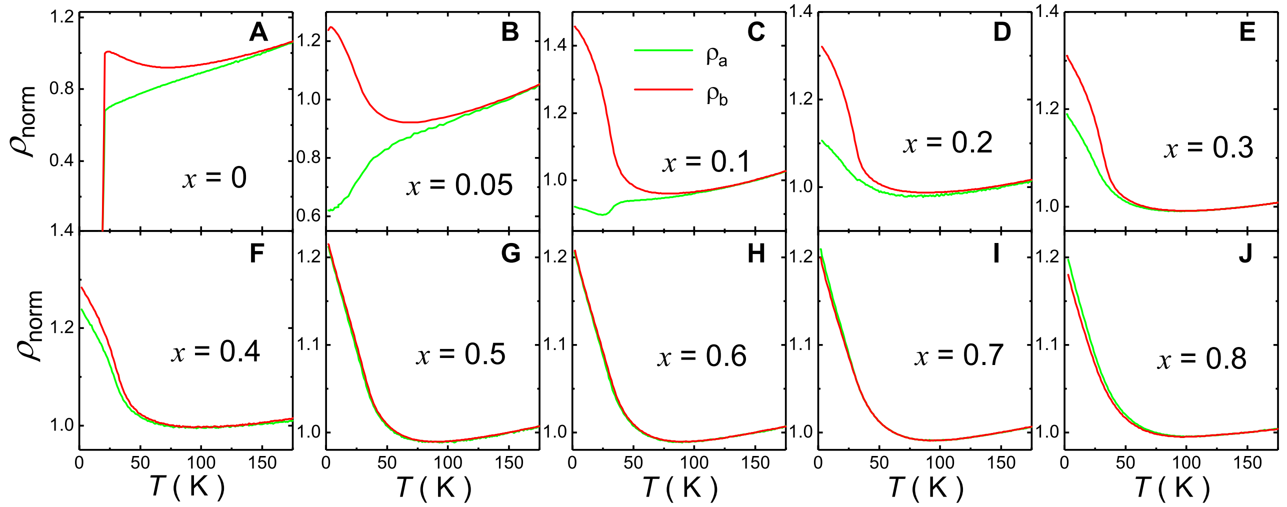

FIGURE 2 | (Color online) In-plane resistivity anisotropy of BaFe$_{1.9-x}$Ni$_{0.1}$Cr$_x$As$_2$ under uniaxial pressure. Here, ρ_b is the in-plane resistivity along the direction of uniaxial pressure, and ρ_a is the in-plane resistivity perpendicular to the direction of uniaxial pressure. For easy comparison, each curve is normalized by its resistivity at 150 K, and there is no resistivity anisotropy above this temperature.

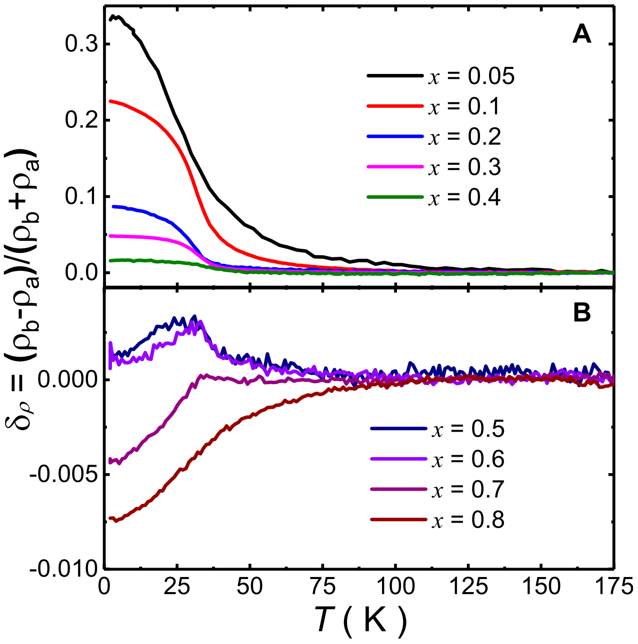

FIGURE 3 | (Color online) Temperature dependence of the in-plane resistivity anisotropy δ_ρ from $x = 0.05$ to 0.8. **(A)** In electron-type compounds, δ_ρ gets weaker but keeps positive when increasing Cr doping. **(B)** In hole-type compounds, δ_ρ is very weak and becomes negative when $x \geq 0.7$.

around the zone center *Γ* point. Near the *X* point, an electron pocket is observed for $x = 0.05$. For $x = 0.5$, however, the Fermi surface resembles that of the hole-doped (Ba,K)Fe$_2$As$_2$ [53]. This is due to the hole doping introduced by the Cr substitution, which also introduces disorder directly in the Fe-planes, thus resulting in spectral features that appear broad [82]. **Figure 4C,D** show the second energy derivatives of the spectral images along the high symmetry direction (Γ-*X*). Larger hole pockets can indeed be seen for $x = 0.5$ compared to $x = 0.05$. As has been demonstrated previously on BaFe$_2$As$_2$, NaFeAs, and FeSe, the onset of T_s is associated with the onset of an observed anisotropic shift of the d_{xz} and d_{yz} orbital-dominated bands where the d_{xz} band shifts down and the d_{yz} band shifts up [52–56]. This shift is most prominently observed near the X point of the Brillouin zone. Moreover, such band splitting as measured on uniaxially strained crystals can be observed above T_s in the presence of this symmetry-breaking field. On a structurally twinned crystal, the anisotropic band shifts would appear in the form of a band splitting due to domain mixing. While we do not observe clearly the band splitting as shown in **Figure 4C,D**, we can clearly observe the lower branch with dominant intensity that shifts with temperature. This can be understood as the lower d_{xz} band. We can fit the energy position of the band extracted from the X point and plot as a function of temperature. The temperature evolution clearly identifies a temperature scale associated with an onset of the band shift [53–55]. As shown in **Figure 4E,F**, the *X* band shifts at low temperature $T \approx 25$ K for $x = 0.05$ and $T \approx 45$ K for $x = 0.5$, respectively, closing to their structural or magnetic transition temperatures. We do note that while we cannot conclusively state that this represents the orbital anisotropy, the behavior we observe here on these twinned crystals is consistent with the expectation of the onset of orbital anisotropy [52, 57, 62]. We note here that the observed onset temperature of band splitting is close to the T_s (or T_N), in contrast to the much higher onset in the resistivity anisotropy shown in **Figure 3** measured on a strained crystal.

We then turn to search the connection between the resistivity anisotropy and the spin excitation anisotropy. The first evidence of spin nematicity was observed in BaFe$_{2-x}$Ni$_x$As$_2$ (x = 0, 0.065, 0.085, 0.10, 0.12) [60–63], where BaFe$_{1.9}$Ni$_{0.1}$As$_2$

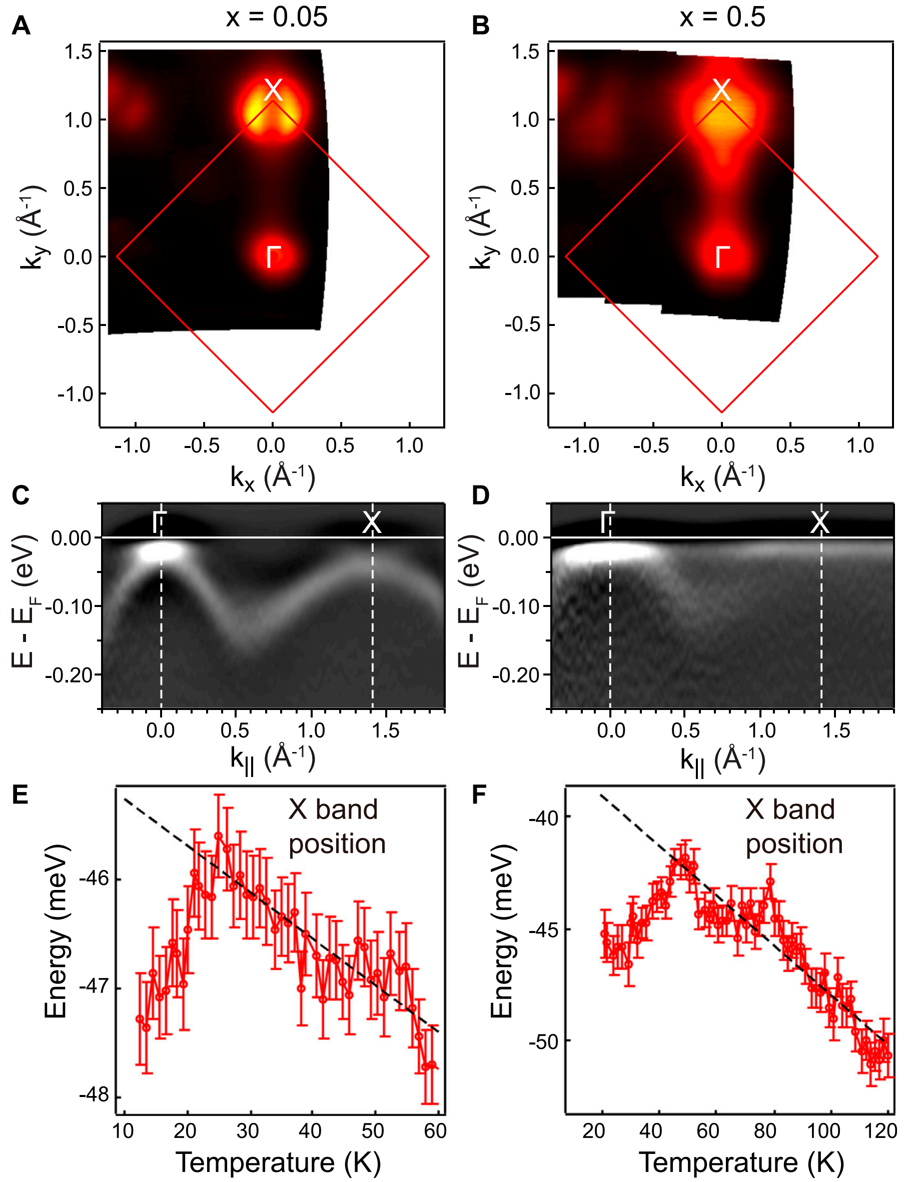

FIGURE 4 | (Color online) ARPES results on $x = 0.05$ (left) and $x = 0.5$ (right) compounds. **(A)–(B)** The measured Fermi surfaces around the Γ and X points. **(C)–(D)** Band dispersions along the high symmetry direction Γ-X obtained from the second derivatives in the energy direction. **(E)–(F)** Temperature dependence of the fitted band position from the X point. All dashed lines are guides for eyes.

is the starting compound of this study. Low-energy spin excitations are measured on the detwinned $BaFe_{1.9-x}Ni_{0.1}Cr_xAs_2$ ($x = 0.05$ and 0.5) samples by INS experiments using two triple-axis spectrometers. The results of constant-energy scans at $E = 3$, 6, 9, and 12 meV are summarized in **Figure 5**. With convenient design of the detwinned device and sample holder, we can easily perform constant-energy scans (Q − scans) either along the $[H, 0, 1]$ or $[0, K, 1]$ direction after rotating the whole sample set by 90°. For the $x = 0.5$ sample, we instead do the $S1$ rocking scans at $Q = (1, 0, 1)$ and $(0, 1, 1)$. It should be noticed that the Néel temperature T_N is slightly enhanced by the applied uniaxial pressure in the $x = 0.05$ sample from 32 to 40 K (so does T_s) but does not change for the $x = 0.5$ sample ($T_N \approx T_N' = 35$ K) (**Figure 6A,B**). Such an effect has been detected in the $BaFe_{2-x}(Ni, Co)_xAs_2$ system [110]. The detwinned ratio can be estimated by comparing the integrated intensities of magnetic Bragg peak between $Q = (1, 0, 1)$ and $Q = (0, 1, 1)$ positions, which is about 10:1 for the $x = 0.05$ samples, and 4:1 for the $x = 0.5$ samples, respectively. Such a large ratio means successful detwin for both sample sets. At the first glance, it is very clear for the difference of the spin excitations between $Q = (1, 0, 1)$ and $Q = (0, 1, 1)$ especially at low temperatures, which could be attributed to the spin Ising-nematic correlations (so-called spin nematicity).

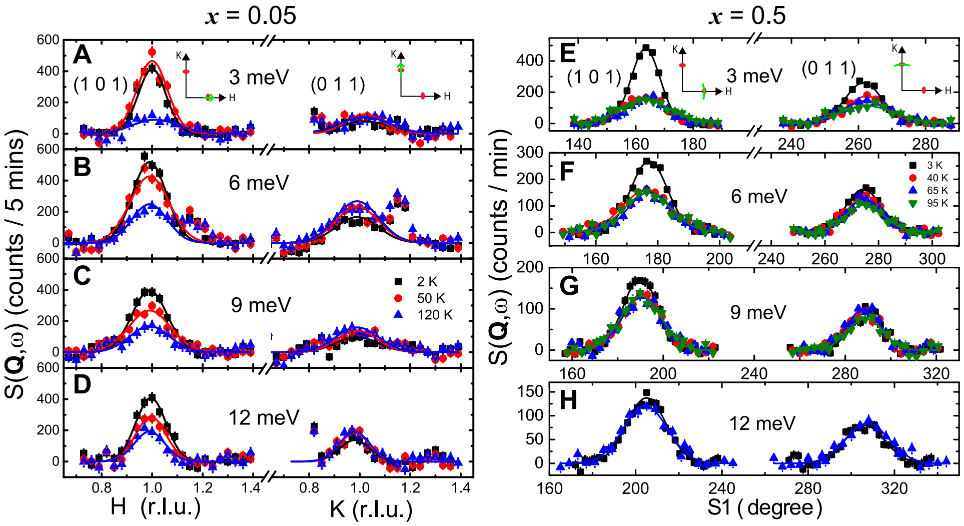

FIGURE 5 | (Color online) Inelastic neutron scattering results on the spin excitations of uniaxially detwinned samples for $x = 0.05$ (left) and $x = 0.5$ (right) compounds measured by two triple-axis spectrometers TAIPAN and PUMA. We compared the constant-energy scans (Q –scans along [H,0,1] or [0, K,1], $S1$ rocking scans at $Q = (1,0,1)$ or (0, 1, 1)) for $E = 3, 6, 9, 12$ meV, respectively. All data are corrected by a linearly Q –dependent background, and the solid lines are Gaussian fittings. The spurious signals in 6 meV data are ignored.

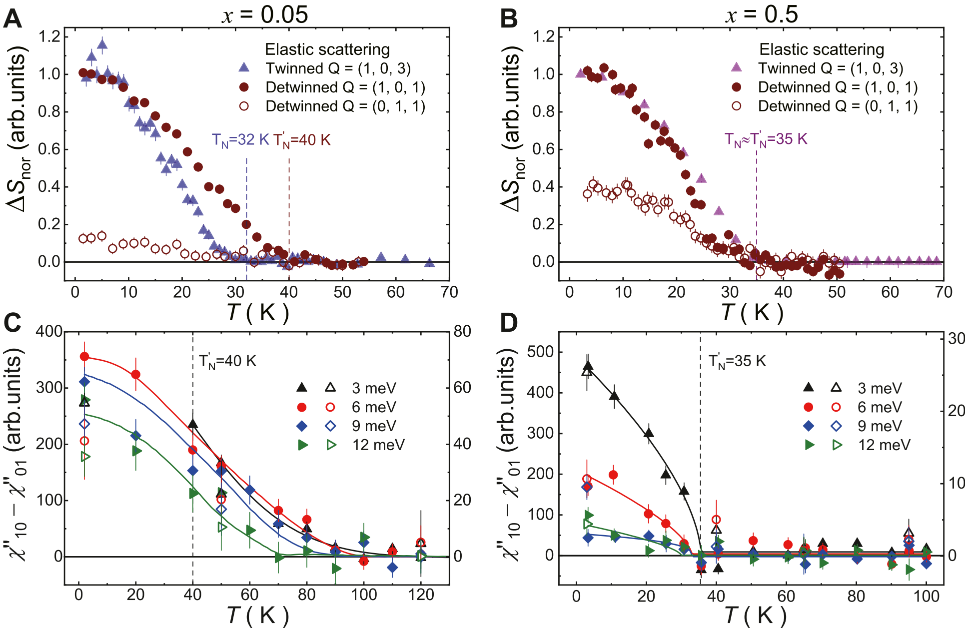

FIGURE 6 | (Color online) The order parameter of antiferromagnetism and spin nematicity $\chi''_{10} - \chi''_{01}$ for $x = 0.05$ and $x = 0.5$ compounds. **(A)** and **(B)** The magnetic order parameters measured at $Q = (1,0,3)$ on twinned samples, $Q = (1,0,1)$ and $Q = (0,1,1)$ on detwinned samples by elastic neutron scattering. All data are subtracted by the normal state background and normalized by the intensity at base temperature for $Q = (1,0,3)$ or $Q = (1,0,1)$. **(C)** and **(D)** Spin nematicity measured by inelastic neutron scattering. The solid symbols are the differences of local susceptibility χ'' between $Q = (1,0,1)$ and $Q = (0,1,1)$ (left y-axis), and the open symbols are similar but obtained by integrating the constant-energy scans in **Figure 5** corrected by the Bose population factor (right y-axis). The vertical dash lines mark the magnetic transition temperature T_N on twinned samples and T'_N on detwinned samples. All solid lines are guides to eyes.

After warming up to high temperatures, the spin excitations at $Q = (1, 0, 1)$ decrease and become nearly identical to those at $Q = (0, 1, 1)$. The nematic order parameter for the spin system can be approximately represented by $\chi''_{nematic} = \chi''_{10} - \chi''_{01}$, in which χ''_{10} (or χ''_{01}) is the local spin susceptibility at $Q = (1, 0, 1)$ (or $Q = (0, 1, 1)$). **Figure 6C,D** show the temperature

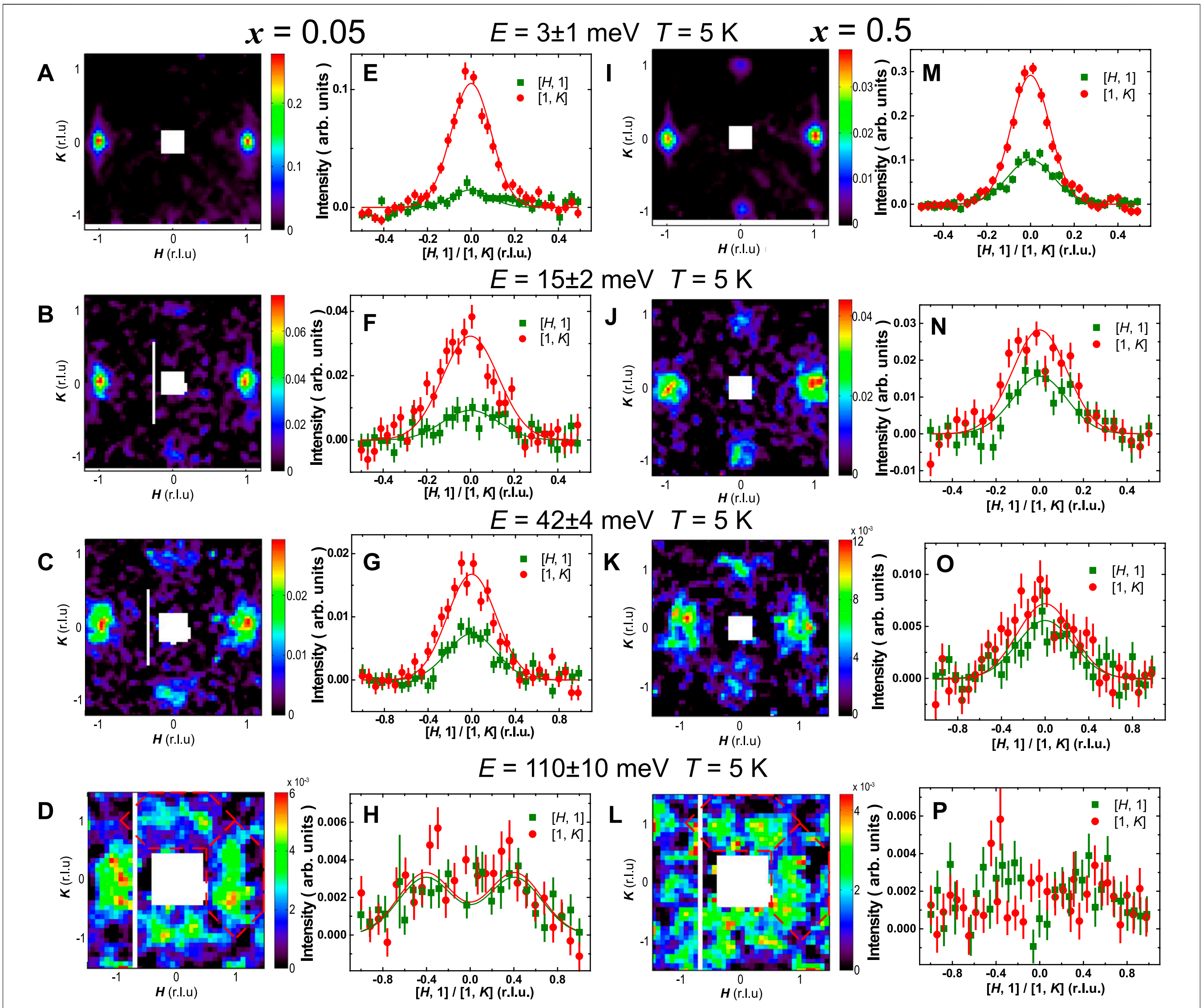

FIGURE 7 | (Color online) Inelastic neutron scattering results on the spin excitations of the uniaxially detwinned samples for $x = 0.05$ (left) and $x = 0.5$ (right) compounds measured at $T = 5$ K by time-of-flight spectrometer 4SEASONS. All data are presented in both 2D slices for the $[H, K]$ plane and 1D cuts along $[H,0]$ or $[0, K]$ at typical energy windows $E = 3±1, 15±2, 42±4, 110±10$ meV. The solid lines are Gaussian fittings guiding for eyes, which are not shown in panel **(P)** due to poor data quality. The dashed diamonds in panel **(D)** and **(L)** illustrate the integrated Brillouin zone for spin excitations around $Q = (1,0)$ and $Q = (0,1)$, respectively.

dependence of $\chi''_{10} - \chi''_{01}$ for both compounds, where the Bose population factor is already corrected. We also plot the data (open symbols) obtained from the integrated intensity of those Q − scans in **Figure 5**. For the $x = 0.05$ compound, the spin nematicity decreases slightly upon increasing energy and terminates well above $T'_N = 40$ K (**Figure 6C**)[73]. For the lowest energy we measured (3 meV), the onset temperature of spin nematicity is about 110 K, similar to the in-plane resistivity anisotropy in **Figure 3A**. The results for $x = 0.5$ compound show markedly differences, where $\chi''_{10} - \chi''_{01}$ quickly decreases with both energy and temperature, and the onset temperature is around $T'_N = 35$ K (**Figure 6D**). No spin anisotropy can be detected above 40 K for both Q − scans and energy scans, and this is also consistent with the very weak in-plane resistivity anisotropy for $x = 0.5$ (**Figure 3B**). The spin nematic theory predicts that the nematic fluctuations enhance both the intensity and the correlation length of spin excitations at $(\pi, 0)$ but suppress those at $(0, \pi)$ even above T_s. This was firstly testified in the detwinned $BaFe_{1.935}Ni_{0.065}As_2$ and can also be seen here in **Figure 5**[61]. Although the peak intensities at $Q = (1, 0, 1)$ seem stronger than those at $Q = (0, 1, 1)$ in **Figure 5G,H**, the peak width is smaller, and the integrated intensity of the Q-scans are closed to each other. The above results of spin nematicity in $BaFe_{1.9-x}Ni_{0.1}Cr_xAs_2$ ($x = 0.05$ and 0.5) resemble to those in $BaFe_{2-x}Ni_xAs_2$, where spin excitations at low energies change from C_4 to C_2 symmetry in the tetragonal

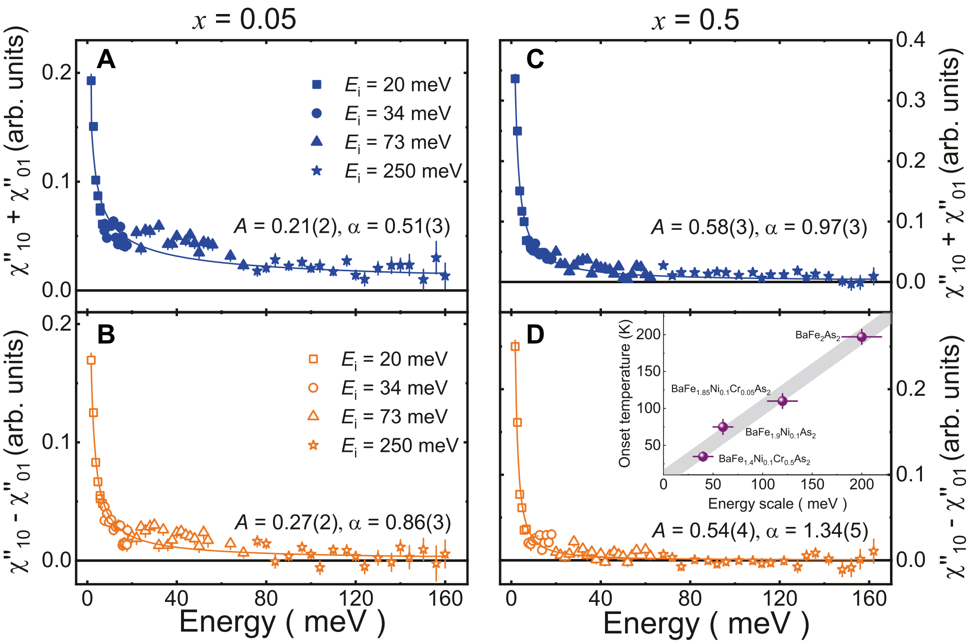

FIGURE 8 | (Color online) Energy dependence of the total spin fluctuations $\chi''_{10} + \chi''_{01}$ and the spin nematicity $\chi''_{10} - \chi''_{01}$ of uniaxially detwinned samples for x =0.05 (left) and x =0.5 (right) compounds. Different symbols correspond to different incident energies in the measurements. Both of $\chi''_{10} + \chi''_{01}$ and $\chi''_{10} - \chi''_{01}$ can be fitted with a power-law dependence on the energy, ~ A/E^{α}, where the amplitude A and exponent α are listed in each panel. The inset of panel **(D)** shows the correlation between the highest energy and the onset temperature at low energy of $\chi''_{10} - \chi''_{01}$.

phase at temperatures approximately corresponding to the onset of the in-plane resistivity anisotropy.

Moreover, INS experiments on detwinned $BaFe_2As_2$ and $BaFe_{1.9}Ni_{0.1}As_2$ suggest that the spin anisotropy can persist to very high energy [62, 63], even in the later case the splitting of the d_{xz} and d_{yz} bands nearly vanishes [57]. To quantitatively determine the energy dependence of spin excitation anisotropy, we have performed time-of-flight INS experiments on the uniaxially detwinned $BaFe_{1.9-x}Ni_{0.1}Cr_xAs_2$ (x = 0.05 and 0.5), and the results are shown in **Figures 7, 8.** It should be noted that for such experiments, the energy transfer is always coupled with L due to $k_i \parallel c$ [102, 103]. The two-dimensional (2D) energy slices and one-dimensional (1D) cuts along $[H, 0]$ and $[0, K]$ at various energies are presented in **Figure 7**. Indeed, the spin excitations are twofold symmetric below 100 meV for both compounds. The spin excitations at E = 3 meV, $Q = (0, \pm1)$ are very weak in the x = 0.05 compound, then continuously increase upon energy, and become nearly the same as $Q = (\pm1, 0)$ around 110 meV. For the x = 0.5 compound, although the spin excitations at $Q = (0, \pm1)$ can be initially observed at E = 3 meV, the spin anisotropy still exists at 15 meV and then disappears above 42 meV. To further compare the spin excitations in both compounds, we have calculated the total spin fluctuations $\chi''_{10} + \chi''_{01}$ and the spin nematicity $\chi''_{10} - \chi''_{01}$ from the integrated intensity marked by the dashed diamonds in **Figure 7D,L**. In principle, the local dynamic susceptibility χ'' can be estimated from the integration outcome of the spin excitations within one Brillouin zone, and here χ'' can be simply calculated through dividing the integration signal in the $Q = (0, 0)$ $(1, 1)$, $(2, 0)$, $(1, -1)$ boxes, giving the diamond shape integration zone [8]. The total spin susceptibility $\chi''_{10} + \chi''_{01}$ in the x = 0.5 compound is stronger than that in x = 0.05 but decays much quickly with energy (**Figure 8A,C**). The spin nematicity $\chi''_{10} - \chi''_{01}$ apparently has different energy scales for two compounds, where it is about 120 meV for x = 0.05 but only 40 meV for x = 0.5, respectively. The energy scale of $\chi''_{10} - \chi''_{01}$ in the superconducting compound $BaFe_{1.9}Ni_{0.1}As_2$ is 60 meV [62], and for the parent compound $BaFe_2As_2$, it is about 200 meV up to the band top of the spin waves [63]. These facts lead to a possible linear correlation between the highest energy and the onset temperature of spin nematicity at low energy (inset of **Figure 8D**). Within the measured energy range, both $\chi''_{10} + \chi''_{01}$ and $\chi''_{10} - \chi''_{01}$ can be fit with a power-law dependence on the energy, ~ A/E^{α}, where the amplitude A and exponent α are listed in each panel of **Figure 8**. Indeed, the larger value of α for x = 0.5 in comparison to that for x = 0.05 suggests faster decay with energy for both the spin fluctuations and the spin nematicity. Similar fitting on the results of $BaFe_{1.9}Ni_{0.1}As_2$ gives parameters in between them [62]. Although the low energy data below 10 meV may be affected by the L-modulation of spin excitations, and by the superconductivity in $BaFe_{1.9}Ni_{0.1}As_2$, the similar quantum critical behavior both for $\chi''_{10} + \chi''_{01}$ and $\chi''_{10} - \chi''_{01}$ in these three compounds is expected by the Ising-nematic scenario [60–63].

In our previous neutron diffraction results on the $BaFe_{1.9-x}Ni_{0.1}Cr_xAs_2$ system, the Cr dopings have limited effects on the magnetically ordered temperature T_N but significantly enhance the effective ordered moment m by reaching a maximum value at x = 0.5 [73]. The Néel temperature T_N is mostly determined by the local magnetic coupling related to the local $FeAs_4$ tetrahedron structure. The evolution of ordered moment probably induced by the changes of the density of states and the orbital angular momentum from itinerant electrons on the Fermi surfaces. The Cr doping introduces both local distortion on the lattices and hole doping on the Fermi pockets, yielding a non-monotonic change of the conductivity of charge carriers. As shown in **Figure 2**, the low-temperature upturn of resistivity is enhanced by Cr doping first but then weakens in those hole-type compounds. Among these dopings, $x = 0.5$ has the most insulating-like behavior, and thus strongly localized charge carriers and maximum ordered moment, but its spin nematicity quickly drops down for both the temperature and energy dependence. In contrast to the magnetically ordered strength, both the structural transition temperature T_s and the lattice orthorhombicity $\delta = (a - b)/(a + b)$ are nearly Cr doping independent [73]. This means the static nematic order is also nearly Cr independent in this system, as opposed to the case for dynamic nematic fluctuations.

The nature of the iron-based superconductor can be theoretically described as a magnetic Hund's metal, in which the strong interplay between the local spins on Fe atoms and the itinerant electrons on Fermi surfaces gives correlated electronic states [80, 81]. Indeed, time-of-flight INS experiments on the detwinned $BaFe_2As_2$ suggest that the spin waves in the parent compound are preferably described by a multi-orbital Hubbard–Hund model based on the itinerant picture with moderate electronic correlation effects, instead of a Heisenberg model with effective exchange couplings from local spins. Upon warming up to high temperatures, the intensities of spin excitation anisotropy decrease gradually with increasing energy and finally cut off at an energy away from the band top of spin waves [63]. Therefore, the energy scale of spin nematicity sets an upper limit for the characteristic temperature for the nematic spin correlations, as well as the onset temperature of resistivity anisotropy. Here, by adding up the results on the in-plane anisotropies of resistivity, orbital energy, and spin excitations in $BaFe_{1.9-x}Ni_{0.1}Cr_xAs_2$, they clearly suggest that the electronic nematicity is intimately related to the spin dynamics, which seems consistent with Hund's metal picture. Specifically, by doping Cr to suppress the superconductivity in $BaFe_{1.9}Ni_{0.1}As_2$, it makes the charge carriers initially localized with enhanced electron correlations [73], which may enhance the electronic correlations by increasing the intra- and inter-orbital onsite repulsion U as well as Hund's coupling J_H [63], and thus gives rise to stronger spin excitations and larger spin anisotropy in the Cr doping $x = 0.05$ compound. Another effect is the lifting up of d_{yz} and d_{xy} along the Γ-X direction to the Fermi level, which primarily contributes to the effective moments [80]. The orbital-weight redistribution triggered by the spin order suggests that the orbital degree of freedom is coupled to the spin degree of freedom [111]. By further increasing Cr doping to $x = 0.5$, the localization effect is so strong that the electron system becomes insulating at low temperature. In this case, the itinerant picture based on Hund's metal may not be applicable anymore. The low density of itinerant electrons weakens the nematic fluctuations and probably limits them inside the magnetically ordered state. In either case for $x = 0.05$ or $x = 0.5$, the band splitting does not directly correspond to the spin nematic correlations but only present below the nematic ordered temperature. This may attribute to the weak spin–orbit coupling in this system, as the spin anisotropy in spin space can only present at very low energies [59]. In addition, our results can rule out the picture of local impurity scattering driven nematicity since the impurity scattering from Cr substitutions is certainly stronger in the $x = 0.5$ compound, but it does not promote the nematic fluctuations.

4 CONCLUSION

In conclusion, we have extensively studied the in-plane resistivity anisotropy, orbital ordering, and spin nematicity in a non-superconducting $BaFe_{1.9-x}Ni_{0.1}Cr_xAs_2$ system. We have found that the Cr doping strongly affect the anisotropy of resistivity and spin excitations along with the itinerancy of charge carriers. While the onset temperatures of resistivity anisotropy and spin nematicity are similar and correlated with the energy scale of spin anisotropy, the orbital anisotropy shows an onset temperature irrelevant to them. These results suggest that the electronic correlations from the interplay between local moments and itinerant electrons are crucial to understand the nematic fluctuations, thus inspiring the quest for the driven force of the electronic nematic phase in iron-pnictide superconductors.

DATA AVAILABILITY STATEMENT

The datasets presented in this article are not readily available because the datasets are currently private. Requests to access the datasets should be directed to HL, hqluo@iphy.ac.cn.

AUTHOR CONTRIBUTIONS

HL and DG proposed and designed the research. DG, TX, WZ, and RZ contributed in sample growth and resistivity measurements. MY, MW, S-KM, MH, DL, and RB contributed to the ARPES measurements. DG and HL carried out the neutron scattering experiments with SD, GD, XL, JP, KI, and KK. DG, HL, SL, and PD analyzed the data. HL, DG, and MY wrote the paper. All authors participated in discussion and comment on the paper.

FUNDING

This work is supported by the National Key Research and Development Program of China (Grant No. 2018YFA0704200, No. 2017YFA0303100, and No. 2017YFA0302900), the National Natural Science Foundation of China (Grants No. 11822411, No. 11961160699, and No. 12061130200), the Strategic Priority Research Program (B) of the CAS (Grant No. XDB25000000 and No. XDB07020300), and the KC Wong Education Foundation (GJTD-2020-01). HL is grateful for the support from the Youth Innovation Promotion Association of CAS (Grant No. Y202001) and the Beijing Natural Science Foundation (Grant No. JQ19002). MW is supported by the National Natural Science Foundation of China (Grant No. 11904414 and No.12174454), the Guangdong Basic and Applied Basic Research Foundation (No. 2021B1515120015), and the National Key Research and Development Program of China (No. 2019YFA0705702). The work at University of California, Berkeley, and Lawrence Berkeley National Laboratory was funded by the U.S. Department of Energy (DOE), Office of Science, Office of Basic Energy Sciences, Materials Sciences and Engineering Division under Contract No. DE-AC02-05-CH11231 within the Quantum Materials Program (KC2202) and the Office of Basic Energy Sciences. The ARPES work at Rice University was supported by the Robert A. Welch Foundation (Grant No. C-2024 (MY)). The neutron scattering work at Rice University was supported by the U.S. DOE, BES (Grant No. DE-SC0012311) and by the Robert A. Welch Foundation (Grant No. C-1839 (PD)).

ACKNOWLEDGMENTS

The authors thank the helpful discussion with Xingye Lu at Beijing Normal University and Yu Song at Zhejiang University. The neutron scattering experiments in this work are performed at thermal triple-axis spectrometer PUMA at Heinz Maier-Leibnitz Zentrum (MLZ), Germany, thermal triple-axis spectrometer TAIPAN at Australian Centre for Neutron Scattering (ACNS), Australian Nuclear Science and Technology Organisation (ANSTO), Australia (Proposal No. P4263), and time-of-flight Fermi-chopper spectrometer 4SEASONS (BL-01) at the Materials and Life Science Experimental Facility of J-PARC (Proposal Nos. 2015A0005, 2016A0169). ARPES measurements were performed at the Advanced Light Source and the Stanford Radiation Lightsource, which are both operated by the Office of Basic Energy Sciences, U.S. DOE.

REFERENCES

1. Oganesyan V, Kivelson SA, Fradkin E. Quantum Theory of a Nematic Fermi Fluid. *Phys Rev B* (2001) 64:195109. doi:10.1103/physrevb.64.195109
2. Fradkin E, Kivelson SA. Electron Nematic Phases Proliferate. *Science* (2010) 327:155–6. doi:10.1126/science.1183464
3. Fradkin E, Kivelson SA, Lawler MJ, Eisenstein JP, Mackenzie AP. Nematic Fermi Fluids in Condensed Matter Physics. *Annu Rev Condens Matter Phys* (2010) 1:153–78. doi:10.1146/annurev-conmatphys-070909-103925
4. Wang W, Luo J, Wang C, Yang J, Kodama Y, Zhou R, et al. Microscopic Evidence for the Intra-unit-cell Electronic Nematicity inside the Pseudogap Phase in YBa$_2$Cu$_4$O$_8$. *Sci China Phys Mech Astron* (2021) 64:237413. doi:10.1007/s11433-020-1615-y
5. Fernandes RM, Schmalian J. Manifestations of Nematic Degrees of Freedom in the Magnetic, Elastic, and Superconducting Properties of the Iron Pnictides. *Supercond Sci Technol* (2012) 25:084005. doi:10.1088/0953-2048/25/8/084005
6. Fernandes RM, Chubukov AV. Low-energy Microscopic Models for Iron-Based Superconductors: a Review. *Rep Prog Phys* (2017) 80:014503. doi:10.1088/1361-6633/80/1/014503
7. Chen X, Dai P, Feng D, Xiang T, Zhang F-C. Iron-based High Transition Temperature Superconductors. *Nat Sci Rev* (2014) 1:371–95. doi:10.1093/nsr/nwu007
8. Dai P. Antiferromagnetic Order and Spin Dynamics in Iron-Based Superconductors. *Rev Mod Phys* (2015) 87:855–96. doi:10.1103/revmodphys.87.855
9. Si Q, Yu R, Abrahams E. High-temperature Superconductivity in Iron Pnictides and Chalcogenides. *Nat Rev Mat* (2016) 1:16017. doi:10.1038/natrevmats.2016.17
10. Gong Dong-Liang D, Luo Hui-Qian H. Antiferromagnetic Order and Spin Dynamics in Iron-Based Superconductors. *Acta Phys Sin* (2018) 67:207407. doi:10.7498/aps.67.20181543
11. Böhmer AE, Meingast C. Electronic Nematic Susceptibility of Iron-Based Superconductors. *Comptes Rendus Phys* (2016) 17:90–112. doi:10.1016/j.crhy.2015.07.001
12. Chu J-H, Kuo H-H, Analytis JG, Fisher IR. Divergent Nematic Susceptibility in an Iron Arsenide Superconductor. *Science* (2012) 337:710–2. doi:10.1126/science.1221713
13. Kuo H-H, Fisher IR. Effect of Disorder on the Resistivity Anisotropy Near the Electronic Nematic Phase Transition in Pure and Electron-Doped BaFe$_2$As$_2$. *Phys Rev Lett* (2014) 112:227001. doi:10.1103/physrevlett.112.227001
14. Kuo H-H, Shapiro MC, Riggs SC, Fisher IR. Measurement of the Elastoresistivity Coefficients of the Underdoped Iron Arsenide Ba(Fe$_{0.975}$Co$_{0.025}$)$_2$As$_2$. *Phys Rev B* (2013) 88:085113. doi:10.1103/physrevb.88.085113
15. Böhmer AE, Burger P, Hardy F, Wolf T, Schweiss P, Fromknecht R, et al. Nematic Susceptibility of Hole-Doped and Electron-Doped BaFe$_2$As$_2$ Iron-Based Superconductors from Shear Modulus Measurements. *Phys Rev Lett* (2014) 112:047001. doi:10.1103/PhysRevLett.112.047001
16. Gong D, Liu Z, Gu Y, Xie T, Ma X, Luo H, et al. Nature of the Antiferromagnetic and Nematic Transitions in Sr$_{1-x}$Ba$_x$Fe$_{1.97}$Ni$_{0.03}$As$_2$. *Phys Rev B* (2017) 96:104514. doi:10.1103/physrevb.96.104514
17. Böhmer AE, Chen F, Meier WR, Xu M, Drachuck G, Merz M, et al. Evolution of Nematic Fluctuations in CaK(Fe$_{1-x}$Ni$_x$)$_4$As$_4$ with Spin-Vortex Crystal Magnetic Order [Preprint] (2020). Available at: https://arxiv.org/abs/2011.13207.
18. Kuo H-H, Chu J-H, Palmstrom JC, Kivelson SA, Fisher IR. Ubiquitous Signatures of Nematic Quantum Criticality in Optimally Doped Fe-Based Superconductors. *Science* (2016) 352:958–62. doi:10.1126/science.aab0103
19. Yoshizawa M, Kimura D, Chiba T, Simayi S, Nakanishi Y, Kihou K, et al. Structural Quantum Criticality and Superconductivity in Iron-Based Superconductor Ba(Fe$_{1-x}$Co$_x$)$_2$As$_2$. *J Phys Soc Jpn* (2012) 81:024604. doi:10.1143/jpsj.81.024604
20. Dai J, Si Q, Zhu J-X, Abrahams E. Iron Pnictides as a New Setting for Quantum Criticality. *Proc Natl Acad Sci USA* (2009) 106:4118–21. doi:10.1073/pnas.0900886106
21. Kasahara S, Shi HJ, Hashimoto K, Tonegawa S, Mizukami Y, Shibauchi T, et al. Electronic Nematicity above the Structural and Superconducting Transition in BaFe$_2$(As$_{1-x}$P$_x$)$_2$. *Nature* (2012) 486:382–5. doi:10.1038/nature11178
22. Shibauchi T, Carrington A, Matsuda Y. A Quantum Critical Point Lying beneath the Superconducting Dome in Iron Pnictides. *Annu Rev Condens Matter Phys* (2014) 5:113–35. doi:10.1146/annurev-conmatphys-031113-133921
23. Lederer S, Schattner Y, Berg E, Kivelson SA. Superconductivity and Non-fermi Liquid Behavior Near a Nematic Quantum Critical Point. *Proc Natl Acad Sci USA* (2015) 114:4905–10. doi:10.1073/pnas.1620651114
24. Luo H, Zhang R, Laver M, Yamani Z, Wang M, Lu X, et al. Coexistence and Competition of the Short-Range Incommensurate Antiferromagnetic Order with the Superconducting State of BaFe$_{2-x}$Ni$_x$As$_2$. *Phys Rev Lett* (2012) 108:247002. doi:10.1103/physrevlett.108.247002
25. Lu X, Gretarsson H, Zhang R, Liu X, Luo H, Tian W, et al. Avoided Quantum Criticality and Magnetoelastic Coupling in BaFe$_{2-x}$Ni$_x$As$_2$. *Phys Rev Lett* (2013) 110:257001. doi:10.1103/physrevlett.110.257001
26. Hu D, Lu X, Zhang W, Luo H, Li S, Wang P, et al. Structural and Magnetic Phase Transitions Near Optimal Superconductivity in BaFe$_2$(As$_{1-x}$P$_x$)$_2$. *Phys Rev Lett* (2015) 114:157002. doi:10.1103/physrevlett.114.157002
27. Zhang W, Wei Y, Xie T, Liu Z, Gong D, Ma X, et al. Unconventional Antiferromagnetic Quantum Critical Point in Ba(Fe$_{0.97}$Cr$_{0.03}$)$_2$(As$_{1-x}P_x$)$_2$. *Phys Rev Lett* (2019) 122:037001. doi:10.1103/physrevlett.122.037001
28. Liu Z, Gu Y, Zhang W, Gong D, Zhang W, Xie T, et al. Nematic Quantum Critical Fluctuations in BaFe$_{2-x}$Ni$_x$As$_2$. *Phys Rev Lett* (2016) 117:157002. doi:10.1103/physrevlett.117.157002
29. Gu Y, Liu Z, Xie T, Zhang W, Gong D, Hu D, et al. Unified Phase Diagram for Iron-Based Superconductors. *Phys Rev Lett* (2017) 119:157001. doi:10.1103/physrevlett.119.157001
30. Chandra P, Coleman P, Larkin AI. Ising Transition in Frustrated Heisenberg Models. *Phys Rev Lett* (1990) 64:88–91. doi:10.1103/physrevlett.64.88
31. Hu J, Xu C. Nematic Orders in Iron-Based Superconductors. *Phys C Supercond* (2012) 481:215–22. doi:10.1016/j.physc.2012.05.002
32. Fernandes RM, Chubukov AV, Schmalian J. What Drives Nematic Order in Iron-Based Superconductors? *Nat Phys* (2014) 10:97–104. doi:10.1038/nphys2877
33. Fernandes RM, Chubukov AV, Knolle J, Eremin I, Schmalian J. Preemptive Nematic Order, Pseudogap, and Orbital Order in the Iron Pnictides. *Phys Rev B* (2012) 85:024534. doi:10.1103/physrevb.85.024534
34. Wang F, Kivelson SA, Lee D-H. Nematicity and Quantum Paramagnetism in FeSe. *Nat Phys* (2015) 11:959–63. doi:10.1038/nphys3456

35. Ma C, Wu L, Yin W-G, Yang H, Shi H, Wang Z, et al. Strong Coupling of the Iron-Quadrupole and Anion-Dipole Polarizations in $Ba(Fe_{1-x}Co_x)_2As_2$. *Phys Rev Lett* (2014) 112:077001. doi:10.1103/physrevlett.112.077001
36. Thorsmølle VK, Khodas M, Yin ZP, Zhang C, Carr SV, Dai P, et al. Critical Quadrupole Fluctuations and Collective Modes in Iron Pnictide Superconductors. *Phys Rev B* (2016) 93:054515. doi:10.1103/physrevb.93.054515
37. Wang Q, Shen Y, Pan B, Hao Y, Ma M, Zhou F, et al. Strong Interplay between Stripe Spin Fluctuations, Nematicity and Superconductivity in FeSe. *Nat Mater* (2015) 15:159–63. doi:10.1038/nmat4492
38. Chubukov AV, Fernandes RM, Schmalian J. Origin of Nematic Order in FeSe. *Phys Rev B* (2015) 91:201105(R). doi:10.1103/physrevb.91.201105
39. Yamakawa Y, Onari S, Kontani H. Nematicity and Magnetism in FeSe and Other Families of F-Based Superconductors. *Phys Rev X* (2016) 6:021032. doi:10.1103/physrevx.6.021032
40. Lee C-C, Yin W-G, Ku W. Ferro-Orbital Order and Strong Magnetic Anisotropy in the Parent Compounds of Iron-Pnictide Superconductors. *Phys Rev Lett* (2009) 103:267001. doi:10.1103/physrevlett.103.267001
41. Krüger F, Kumar S, Zaanen J, van den Brink J. Spin-orbital Frustrations and Anomalous Metallic State in Iron-Pnictide Superconductors. *Phys Rev B* (2009) 79:054504. doi:10.1103/physrevb.79.054504
42. Lv W, Wu J, Phillips P. Orbital Ordering Induces Structural Phase Transition and the Resistivity Anomaly in Iron Pnictides. *Phys Rev B* (2009) 80:224506. doi:10.1103/physrevb.80.224506
43. Chen C-C, Maciejko J, Sorini AP, Moritz B, Singh RRP, Devereaux TP. Orbital Order and Spontaneous Orthorhombicity in Iron Pnictides. *Phys Rev B* (2010) 82:100504(R). doi:10.1103/physrevb.82.100504
44. Valenzuela B, Bascones E, Calderón MJ. Conductivity Anisotropy in the Antiferromagnetic State of Iron Pnictides. *Phys Rev Lett* (2010) 105:207202. doi:10.1103/physrevlett.105.207202
45. Chu J-H, Analytis JG, De Greve K, McMahon PL, Islam Z, Yamamoto Y, et al. In-Plane Resistivity Anisotropy in an Underdoped Iron Arsenide Superconductor. *Science* (2010) 329:824–6. doi:10.1126/science.1190482
46. Tanatar MA, Blomberg EC, Kreyssig A, Kim MG, Ni N, Thaler A, et al. Uniaxial-strain Mechanical Detwinning of $CaFe_2As_2$ and $BaFe_2As_2$ Crystals: Optical and Transport Study. *Phys Rev B* (2010) 81:184508. doi:10.1103/physrevb.81.184508
47. Ying JJ, Wang XF, Wu T, Xiang ZJ, Liu RH, Yan YJ, et al. Measurements of the Anisotropic In-Plane Resistivity of Underdoped FeAs-Based Pnictide Superconductors. *Phys Rev Lett* (2011) 107:067001. doi:10.1103/PhysRevLett.107.067001
48. Man H, Lu X, Chen JS, Zhang R, Zhang W, Luo H, et al. Electronic Nematic Correlations in the Stress-free Tetragonal State of $BaFe_{2-x}Ni_xAs_2$. *Phys Rev B* (2015) 92:134521. doi:10.1103/physrevb.92.134521
49. Luo X, Stanev V, Shen B, Fang L, Ling XS, Osborn R, et al. Antiferromagnetic and Nematic Phase Transitions in $BaFe_2(As_{1-x}P_x)_2$ Studied by Ac Microcalorimetry and SQUID Magnetometry. *Phys Rev B* (2015) 91:094512. doi:10.1103/physrevb.91.094512
50. Mirri C, Dusza A, Bastelberger S, Chu J-H, Kuo H-H, Fisher IR, et al. Hysteretic Behavior in the Optical Response of the Underdoped Fe Arsenide $Ba(Fe_{1-x}Co_x)_2As_2$ in the Electronic Nematic Phase. *Phys Rev B* (2014) 89:060501(R). doi:10.1103/physrevb.89.060501
51. Fisher IR, Degiorgi L, Shen ZX. In-plane Electronic Anisotropy of Underdoped '122' Fe-Arsenide Superconductors Revealed by Measurements of Detwinned Single Crystals. *Rep Prog Phys* (2011) 74:124506. doi:10.1088/0034-4885/74/12/124506
52. Yi M, Lu D, Chu J-H, Analytis JG, Sorini AP, Kemper AF, et al. Symmetry-breaking Orbital Anisotropy Observed for Detwinned $Ba(Fe_{1-x}Co_x)_2$ as 2 above the Spin Density Wave Transition. *Proc Natl Acad Sci USA* (2011) 108:6878–83. doi:10.1073/pnas.1015572108
53. Yi M, Zhang Y, Liu Z-K, Ding X, Chu J-H, Kemper AF, et al. Dynamic Competition between Spin-Density Wave Order and Superconductivity in Underdoped $Ba_{1-x}K_xFe_2As_2$. *Nat Commun* (2014) 5:3711. doi:10.1038/ncomms4711
54. Yi M, Lu DH, Moore RG, Kihou K, Lee C-H, Iyo A, et al. Electronic Reconstruction through the Structural and Magnetic Transitions in Detwinned NaFeAs. *New J Phys* (2012) 14:073019. doi:10.1088/1367-2630/14/7/073019
55. Yi M, Pfau H, Zhang Y, He Y, Wu H, Chen T, et al. Nematic Energy Scale and the Missing Electron Pocket in FeSe. *Phys Rev X* (2019) 9:041049. doi:10.1103/physrevx.9.041049
56. Zhang Y, He C, Ye ZR, Jiang J, Chen F, Xu M, et al. Symmetry Breaking via Orbital-dependent Reconstruction of Electronic Structure in Detwinned NaFeAs. *Phys Rev B* (2012) 85:085121. doi:10.1103/physrevb.85.085121
57. Yi M, Zhang Y, Shen Z-X, Lu D. Role of the Orbital Degree of Freedom in Iron-Based Superconductors. *npj Quant Mater* (2017) 2:57. doi:10.1038/s41535-017-0059-y
58. Watson MD, Dudin P, Rhodes LC, Evtushinsky DV, Iwasawa H, Aswartham S, et al. Probing the Reconstructed Fermi Surface of Antiferromagnetic $BaFe_2As_2$ in One Domain. *npj Quantum Mat* (2019) 4:36. doi:10.1038/s41535-019-0174-z
59. Luo H, Wang M, Zhang C, Lu X, Regnault L-P, Zhang R, et al. Spin Excitation Anisotropy as a Probe of Orbital Ordering in the Paramagnetic Tetragonal Phase of Superconducting $BaFe_{1.904}Ni_{0.096}As_2$. *Phys Rev Lett* (2013) 111:107006. doi:10.1103/physrevlett.111.107006
60. Lu X, Park JT, Zhang R, Luo H, Nevidomskyy AH, Si Q, et al. Nematic Spin Correlations in the Tetragonal State of Uniaxial-Strained $BaFe_{2-x}Ni_x$ as 2. *Science* (2014) 345:657–60. doi:10.1126/science.1251853
61. Zhang W, Park JT, Lu X, Wei Y, Ma X, Hao L, et al. Effect of Nematic Order on the Low-Energy Spin Fluctuations in Detwinned $BaFe_{1.935}Ni_{0.065}As_2$. *Phys Rev Lett* (2016) 117:227003. doi:10.1103/physrevlett.117.227003
62. Song Y, Lu X, Abernathy DL, Tam DW, Niedziela JL, Tian W, et al. Energy Dependence of the Spin Excitation Anisotropy in Uniaxial-Strained $BaFe_{1.9}Ni_{0.1}As_2$. *Phys Rev B* (2015) 92:180504(R). doi:10.1103/physrevb.92.180504
63. Lu X, Scherer DD, Tam DW, Zhang W, Zhang R, Luo H, et al. Spin Waves in Detwinned $BaFe_2As_2$. *Phys Rev Lett* (2018) 121:067002. doi:10.1103/physrevlett.121.067002
64. Ren X, Duan L, Hu Y, Li J, Zhang R, Luo H, et al. Nematic Crossover in $BaFe_2As_2$ under Uniaxial Stress. *Phys Rev Lett* (2015) 115:197002. doi:10.1103/physrevlett.115.197002
65. Hu Y, Ren X, Zhang R, Luo H, Kasahara S, Watashige T, et al. Nematic Magnetoelastic Effect Contrasted between $Ba(Fe_{1-x}Co_x)_2As_2$ and FeSe. *Phys Rev B* (2016) 93:060504(R). doi:10.1103/physrevb.93.060504
66. Baek S-H, Efremov DV, Ok JM, Kim JS, van den Brink J, Büchner B. Orbital-driven Nematicity in FeSe. *Nat Mater* (2015) 14:210–4. doi:10.1038/nmat4138
67. Iye T, Julien M-H, Mayaffre H, Horvatić M, Berthier C, Ishida K, et al. Emergence of Orbital Nematicity in the Tetragonal Phase of $BaFe_2(As_{1-x}P_x)_2$. *J Phys Soc Jpn* (2015) 84:043705. doi:10.7566/jpsj.84.043705
68. Rosenthal EP, Andrade EF, Arguello CJ, Fernandes RM, Xing LY, Wang XC, et al. Visualization of Electron Nematicity and Unidirectional Antiferroic Fluctuations at High Temperatures in NaFeAs. *Nat Phys* (2014) 10:225–32. doi:10.1038/nphys2870
69. Ishida S, Nakajima M, Liang T, Kihou K, Lee CH, Iyo A, et al. Anisotropy of the In-Plane Resistivity of Underdoped $Ba(Fe_{1-x}Co_x)_2As_2$ Superconductors Induced by Impurity Scattering in the Antiferromagnetic Orthorhombic Phase. *Phys Rev Lett* (2013) 110:207001. doi:10.1103/physrevlett.110.207001
70. Allan MP, Chuang T-M, Massee F, Xie Y, Ni N, Bud'ko SL, et al. Anisotropic Impurity States, Quasiparticle Scattering and Nematic Transport in Underdoped $Ca(Fe_{1-x}Co_x)_2As_2$. *Nat Phys* (2013) 9:220–4. doi:10.1038/nphys2544
71. Zhang R, Gong D, Lu X, Li S, Dai P, Luo H. The Effect of Cr Impurity to Superconductivity in Electron-Doped $BaFe_{2-x}Ni_xAs_2$. *Supercond Sci Technol* (2014) 27:115003. doi:10.1088/0953-2048/27/11/115003
72. Zhang R, Gong D, Lu X, Li S, Laver M, Niedermayer C, et al. Doping Evolution of Antiferromagnetism and Transport Properties in Nonsuperconducting $BaFe_{2-2x}Ni_xCr_xAs_2$. *Phys Rev B* (2015) 91:094506. doi:10.1103/physrevb.91.094506
73. Gong D, Xie T, Zhang R, Birk J, Niedermayer C, Han F, et al. Doping Effects of Cr on the Physical Properties of $BaFe_{1.9-x}Ni_{0.1}Cr_xAs_2$. *Phys Rev B* (2018) 98:014512. doi:10.1103/physrevb.98.014512
74. Pizarro JM, Calderón MJ, Liu J, Muñoz MC, Bascones E. Strong Correlations and the Search for High-T_c Superconductivity in Chromium Pnictides and Chalcogenides. *Phys Rev B* (2017) 95:075115. doi:10.1103/physrevb.95.075115

75. Edelmann M, Sangiovanni G, Capone M, de' Medici L. Chromium Analogs of Iron-Based Superconductors. *Phys Rev B* (2017) 95:205118. doi:10.1103/physrevb.95.205118
76. de'Medici L, Giovannetti G, Capone M. Selective Mott Physics as a Key to Iron Superconductors. *Phys Rev Lett* (2014) 112:177001. doi:10.1103/physrevlett.112.177001
77. Lee PA, Nagaosa N, Wen X-G. Doping a Mott Insulator: Physics of High-Temperature Superconductivity. *Rev Mod Phys* (2006) 78:17–85. doi:10.1103/revmodphys.78.17
78. Gu Q, Wen H-H. Superconductivity in Nickel-Based 112 Systems. *The Innovation* (2022) 3:100202. doi:10.1016/j.xinn.2021.100202
79. Song Y, Yamani Z, Cao C, Li Y, Zhang C, Chen JS, et al. A Mott Insulator Continuously Connected to Iron Pnictide Superconductors. *Nat Commun* (2016) 7:13879. doi:10.1038/ncomms13879
80. Yin ZP, Haule K, Kotliar G. Kinetic Frustration and the Nature of the Magnetic and Paramagnetic States in Iron Pnictides and Iron Chalcogenides. *Nat Mater* (2011) 10:932–5. doi:10.1038/nmat3120
81. Georges A, Medici Ld., Mravlje J. Strong Correlations from Hund's Coupling. *Annu Rev Condens Matter Phys* (2013) 4:137–78. doi:10.1146/annurev-conmatphys-020911-125045
82. Yi M, Lu DH, Analytis JG, Chu J-H, Mo S-K, He R-H, et al. Electronic Structure of the $BaFe_2As_2$ Family of Iron-Pnictide Superconductors. *Phys Rev B* (2009) 80:024515. doi:10.1103/physrevb.80.024515
83. Richard P, Sato T, Nakayama K, Takahashi T, Ding H. Fe-based Superconductors: an Angle-Resolved Photoemission Spectroscopy Perspective. *Rep Prog Phys* (2011) 74:124512. doi:10.1088/0034-4885/74/12/124512
84. Song Y, Wang W, Zhang C, Gu Y, Lu X, Tan G, et al. Temperature and Polarization Dependence of Low-Energy Magnetic Fluctuations in Nearly Optimally Doped $NaFe_{0.9785}Co_{0.0215}As$. *Phys Rev B* (2017) 96:184512. doi:10.1103/physrevb.96.184512
85. Song Y, Man H, Zhang R, Lu X, Zhang C, Wang M, et al. Spin Anisotropy Due to Spin-Orbit Coupling in Optimally Hole-Doped $Ba_{0.67}K_{0.33}Fe_2As_2$. *Phys Rev B* (2016) 94:214516. doi:10.1103/physrevb.94.214516
86. Xie T, Wei Y, Gong D, Fennell T, Stuhr U, Kajimoto R, et al. Odd and Even Modes of Neutron Spin Resonance in the Bilayer Iron-Based Superconductor $CaKFe_4As_4$. *Phys Rev Lett* (2018) 120:267003. doi:10.1103/physrevlett.120.267003
87. Xie T, Gong D, Ghosh H, Ghosh A, Soda M, Masuda T, et al. Neutron Spin Resonance in the 112-Type Iron-Based Superconductor. *Phys Rev Lett* (2018) 120:137001. doi:10.1103/physrevlett.120.137001
88. Xie T, Liu C, Bourdarot F, Regnault L-P, Li S, Luo H. Spin-excitation Anisotropy in the Bilayer Iron-Based Superconductor $CaKFe_4As_4$. *Phys Rev Res* (2020) 2:022018(R). doi:10.1103/physrevresearch.2.022018
89. Wang T, Zhang C, Xu L, Wang J, Jiang S, Zhu Z, et al. Strong Pauli Paramagnetic Effect in the Upper Critical Field of $KCa_2Fe_4As_4F_2$. *Sci China Phys Mech Astron* (2020) 63:227412. doi:10.1007/s11433-019-1441-4
90. Guo J, Yue L, Iida K, Kamazawa K, Chen L, Han T, et al. Preferred Magnetic Excitations in the Iron-Based $Sr_{1-x}Na_xFe_2As_2$ Superconductor. *Phys Rev Lett* (2019) 122:017001. doi:10.1103/physrevlett.122.017001
91. Liu C, Bourges P, Sidis Y, Xie T, He G, Bourdarot F, et al. Preferred Spin Excitations in the Bilayer Iron-Based Superconductor $CaK(Fe_{0.96}Ni_{0.04})_4As_4$ with Spin-Vortex Crystal Order. *Phys Rev Lett* (2022) 128:137003. doi:10.1103/physrevlett.128.137003
92. Luo H, Wang Z, Yang H, Cheng P, Zhu X, Wen H-H. Growth and Characterization of $A_{1-x}K_xFe_2As_2$(A = Ba, Sr) Single Crystals With x= 0-0.4. *Supercond Sci Technol* (2008) 21:125014. doi:10.1088/0953-2048/21/12/125014
93. Chen Y, Lu X, Wang M, Luo H, Li S. Systematic Growth of $BaFe_{2-x}Ni_xAs_2$ Large Crystals. *Supercond Sci Technol* (2011) 24:065004. doi:10.1088/0953-2048/24/6/065004
94. Xie T, Gong D, Zhang W, Gu Y, Huesges Z, Chen D, et al. Crystal Growth and Phase Diagram of 112-type Iron Pnictide Superconductor $Ca_{1-y}La_yFe_{1-x}Ni_xAs_2$. *Supercond Sci Technol* (2017) 30:095002. doi:10.1088/1361-6668/aa7994
95. Wang T, Chu J, Feng J, Wang L, Xu X, Li W, et al. Low Temperature Specific Heat of 12442-type $KCa_2Fe_4As_4F_2$ Single Crystals. *Sci China Phys Mech Astron* (2020) 63:297412. doi:10.1007/s11433-020-1549-9
96. Lu X, Tseng K-F, Keller T, Zhang W, Hu D, Song Y, et al. Impact of Uniaxial Pressure on Structural and Magnetic Phase Transitions in Electron-Doped Iron Pnictides. *Phys Rev B* (2016) 93:134519. doi:10.1103/physrevb.93.134519
97. Tam DW, Wang W, Zhang L, Song Y, Zhang R, Carr SV, et al. Weaker Nematic Phase Connected to the First Order Antiferromagnetic Phase Transition in $SrFe_2As_2$ Compared to $BaFe_2As_2$. *Phys Rev B* (2019) 99:134519. doi:10.1103/physrevb.99.134519
98. Tam DW, Yin ZP, Xie Y, Wang W, Stone MB, Adroja DT, et al. Orbital Selective Spin Waves in Detwinned NaFeAs. *Phys Rev B* (2020) 102:054430. doi:10.1103/physrevb.102.054430
99. Liu P, Klemm ML, Tian L, Lu X, Song Y, Tam DW, et al. In-plane Uniaxial Pressure-Induced Out-of-Plane Antiferromagnetic Moment and Critical Fluctuations in $BaFe_2As_2$. *Nat Commun* (2020) 11:5728. doi:10.1038/s41467-020-19421-5
100. Sobolev O, Park JT. PUMA: Thermal Three Axes Spectrometer. *J Large Scale Res Facil* (2015) 1:A13. doi:10.17815/jlsrf-1-36
101. Danilkin SA, Yethiraj M. TAIPAN: Thermal Triple-Axis Spectrometer. *Neutron News* (2009) 20:37–9. doi:10.1080/10448630903241217
102. Nakamura M, Kajimoto R, Inamura Y, Mizuno F, Fujita M, Yokoo T, et al. First Demonstration of Novel Method for Inelastic Neutron Scattering Measurement Utilizing Multiple Incident Energies. *J Phys Soc Jpn* (2009) 78:093002. doi:10.1143/jpsj.78.093002
103. Kajimoto R, Nakamura M, Inamura Y, Mizuno F, Nakajima K, Ohira-Kawamura S, et al. The Fermi Chopper Spectrometer 4SEASONS at J-PARC. *J Phys Soc Jpn* (2011) 80:SB025. doi:10.1143/jpsjs.80sb.sb025
104. Inamura Y, Nakatani T, Suzuki J, Otomo T. Development Status of Software "Utsusemi" for Chopper Spectrometers at MLF, J-PARC. *J Phys Soc Jpn* (2013) 82:SA031. doi:10.7566/jpsjs.82sa.sa031
105. ISIS Facility. *ISIS Facility, Rutherford Appleton Laboratory, UK* (2000). Available at: https://www.isis.stfc.ac.uk/Pages/Excitations-Software.aspx.
106. Blomberg EC, Tanatar MA, Fernandes RM, MazinII, Shen B, Wen H-H, et al. Sign-reversal of the In-Plane Resistivity Anisotropy in Hole-Doped Iron Pnictides. *Nat Commun* (2013) 4:1914. doi:10.1038/ncomms2933
107. Ma JQ, Luo XG, Cheng P, Zhu N, Liu DY, Chen F, et al. Evolution of Anisotropic In-Plane Resistivity with Doping Level in $Ca_{1-x}Na_xFe_2As_2$ Single Crystals. *Phys Rev B* (2014) 89:174512. doi:10.1103/physrevb.89.174512
108. Kobayashi T, Tanaka K, Miyasaka S, Tajima S. Importance of Fermi Surface Topology for In-Plane Resistivity Anisotropy in Hole- and Electron-Doped $Ba(Fe_{1-x}TM_x)_2As_2$ (TM = Cr, Mn, and Co). *J Phys Soc Jpn* (2015) 84:094707. doi:10.7566/jpsj.84.094707
109. Ishida K, Tsujii M, Hosoi S, Mizukami Y, Ishida S, Iyo A, et al. Novel Electronic Nematicity in Heavily Hole-Doped Iron Pnictide Superconductors. *Proc Natl Acad Sci USA* (2020) 117:6424–9. doi:10.1073/pnas.1909172117
110. Tam DW. Uniaxial Pressure Effect on the Magnetic Ordered Moment and Transition Temperatures in $BaFe_{2-x}T_xAs_2$ (T = Co, Ni). *Phys Rev B* (2017) 95:060505(R). doi:10.1103/physrevb.95.060505
111. Daghofer M, Luo Q-L, Yu R, Yao DX, Moreo A, Dagotto E. Orbital-weight Redistribution Triggered by Spin Order in the Pnictides. *Phys Rev B* (2010) 81:180514(R). doi:10.1103/physrevb.81.180514

Conflict of Interest: The authors declare that the research was conducted in the absence of any commercial or financial relationships that could be construed as a potential conflict of interest.

frontiers | Frontiers in Physics

ORIGINAL RESEARCH
published: 15 June 2022
doi: 10.3389/fphy.2022.919784

Feedback of Non-Local d_{xy} Nematicity on the Magnetic Anisotropy in FeSe

Steffen Bötzel and Ilya M. Eremin*

Institut für Theoretische Physik III, Fakultät für Physik und Astronomie, Ruhr-Universität Bochum, Bochum, Germany

We analyze theoretically the magnetic anisotropy in the nematic phase of FeSe by computing the spin and the orbital susceptibilities from the microscopic multiorbital model. In particular, we take into account both the *xz/yz* and the recently proposed non-local *xy* nematic ordering and show that the latter one could play a crucial role in reproducing the experimentally-measured temperature dependence of the magnetic anisotropy. This provides a direct fingerprint of the different nematic scenarios on the magnetic properties of FeSe.

Keywords: iron-based superconductors, nematic ordering, magnetic susceptibility, uniform susceptibility, spin-orbit coupling

Edited by:
Laura Fanfarillo,
International School for Advanced Studies (SISSA), Italy

Reviewed by:
Belén Valenzuela,
Institute of Materials Science of Madrid (CSIC), Spain
Emmanuele Cappelluti,
Istituto di Struttura della Materia (ISM), CNR, Trieste, Italy

Correspondence:
Ilya M. Eremin
Ilya.Eremin@rub.de

Specialty section:
This article was submitted to Condensed Matter Physics, a section of the journal Frontiers in Physics

Received: *13 April 2022*
Accepted: *11 May 2022*
Published: *15 June 2022*

Citation:
Bötzel S and Eremin IM (2022) Feedback of Non-Local d_{xy} Nematicity on the Magnetic Anisotropy in FeSe. Front. Phys. 10:919784. doi: 10.3389/fphy.2022.919784

1 INTRODUCTION

Iron-based superconductors offer the opportunity to explore the interplay between electronic nematicity, magnetism and superconductivity. While the broad studies on cuprates already provide insights into the competition between magnetism and superconductivity [1, 2], the role of the still enigmatic nematic state is of particular interest. Since anisotropy arises in crystal structure, orbital and spin degrees of freedom, it is intricate to decipher the underlying mechanism [3, 4]. In most of the iron pnictides the structural transition precedes or coincides with the magnetic transition at T_N, below which long-range antiferromagnetic order sets in [5], supporting the idea that nematicity (spin nematicity) is driven by magnetic interactions [6]. Note that the spin-nematic scenario can also lead to an effective orbital ordering once one takes the orbital content of the spin fluctuations within the so-called orbital-selective spin-fluctuation scenario into account [7–9].

Among various iron-based superconductors, FeSe with a simple crystal structure of the stacked FeSe layers has a rather unique behavior due to the presence of a marked nematic (structural) transition at $T_S = 90$ K and a transition to superconductivity below $T_c = 9$ K, while magnetic order is absent [10–15]. Consequently, orbital degrees of freedom have also been proposed as the underlying mechanism for nematic order in FeSe [16–22]. The small lattice distortion contrasts with strong in-plane anisotropy of resistivity, magnetic susceptibility, electronic structure and orbital and momentum structure of the superconducting gap [23–34]. The phase diagram of FeSe is rich and sensitive to the application of hydrostatic pressure or chemical substitution [35–38]. Furthermore, various exotic superconducting states have been recently reported in this compound [15].

Recent experiments have overcame the intricacies of the formation of orthorombic domains in FeSe by applying uniaxial strain [39–43]. Using this technique, the in-plane anisotropy of resistivity, uniform magnetic susceptibility and the Knight shift have been found to exhibit the opposite sign of the anisotropy as compared to iron-pnictides [24, 25, 44–46]. Moreover, carefully avoiding eddy-current heating, a slight suppression of the Knight shift in the superconducting state has been measured recently, while superconductivity and nematicity seem to coexist [47–49]. This agrees with direct magnetization measurements [25].

From the experimental point of view the systematic investigation of the band-structure of FeSe by means of ARPES and quantum oscillations revealed a sizeable deformation of the Fermi surface, that can be described by the interplay of the d_{xz}, d_{yz} and d_{xy} orbitals, their spin-orbit coupling and the nematic order [50–53]. Concerning the nematic order there is general understanding about the existence of a *xz*/*yz* splitting that changes sign in going from the Brillouin-zone center to momenta around $\mathbf{Q}_X = (\pi, 0)$ and $\mathbf{Q}_Y = (0, \pi)$ points of the 1-Fe-unit cell Brillouin Zone (BZ) (both folded onto the *M*-point of the folded BZ with 2-Fe ions per unit cell). This can be represented by a nematic order parameter $\Phi^{xz/yz} = \langle d^\dagger_{xz} d_{xz} - d^\dagger_{yz} d_{yz} \rangle$, that is positive around the Γ point and is negative around the *M* point of the BZ. Accounting for this nematic order is straightforward but yields rather controversial electronic structure. In particular, a large electron pocket with mixed *xz* and *xy* character is expected at the *M* point of the BZ, which has not been resolved in the most recent ARPES measurements in detwinned samples [40–42]. One approach to explain these experimental data and to suppress modelled contributions associated with this pocket, is to include orbital-selective quasiparticle weights [26, 44, 54, 55]. More recently an alternative scenario has been proposed [56–59], where an additional non-local nematic order parameter accounting for the splitting of the *xy* occupancy in the two electron pockets $\Phi^{xy} = \langle d^{X\dagger}_{xy} d^X_{xy} - d^{Y\dagger}_{xy} d^Y_{xy} \rangle$ [56–58] plays a crucial role. An important consequence of this scenario is a resulting occurrence of a Lifshitz transition at the *M*-point leaving only one electron pocket at the Fermi level.

This possibility to have a non-local nematic ordering of the d_{xy} states was previously outlined in the literature [60–62] but assumed to be small in the models having on-site interaction terms only. However, an inclusion of the nearest-neighbor interaction terms (such as nearest neighbor exchange or Coulomb interaction) would change this picture. Note, recent NMR [63] and ARPES [41, 42] have also suggested that the d_{xy} orbital may be strongly affected by the onset of the nematic state.

In this manuscript we investigate the consequences of the non-local d_{xy}-nematic scenario for the magnetic susceptibility taking into account spin and orbital contributions. We analyze its temperature and doping dependencies and compare the results to the available experiments. We show that the non-local nematicity is responsible for the non-monotonic temperature dependence of the susceptibility and predict how it evolves with doping in $\mathrm{FeSe}_{1-x}\mathrm{S}_x$. Finally we studied how the magnetic anisotropy is affected in the superconducting state.

2 METHODS

We adopt the low energy model for FeSe, previously employed in Ref. [56], and fitted to the available ARPES experiments [40, 45, 64]. It is based on the generalized low-energy effective model for iron-based superconductors, formulated by Cvetkovic and Vafek [65].

2.1 Tetragonal State

In particular, to describe the tetragonal state of FeSe, we start by describing the low-energy states near the corresponding symmetry points of the BZ. In particular, near the Γ point of the BZ there are two Fermi surface pockets formed by the hybridized *xz*- and *yz*-orbitals. For completeness we also take the *xy*-orbital band into account which is located approximately 50 meV below the Fermi level [64]. Its inclusion allows to treat correctly the spin-orbit coupling (SOC) within the t_{2g} manifold. The states can be described by the spinor $\Psi^\dagger_{\Gamma,\mathbf{k}} = (d^\dagger_{xz\uparrow}, d^\dagger_{yz\uparrow}, d^\dagger_{xy\downarrow})$, where the other ("lower") spin part of the Hamiltonian is related by symmetry. For readability we omit the momentum index in the creation and annihilation operators here and in what follows. In particular, for each momentum **k** the Hamiltonian is given by

$$H^\Gamma(\mathbf{k}) = \begin{pmatrix} \epsilon_{xz,\mathbf{k}} - \frac{b}{2}\left(k_x^2 - k_y^2\right) & bk_xk_y - i\frac{\lambda_1}{2} & \frac{i\lambda_2}{2} \\ bk_xk_y + i\frac{\lambda_1}{2} & \epsilon_{yz,\mathbf{k}} - \frac{b}{2}\left(k_y^2 - k_x^2\right) & -\frac{\lambda_2}{2} \\ -\frac{i\lambda_2}{2} & -\frac{\lambda_2}{2} & \epsilon_{xy,\mathbf{k}} \end{pmatrix}, \quad (1)$$

where $\epsilon_{\mu,\mathbf{k}} = \epsilon_{\mu,0} - \frac{\mathbf{k}^2}{2m_\mu} - \mu$. **Figure 1A** shows the resulting band dispersion for the tetragonal state. The orbital weights of the bands are illustrated in the usual red-green-blue-color scheme for d_{xz}, d_{yz} and d_{xy}-orbitals, respectively.

To describe the electronic states near the *M*-point of the 2-Fe unit cell we introduce the spinors $\Psi^\dagger_{X/Y,\mathbf{k}} = (d^\dagger_{yz/xz\uparrow}, d^\dagger_{xy\uparrow})$. The momenta are defined with respect to *X*/*Y* point of the 1-Fe unit cell, which are folded into the *M*-point. The Hamiltonian reads

$$H^{X/Y}(\mathbf{k}) = \begin{pmatrix} A^{X/Y}_{yz/xz,\mathbf{k}} & -iV^{X/Y}_{\mathbf{k}}, \\ iV^{X/Y}_{\mathbf{k}} & A^{X/Y}_{xy,\mathbf{k}}. \end{pmatrix}. \quad (2)$$

and the elements are

$$A^{X/Y}_{\mu,\mathbf{k}} = \epsilon_{\mu,0} - \frac{\mathbf{k}^2}{2m_\mu} \mp \frac{a_\mu}{2}\left(k_x^2 - k_y^2\right) - \mu, \quad (3)$$

$$V^{X/Y} = \sqrt{2}vk_{y/x} + \frac{p_1}{\sqrt{2}}\left(k^3_{y/x} + 3k_{y/x}k^2_{x/y}\right) \mp \frac{p_2}{\sqrt{2}}k_{y/x}\left(k_x^2 - k_y^2\right). \quad (4)$$

The orbitals are coupled by the in-plane SOC λ_2

$$H^M_{\mathrm{SOC}} = \frac{\lambda_2}{2}\sum_{\mathbf{k}}\left(i^{X\dagger}_{yz\uparrow} d^Y_{xy\downarrow} + d^{X,\dagger}_{xy\uparrow} d^Y_{xz\downarrow} + h.c.\right). \quad (5)$$

The band dispersion for the tetragonal state near the *M* point is shown in the bottom panel of the **Figure 1D**. Note the value of SOC is taken different if the orbitals originate from the same sublattice in the 1-Fe unit cell, $\lambda_1 = 23$ meV or from the two different sublattices, $\lambda_2 = 4$ meV [66]. This agrees with the experimental ARPES observation, which measured different values of the SOC near different symmetry points of the BZ [67, 68].

2.2 Nematic State

To describe the nematic state in FeSe, which forms below the $T_S = 90$ K, we add the nematic order to the Hamiltonian in a phenomenological fashion. We assumed the nematic order

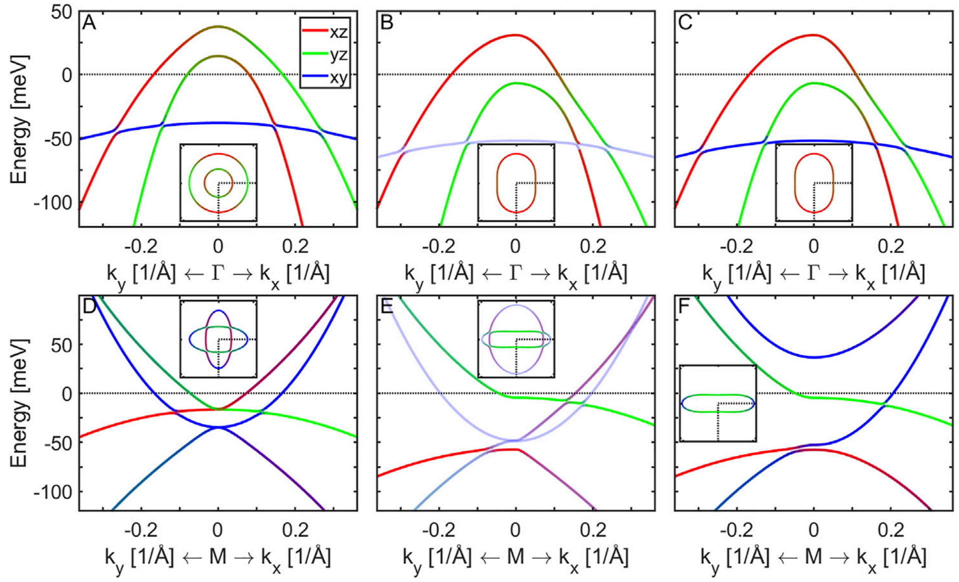

FIGURE 1 | The band structure of the 2-Fe Brillouin zone around the Γ and the M point is presented comparing the tetragonal state and scenarios A and B for the nematic state in FeSe as described in the text. Panels **(A)–(C)** show the energy dispersion near the Γ point in the tetragonal state **(A)** and two nematic states without (Scenario A) **(B)** and with **(C)** non-local d_{xy} nematicity (Scenario B). Panels **(D–F)** display the corresponding band structure near the M point. Red, green and blue colors illustrate the orbital weights of the d_{xz}, d_{yz} and d_{xy} Fe-orbitals, respectively. The insets show the corresponding Fermi surface and demonstrate the cuts performed. Shading according to the d_{xy} orbital weight in panels **(B)** and **(E)** reflects the Z-factors used in [44].

parameters follow a mean-field temperature dependence $\Phi(T) = \Phi(0)\sqrt{1 - T/T_S}$. As described in the Introduction we distinguish two scenarios: **Scenario A** containing an order parameter $\Phi^{h,e}$ that lifts the d_{xz} and d_{yz} degeneracy, and **Scenario B** in which an additional non-local d_{xy}-order parameter Φ_{xy} and a d_{xy}-Hatree shift $\Delta\epsilon_{xy}$ are added [56].

In particular, the xz/yz nematic order parameter near the Γ point can be described as:

$$H^{\Gamma}_{\text{nem}} = \Phi^h \sum_{\mathbf{k},\sigma\in(\uparrow,\downarrow)} \left(d^\dagger_{xz,\sigma} d_{xz,\sigma} - d^\dagger_{yz,\sigma} d_{yz,\sigma,}\right). \qquad (6)$$

For a given value of the SOC λ_1, adding a nematic order parameter yields a Lifshitz transition such that one of the Fermi surface pockets near the Γ point sinks below the Fermi level as shown in panels 1B and 1C for $\Phi^h(10\,\text{K}) = 15$ meV. Near the M point the xz/yz nematic order has opposite sign to Φ^h and we also include an additional non-local d_{xy}-nematic order [56]:

$$H^{M}_{\text{nem}} = \sum_{\mathbf{k},\sigma}\Big(\Phi^e\big(d^{Y\dagger}_{xz,\sigma} d^{Y}_{xz,\sigma} - d^{X\dagger}_{yz,\sigma} d^{X}_{yz,\sigma}\big) + \big(\Delta\epsilon_{xy} + \Phi_{xy}\big) d^{Y\dagger}_{xy,\sigma} d^{Y}_{xy,\sigma}$$

$$+\big(\Delta\epsilon_{xy} - \Phi_{xy}\big) d^{X\dagger}_{xy,\sigma} d^{X}_{xy,\sigma}\Big). \qquad (7)$$

In the conventional scenario of nematicity (Scenario A), only $\Phi^e(10\,\text{K}) = -26$ meV is included and the resulting band structure near the M point is illustrated in **Figure 1E**. Observe two electron pockets at the M point, which exist for all temperatures. To connect Scenario A with experimental ARPES results in the nematic state, which do not observe the larger electron pocket, orbital-selective quasiparticle weights are introduced in various works [26, 30, 44, 54, 69], see also for a recent review Ref. [70]. Within this scenario the quasiparticle weight of the d_{xy} orbital is claimed to be much smaller than that of the d_{yz}/d_{xz} orbitals. This would lead to a suppression of the quasiparticle weight of the d_{xy} dominated bands and especially of the outer electron pocket at M point, making d_{xy}- rbital states invisible in the ARPES experiment. This is illustrated in panels 1B and 1E by orbital-selective shading. The idea of orbital-selective spectral weights is motivated also by the previous results of the dynamical mean-field theory calculations [71]. This scenario was claimed to be in agreement with STM measurements of the electronic structure [69], the superconducting gap properties [30], and the magnetic susceptibility measured by inelastic neutron scattering [26]. A problem of this scenario is that both in the tetragonal and the nematic state of FeSe, bands of d_{xy} orbital character have been identified around the M point [28]. Although d_{xy} orbital appears indeed to exhibit a larger effective mass renormalization than the other two orbitals, it is not sufficiently large to mask d_{xy} spectral weight completely in the ARPES experiments [64].

Within the Scenario B one introduces the non-local nematic order within the xy-orbital: $\Phi_{xy}(10\,\text{K}) = 45$ meV and $\Delta\epsilon_{xy}(10\,\text{K}) = 40$ meV and the resulting band structure is shown in **Figure 1F**. As the band structure evolves from the tetragonal to the nematic state, an additional Lifshitz transition occurs around 70 K, leaving a single electron Fermi surface pocket at 10 K. The Scenario B assumes that the nematic ordering near the M point does not cause a minor perturbation of the electronic structure, but can lift an entire electron pocket away from the Fermi level. Its consequences for various experiments were reviewed in Ref. [59] and present an alternative description of the nematicity in FeSe. The chemical potential μ is renormalized to fulfill the Luttinger theorem and is set to zero at 10 K [56].

2.3 Superconducting State

It was argued in the past that within both the Scenario A and the Scenario B the superconducting order parameter and its angular dependence on the Fermi surface pockets can be equally well described within a microscopic description [54, 56]. This indicates that superconductivity just adopts the existing electronic structure in the nematic state without further significant feedback on the nematicity. So within Scenario B we use the microscopic description of Ref. [56]. In particular, below the superconducting transition at $T_c = 8$ K, we additionally include superconducting gaps in the d_{xz} and d_{yz} orbitals and use previously found values from a microscopic calculations describing an extended s-wave gap structure [56]. The values are obtained solving the gap equations at $T = 0$ K focusing on the bands crossing the Fermi surface. Possible d_{xy} contributions to the pairing interaction are neglected. To describe the temperature dependence we assume a typical BCS form $\Delta_\mu(T) = \Delta_\mu(0\,\mathrm{K})\tanh(1.74\sqrt{T_c/T-1})$. For the Γ point we use

$$H^{\Gamma}_{\mathrm{sc}} = \sum_{\mathbf{k},\mu\in\{\mathrm{xz},\,\mathrm{yz}\}} \left(\Delta^{\Gamma}_{\mu} d^{\dagger}_{\mu,\uparrow,\mathbf{k}} d^{\dagger}_{\mu,\downarrow,-\mathbf{k}} + h.c.\right) \tag{8}$$

with $\Delta^{\Gamma}_{xz}(0\,\mathrm{K}) = -0.1$ meV and $\Delta^{\Gamma}_{yz}(0\,\mathrm{K}) = -5.3$ meV. For the M point we use

$$H^{M}_{\mathrm{sc}} = \sum_{\mathbf{k},\mu\in\{\mathrm{yz}(\mathrm{X}),\mathrm{xz}(\mathrm{Y})\}} \left(\Delta^{X/Y}_{\mu} d^{\dagger}_{\mu,\uparrow,\mathbf{k}} d^{\dagger}_{\mu,\downarrow,-\mathbf{k}} + h.c.\right) \tag{9}$$

with $\Delta^{Y}_{xz}(0\,\mathrm{K}) = 3.1$ meV and $\Delta^{X}_{yz}(0\,\mathrm{K}) = 1.6$ meV. The resulting Bogoliubov-de Gennes Hamiltonian is diagonalized numerically.

2.4 Magnetic Susceptibility

Within random phase approximation (RPA) analysis of the magnetic susceptibility χ [72–74] the bare part of the susceptibility is given by a combination of normal and anomalous contributions (*GG* and *FF*-terms)

$$\chi^{\eta_2\eta_3}_{\eta_1\eta_4}(q) = \sum_k \left[F_{\eta_2\eta_4}(k)\bar{F}_{\eta_1\eta_3}(k+q) - G_{\eta_2\eta_1}(k)G_{\eta_4\eta_3}(k+q)\right], \tag{10}$$

where G and F denote the single-particle normal and anomalous Green's functions and the *FF*-term vanishes above T_c. We use the short hand notations $k = (\mathbf{k}, i\omega_n)$ and $\eta = (\mu, \sigma)$ denoting orbital and spin degrees of freedom. The sum of Matsubara frequencies is carried out analytically and yields a Lindhard-type expression for the bare susceptibilities. Further details can be found in the **Supplementary Material S1**.

Within RPA we include the local interactions from a Hubbard-Hund Hamiltonian

$$\begin{aligned} H_{int} = {} & \frac{U}{2} \sum_{\mu\sigma\mathbf{k}\mathbf{k}'\mathbf{q}} d^{\dagger}_{\mu\sigma\mathbf{k}+\mathbf{q}} d^{\dagger}_{\mu\bar{\sigma}\mathbf{k}'-\mathbf{q}} d_{\mu\bar{\sigma}\mathbf{k}'} d_{\mu\sigma\mathbf{k}} + \frac{U'}{2} \sum_{\mu\neq\nu\sigma\sigma'\mathbf{k}\mathbf{k}'\mathbf{q}} d^{\dagger}_{\mu\sigma\mathbf{k}+\mathbf{q}} d^{\dagger}_{\nu\sigma'\mathbf{k}'-\mathbf{q}} d_{\nu\sigma'\mathbf{k}'} d_{\mu\sigma\mathbf{k}} \\ & + \frac{J}{2} \sum_{\mu\neq\nu\sigma\sigma'\mathbf{k}\mathbf{k}'\mathbf{q}} d^{\dagger}_{\nu\sigma\mathbf{k}+\mathbf{q}} d^{\dagger}_{\mu\sigma'\mathbf{k}'-\mathbf{q}} d_{\nu\sigma'\mathbf{k}'} d_{\mu\sigma\mathbf{k}} + \frac{J'}{2} \sum_{\mu\neq\nu\sigma\mathbf{k}\mathbf{k}'\mathbf{q}} d^{\dagger}_{\mu\sigma\mathbf{k}+\mathbf{q}} d^{\dagger}_{\mu\bar{\sigma}\mathbf{k}'-\mathbf{q}} d_{\nu\bar{\sigma}\mathbf{k}'} d_{\nu\sigma\mathbf{k}}. \end{aligned} \tag{11}$$

In what follows we set the intraorbital Coulomb repulsion interaction $U = 1$ eV. For the interorbital Coulomb repulsion U', the residual Hund interaction J and the pair hopping J' terms we use the standard spin-rotational relations $U' = U - 2J$ and $J = J'$ and set $J/U = 1/6$ similar to previous studies [26, 44].

The RPA treatment yields a Dyson type equation with a symbolic solution

$$\chi_{RPA} = \left[1 - \chi_0\hat{U}\right]^{-1}\chi_0. \tag{12}$$

The interaction matrix $\hat{U}$ results from **Eq. 11** and the free spin and orbital indices are contracted with matrix elements from the magnetic operator, which is a combination of spin and angular momentum operators

$$\mu^{a}_{\eta_1\eta_4} = \left(\frac{g}{2}\sigma^{a}_{\sigma_1\sigma_4}\delta_{\mu_1\mu_4} + L^{a}_{\mu_1\mu_4}\delta_{\sigma_1\sigma_4}\right). \tag{13}$$

The magnetic susceptibility tensor component χ^{ab} results from the contraction of the external spin and orbital indices of the solution with the a-th and b-th component of the operator. We can separate the spin χ_{spin}, the orbital χ_{orb} and mixed χ_{mix} components of the susceptibility. In this manuscript we focus on the static limit of uniform susceptibility $\chi^{ab}(q \to 0)$ and further details of the calculation can be found in the **Supplementary Material S1**.

3 RESULTS

In the following we present the results for the magnetic susceptibility $\chi(q \to 0)$ and its anisotropy following Scenario B. Note that within Scenario A the behavior of the magnetic susceptibility was considered in Ref. [44]. One of the main findings of this study was that in order to reproduce the correct sign of the magnetic anisotropy at low temperatures, *i.e.* $\chi^{yy} < \chi^{xx}$, the quasiparticle weight of various orbitals has to fulfil $Z_{xy} < Z_{xz} < Z_{yz}$. Within Scenario B this assumption is not necessary as the d_{xy} orbital is weakly present at the Fermi level and this should yield in principle the right sign of the magnetic anisotropy. We show in the Supplementary that further factors can affect the signs of the anisotropy as well and the situation depends on the details of the electronic structure in both Scenarios. In addition, in our case we find the dominance of the spin component of the susceptibility $\chi_{\mathrm{mix}} < \chi_{\mathrm{orb}} < \chi_{\mathrm{spin}}$, which is a consequence of the low-energy model we used. Moreover, we find that RPA primarily amplifies the spin contribution. Including the whole $3d$ state manifold would increase the temperature-independent orbital contribution to the susceptibility, which can be treated as a constant.

Nevertheless, one of the interesting questions is how to distinguish between both scenarios and whether one is able to identify an additional Lifshitz transition associated with the removal of the second electron pocket from the Fermi level at the M point both theoretically and experimentally. To do so we calculate the temperature dependence of the static uniform susceptibility and compare our results with experimental data of Ref. [25] where the standard notations $x\|a$, $y\|b$ and $z\|c$ are used.

The temperature dependence of the static uniform susceptibility is shown in **Figure 2A**. For comparison we also

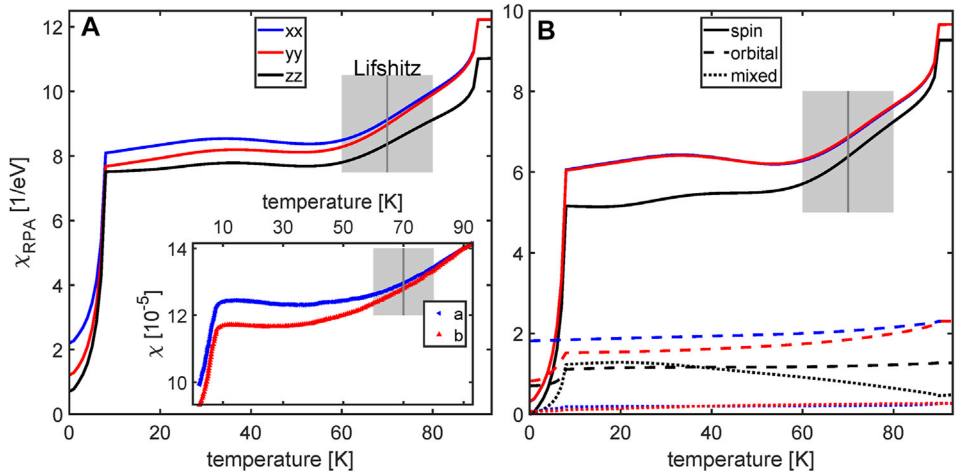

FIGURE 2 | Calculated temperature dependence of the magnetic susceptibility $\chi(q \to 0)$ calculated with an RPA approach. In **(A)** the total diagonal components χ^{xx}, χ^{yy} and χ^{zz} of the susceptibility calculated for scenario B are presented as blue, red and black curves, respectively. The corresponding spin, orbital and mixed contributions to the different components are shown in **(B)** as solid, dashed and dotted curves, respectively. The inset in **(A)** shows the experimental data extracted from [25] for comparison. The markers do not represent data points from the experiment. The gray boxes illustrate the decrease in susceptibility due to the Lifshitz transition of the *Y*-band. The boxes are centered around the Lifshitz transition temperature (dark gray line). Notice that the blue solid curve for the χ^{xx}_{spin} component in **(B)** is almost completely hidden behind the red curve for the χ^{yy}_{spin} component due to tiny in-plane anisotropy in the spin susceptibility.

display the experimental data from Ref. [25] in the inset. Above the nematic transition the magnetic anisotropy is governed by the spin-orbit coupling and shows an easy-plane anisotropy $\chi^{xx} = \chi^{yy} > \chi^{zz}$. Below T_S, one observes two characteristic features. First we find that χ^{xx} becomes progressively larger than χ^{yy} as a result of the nematic order and the splitting between them increases continuously upon decreasing temperature. At the same time all three components of the magnetic susceptibility show a non-monotonic temperature dependence characterized by a rapid decrease below T_S and a plateau-like behavior, which starts around 60 K. Both, a continuous increase of the anisotropy upon lowering temperature and the non-monotonic temperature dependence of the susceptibilities agree well with the available experimental data of Ref. [75], shown in the inset.

To understand better the origin of these effects we show in **Figure 2B** the spin, the orbital, and the mixed susceptibilities. Note, the spin component of the magnetic susceptibility is the largest in magnitude and its non-monotonic temperature dependence is connected to the Lifshitz transition within Scenario B. In this scenario, the non-local d_{xy} nematic order parameter induces the shift of the larger electron pocket away from the Fermi level, which occurs in the temperature interval 60 K $< T < T_S$ and is clearly visible in the spin part of each (*xx*, *yy* and *zz*) component of the magnetic susceptibility. At the same time the main origin of the continuous increase of the magnetic in-plane anisotropy $\chi^{xx} > \chi^{yy}$ comes from the orbital part of the magnetic susceptibility as evident from **Figure 2B**. The in-plane anisotropy for the spin susceptibility is three orders of magnitude smaller within our modeling, which is a consequence of the small in-plane SOC λ_2 present at the *M* point and of the out-of-plane SOC between *xz* and *yz* orbitals present at hole pockets only transferring out-of-plane anisotropy to the spin susceptibility. Overall the orbital susceptibility is less sensitive to the orbital content of the Fermi surface but to overall orbital structure at low energies. This indicates that not only the pockets at the Fermi level but the overall electronic structure (also away from the Fermi level) is responsible for the continuous increase of the magnetic anisotropy and its correct sign. Note that within both Scenario A and Scenario B of the nematicity in FeSe the correct sign of the magnetic in-plane anisotropy in the uniform susceptibility can be successfully reproduced. What, however, remains unclear in the Scenario A is whether the non-monotonous temperature dependence, which in Scenario B is a clear signature of a Lifshitz transition, could be reproduced in the Scenario A as well.

We also note that in the iron pnictides, where nematicity coexists with the antiferromagnetic order an in-plane anisotropy of the magnetic susceptibility would give a corresponding feedback on the magnetic order parameter and also enhance the anisotropy of the spin susceptibility below the magnetic transition temperature, see for example Ref. [76]. However, as the magnetic transition in FeSe appears only upon applying pressure and bearing in mind that the in-plane anisotropy we found is only few percent of the total magnitude of the spin susceptibility, the anisotropy of the orbital susceptibility will be the main origin of the magnetic anisotropy in FeSe.

To complete the analysis we also computed the change of the uniform superconductivity in the superconducting state. Due to the spin singlet superconducting order parameter in FeSe we see a sharp drop in the uniform susceptibility upon entering the superconducting state, see **Figure 2A**. This is due to the strong reduction of the spin component of the susceptibility, as evident from **Figure 2B**. Note the small admixture of the spin-triplet component of the superconducting gap due to the finite spin-orbit coupling does not affect much the magnetic anisotropy in the spin part. The residual contribution to the magnetic

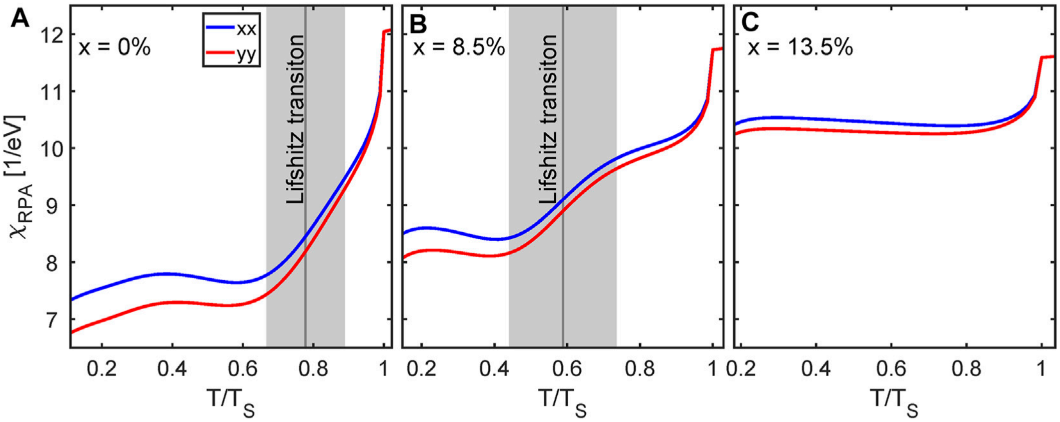

FIGURE 3 | Calculated effect of sulphur doping of $FeSe_{1-x}S_x$ on temperature dependence of the magnetic susceptibility $\chi(q \to 0)$. The panels **(A)–(C)** compare the doping values $x = 0$, $x = 0.085$ and $x = 0.135$. As in 2, the gray boxes illustrate the Lifshitz transition region of the Y-band. For $x = 13.5$, the Lifshitz transition is absent.

susceptibility stems largely from the orbital part of the susceptibility and corresponds to inter-orbital contributions, which is slightly affected by the onset of superconductivity. The decrease in χ^{yy}_{orb} yields an increase of the in-plane anisotropy and results from intra-band contributions, which appear due to hybridization of d_{yz} and d_{xy} orbitals at Fermi level (compare **Figure 1F**).

To make a qualitative prediction on the evolution of the uniform susceptibility and its in-plane magnetic anisotropy in **Figure 3**, we present our calculations for the susceptibility in the doped $FeSe_{1-x}S_x$ compounds, following previous analysis of superconductivity and nematicity [56]. In particular, we show χ^{xx} and χ^{yy} for $x = 0$, $x = 0.085$ and $x = 0.135$ in panels 3A-3C, respectively. The doping evolution of the nematic order parameters is modeled with a mean-field dependence $\Phi(x) = \Phi(0)\sqrt{1 - x/x_0}$. Here we estimate $x_0 = 0.18$, $T_S(x = 0.085) = 68$ K and $T_S(x = 0.135) = 55$ K from interpolation of the phase diagram given in [77]. The Lifshitz transition is shifted to lower (relative) temperatures with increasing doping and is expected to disappear at around $x \approx 0.13$. Thus, for intermediate doping, we expect to see further the Lifshitz transition and significant changed temperature dependence for doping above $x = 0.135$. As the orbital part is not as sensitive to the Lifshitz transition, significant residual in-plane anisotropy is expected for all dopings.

4 DISCUSSION AND CONCLUSION

Our calculated results for the uniform magnetic susceptibility within the non-local d_{xy} nematicity agree well with experimental observations including the Knight shift measurements [16, 21, 25, 47, 48, 75]. Within this scenario there is no necessity to use orbital-selective quasiparticle weights. Furthermore, this scenario can also successfully explain the non-monotonic temperature dependence of the uniform susceptibility as resulting from the Lifshitz transition of the larger electron pocket, which rapidly shifts away from the Fermi level within 60 K $< T < T_S$ temperature interval.

Our studies suggest that both spin and orbital contributions and their temperature dependencies are important in describing the uniform magnetic susceptibility or the Knight shift. While the spin part provides the main contribution to the temperature dependence, the orbital part is crucial for a sizeable in-plane anisotropy as observed in experiments. The temperature dependence of the spin part fits very well to the scenario of a Lifshitz transition at Y-point, which appears due to the inclusion of the non-local d_{xy}-nematicity. The finite temperature dependence of the orbital susceptibility breaks linear relation between the bulk magnetic susceptibility and the Knight shift and naturally explains the observed Knight shift anomaly [47, 75]. We note further that the orbital contribution can be in fact larger if one includes larger energy window for the considered model. This should result in the larger in-plane anisotropy but will not affect the non-monotonic temperature dependence of the spin susceptibility.

Our results for the superconducting state also agree qualitatively with recent measurements. The decrease below T_c is seen in measurement of the static, uniform bulk susceptibility [25, 75] and also in the Knight shift measurements [47, 48]. Moreover, in agreement with our results, a slight enhancement of in-plane anisotropy is observed [47].

In summary, we have studied the uniform magnetic susceptibility for a model of FeSe and $FeSe_{1-x}S_x$ compounds with particular attention on the consequences of non-local d_{xy}-nematicity. We associate the corresponding Lifshitz transition of a Y-electron pocket with a sharp decrease of the spin component of the magnetic susceptibility, whereas large in-plane anisotropy of the magnetic susceptibility is linked to the orbital susceptibility. The hierarchy of the anisotropy depend on orbital structure of the electronic bands at and away from the Fermi level where the orbital selective quasiparticle weights could be only one potential factor affecting the anisotropy.

We further note that the nematicity also affects the anisotropy of the spin fluctuations at the antiferromagnetic momentum near $(\pi, 0)$ or $(0, \pi)$ wavevectors. This anisotropy we also found in our calculations by computing the spin response at large momenta (not shown). This behavior is quite similar in both scenarios of nematicity, while we expect a different temperature dependence of the uniform magnetic susceptibility at $q = 0$ in both cases.

DATA AVAILABILITY STATEMENT

The original contributions presented in the study are included in the article/**Supplementary Material**, further inquiries can be directed to the corresponding author/s.

AUTHOR CONTRIBUTIONS

SB made the analytical and numercial calculations under the supervision of IE, both discussed the obtained results and wrote the manuscript.

FUNDING

This work was supported by a joint NSFC-DFG grant (ER 463/14-1).

ACKNOWLEDGMENTS

We are thankful to Jakob Böker and Luke Rhodes for fruitful discussions. We also acknowledge support by the Open Access Publication Funds of the Ruhr-Universität Bochum.

SUPPLEMENTARY MATERIAL

The Supplementary Material for this article can be found online at: https://www.frontiersin.org/articles/10.3389/fphy.2022.919784/full#supplementary-material

REFERENCES

1. Kastner MA, Birgeneau RJ, Shirane G, Endoh Y. Magnetic, Transport, and Optical Properties of Monolayer Copper Oxides. *Rev Mod Phys* (1998) 70:897–928. doi:10.1103/RevModPhys.70.897
2. Tranquada JM, Xu G, Zaliznyak IA. Superconductivity, Antiferromagnetism, and Neutron Scattering. *J magnetism Magn Mater* (2014) 350:148–60. doi:10.1016/j.jmmm.2013.09.029
3. Fernandes RM, Chubukov AV, Schmalian J. What Drives Nematic Order in Iron-Based Superconductors? *Nat Phys* (2014) 10:97–104. doi:10.1038/nphys2877
4. Böhmer AE, Kreisel A. Nematicity, Magnetism and Superconductivity in Fese. *J Phys Condensed Matter* (2017) 30:023001.
5. Dai P. Antiferromagnetic Order and Spin Dynamics in Iron-Based Superconductors. *Rev Mod Phys* (2015) 87:855–96. doi:10.1103/revmodphys.87.855
6. Fernandes RM, Schmalian J. Manifestations of Nematic Degrees of freedom in the Magnetic, Elastic, and Superconducting Properties of the Iron Pnictides. *Supercond Sci Technol* (2012) 25:084005. doi:10.1088/0953-2048/25/8/084005
7. Fanfarillo L, Cortijo A, Valenzuela B. Spin-orbital Interplay and Topology in the Nematic Phase of Iron Pnictides. *Phys Rev B* (2015) 91:214515. doi:10.1103/PhysRevB.91.214515
8. Fanfarillo L, Mansart J, Toulemonde P, Cercellier H, Le Fèvre P, Bertran F, et al. Orbital-dependent Fermi Surface Shrinking as a Fingerprint of Nematicity in Fese. *Phys Rev B* (2016) 94:155138. doi:10.1103/PhysRevB.94.155138
9. Fanfarillo L, Benfatto L, Valenzuela B. Orbital Mismatch Boosting Nematic Instability in Iron-Based Superconductors. *Phys Rev B* (2018) 97:121109. doi:10.1103/PhysRevB.97.121109
10. Hsu FC, Luo JY, Yeh KW, Chen TK, Huang TW, Wu PM, et al. Superconductivity in the Pbo-type Structure α-fese. *Proc Natl Acad Sci* (2008) 105:14262–4. doi:10.1073/pnas.0807325105
11. McQueen T, Williams A, Stephens P, Tao J, Zhu Y, Ksenofontov V, et al. Tetragonal-to-orthorhombic Structural Phase Transition at 90 K in the Superconductor Fe 1.01 Se. *Phys Rev Lett* (2009) 103:057002. doi:10.1103/PhysRevLett.103.057002
12. Bendele M, Amato A, Conder K, Elender M, Keller H, Klauss HH, et al. Pressure Induced Static Magnetic Order in Superconducting Fese$_{1-x}$. *Phys Rev Lett* (2010) 104:087003. doi:10.1103/PhysRevLett.104.087003
13. Gallais Y, Paul I. Charge Nematicity and Electronic Raman Scattering in Iron-Based Superconductors. *Comptes Rendus Physique* (2016) 17:113–39. Iron-based superconductors /Supraconducteurs à base de fer. doi:10.1016/j.crhy.2015.10.001
14. Coldea AI, Watson MD. The Key Ingredients of the Electronic Structure of Fese. *Annu Rev Condensed Matter Phys* (2018) 9:125–46. doi:10.1146/annurev-conmatphys-033117-054137
15. Shibauchi T, Hanaguri T, Matsuda Y. Exotic Superconducting States in Fese-Based Materials. *J Phys Soc Jpn* (2020) 89:102002. doi:10.7566/jpsj.89.102002
16. Baek SH, Efremov D, Ok J, Kim J, Van Den Brink J, Büchner B. Orbital-driven Nematicity in Fese. *Nat Mater* (2015) 14:210–4. doi:10.1038/nmat4138
17. Su Y, Liao H, Li T. The Form and Origin of Orbital Ordering in the Electronic Nematic Phase of Iron-Based Superconductors. *J Phys Condensed Matter* (2015) 27:105702. doi:10.1088/0953-8984/27/10/105702
18. Mukherjee S, Kreisel A, Hirschfeld PJ, Andersen BM. Model of Electronic Structure and Superconductivity in Orbitally Ordered Fese. *Phys Rev Lett* (2015) 115:026402. doi:10.1103/PhysRevLett.115.026402
19. Jiang K, Hu J, Ding H, Wang Z. Interatomic Coulomb Interaction and Electron Nematic Bond Order in Fese. *Phys Rev B* (2016) 93:115138. doi:10.1103/PhysRevB.93.115138
20. Yamakawa Y, Onari S, Kontani H. Nematicity and Magnetism in Fese and Other Families of Fe-Based Superconductors. *Phys Rev X* (2016) 6:021032. doi:10.1103/physrevx.6.021032
21. Böhmer A, Arai T, Hardy F, Hattori T, Iye T, Wolf T, et al. Origin of the Tetragonal-To-Orthorhombic Phase Transition in Fese: A Combined Thermodynamic and Nmr Study of Nematicity. *Phys Rev Lett* (2015) 114:027001. doi:10.1103/PhysRevLett.114.027001
22. Xing RQ, Classen L, Khodas M, Chubukov AV. Competing Instabilities, Orbital Ordering, and Splitting of Band Degeneracies from a Parquet Renormalization Group Analysis of a Four-Pocket Model for Iron-Based Superconductors: Application to Fese. *Phys Rev B* (2017) 95:085108. doi:10.1103/PhysRevB.95.085108
23. Margadonna S, Takabayashi Y, McDonald MT, Kasperkiewicz K, Mizuguchi Y, Takano Y, et al. Crystal Structure of the New Fese 1- X Superconductor. *Chem Commun* (2008) 5607–9. doi:10.1039/b813076k
24. Tanatar MA, Böhmer AE, Timmons EI, Schütt M, Drachuck G, Taufour V, et al. Origin of the Resistivity Anisotropy in the Nematic Phase of Fese. *Phys Rev Lett* (2016) 117:127001. doi:10.1103/physrevlett.117.127001
25. He M, Wang L, Hardy F, Xu L, Wolf T, Adelmann P, et al. Evidence for Short-Range Magnetic Order in the Nematic Phase of Fese from Anisotropic In-Plane Magnetostriction and Susceptibility Measurements. *Phys Rev B* (2018) 97:104107. doi:10.1103/physrevb.97.104107
26. Chen T, Chen Y, Kreisel A, Lu X, Schneidewind A, Qiu Y, et al. Anisotropic Spin Fluctuations in Detwinned Fese. *Nat Mater* (2019) 18:709–16. doi:10.1038/s41563-019-0369-5
27. Lu X, Zhang W, Tseng Y, Liu R, Tao Z, Paris E, et al. *Spin-excitation Anisotropy in the Nematic State of Detwinned Fese* (2021). *arXiv preprint arXiv:2108.04484*.

28. Coldea AI, Watson MD. The Key Ingredients of the Electronic Structure of Fese. *Annu Rev Condensed Matter Phys* (2018) 9:125–46. doi:10.1146/annurev-conmatphys-033117-054137
29. Xu H, Niu X, Xu D, Jiang J, Yao Q, Chen Q, et al. Highly Anisotropic and Twofold Symmetric Superconducting gap in Nematically Ordered Fese 0.93 S 0.07. *Phys Rev Lett* (2016) 117:157003. doi:10.1103/physrevlett.117.157003
30. Sprau PO, Kostin A, Kreisel A, Böhmer AE, Taufour V, Canfield PC, et al. Discovery of Orbital-Selective cooper Pairing in Fese. *Science* (2017) 357: 75–80. doi:10.1126/science.aal1575
31. Rhodes LC, Watson MD, Haghighirad AA, Evtushinsky DV, Eschrig M, Kim TK. Scaling of the Superconducting gap with Orbital Character in Fese. *Phys Rev B* (2018) 98:180503. doi:10.1103/physrevb.98.180503
32. Kushnirenko Y, Fedorov A, Haubold E, Thirupathaiah S, Wolf T, Aswartham S, et al. Three-dimensional Superconducting gap in Fese from Angle-Resolved Photoemission Spectroscopy. *Phys Rev B* (2018) 97:180501. doi:10.1103/physrevb.97.180501
33. Liu D, Li C, Huang J, Lei B, Wang L, Wu X, et al. Orbital Origin of Extremely Anisotropic Superconducting gap in Nematic Phase of Fese Superconductor. *Phys Rev X* (2018) 8:031033. doi:10.1103/physrevx.8.031033
34. Hashimoto T, Ota Y, Yamamoto HQ, Suzuki Y, Shimojima T, Watanabe S, et al. Superconducting gap Anisotropy Sensitive to Nematic Domains in Fese. *Nat Commun* (2018) 9:1–7. doi:10.1038/s41467-017-02739-y
35. Huh S, Lu Z, Kim YS, Kim D, Liu S, Ma M, et al. *Cu Doping Effects on the Electronic Structure of Fe1-Xcuxse* (2021). *arXiv preprint arXiv:2110.14463.*
36. Mizuguchi Y, Tomioka F, Tsuda S, Yamaguchi T, Takano Y. Substitution Effects on Fese Superconductor. *J Phys Soc Jpn* (2009) 78:074712. doi:10.1143/jpsj.78.074712
37. Schoop LM, Medvedev SA, Ksenofontov V, Williams A, Palasyuk T, Troyan IA, et al. Pressure-restored Superconductivity in Cu-Substituted Fese. *Phys Rev B* (2011) 84:174505. doi:10.1103/physrevb.84.174505
38. Medvedev S, McQueen T, Troyan I, Palasyuk T, Eremets M, Cava R, et al. Electronic and Magnetic Phase Diagram of β-fe1. 01se with Superconductivity at 36.7 K under Pressure. *Nat Mater* (2009) 8:630–3. doi:10.1038/nmat2491
39. Shimojima T, Suzuki Y, Sonobe T, Nakamura A, Sakano M, Omachi J, et al. Lifting of Xz/yz Orbital Degeneracy at the Structural Transition in Detwinned Fese. *Phys Rev B* (2014) 90:121111. doi:10.1103/PhysRevB.90.121111
40. Watson MD, Haghighirad AA, Rhodes LC, Hoesch M, Kim TK. Electronic Anisotropies Revealed by Detwinned Angle-Resolved Photo-Emission Spectroscopy Measurements of Fese. *New J Phys* (2017) 19:103021. doi:10.1088/1367-2630/aa8a04
41. Yi M, Pfau H, Zhang Y, He Y, Wu H, Chen T, et al. Nematic Energy Scale and the Missing Electron Pocket in Fese. *Phys Rev X* (2019) 9:041049. doi:10.1103/physrevx.9.041049
42. Huh S, Seo J, Kim B, Cho S, Jung JK, Kim S, et al. Absence of Y-Pocket in 1-fe Brillouin Zone and Reversed Orbital Occupation Imbalance in Fese. *Commun Phys* (2020) 3:1–7.
43. Pfau H, Yi M, Hashimoto M, Chen T, Dai PC, Shen ZX, et al. Quasiparticle Coherence in the Nematic State of Fese. *Phys Rev B* (2021) 104:L241101. doi:10.1103/physrevb.104.l241101
44. Zhou R, Scherer DD, Mayaffre H, Toulemonde P, Ma M, Li Y, et al. Singular Magnetic Anisotropy in the Nematic Phase of Fese. *npj Quan Mater* (2020) 5: 1–9. doi:10.1038/s41535-020-00295-1
45. Watson MD, Kim TK, Haghighirad AA, Davies NR, McCollam A, Narayanan A, et al. Emergence of the Nematic Electronic State in Fese. *Phys Rev B* (2015) 91:155106. doi:10.1103/PhysRevB.91.155106
46. Chu JH, Analytis JG, De Greve K, McMahon PL, Islam Z, Yamamoto Y, et al. In-plane Resistivity Anisotropy in an Underdoped Iron Arsenide Superconductor. *Science* (2010) 329:824–6. doi:10.1126/science.1190482
47. Vinograd I, Edwards S, Wang Z, Kissikov T, Byland J, Badger J, et al. Inhomogeneous Knight Shift in Vortex Cores of Superconducting Fese. *Phys Rev B* (2021) 104:014502. doi:10.1103/physrevb.104.014502
48. Li J, Kang B, Zhao D, Lei B, Zhou Y, Song D, et al. Se 77-nmr Evidence for Spin-Singlet Superconductivity with Exotic Superconducting Fluctuations in Fese. *Phys Rev B* (2022) 105:054514. doi:10.1103/physrevb.105.054514
49. Pustogow A, Luo Y, Chronister A, Su YS, Sokolov D, Jerzembeck F, et al. Constraints on the Superconducting Order Parameter in Sr2ruo4 from Oxygen-17 Nuclear Magnetic Resonance. *Nature* (2019) 574:72–5. doi:10.1038/s41586-019-1596-2
50. Zhang P, Qian T, Richard P, Wang XP, Miao H, Lv BQ, et al. Observation of Two Distinct D_{xz}/d_{yz} Band Splittings in Fese. *Phys Rev B* (2015) 91:214503. doi:10.1103/PhysRevB.91.214503
51. Suzuki Y, Shimojima T, Sonobe T, Nakamura A, Sakano M, Tsuji H, et al. Momentum-dependent Sign Inversion of Orbital Order in Superconducting Fese. *Phys Rev B* (2015) 92:205117. doi:10.1103/PhysRevB.92.205117
52. Zhang Y, Yi M, Liu ZK, Li W, Lee JJ, Moore RG, et al. Distinctive Orbital Anisotropy Observed in the Nematic State of a Fese Thin Film. *Phys Rev B* (2016) 94:115153. doi:10.1103/PhysRevB.94.115153
53. Watson MD, Haghighirad AA, Takita H, Mansuer W, Iwasawa H, Schwier EF, et al. Shifts and Splittings of the Hole Bands in the Nematic Phase of Fese. *J Phys Soc Jpn* (2017) 86:053703. doi:10.7566/JPSJ.86.053703
54. Kreisel A, Andersen BM, Sprau PO, Kostin A, Davis JS, Hirschfeld P. Orbital Selective Pairing and gap Structures of Iron-Based Superconductors. *Phys Rev B* (2017) 95:174504. doi:10.1103/physrevb.95.174504
55. Hu H, Yu R, Nica EM, Zhu JX, Si Q. Orbital-selective Superconductivity in the Nematic Phase of Fese. *Phys Rev B* (2018) 98:220503. doi:10.1103/physrevb.98.220503
56. Rhodes LC, Böker J, Müller MA, Eschrig M, Eremin IM. Non-local D Xy Nematicity and the Missing Electron Pocket in Fese. *npj Quan Mater* (2021) 6: 1–14. doi:10.1038/s41535-021-00341-6
57. Islam KR, Böker J, Eremin IM, Chubukov AV. Specific Heat and gap Structure of a Nematic Superconductor: Application to Fese. *Phys Rev B* (2021) 104: 094522. doi:10.1103/physrevb.104.094522
58. Marciani M, Benfatto L. *Resistivity Anisotropy from Multiorbital Boltzmann Equation in Nematic Fese* (2022). *arXiv preprint arXiv:2202.12070.*
59. Rhodes LC, Eschrig M, Kim TK, Watson MD. Fese and the Missing Electron Pocket Problem. *Frontiers in Physics* (2022) 10:859017. doi:10.3389/fphy.2022.859017
60. Fernandes RM, Vafek O. Distinguishing Spin-Orbit Coupling and Nematic Order in the Electronic Spectrum of Iron-Based Superconductors. *Phys Rev B* (2014) 90:214514. doi:10.1103/PhysRevB.90.214514
61. Classen L, Xing RQ, Khodas M, Chubukov AV. Interplay between Magnetism, Superconductivity, and Orbital Order in 5-pocket Model for Iron-Based Superconductors: Parquet Renormalization Group Study. *Phys Rev Lett* (2017) 118:037001. doi:10.1103/PhysRevLett.118.037001
62. Christensen MH, Fernandes RM, Chubukov AV. Orbital Transmutation and the Electronic Spectrum of Fese in the Nematic Phase. *Phys Rev Res* (2020) 2: 013015. doi:10.1103/PhysRevResearch.2.013015
63. Li J, Lei B, Zhao D, Nie LP, Song DW, Zheng LX, et al. Spin-orbital-intertwined Nematic State in Fese. *Phys Rev X* (2020) 10:011034. doi:10.1103/PhysRevX.10.011034
64. Watson M, Kim T, Haghighirad A, Davies N, McCollam A, Narayanan A, et al. Emergence of the Nematic Electronic State in Fese. *Phys Rev B* (2015) 91: 155106. doi:10.1103/physrevb.91.155106
65. Cvetkovic V, Vafek O. Space Group Symmetry, Spin-Orbit Coupling, and the Low-Energy Effective Hamiltonian for Iron-Based Superconductors. *Phys Rev B* (2013) 88:134510. doi:10.1103/physrevb.88.134510
66. Scherer DD, Jacko A, Friedrich C, Şaşıoğlu E, Blügel S, Valentí R, et al. Interplay of Nematic and Magnetic Orders in Fese under Pressure. *Phys Rev B* (2017) 95:094504. doi:10.1103/physrevb.95.094504
67. Borisenko S, Evtushinsky DV, Liu ZH, Morozov I, Kappenberger R, Wurmehl S, et al. Direct Observation of Spin–Orbit Coupling in Iron-Based Superconductors. *Nat Phys* (2015) 12:311. doi:10.1038/nphys3594
68. Day RP, Levy G, Michiardi M, Zwartsenberg B, Zonno M, Ji F, et al. Influence of Spin-Orbit Coupling in Iron-Based Superconductors. *Phys Rev Lett* (2018) 121:076401. doi:10.1103/PhysRevLett.121.076401
69. Kostin A, Sprau PO, Kreisel A, Chong YX, Böhmer AE, Canfield PC, et al. Imaging Orbital-Selective Quasiparticles in the Hund's Metal State of Fese. *Nat Mater* (2018) 17:869. doi:10.1038/s41563-018-0151-0
70. Kreisel A, Hirschfeld PJ, Andersen BM. On the Remarkable Superconductivity of Fese and its Close Cousins. *Symmetry* (2020) 12. doi:10.3390/sym12091402
71. Yin ZP, Haule K, Kotliar G. Kinetic Frustration and the Nature of the Magnetic and Paramagnetic States in Iron Pnictides and Ironchalcogenide. *Nat Mater* (2018) 10:932. doi:10.1038/nmat3120
72. Maier T, Graser S, Scalapino D, Hirschfeld P. Neutron Scattering Resonance and the Iron-Pnictide Superconducting gap. *Phys Rev B* (2009) 79:134520. doi:10.1103/physrevb.79.134520

73. Graser S, Maier T, Hirschfeld P, Scalapino D. Near-degeneracy of Several Pairing Channels in Multiorbital Models for the Fe Pnictides. *New J Phys* (2009) 11:025016. doi:10.1088/1367-2630/11/2/025016
74. Kemper AF, Maier TA, Graser S, Cheng HP, Hirschfeld P, Scalapino D. Sensitivity of the Superconducting State and Magnetic Susceptibility to Key Aspects of Electronic Structure in Ferropnictides. *New J Phys* (2010) 12: 073030. doi:10.1088/1367-2630/12/7/073030
75. Li J, Lei B, Zhao D, Nie L, Song D, Zheng L, et al. Spin-orbital-intertwined Nematic State in Fese. *Phys Rev X* (2020) 10:011034. doi:10.1103/physrevx.10.011034
76. He M, Wang L, Ahn F, Hardy F, Wolf T, Adelmann P, et al. Dichotomy between In-Plane Magnetic Susceptibility and Resistivity Anisotropies in Extremely Strained Bafe$_2$as$_2$. *Nat Commun* (2017) 8. doi:10.1038/s41467-017-00712-3
77. Coldea AI, Blake SF, Kasahara S, Haghighirad AA, Watson MD, Knafo W, et al. Evolution of the Low-Temperature Fermi Surface of Superconducting Fese1- Xsx across a Nematic Phase Transition. *npj Quan Mater* (2019) 4:1–7. doi:10.1038/s41535-018-0141-0

Conflict of Interest: The authors declare that the research was conducted in the absence of any commercial or financial relationships that could be construed as a potential conflict of interest.

ORIGINAL RESEARCH
published: 19 July 2022
doi: 10.3389/fphy.2022.915619

Diverse Exotic Orders and Fermiology in Fe-Based Superconductors: A Unified Mechanism for B_{1g}/B_{2g} Nematicity in FeSe/(Cs,Rb)Fe_2As_2 and Smectic Order in $BaFe_2As_2$

Seiichiro Onari and Hiroshi Kontani*

Department of Physics, Nagoya University, Nagoya, Japan

A rich variety of nematic/smectic orders in Fe-based superconductors is an important unsolved problem in strongly correlated electron systems. A unified understanding of these orders has been investigated for the last decade. In this study, we explain the B_{1g} symmetry nematic transition in $FeSe_{1-x}Te_x$, the B_{2g} symmetry nematicity in AFe_2As_2 (A = Cs, Rb), and the smectic state in $BaFe_2As_2$ based on the same framework. We investigate the quantum interference mechanism between spin fluctuations by developing the density wave equation. The observed rich variety of nematic/smectic orders is naturally understood in this mechanism. The nematic/smectic orders depend on the characteristic shape and topology of the Fermi surface (FS) of each compound. 1) In $FeSe_{1-x}Te_x$ (n_d = 6.0), each FS is very small and the d_{xy}-orbital hole pocket is below the Fermi level. In this case, the small spin fluctuations on three d_{xz}, d_{yz}, and d_{xy} orbitals cooperatively lead to the B_{1g} nematic ($\boldsymbol{q} = \mathbf{0}$) order without magnetization. The experimental Lifshitz transition below the nematic transition temperature (T_S) is naturally reproduced. 2) In $BaFe_2As_2$ (n_d = 6.0), the d_{xy}-orbital hole pocket emerges around the M point, and each FS is relatively large. The strong spin fluctuations due to the d_{xy}-orbital nesting give rise to the B_{1g} nematic ($\boldsymbol{q} = \mathbf{0}$) order and the smectic [$\boldsymbol{q} = (0, \pi)$] order, and the latter transition temperature ($T^* \sim 170$K) exceeds the former one ($T_S \sim 140$K). 3) In heavily hole-doped AFe_2As_2 (n_d = 5.5), the large d_{xy}-orbital hole pocket and the four tiny Dirac pockets appear due to the hole-doping. The B_{2g} nematic bond order emerges on the d_{xy}-orbital hole pocket because of the same interference mechanism. The present paramagnon interference mechanism provides a unified explanation of why the variety of nematic/smectic orders in Fe-based superconductors is so rich, based on the well-established fermiology of Fe-based superconductors.

Keywords: nematic order, smectic order, orbital order, bond order, quantum critical point, iron-based superconductors

Edited by:
Laura Fanfarillo,
International School for Advanced Studies (SISSA), Italy

Reviewed by:
Avraham Klein,
Ariel University, Israel
Samuel Lederer,
University of California, Berkeley, United States

***Correspondence:**
Seiichiro Onari
onari@s.phys.nagoya-u.ac.jp

Specialty section:
This article was submitted to Condensed Matter Physics, a section of the journal Frontiers in Physics

Received: *08 April 2022*
Accepted: *14 June 2022*
Published: *19 July 2022*

Citation:
Onari S and Kontani H (2022) Diverse Exotic Orders and Fermiology in Fe-Based Superconductors: A Unified Mechanism for B_{1g}/B_{2g} Nematicity in FeSe/(Cs,Rb)Fe_2As_2 and Smectic Order in $BaFe_2As_2$. Front. Phys. 10:915619. doi: 10.3389/fphy.2022.915619

1 INTRODUCTION

The emergence of an electron nematic ($\boldsymbol{q} = \boldsymbol{0}$) state is one of the most important unsolved problems in Fe-based superconductors [1]. In LaFeAsO and Ba122 compounds, the antiferro (AF) magnetic state appears at the Néel temperature T_N, which is lower than the nematic transition temperature T_S. Since the superconducting phase with a high transition temperature (T_c) appears near the nematic phase and the AF magnetic phase, it is expected that the nematic fluctuations and the spin fluctuations are related to the mechanism of the high-T_c superconductivity. However, the questions appear before discussing the superconductivity: 1) what is the order parameter of the nematic state? 2) What is the driving force of the nematic state? 3) Why do the diverse nematic states emerge in various compounds?

It is known that the nematic order cannot be derived from the mean-field theory since the spin-channel order always dominates over the nematic order unless unphysical parameters (such as negative Hund's coupling) are assumed. Previously, to explain the nematic state [2], the vestigial order (spin nematic) scenario [3–9] and the orbital order scenario [10–22] have been proposed.

To investigate the nematic state, the FeSe family is an ideal platform since the AF magnetic state is absent [23–26]. This family is also ideal from the aspect of superconductivity since the highest $T_c \gtrsim 65$K in Fe-based superconductors has been reported in electron-doped FeSe [27–31]. In FeSe, the orbital polarization between d_{xz} and d_{yz} orbitals in the nematic state has been observed by angle-resolved-photoemission spectroscopy (ARPES) [32–36]. To be more precise, the orbital polarization energy $E_{xz} - E_{yz}$ has $\boldsymbol{k}$ dependence and changes the sign between the Γ point and the X (Y) point. This sign reversal orbital polarization has been explained by the orbital order scenario [16, 17, 19, 20] based on the paramagnon interference mechanism and by the renormalization group (RG) theory [37, 38]. In both theories, the vertex correction (VC) of the Coulomb interaction, which corresponds to the higher-order many-body effect, plays an essential role. Since the AF magnetic correlation is weak in FeSe, it is difficult to explain the nematic state by the vestigial order (spin nematic) scenario. Based on the paramagnon interference mechanism, the B_{1g} nematic orders in LaFeAsO and FeSe [14–18] and the nematic orders in cuprate superconductors [39–41] and magic-angle twisted bilayer graphene [42] have been explained as the orbital/bond orders. CDW orders in the transition metal dichalcogenide [43] and kagome metal [44] have also been explained by the paramagnon interference mechanism.

The rich variety of nematicity in the FeSe family remains a significant open problem. In FeSe$_{1-x}$S$_x$, T_S disappears at $x \sim 0.17$, where the emergence of the nematic quantum critical point (QCP) has been suggested by experiments [45–48]. Recently, the whole x dependent phase diagram for FeSe$_{1-x}$Te$_x$ ($x \lesssim 0.6$) has been reported [49–51]. In the phase diagram shown in **Figure 1A**, T_S decreases with Te doping x, and T_S disappears at $x \sim 0.5$. T_c becomes maximum ~ 15K at $x \sim 0.6$, which indicates that the nematic fluctuations enlarge the superconducting pairing interaction near the nematic QCP. Thus, it is essential to clarify the mechanism of x dependence of T_S to understand the mechanism of superconductivity in the FeSe family.

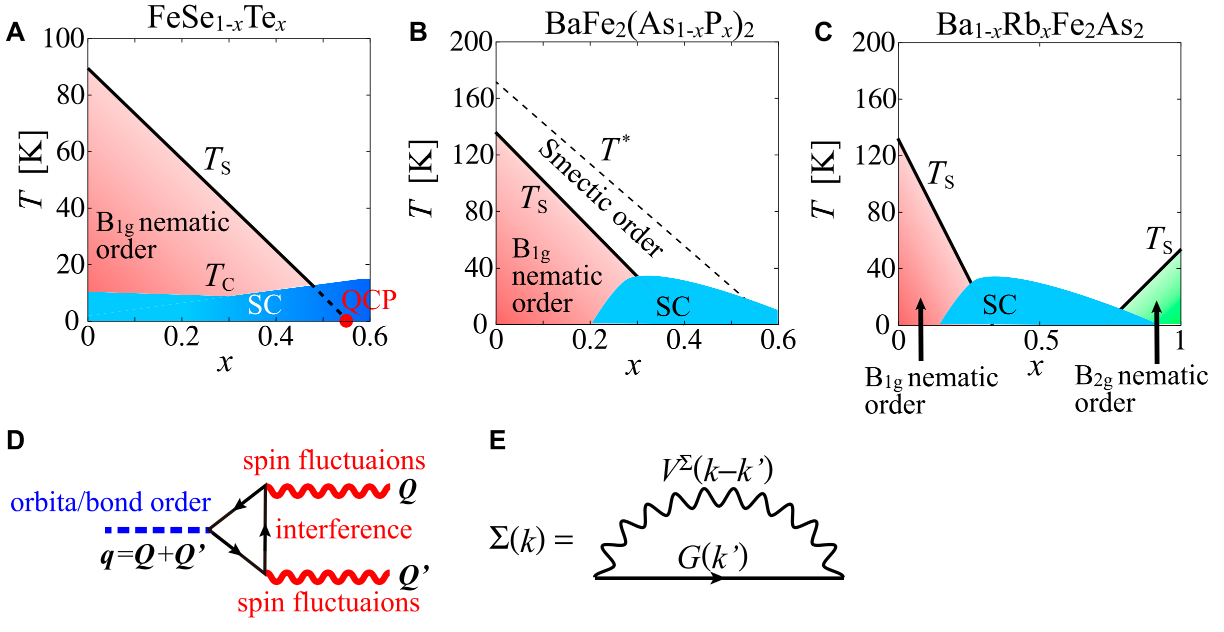

FIGURE 1 | (A) Schematic x-T phase diagram of FeSe$_{1-x}$Te$_x$, where T_S decreases with x, and T_c becomes maximum near the nematic QCP. **(B)** Schematic x-T phase diagram of BaFe$_2$ (As$_{1-x}$P$_x$)$_2$, where tiny nematicity appears for $T_S < T < T^*$. We explain that "tiny nematicity" above T_S originates from the smectic bond order in later sections. **(C)** Schematic x-T phase diagram of Ba$_{1-x}$Rb$_x$Fe$_2$As$_2$. The B_{2g} nematic order appears for the heavily hole-doped region $x > 0.5$. **(D)** Feynman diagram of the paramagnon interference mechanism for the orbital/bond order. **(E)** Feynman diagram of self-energy $\Sigma(k)$.

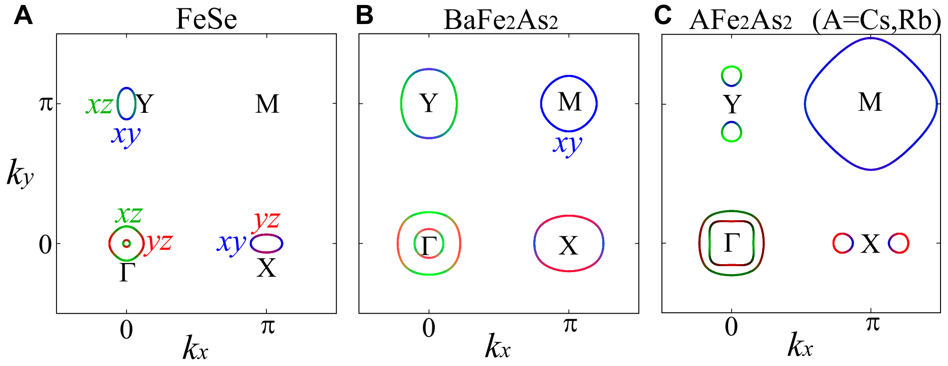

FIGURE 2 | FSs of **(A)** FeSe ($n_d = 6.0$), **(B)** $BaFe_2As_2$ ($n_d = 6.0$), and **(C)** AFe_2As_2 (A = Cs, Rb) ($n_d = 5.5$). The colors green, red, and blue correspond to orbitals 2, 3, and 4, respectively. A variety of nematic/smectic states originates from the characteristic structure of FSs.

In addition, a significant open issue in nematicity is the emergence of another type of nematicity in various Ba122 compounds below $T = T^*$, which is higher than T_S by tens of Kelvin, as shown in **Figure 1B**. An actual bulk nematic transition at $T = T^*$ has been reported in many experimental studies, such as a magnetic torque study [52], an X-ray study [53], an optical measurement study [54], and a laser photoemission electron microscope (PEEM) study [55]. Since the orthorhombicity $(a - b)/(a + b) \ll 0.1\%$ below T^* is tiny, an extrinsic origin such as inhomogeneity of the nematic transition temperature T_S due to local uniaxial pressure and randomness was proposed [4, 56–60]. On the other hand, T^* seems not to be sensitive to the sample quality and the local strain, and the domain structure of nematicity observed above T_S is homogeneous [54, 55]. It is noteworthy that bulk orbital polarization starts to emerge at $T = T^*(>T_S)$ in Ba122 compounds, according to the recent PEEM study [55]. In this study, we will explain the multistage smectic/nematic transitions: the smectic order ($\boldsymbol{q} \neq \boldsymbol{0}$) at $T = T^*$ and the nematic order ($\boldsymbol{q} = \boldsymbol{0}$) at T_S. In this scenario, T^* is given by the intrinsic smectic order free from randomness.

In contrast to B_{1g} nematicity in typical Fe-based superconductors, the emergence of 45°-rotated B_{2g} nematicity in heavily hole-doped AFe_2As_2 (A = Cs, Rb) has been reported in Refs. [61–64], while Refs. [65, 66] have reported the absence of the nematic order. As shown in **Figure 1C**, the dominant B_{1g} nematicity changes to B_{2g} nematicity with doping x in $Ba_{1-x}Rb_xFe_2As_2$. As for the mechanism of B_{2g} nematicity, vestigial nematic order by using the double-stripe magnetic configuration was suggested [67]. However, no SDW transition has been observed [64, 68] in AFe_2As_2, and the spin fluctuations are weak around T_S in $RbFe_2As_2$ [69]. In this study, we reveal the emergence of B_{2g}-symmetry bond order in AFe_2As_2.

As described previously, the variety of nematicity in Fe-based superconductors is very rich. To understand the mechanism of nematic/smectic states and superconductivity, it is important to explain these nematic/smectic states in the same theoretical framework.

In this study, we study B_{1g} nematicity in $FeSe_{1-x}Te_x$ ($n_d = 6.0$), the tiny nematicity below T^* in $BaFe_2As_2$ ($n_d = 6.0$), and B_{2g} nematicity in AFe_2As_2 (A = Cs, Rb) ($n_d = 5.5$) by developing the density wave (DW) equation theory. In this theory, the paramagnon interference mechanism due to the Aslamazov–Larkin (AL) type VCs shown in **Figure 1D** is taken into account. We also take into account of the self-energy effect shown in **Figure 1E**. In this mechanism, the rich variety of nematicity is naturally understood. The obtained nematicity depends on the shape and topology of FSs, as shown in **Figures 2A–C**. 1) In $FeSe_{1-x}Te_x$, all FSs are very small, and d_{xy}-orbital hole pocket is absent. The small spin fluctuations on the three d_{xz}, d_{yz}, and d_{xy} orbitals cooperatively lead to the B_{1g} nematic order, where the orbital order for d_{xz} and d_{yz} orbitals coexists with the bond order for the d_{xy} orbital. The experimental Lifshitz transition below T_S is naturally explained by the nematic order. 2) In $BaFe_2As_2$, the d_{xy} hole pocket emerges, and each FS is relatively large. The smectic order at $T = T^*(>T_S)$ and the nematic order at $T = T_S$ emerge due to the strong d_{xy}-orbital nesting. The smectic order explains the tiny nematicity below T^*, and the multistage transitions are explained by the smectic and nematic orders. 3) In heavily hole-doped AFe_2As_2, the large d_{xy}-orbital hole pocket and the four tiny Dirac pockets appear. The B_{2g} nematic bond order emerges due to the d_{xy}-orbital paramagnon interference mechanism, where the nesting between the Dirac pockets and the large d_{xy}-orbital hole pocket plays an important role. By considering the fermiology of each compound, these various nematic/smectic states are explained by the same theoretical framework based on the paramagnon interference mechanism.

In the present study, we intensively study the effect of self-energy on the nematic/smectic orders. It has been dropped in many previous studies, despite the fact that self-energy is necessary to satisfy the criteria of Baym–Kadanoff's conserving approximation [70, 71]. We revealed that 1) the nematic/smectic order is stabilized by the AL-type VCs, while 2) T_S is reduced to become realistic (~ 100K) by introducing self-energy. These results validate the idea of the "nematic/smectic state due to the paramagnon interference mechanism" proposed in our previous studies [14–20, 39–44]. In addition, 3) the phase diagram of $\mathrm{FeSe}_{1-x}\mathrm{Te}_x$ [49–51] is understood by using a fixed Coulomb interaction because of self-energy (in the absence of self-energy, add-hoc doping x dependence of the Coulomb interaction has to be introduced). The main merits (1)–(3) in the present study strongly indicate that the nematic/smectic states originate from the paramagnon interference mechanism [14–20, 39–44].

2 MULTIORBITAL MODELS AND FORMULATION

2.1 Multiorbital Models

Here, we introduce multiorbital models based on the first principle's calculations. We analyze the following two-dimensional *d-p* Hubbard model with a unique parameter r, which controls the strength of the Coulomb interaction [16]:

$$H_x = H_x^0 + rH^U, \tag{1}$$

where H_x^0 is the first-principle's model, and H^U is the Coulomb interaction for d-orbitals. We neglect the Coulomb interaction for p-orbitals. We denote the five Fe d-orbitals $d_{3z^2-r^2}$, d_{xz}, d_{yz}, and d_{xy}, $d_{x^2-y^2}$ as $l = 1, 2, 3, 4$, and 5, and three Se(As) p-orbitals p_x, p_y, and p_z as $l = 6, 7$, and 8. To obtain the model, we first use the WIEN2k [72] and Wannier90 [73] codes. Next, to reproduce the experimentally observed FSs, we introduce the $\boldsymbol{k}$-dependent shifts for orbital l, δE_l, by modifying the intra-orbital hopping parameters, as explained in Ref. [17]. In the $\mathrm{FeSe}_{1-x}\mathrm{Te}_x$ model, we shift the d_{xy}-orbital band and the $d_{xz/yz}$-orbital band at [Γ, M, X] points by [0eV, − 0.27 eV, + 0.40 eV] and [− 0.24 eV, 0 eV, + 0.13 eV], respectively. In the $\mathrm{BaFe_2As_2}$ model, the shifts are absent. In the $\mathrm{CsFe_2As_2}$ model, we shift the d_{xy}-orbital band and the $d_{xz/yz}$-orbital band at [Γ, M, X] points by [0 eV, + 0.40 eV, 0 eV] and [− 0.40 eV, 0 eV, + 0.10 eV], respectively.

We use the d-orbital Coulomb interaction introduced by the constraint random phase approximation (RPA) method in Ref. [74]. The Coulomb interactions for the spin and charge channels are generally given as

$$U^{\mathrm{s}}_{l_1,l_2;l_3,l_4} = \begin{cases} U_{l_1,l_1}, & l_1 = l_2 = l_3 = l_4 \\ U'_{l_1,l_2}, & l_1 = l_3 \neq l_2 = l_4 \\ J_{l_1,l_3}, & l_1 = l_2 \neq l_3 = l_4 \\ J_{l_1,l_2}, & l_1 = l_4 \neq l_2 = l_3 \\ 0, & \text{otherwise.} \end{cases} \tag{2}$$

$$U^{\mathrm{c}}_{l_1,l_2;l_3,l_4} = \begin{cases} -U_{l_1,l_1}, & l_1 = l_2 = l_3 = l_4 \\ U'_{l_1,l_2} - 2J_{1_1,l_2}, & l_1 = l_3 \neq l_2 = l_4 \\ -2U'_{l_1,l_3} + J_{l_1,l_3}, & l_1 = l_2 \neq l_3 = l_4 \\ -J_{1_1,l_2}, & l_1 = l_4 \neq l_2 = l_3 \\ 0. & \text{otherwise.} \end{cases} \tag{3}$$

The Hamiltonian of the Coulomb interaction is given as

$$H^U = -\sum_{\boldsymbol{k}\boldsymbol{k}'\boldsymbol{q},\sigma\sigma'} \sum_{l_1l_2l_3l_4} \left(\frac{U^c + U^s\sigma\sigma'}{4}\right)_{l_1,l_2;l_3,l_4}, \\ \times c^{l_1\dagger}_{\boldsymbol{k}+\boldsymbol{q},\sigma} c^{l_2}_{\boldsymbol{k},\sigma} c^{l_3\dagger}_{\boldsymbol{k}'-\boldsymbol{q},\sigma'} c^{l_4}_{\boldsymbol{k}',\sigma'}, \tag{4}$$

where $\sigma, \sigma' = \pm 1$ denote spin.

By using the multiorbital Coulomb interaction, the spin (charge) susceptibility $\hat{\chi}^{s(c)}(q)$ for $q = (\boldsymbol{q}, \omega_m = 2m\pi T)$ is given by

$$\hat{\chi}^{s(c)}(q) = \hat{\chi}^0(q)\left[1 - \hat{U}^{s(c)}\hat{\chi}^0(q)\right]^{-1}, \tag{5}$$

where irreducible susceptibility is

$$\chi^0_{l,l';m,m'}(q) = -\frac{T}{N}\sum_k G_{l,m}(k+q)G_{m',l'}(k). \tag{6}$$

$\hat{G}(k)$ is the multiorbital Green function with the self-energy $\hat{\Sigma}$ and given as $\hat{G}(k) = [(i\epsilon_n + \mu)\hat{1} - \hat{h}^0(\boldsymbol{k}) - \hat{\Sigma}(k)]^{-1}$ for = [$\boldsymbol{k}$, $\epsilon_n = (2n+1)\pi T$]. Here, $\hat{h}^0(\boldsymbol{k})$ is the matrix expression of H^0, and μ is the chemical potential. The spin (charge) Stoner factor $\alpha_{s(c)}$ is defined as the maximum eigenvalue of $\hat{U}^{s(c)}\hat{\chi}^0(\boldsymbol{q}, 0)$. Since $\hat{\chi}^{s(c)}(q) \propto (1 - \alpha_{s(c)})^{-1}$ holds, spin (charge) fluctuations develop with increasing $\alpha_{s(c)}$, and $\alpha_{s(c)} = 1$ corresponds to the spin- (charge)-channel ordered state.

2.2 FLEX Approximation

Here, we introduce the multiorbital fluctuation exchange (FLEX) approximation [15, 75]. The FLEX approximation satisfies the conserving approximation formalism of Baym and Kadanoff [70, 71]. In the FLEX approximation, self-energy is given as

$$\hat{\Sigma}(k) = \frac{T}{N}\sum_{k'}\hat{V}^{\Sigma}(k-k')\hat{G}(k'), \tag{7}$$

which is shown by the Feynman diagram in **Figure 1E**. The effective interaction $\hat{V}^{\Sigma}$ for self-energy in the FLEX approximation is given as

$$\hat{V}^{\Sigma}(q) = \frac{3}{2}\hat{U}^s\hat{\chi}^s(q)\hat{U}^s + \frac{1}{2}\hat{U}^c\hat{\chi}^c(q)\hat{U}^c + \frac{3}{2}\hat{U}^s + \frac{1}{2}\hat{U}^c \\ - \hat{U}^{\uparrow\downarrow}\hat{\chi}^0(q)\hat{U}^{\uparrow\downarrow} - \frac{1}{2}\hat{U}^{\uparrow\uparrow}\hat{\chi}^0(q)\hat{U}^{\uparrow\uparrow}, \tag{8}$$

where $\hat{U}^{\uparrow\downarrow} \equiv \frac{\hat{U}^c - \hat{U}^s}{2}$ and $\hat{U}^{\uparrow\uparrow} \equiv \frac{\hat{U}^c + \hat{U}^s}{2}$ are denoted. We set $\mu = 0$. $\hat{\chi}^{s(c)}(q)$, $\hat{\Sigma}(k)$, and $\hat{G}(k)$ are calculated self-consistently. In multiband systems, the FSs are modified from the original FSs because of the self-energy correction. To escape from this difficulty, we subtract the Hermite term $[\hat{\Sigma}(\boldsymbol{k}, +i0) + \hat{\Sigma}(\boldsymbol{k}, -i0)]/2$ from the original self-energy, which corresponds to the elimination of double-counting terms between the LDA and FLEX.

2.3 Density-Wave Equation

We derive the strongest charge-channel density-wave (DW) instability without assuming the order parameter and wave vector. For this purpose, we use the DW equation method developed in Refs. [16, 19, 76]. We obtain the optimized non-local form factor $\hat{f}^{\boldsymbol{q}}(k)$ with the momentum and orbital dependences by solving the following linearized DW equation shown in **Figure 3A**:

$$\lambda_{\boldsymbol{q}} f^{\boldsymbol{q}}_{l,l'}(k) = \frac{T}{N}\sum_{k',m,m'} K^{\boldsymbol{q}}_{l,l';m,m'}(k,k') f^{\boldsymbol{q}}_{m,m'}(k'), \tag{9}$$

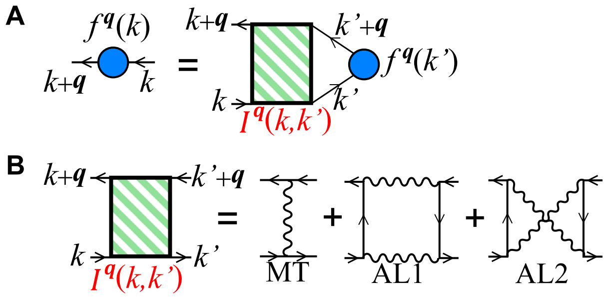

FIGURE 3 | Feynman diagrams of **(A)** DW equation and **(B)** charge-channel irreducible four-point vertex. Each wavy line represents a spin-fluctuation-mediated interaction.

$$K^{q}_{l,l';m,m'}(k,k') = \sum_{m_1,m_2} I^{q}_{l,l';m_1,m_2}(k,k')\, g^{q}_{m_1,m_2;m,m'}(k'), \tag{10}$$

where λ_{q} is the eigenvalue of the form factor $\hat{f}^{q}(k)$, $g^{q}_{l,l';m,m'}(k) \equiv -G_{l,m}(k+q)G_{m',l'}(k)$, and $\hat{I}^{q}(k,k')$ is the charge-channel irreducible four-point vertex shown in **Figure 3B**. The four-point vertex interaction $\hat{I}^{q}(k,k')$ in the DW **Eq. 10** [16, 19] is given by

$$I^{q}_{l,l';m,m'}(k,k') = \sum_{b=s,c}\Bigg[-\frac{a^b}{2}V^{b}_{l,m;l',m'}(k-k') + \frac{T}{N}\sum_{p,l_1,l_2,m_1,m_2}\frac{a^b}{2}V^{b}_{l,l_1;m,m_2}$$

$$(p+q)V^{b}_{m',l_2;l',m_1}(p)G_{l_1,m_1}(k-p)G_{l_2,m_2}(k'-p) \quad +\frac{T}{N}\sum_{p,l_1,l_2,m_1,m_2}\frac{a^b}{2}V^{b}_{l,l_1;l_2,m'}$$

$$(p+q)V^{b}_{m_2,m;l',m_1}(p)G_{l_1,m_1}(k-p)G_{l_2,m_2}(k'+p+q)\Bigg], \tag{11}$$

where $a^s = 3$, $a^c = 1$, $p = (\boldsymbol{p}, \omega_l)$, and $\hat{V}^{s(c)}(q) = \hat{U}^{s(c)} + \hat{U}^{s(c)}\hat{\chi}^{s(c)}(q)\hat{U}^{s(c)}$.

In **Eq. 11**, the first line corresponds to the Maki-Thompson (MT) term, and the second and third lines give the AL terms, respectively. Feynman diagrams of the MT terms and AL terms are shown in **Figure 3B**.

The AL terms are enhanced by the paramagnon interference $\hat{\chi}^{s}(\boldsymbol{Q}) \times \hat{\chi}^{s}(\boldsymbol{Q}')$ shown in **Figure 1D**. Thus, $\boldsymbol{q} = \boldsymbol{Q} + \boldsymbol{Q}' = \boldsymbol{0}$ nematic order is naturally induced by the paramagnon interference at the same nesting vector ($\boldsymbol{Q}' = -\boldsymbol{Q}$). In the MT term, the first-order term with respect to $\hat{U}^{s,c}$ gives the Hartree–Fock (HF) term in the mean-field theory. The charge-channel DW with wave vector $\boldsymbol{q}$ is established when the largest $\lambda_{\boldsymbol{q}} = 1$. Thus, the smaller $\lambda_{\boldsymbol{q}}$ corresponds to the lower T_S. DW susceptibility is proportional to $1/(1-\lambda_{\boldsymbol{q}})$ as explained in Ref. [20]. Therefore, $\lambda_{\boldsymbol{q}}$ represents the strength of the DW instability.

3 RESULTS AND DISCUSSIONS

3.1 Results of $FeSe_{1-x}Te_x$

In this section, we show that 1) the B_{1g} nematic orbital + bond order originates from the paramagnon interference, and 2) the effect of self-energy is essential to reproduce the x dependence of T_S as shown in **Figure 1A** in $FeSe_{1-x}Te_x$. The effect of self-energy on the nematic/smectic order caused by the VCs is systematically studied in the present work. Because of self-energy, T_S is reduced to become realistic (~ 100K), while the symmetry of the nematic/smectic order is unchanged. Thus, the idea of electronic nematicity due to "the paramagnon-interference mechanism" proposed in Refs. [14–20, 39–44] has been confirmed by the present study.

Hereafter, we fix $r = 0.35$, $T = 15$ meV in calculations with self-energy and $r = 0.15$, $T = 15$ meV in calculations without the self-energy, unless otherwise noted.

Figures 4A,B show x dependent FSs and band structures, respectively. The FSs are small compared to other Fe-based superconductors. The d_{xy} orbital level E^{M}_{xy} at the M point increases with increasing x, as shown in **Figure 4C**. This behavior is consistent with ARPES measurements [77, 78]. On the other hand, the d_{xy} orbital level E^{Γ}_{xy} at the Γ point decreases with increasing x. E^{Γ}_{xy} becomes lower than the $d_{xz(yz)}$ orbital level for $x \gtrsim 0.3$, and the topology of band changes. The change in topology has been observed between Γ and Z points in ARPES measurements of $FeSe_{0.5}Te_{0.5}$ [79, 80]. **Figure 4D** shows the density of state (DOS) of orbitals 3 and 4 for $x = 0, 0.5$. The DOS near the Fermi level for $x = 0.5$ is larger than that for $x = 0$ since the bandwidth decreases, and E^{M}_{xy} comes close to the Fermi level with increasing x. In addition, the dispersion of orbitals 2 and 3 at the Γ point becomes flat as E^{Γ}_{xy} decreases with increasing x, which also enlarges the DOS for orbitals 2 and 3 near the Fermi level.

To discuss the self-energy effect, we calculate the mass enhancement factors. **Figure 5** shows the obtained x dependence of the mass enhancement factors $z_l^{-1}(\pi,0)$ for orbital $l = 3, 4$, which are given by $z_l^{-1}(\boldsymbol{k}) = 1 - \mathrm{Im}\Sigma_{l,l}(\boldsymbol{k},\pi T)/\pi T$ in the FLEX approximation. The value of $z_l^{-1}(\pi,0)$ increases with increasing x since the electron correlation increases due to the reduction in the bandwidth and the increase in the DOS as shown in **Figure 4D**. Particularly, $z_4^{-1}(\pi,0)$ is enhanced by the d_{xy} orbital electron correlation between the electron pockets and the band around the M point since E^{M}_{xy} comes close to the Fermi level, as shown in **Figure 4C**. The behaviors of z_l^{-1} are similar to those given by the dynamical mean-field theory [81] and experiment [82].

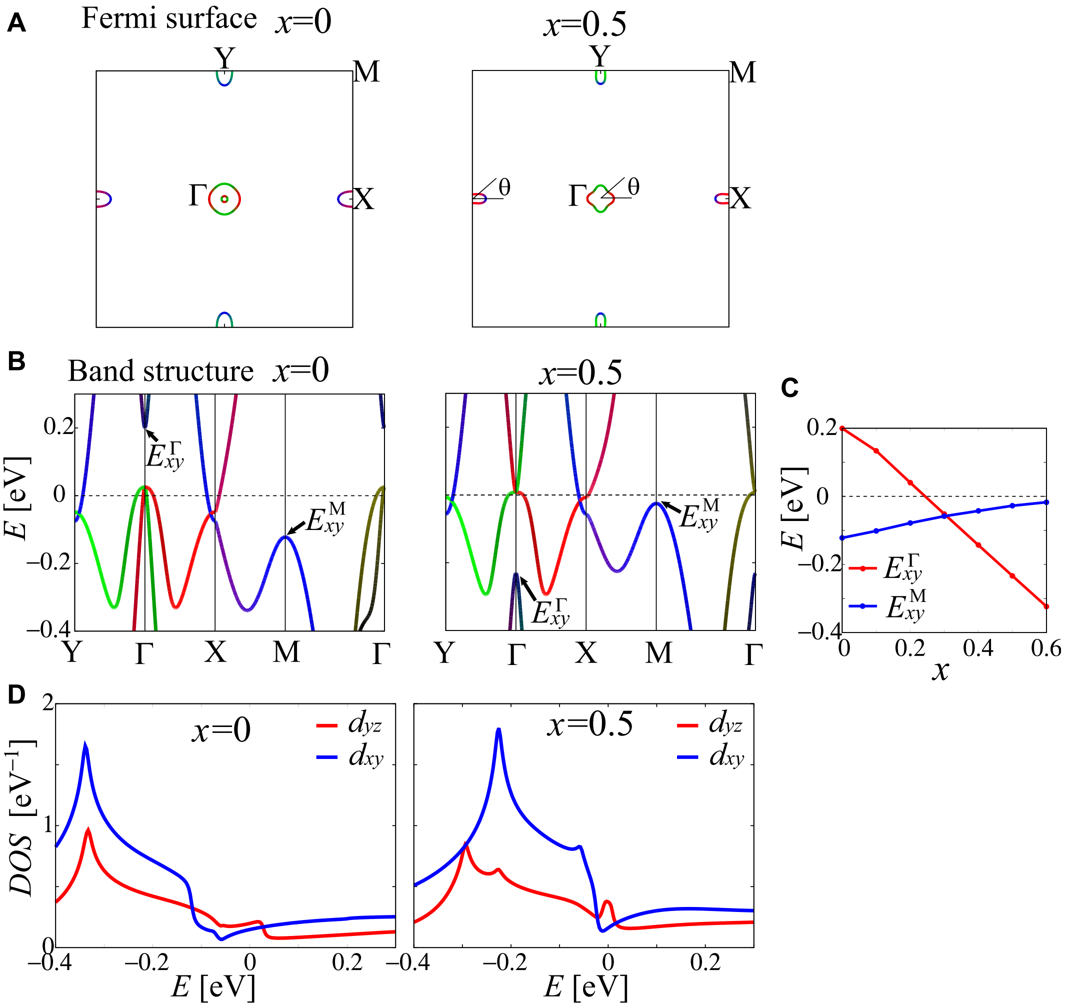

FIGURE 4 | (A) FSs and **(B)** band structures of FeSe$_{1-x}$Te$_x$ for x = 0 and 0.5. **(C)** x dependences of E^Γ_{xy} and E^M_{xy}. **(D)** DOS of orbitals 3 and 4 for x = 0, 0.5.

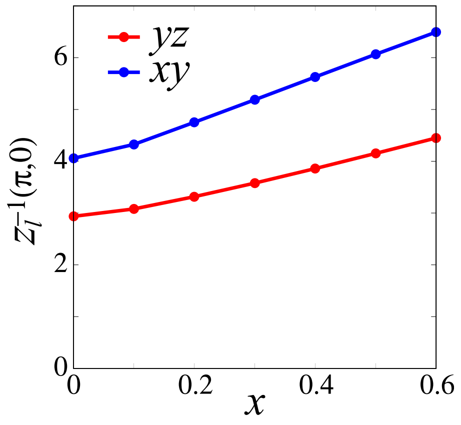

FIGURE 5 | x dependences of the mass enhancement factor $z_l^{-1}(\pi,0)$ for orbitals l = 3 and 4.

Figure 6 shows x dependences of $\chi^s_{3,3;3,3}(\pi,0)$ and $\chi^s_{4,4;4,4}(\pi,0)$ in the FLEX approximation and the RPA. $\chi^s_{3,3;3,3}(\pi,0)$ is almost independent of doping x, which means that change in topology or the number of FS around Γ comprising d_{xz} and d_{yz} orbitals does not strongly affect the spin fluctuation for the $d_{xz(yz)}$ orbital. On the other hand, $\chi^s_{4,4;4,4}(\pi,0)$ in the RPA without self-energy is strongly enhanced with increasing x since the electron correlation for the d_{xy} orbital between electron pockets and the band around the M point is significant for the enhancement of $\chi^s_{4,4;4,4}(\pi,0)$. The strong enhancement of $\chi^s_{4,4;4,4}(\pi,0)$ is suppressed by the self-energy in the FLEX approximation. This suppression is necessary to reproduce the x dependence of T_S in the phase diagram.

Hereafter, we discuss the DW instability given by the DW **Eq. 9**. **Figure 7A** shows x dependences of λ_0 for the B_{1g} nematic state with and without the self-energy. λ_0 without the self-energy rapidly increases with doping x due to the paramagnon interference shown in **Figure 1D**. λ_0 is enlarged by the

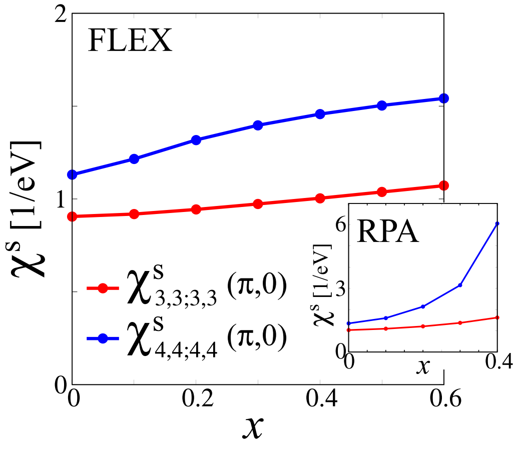

FIGURE 6 | x dependences of $\chi^s_{3,3;3,3(4,4;4,4)}(\pi,0)$ in the FLEX approximation. Those in the RPA are shown in the inset.

interference between $\chi^s_{4,4;4,4}$ strongly enhanced in the RPA, as shown in **Figure 6**. Since this result means T_S increases with x, the phase diagram in **Figure 1A** cannot be explained when the self-energy is absent. However, $\lambda_{\mathbf{0}}$ including the self-energy decreases with doping x since the enhancement of $\chi^s_{4,4;4,4}$ in the FLEX approximation is moderate and the self-energy suppresses the $\hat{G}$ and $\hat{I}$ in the DW **Eq. 10**. The value of $\lambda_{\mathbf{0}}$ increases with decreasing T, as shown in **Figure 7B**, and $T = T_S$ is given when $\lambda_{\mathbf{0}} = 1$ is satisfied. Thus, T_S at $x = 0$ is higher than that at $x = 0.5$, and T_S at $x = 0.65$ cannot be obtained for $T > 6$ meV. The x dependence of T_S obtained by the paramagnon interference mechanism is consistent with the phase diagram in **Figure 1A** [49]. We see that T dependences of the strength of nematic fluctuations $1/(1-\lambda_{\mathbf{0}})$ satisfy the Curie–Weiss law at low temperatures, as shown in **Figure 7C**. We note that the B_{1g} nematic state is realized because of the small FSs even for the weak spin fluctuations [16, 17].

Here, we analytically explain that T_S is reduced by self-energy by focusing on the mass renormalization factor z. As discussed in Ref. [17], $\alpha_{s(c)}$ is independent of z under the scaling $T \to zT$ and $r \to r/z$. Under this scaling, the eigenvalue of the DW equation is unchanged [17]. Thus, T_S obtained by the DW equation without the self-energy is reduced to zT_S because of the self-energy. As a result, realistic T_S is obtained by taking self-energy into account.

Figure 8A shows $\boldsymbol{q}$ dependences of $\lambda_{\boldsymbol{q}}$ with the self-energy at $x = 0, 0.5$. $\lambda_{\boldsymbol{q}}$ has peak at $\boldsymbol{q} = \mathbf{0}$, which means that the ferro nematic order is favored. **Figure 8B** shows $\boldsymbol{k}$ dependences of the static form factors $f^{\mathbf{0}}_{33}(\boldsymbol{k})$ and $f^{\mathbf{0}}_{44}(\boldsymbol{k})$, where $\hat{f}^{\boldsymbol{q}}(\boldsymbol{k})$ is given by the analytic continuation of $\hat{f}^{\boldsymbol{q}}(k)$. $f^{\mathbf{0}}_{33}(k_x, k_y) = -f^{\mathbf{0}}_{22}(k_y, k_x)$ represents B_{1g} orbital order between orbitals 2 and 3. From the $\boldsymbol{k}$ dependence of $f^{\mathbf{0}}_{33(22)}(\boldsymbol{k})$, the sign-reversing orbital order is confirmed along the $k_x(k_y)$ axis. As shown in **Figure 8C**, $\boldsymbol{k}$ dependence of $f^{\mathbf{0}}_{44}(\boldsymbol{k}) \propto \cos(k_x) - \cos(k_y)$ causes the B_{1g} nearest-neighbor bond order, which is the modulation of correlated hopping. Based on the paramagnon interference mechanism, we find that the small spin fluctuations on the three d_{xz}, d_{yz}, and d_{xy} orbitals cooperatively cause the B_{1g} nematic orbital + bond order. The FSs and the band structure under the nematic order with the maximum value of the form factor $f^{\mathbf{0}}_{\max} = 80$meV are shown in **Figures 8D,E**. $f^{\mathbf{0}}_{\max} = 80$meV with the mass enhancement factor $z_l^{-1} = 2 \sim 4$ is consistent with ARPES measurements [35, 36]. The Lifshitz transition, where the FS around the Y point is missing, has been reported in recent experiments [83–86]. The Lifshitz transition is naturally explained by the increase of the d_{xy} level around the Y point induced by $f^{\mathbf{0}}_{44}(\boldsymbol{k})$. We note that the obtained coexistence of the bond order on the d_{xy} orbital and the orbital order on the (d_{xz}, d_{yz}) orbitals has already been shown in the supplementary material of Refs. [19, 20]. In **Figure 8D**, we derived the Lifshitz transition by setting $f^{\mathbf{0}}_{\max} = 80$meV by hand. It is noteworthy that the same result is recently obtained by solving the full DW equation in Ref. [87]. The full DW equation enables us to study the electronic states below T_S without introducing additional fitting parameters.

Here, we confirm that the d_{xy} orbital levels at Γ and M points are important for the x dependence of $\lambda_{\mathbf{0}}$. We use the simple model, where only the shift of E^{Γ}_{xy} or E^{M}_{xy} is introduced for the $x = 0$ model. **Figure 9A** shows E^{Γ}_{xy} dependences of $z_l^{-1}(\pi,0)$ and $\lambda_{\mathbf{0}}$,

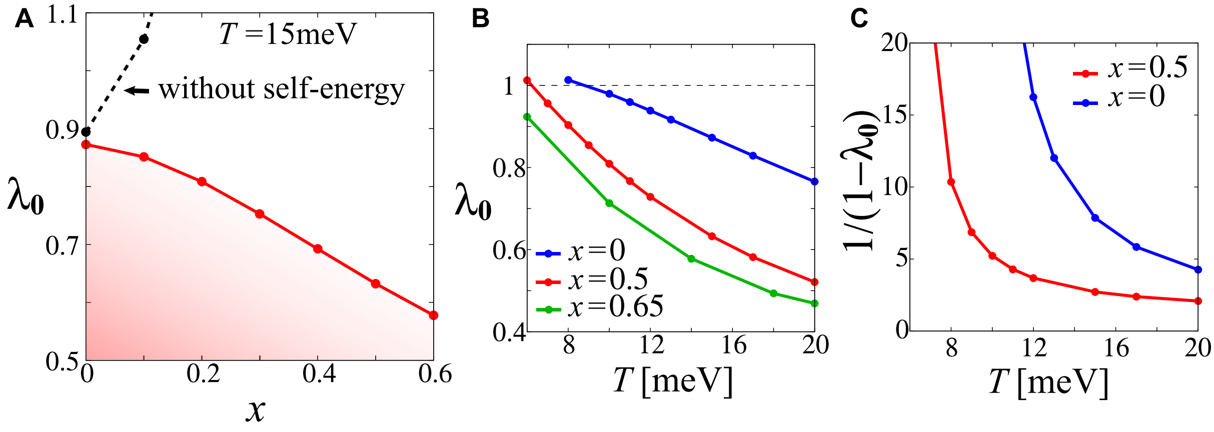

FIGURE 7 | (A) x dependences of $\lambda_{\mathbf{0}}$ in the DW equation with and without self-energy at $T = 15$ meV. **(B)** T dependences of $\lambda_{\mathbf{0}}$ with self-energy for $x = 0, 0.5, 0.65$. **(C)** T dependences of $1/(1-\lambda_{\mathbf{0}})$ with self-energy for $x = 0, 0.5$.

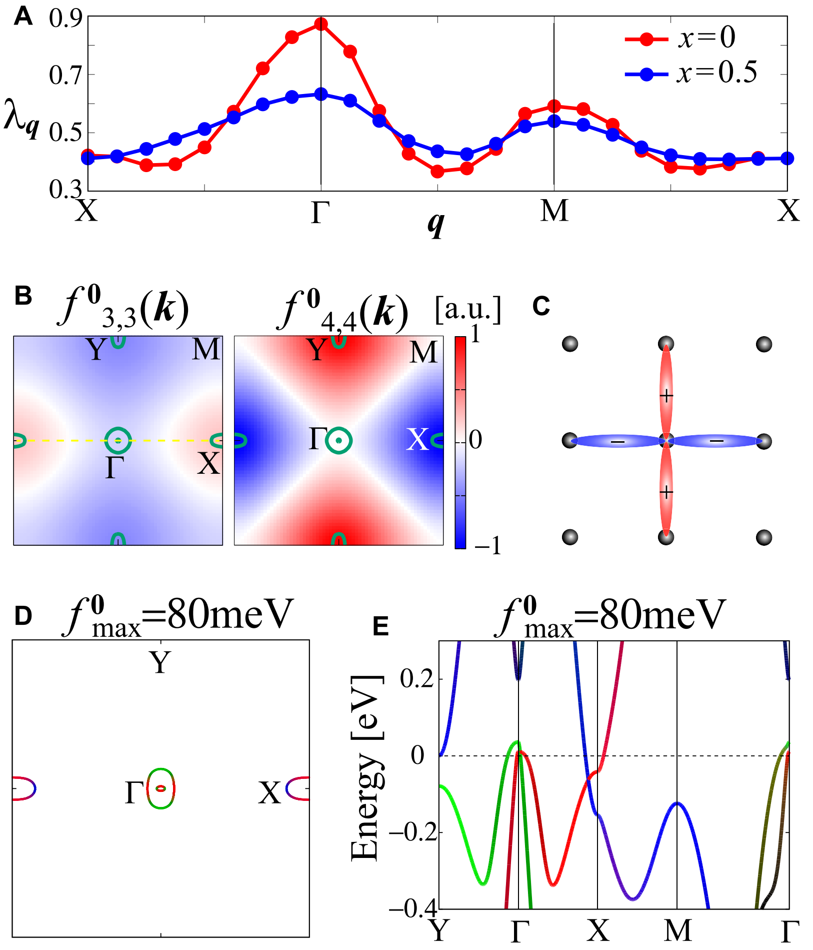

FIGURE 8 | (A) $\boldsymbol{q}$ dependences of $\lambda_{\boldsymbol{q}}$ with self-energy for $x = 0, 0.5$. **(B)** $\boldsymbol{k}$ dependences of $f^{\mathbf{0}}_{3,3}(\boldsymbol{k})$ and $f^{\mathbf{0}}_{4,4}(\boldsymbol{k})$ for $x = 0$, where green lines denote FSs. $f^{\mathbf{0}}_{3,3}(\boldsymbol{k})$ changes sign along the k_x axis (yellow dashed line). **(C)** B_{1g} nearest-neighbor bond order corresponding to $f^{\mathbf{0}}_{4,4}(\boldsymbol{k})$. **(D)** FSs and **(E)** band structure under the nematic order with $f^{\mathbf{0}}_{\max} = 80$meV for $x = 0$.

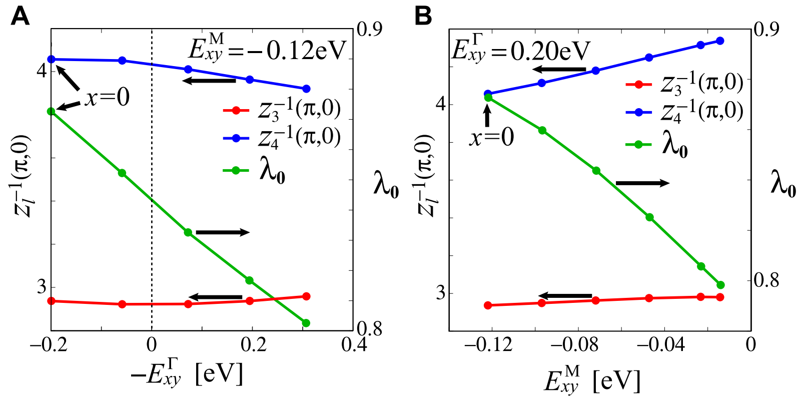

FIGURE 9 | (A) E^{Γ}_{xy} dependences of $z_l^{-1}(\pi, 0)$ for $l = 3, 4$, and $\lambda_{\mathbf{0}}$ given by introducing only E^{Γ}_{xy} shift for the $x = 0$ model. **(B)** E^{M}_{xy} dependences of $z_l^{-1}(\pi, 0)$ for $l = 3, 4$, and $\lambda_{\mathbf{0}}$ given by introducing only E^{M}_{xy} shift for the $x = 0$ model.

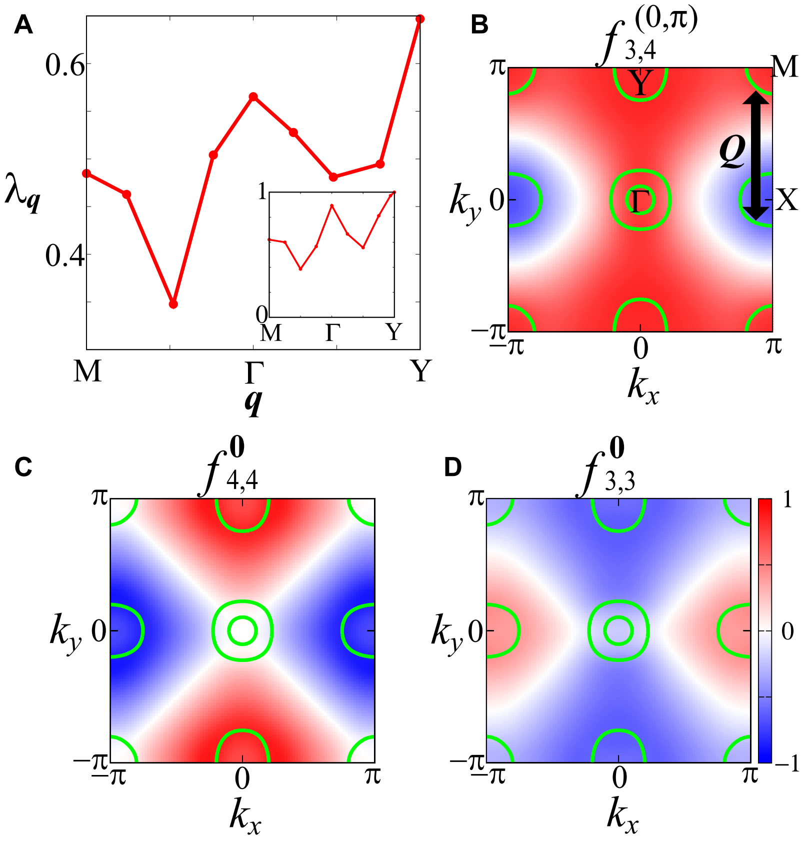

FIGURE 10 | (A) $\boldsymbol{q}$ dependence of $\lambda_{\boldsymbol{q}}$ with self-energy for $r = 0.68$ at $T = 5$ meV in BaFe$_2$As$_2$, and that without self-energy for $r = 0.30$ at $T = 32.4$ meV in the inset. **(B)** $\boldsymbol{k}$ dependence of the dominant form factor at $\boldsymbol{q} = (0, \pi)$, $f^{\boldsymbol{q}}_{3,4}(\boldsymbol{k})$ with self-energy, which is given by the off-diagonal orbitals 3 and 4. $\boldsymbol{k}$ dependences of form factors at $\boldsymbol{q} = \mathbf{0}$, **(C)** $f^{\mathbf{0}}_{4,4}(\boldsymbol{k})$, and **(D)** $f^{\mathbf{0}}_{3,3}(\boldsymbol{k})$ with self-energy. Green lines denote FSs.

respectively. $z_l^{-1}(\pi, 0)$ is almost independent of the value of E^{Γ}_{xy}. $\lambda_{\mathbf{0}}$ decreases with decreasing E^{Γ}_{xy}, which is consistent with the result shown in **Figure 7A**. The topology of the band structure changes at the Γ point with decreasing E^{Γ}_{xy}, which plays an important role in decreasing $\lambda_{\mathbf{0}}$. **Figure 9B** shows E^{M}_{xy} dependences of $z_l^{-1}(\pi, 0)$ and $\lambda_{\mathbf{0}}$, respectively. The behaviors of $z_4^{-1}(\pi, 0)$ and $\lambda_{\mathbf{0}}$ are similar to the results shown in **Figure 5**, **Figure 7A**. The x dependences of $z_4^{-1}(\pi, 0)$ and $\lambda_{\mathbf{0}}$ are explained by the electron correlation between the electron pockets and the d_{xy} band around the M point. $\lambda_{\mathbf{0}}$ is suppressed by self-energy for the d_{xy} orbital. The suppression becomes strong with increasing E^{M}_{xy} due to the feedback effect of the self-energy. To summarize, the B_{1g} nematic orbital + bond order is explained by the paramagnon interference mechanism in FeSe$_{1-x}$Te$_x$, and x dependence of T_S is well reproduced by the self-energy effect for the d_{xy} orbital.

3.2 Results of BaFe$_2$As$_2$

In this section, we discuss the multi-nematicity in BaFe$_2$As$_2$ [20].

The effect of self-energy on the nematic/smectic orders caused by the VCs is studied in the present work. Transition temperatures are reduced to become realistic because of the self-energy, while the symmetries of the nematic/smectic orders are unchanged. We reveal the origin of the tiny nematicity below $T = T^*$ and explain the multistage transitions at $T = T^*$ and T_S in the phase diagram shown in **Figure 1B**. As shown in **Figure 2B**, the size of the hole FS around the M point comprising the d_{xy} orbital is similar to that of electron FSs around the X and Y points, which causes good intra- and inter-orbital nestings. As explained later, inter-orbital nesting is important to realize the smectic state at $T = T^*$.

Figure 10A shows the $\boldsymbol{q}$-dependence of $\lambda_{\boldsymbol{q}}$ with and without self-energy. The $\boldsymbol{q} = (0, \pi)$ smectic bond order is dominant over the $\boldsymbol{q} = \mathbf{0}$ nematic orbital + bond order because of the relation $\lambda_{(0,\pi)} > \lambda_{\mathbf{0}}$, which is robust in the presence of moderate spin fluctuations $\alpha_s \gtrsim 0.85$. Thus, the nematic orbital + bond transition temperature T_S is lower than T^*, where the smectic bond order appears. **Figure 10B** shows the dominant component of the static form factor, $f^{\boldsymbol{q}}_{3,4}(\boldsymbol{k})$, for $\boldsymbol{q} = (0, \pi)$. Focusing on the X and M points, $f^{(0,\pi)}_{3,4}(\boldsymbol{k})$ is proportional to $-\cos(k_y)$, which corresponds to the inter-orbital smectic bond order, where the y-direction hoppings between orbitals 3 and 4 are modulated by the correlated hopping $\delta t_{3,4}(y; y \pm 1) = -\delta t_{4,3}(y; y \pm 1) = \delta t(-1)^y$. It is to be noted that $\delta t_{l,m}(y; y')$ is real and equal to $\delta t_{m,l}(y'; y)$.

As shown in **Figure 1D**, the origin of the smectic bond order $f^{(0,\pi)}_{3,4}$ is the quantum interference between the spin fluctuations $\chi^s(\mathbf{Q})$ for $\mathbf{Q} \approx (0, \pi)$ and $\chi^s(\mathbf{0})$ due to the AL terms. In this case, $\boldsymbol{q} = (0, \pi)$ $(= \mathbf{Q} + \mathbf{Q}')$ is given by $\mathbf{Q}' = \mathbf{0}$. $\chi^s(\mathbf{Q})$ is enhanced when the FS appears around the M point since nesting between FSs around the

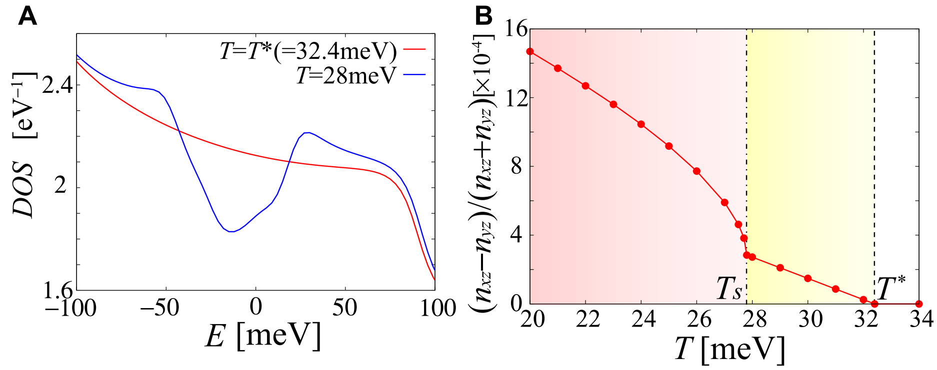

FIGURE 11 | (A) DOS at $T = T^* = 32.4$ meV and that at $T = 28$ meV($<T^*$), including the smectic bond order. **(B)** T dependence of nematicity $\psi = (n_2 - n_3)/(n_2 + n_3)$ including both the smectic-bond order for $T < T^*$ and the ferro-orbital/bond order for $T < T_S$.

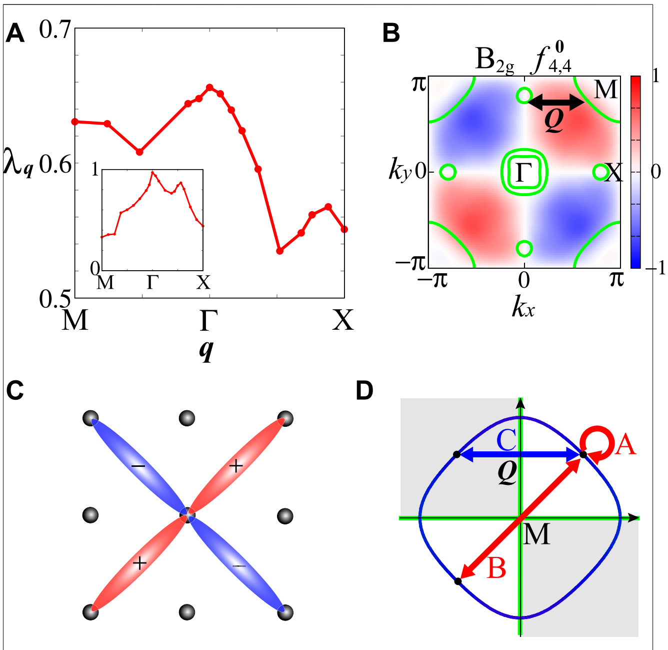

FIGURE 12 | (A) $\boldsymbol{q}$ dependence of $\lambda_{\boldsymbol{q}}$ with self-energy in $\mathrm{CsFe_2As_2}$, and that without self-energy in the inset. **(B)** $\boldsymbol{k}$ dependence of the B_{2g} form factor $f^{\boldsymbol{0}}_{4,4}(\boldsymbol{k}) \propto \sin(k_x)\sin(k_y)$, where the green lines and black arrow denote FSs and nesting vector $\boldsymbol{Q} \sim (0.5\pi, 0)$, respectively. **(C)** B_{2g} next-nearest-neighbor bond order corresponding to the $f^{\boldsymbol{0}}_{4,4}(\boldsymbol{k})$. **(D)** B_{2g} form factor $\propto \sin(k_x)\sin(k_y)$ driven by the attractive interactions (red arrows) A and B, and the repulsive interaction (blue arrow) C in the DW equation, where green lines denote nodes in the B_{2g} form factor.

X and M points becomes good, while the moderate $\chi^s(\boldsymbol{0})$ is caused by forward scattering. We find that $f^{(0,\pi)}_{3,4}$ is significantly enlarged by inter-orbital nesting between the d_{xy}-orbital FS around the M point and the d_{yz}-orbital FS around the X point. In addition to the quantum interference due to the AL terms, the MT terms strengthen the sign change of $f^{(0,\pi)}_{3,4}(\boldsymbol{k})$ between the X and M points, as reported previously [16, 19, 37]. Thus, the smectic bond order originates from the cooperation between the AL and MT terms due to good inter-orbital nesting between FSs around the X and M points. In contrast, the B_{1g} nematic orbital + bond order shown in **Figures 10C,D** originates from the interference between $\chi^s(\boldsymbol{Q})$ and $\chi^s(-\boldsymbol{Q})$. This nematic orbital + bond order is similar to that in FeSe and $\mathrm{FeSe_{1-\mathit{x}}Te_{\mathit{x}}}$.

Here, we examine the DOS under the smectic bond order to verify the present theory. For $T < T^* = 32.4$ meV without self-energy, we introduce the mean-field-like T-dependent form factor $\hat{f}^{\boldsymbol{q}}(T) = f^{\max}\tanh\left(1.74\sqrt{T^*/T - 1}\right)\hat{f}^{\boldsymbol{q}}$, where $\hat{f}^{\boldsymbol{q}}$ is the obtained form factor for $\boldsymbol{q} = (0, \pi)$ normalized as $\max_{\boldsymbol{k}}|\hat{f}^{\boldsymbol{q}}(\boldsymbol{k})| = 1$. We put $f^{\max} = 60$ meV. **Figure 11A** shows the DOS at $T = T^*$ and 28 meV($<T^*$). For $T < T^*$, a pseudogap appears due to the smectic bond order, which is consistent with the experiments [88, 89]. Since the smectic bond order is an antiferroic order, the folded band structure emerges below T^*, which is also consistent with the experiment [90].

Next, we focus on another mystery, the T-linear behavior of tiny nematicity ψ in Ba122 [52] below T^*. To solve this mystery, we calculate the T dependence of uniform nematicity $\psi = (n_2 - n_3)/(n_2 + n_3)$ in **Figure 11B**, where both $\hat{f}^{(0,\pi)}(T)$ for $T < T^*$ and the ferro nematic orbital + bond order $\hat{f}^{\boldsymbol{0}}(T)$ for $T < T_S = 27.8$meV) are introduced. For $T < T_S$, we assume $\hat{f}^{\boldsymbol{0}}(T) = f^{\max}\tanh\left(1.74\sqrt{T_S/T - 1}\right)\hat{f}^{\boldsymbol{0}}$, where $\hat{f}^{\boldsymbol{0}}$ is the obtained form factor normalized as $\max_{\boldsymbol{k}}|\hat{f}^{\boldsymbol{0}}(\boldsymbol{k})| = 1$. We use $f^{\max} = 60$ meV, which corresponds to the $d_{xz(yz)}$ orbital energy split ~ 60meV in the ARPES measurements [91] by considering the mass enhancement factor $z_l^{-1} \sim 2$ for $l = 2, 3$. The T-linear behavior $\psi \propto (T^* - T)$ for $T_S < T < T^*$ is a consequence of the relation $\psi \propto [f^{(0,\pi)}(T)]^2$ because the $f^{(0,\pi)}$ term cannot contribute to any $\boldsymbol{q} = \boldsymbol{0}$ linear response. It is to be noted that the form factor $\hat{f}^{(\pi,0)}$ for $\boldsymbol{q} = (\pi, 0)$ gives $\psi < 0$. Thus, the T-linear behavior of ψ below T^* is also naturally explained by the smectic bond order. On the other hand, $\psi \propto \sqrt{T_S - T}$ for $T < T_S$ is induced by the nematic orbital + bond order. To summarize, the multistage transitions at $T = T^*$ and T_S, and the T-linear ψ below T^*, are naturally explained by the smectic bond order and nematic orbital + bond order. The hole pocket around the M point is necessary to realize the smectic bond order by the paramagnon interference mechanism.

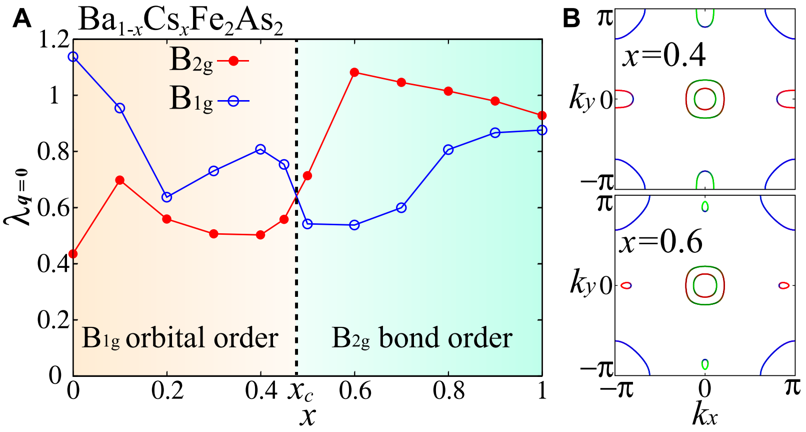

FIGURE 13 | (A) x dependences of $\lambda_{q=0}$ without self-energy for B_{1g} and B_{2g} symmetries in $Ba_{1-x}Cs_xFe_2As_2$. **(B)** FSs for $x = 0.4$ and $x = 0.6$. The dominant nematic order changes at $x = x_c \sim 0.5$ near the Lifshitz transition, where the electron FSs split into the four tiny Dirac pockets.

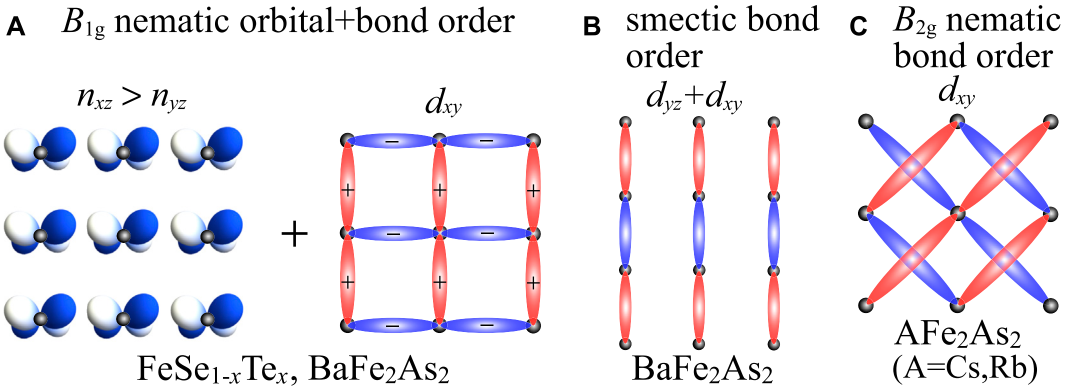

FIGURE 14 | (A) Schematic picture of the B_{1g} nematic orbital + bond order in $FeSe_{1-x}Te_x$ and $BaFe_2As_2$, where the orbital order for the d_{xz} and d_{yz} orbitals coexists with the bond order for the d_{xy} orbital. **(B)** Schematic picture of the smectic bond order for d_{yz} and d_{xy} orbitals in $BaFe_2As_2$. **(C)** Schematic picture of the B_{2g} nematic bond order for the d_{xy} orbital in AFe_2As_2 (A = Cs, Rb).

We stress that the present mechanism of the bulk nematicity for $T_S < T < T^*$ is intrinsic and free from the strength of the disorder and local strain in the system. The present smectic order originates from the AL–VC and the FS nesting between the d_{xy}-orbital hole pocket and the electron pockets [20]. We stress that the present theory explains the absence of the smectic order in bulk FeSe [55] because the d_{xy}-orbital hole pocket, which is necessary for smectic order formation, is below the Fermi level in FeSe.

Here, we explain the details of the recent microscopic measurements in P-doped Ba122 [54, 55] that support the present intrinsic scenario. These are bulk and real-space measurements. In the PEEM measurement [55], very uniform bulk nematic domains have been observed for $T_S < T < T^*$. The width of each nematic domain is about 500 nm. The structure of the nematic domains is unchanged for $T < T_S$. In addition, once the nematic domain completely disappears by increasing T, it never appears at the same location if the temperature is lowered again. These results are consistent with the present intrinsic smectic order scenario for $T_S < T < T^*$ in P-doped Ba122. In the photo-modulation measurement [54], uniform nematic domains have also been observed. The observed nematicity becomes small near the nematic domain boundary, irrespective of the fact that large local strain anisotropy is observed at the domain boundary. The observed anticorrelation between the nematicity and the local strain anisotropy may conflict with the assumption of the extrinsic scenario of the nematicity above T_S.

In contrast, the extrinsic scenario has been proposed by other groups [4, 56–60]. In the extrinsic mechanism, nematicity for $T > T_S$ in Co-doped Ba122, which exhibits large residual resistivity (>100 $\mu\Omega cm$), has been explained by the inhomogeneity of T_S induced by the disorder and local strain. However, it is not easy to explain the nematicity above T_S in clean P-doped (non-doped) Ba122 on the same footing in the extrinsic scenario.

We note that the multistage smectic/nematic transitions observed in NaFeAs [92] are also explained by the present intrinsic mechanism [20].

3.3 Results of $Ba_{1-x}Cs_xFe_2As_2$

In this section, we discuss B_{2g} nematicity in heavily hole-doped compound AFe_2As_2 (A = Cs, Rb) [19]. The effect of self-energy on the nematic order caused by the VCs is studied in the present work. Because of self-energy, T_S is reduced to become realistic, whereas the symmetry of the nematic order is unchanged. The direction of B_{2g} nematicity is rotated by 45° from that of the conventional B_{1g} nematicity. **Figure 2C** shows FSs of $CsFe_2As_2$: the hole FS around the M point comprising the d_{xy}-orbital is large, whereas the Dirac pockets near the X and Y points are small. In this system, the d_{xy}-orbital spin fluctuations are dominant.

Figure 12A shows the $\boldsymbol{q}$ dependence of the largest eigenvalue $\lambda_{\boldsymbol{q}}$ with self-energy for $r = 0.96$ at $T = 5$ meV and that without self-energy for $r = 0.30$ at $T = 20$ meV $\lambda_{\boldsymbol{q}}$ becomes maximum at $\boldsymbol{q} = \mathbf{0}$ and the dominant form factor $f^{\mathbf{0}}_{4,4}(\boldsymbol{k}) \propto \sin(k_x)\sin(k_y)$ at $\boldsymbol{q} = \mathbf{0}$ is shown in **Figure 12B**. As shown in **Figure 12C**, this form factor corresponds to the B_{2g} next-nearest-neighbor bond order for the d_{xy} orbital, which is consistent with the experimentally observed B_{2g} nematicity [61–64]. By analyzing the irreducible four-point vertex $I^{\mathbf{0}}_{4,4;4,4}(k,k')$ in the DW **Eq. 10**, we find that the attractive (repulsive) interactions originate from the AL (MT) terms, as shown in **Figure 12D**. The obtained $\boldsymbol{q} = \mathbf{0}$ B_{2g} bond order is derived from these interactions. Since the AL terms are enhanced by the quantum interference between the spin fluctuations with $\boldsymbol{Q}$ and $\boldsymbol{Q}'(= -\boldsymbol{Q})$, as shown in **Figure 1D**, the $\boldsymbol{q} = \mathbf{0}$ nematic bond order is realized. The value of $\lambda_{\mathbf{0}}$ is strongly enhanced by the attractive interactions for the d_{xy} orbital due to the AL terms. In this system, the nesting vector is short $\boldsymbol{Q} \sim (0.5\pi, 0)$, as shown in **Figure 12B**. Because of repulsive interaction by the MT terms, $f^{\mathbf{0}}_{4,4}(\boldsymbol{k})$ changes sign between the $\boldsymbol{k}$ points on the FSs connected by $\boldsymbol{Q}$, as shown in **Figure 12D**. To summarize, the AL terms strongly enlarge $\lambda_{\mathbf{0}}$ due to the paramagnon interference mechanism, and the MT terms favor B_{2g} symmetry. Cooperation of the AL and MT terms is important to realize the B_{2g} bond order.

We comment on the recent experiments on $RbFe_2As_2$. The specific heat jump at $T_S = 40$K ($\Delta C/T_S$) is very small [64]. However, it is naturally understood based on the recent theoretical scaling relation $\Delta C/T_S \propto T_S^b$ with $b \sim 3$ derived in Ref. [87]. Although the smallness of B_{2g} nematic susceptibility in $RbFe_2As_2$ was recently reported in Refs. [65, 66], the field angle-dependent specific heat measurement has shown finite B_{2g} nematicity above T_c [93]. Further experimental and theoretical studies are necessary to clarify the nematicity in AFe_2As_2 (A = Cs, Rb).

Finally, we discuss the x dependence of nematicity in $Ba_{1-x}A_xFe_2As_2$ (A = Cs, Rb). The schematic phase diagram of $Ba_{1-x}Rb_xFe_2As_2$ given by the experiment [64] is shown in **Figure 1C**. We introduce the model Hamiltonian for $Ba_{1-x}Cs_xFe_2As_2$, by interpolating between the $BaFe_2As_2$ model and the $CsFe_2As_2$ model with the ratio $1 - x$: x. **Figure 13A** shows x dependences of $\lambda_{\boldsymbol{q}=\mathbf{0}}$ without self-energy for the B_{2g} and the B_{1g} symmetries by fixing $T = 30$ meV and $r = 0.30$. Below $x = x_c \sim 0.5$, the B_{1g} nematic orbital order is dominant as discussed in the previous section, while the B_{2g} nematic bond order dominates over the B_{1g} nematic orbital order for $x > x_c$. As shown in **Figure 13B**, the Lifshitz transition occurs at $x \sim x_c$, where the electron pockets split into the four tiny Dirac pockets. Thus, the B_{2g} nematic bond order appears when the nesting vector $\boldsymbol{Q}$ between the electron pockets and hole pocket around the M point becomes short $\boldsymbol{Q} \sim (0.5\pi, 0)$. By taking account of the Lifshitz transition at $x \sim x_c$, the schematic phase diagram in **Figure 1C** is also well reproduced by the orbital/bond order because of the paramagnon interference mechanism. We note that the $\boldsymbol{q} = (0, \pi)$ smectic order is dominant over the $\boldsymbol{q} = \mathbf{0}$ B_{1g} nematic order at $x = 0$, as shown in the previous section.

4 CONCLUSION

We discussed the rich variety of nematic/smectic states in Fe-based superconductors in the same theoretical framework based on the paramagnon interference mechanism. In this mechanism, the charge-channel order is induced by the quantum interference between the spin fluctuations, as shown in **Figure 1D**. The form factor and wave vector of the DW instability are derived from the DW equation based on the paramagnon interference mechanism. Recently, a rigorous formalism of the DW equation has been constructed based on the Luttinger–Ward (LW) theory in Ref. [87]. According to Ref. [87], the solution of the DW equation gives the minimum of the grand potential in the LW theory. Thus, the nematic/smectic order discussed in the present study is thermodynamically stable in the framework of the conserving approximation.

By considering the characteristic fermiology of each compound, the paramagnon interference mechanism explains the rich variety of the nematic/smectic states. In **Figures 14A–C**, we summarized the nematic/smectic orders revealed by the mechanism in the present study. 1) In $FeSe_{1-x}Te_x$, each FS is very small and the d_{xy}-orbital hole pocket is absent. In this case, the small spin fluctuations on the three orbitals cooperatively lead to the B_{1g} orbital order for the d_{xz} and d_{yz} orbitals coexisting with the d_{xy}-orbital bond order, as shown in **Figure 14A**. The nematic orbital + bond order causes the Lifshitz transition, where the FS around the Y point disappears, which is consistent with the recent experiments. The x dependence of T_S in the phase diagram is reproduced by introducing self-energy. 2) In $BaFe_2As_2$, the d_{xy}-orbital hole pocket emerges. Since each electron and hole pocket is relatively large and similar in size, the strong d_{xy}-orbital spin fluctuations due to good nesting give rise to the smectic order shown in **Figure 14B** and the B_{1g} nematic order. The smectic order explains the tiny T-linear nematicity below $T = T^*(>T_S)$. We predict the multistage transitions with the smectic order at $T = T^*$ and the nematic order at T_S. 3) In heavily hole-doped AFe_2As_2 (A = Cs, Rb), the tiny Dirac pockets around the X(Y) point and the large d_{xy}-orbital hole pocket appear due to hole-doping. The B_{2g} bond order for the d_{xy} orbital shown in **Figure 14C** emerges due to the d_{xy}-orbital paramagnon interference mechanism. The B_{2g} bond order is triggered by the Lifshitz transition of the electron FSs by hole-doping.

The limitation of this theory is that the calculated VCs are reduced to an infinite series of the MT and AL terms. To verify the validity of the present theory, we performed the functional renormalization group (fRG) analysis for the single-orbital Hubbard model for cuprates [41] and the two-orbital Hubbard model for ruthenates [94], and obtained the bond-order (orbital order) in the former (latter) model. These results are consistent with previous experiments, and they are also obtained by the DW equation analysis. In the fRG theory, a huge number of higher-order VCs are generated in an unbiased manner by solving the RG equation. Thus, the significance of the MT and AL terms in the present theory has been confirmed by the different and excellent theoretical frameworks.

In future, it is to clarify the mechanism of superconductivity and non-Fermi-liquid behaviors of transport phenomena in the FeSe family by considering the nematic fluctuations enlarged near the nematic QCP. This issue will be discussed in future studies [95].

DATA AVAILABILITY STATEMENT

The original contributions presented in the study are included in the article; further inquiries can be directed to the corresponding author.

AUTHOR CONTRIBUTIONS

SO performed all calculations with contributions from HK. SO and HK wrote the manuscript.

FUNDING

This work was supported by Grants-in-Aid for Scientific Research from MEXT, Japan (No.s JP19H05825, JP18H01175, and JP17K05543), and Nagoya University Research Fund.

ACKNOWLEDGMENTS

We acknowledge Y. Yamakawa, R. Tazai, and S. Matsubara for their collaboration in the theoretical studies. We are grateful to Y. Matsuda, T. Hanaguri, T. Shibauchi, S. Kasahara, T. Shimojima, and Y. Mizukami for useful discussions about experiments.

REFERENCES

1. Hosono H, Kuroki K. Iron-based Superconductors: Current Status of Materials and Pairing Mechanism. *Physica C: Superconductivity its Appl* (2015) 514: 399–422. doi:10.1016/j.physc.2015.02.020
2. Hirschfeld PJ, Korshunov MM, Mazin II. Gap Symmetry and Structure of Fe-Based Superconductors. *Rep Prog Phys* (2011) 74:124508. doi:10.1088/0034-4885/74/12/124508
3. Fernandes RM, VanBebber LH, Bhattacharya S, Chandra P, Keppens V, Mandrus D, et al. Effects of Nematic Fluctuations on the Elastic Properties of Iron Arsenide Superconductors. *Phys Rev Lett* (2010) 105:157003. doi:10.1103/PhysRevLett.105.157003
4. Fernandes RM, Abrahams E, Schmalian J. Anisotropic In-Plane Resistivity in the Nematic Phase of the Iron Pnictides. *Phys Rev Lett* (2011) 107:217002. doi:10.1103/PhysRevLett.107.217002
5. Wang F, Kivelson SA, Lee D-H. Nematicity and Quantum Paramagnetism in FeSe. *Nat Phys* (2015) 11:959–63. doi:10.1038/nphys3456
6. Yu R, Si Q. Antiferroquadrupolar and Ising-Nematic Orders of a Frustrated Bilinear-Biquadratic Heisenberg Model and Implications for the Magnetism of FeSe. *Phys Rev Lett* (2015) 115:116401. doi:10.1103/PhysRevLett.115.116401
7. Glasbrenner JK, Mazin II, Jeschke HO, Hirschfeld PJ, Fernandes RM, Valentí R. Effect of Magnetic Frustration on Nematicity and Superconductivity in Iron Chalcogenides. *Nat Phys* (2015) 11:953–8. doi:10.1038/nphys3434
8. Fang C, Yao H, Tsai WF, Hu J, Kivelson SA. Theory of Electron Nematic Order in LaFeAsO. *Phys Rev B* (2008) 77:224509. doi:10.1103/PhysRevB.77.224509
9. Fernandes RM, Chubukov AV. Low-energy Microscopic Models for Iron-Based Superconductors: a Review. *Rep Prog Phys* (2017) 80:014503. doi:10.1088/1361-6633/80/1/014503
10. Krüger F, Kumar S, Zaanen J, van den Brink J. Spin-orbital Frustrations and Anomalous Metallic State in Iron-Pnictide Superconductors. *Phys Rev B* (2009) 79:054504. doi:10.1103/PhysRevB.79.054504
11. Lv W, Wu J, Phillips P. Orbital Ordering Induces Structural Phase Transition and the Resistivity Anomaly in Iron Pnictides. *Phys Rev B* (2009) 80:224506. doi:10.1103/physrevb.80.224506
12. Lee CC, Yin WG, Ku W. Ferro-Orbital Order and Strong Magnetic Anisotropy in the Parent Compounds of Iron-Pnictide Superconductors. *Phys Rev Lett* (2009) 103:267001. doi:10.1103/PhysRevLett.103.267001
13. Kontani H, Onari S. Orbital-Fluctuation-Mediated Superconductivity in Iron Pnictides: Analysis of the Five-Orbital Hubbard-Holstein Model. *Phys Rev Lett* (2010) 104:157001. doi:10.1103/PhysRevLett.104.157001
14. Onari S, Kontani H. Self-consistent Vertex Correction Analysis for Iron-Based Superconductors: Mechanism of Coulomb Interaction-Driven Orbital Fluctuations. *Phys Rev Lett* (2012) 109:137001. doi:10.1103/PhysRevLett.109.137001
15. Onari S, Yamakawa Y, Kontani H. High-TcSuperconductivity Near the Anion Height Instability in Fe-Based Superconductors: Analysis ofLaFeAsO1−xHx. *Phys Rev Lett* (2014) 112:187001. doi:10.1103/PhysRevLett.112.187001
16. Onari S, Yamakawa Y, Kontani H. Sign-Reversing Orbital Polarization in the Nematic Phase of FeSe Due to theC2Symmetry Breaking in the Self-Energy. *Phys Rev Lett* (2016) 116:227001. doi:10.1103/physrevlett.116.227001
17. Yamakawa Y, Onari S, Kontani H. Nematicity and Magnetism in FeSe and Other Families of Fe-Based Superconductors. *Phys Rev X* (2016) 6:021032. doi:10.1103/PhysRevX.6.021032
18. Yamakawa Y, Kontani H. Nematicity, Magnetism, and Superconductivity in FeSe under Pressure: Unified Explanation Based on the Self-Consistent Vertex Correction Theory. *Phys Rev B* (2017) 96:144509. doi:10.1103/PhysRevB.96.144509
19. Onari S, Kontani H. Origin of Diverse Nematic Orders in Fe-Based Superconductors: 45° Rotated Nematicity in AFe_2As_2(A=Cs,Rb). *Phys Rev B* (2019) 100:020507(R). doi:10.1103/physrevb.100.020507
20. Onari S, Kontani H. Hidden Antiferronematic Order in Fe-Based Superconductor BaFe2As2 and NaFeAs above TS. *Phys Rev Res* (2020) 2: 042005(R). doi:10.1103/PhysRevResearch.2.042005
21. Jiang K, Hu J, Ding H, Wang Z. Interatomic Coulomb Interaction and Electron Nematic Bond Order in FeSe. *Phys Rev B* (2016) 93:115138. doi:10.1103/PhysRevB.93.115138
22. Fanfarillo L, Giovannetti G, Capone M, Bascones E. Nematicity at the Hund's Metal Crossover in Iron Superconductors. *Phys Rev B* (2017) 95:144511. doi:10.1103/PhysRevB.95.144511
23. Hsu FC, Luo JY, Yeh KW, Chen TK, Huang TW, Wu PM, et al. Superconductivity in the PbO-type Structure α-FeSe. *Proc Natl Acad Sci U.S.A* (2008) 105:14262–4. doi:10.1073/pnas.0807325105
24. Böhmer AE, Kreisel A. Nematicity, Magnetism and Superconductivity in FeSe. *J Phys Condens Matter* (2018) 30:023001. doi:10.1088/1361-648X/aa9caa
25. Kreisel A, Hirschfeld P, Andersen B. On the Remarkable Superconductivity of FeSe and its Close Cousins. *Symmetry* (2020) 12:1402. doi:10.3390/sym12091402
26. Shibauchi T, Hanaguri T, Matsuda Y. Exotic Superconducting States in FeSe-Based Materials. *J Phys Soc Jpn* (2020) 89:102002. doi:10.7566/jpsj.89.102002
27. Wang QY, Li Z, Zhang WH, Zhang ZC, Zhang JS, Li W, et al. Interface-Induced High-Temperature Superconductivity in Single Unit-Cell FeSe Films on SrTiO 3. *Chin Phys. Lett.* (2012) 29:037402. doi:10.1088/0256-307x/29/3/037402
28. Ge JF, Liu ZL, Liu C, Gao CL, Qian D, Xue QK, et al. Superconductivity above 100 K in Single-Layer FeSe Films on Doped SrTiO3. *Nat Mater* (2015) 14: 285–9. doi:10.1038/nmat4153

29. Fan Q, Zhang WH, Liu X, Yan YJ, Ren MQ, Peng R, et al. Plain S-Wave Superconductivity in Single-Layer FeSe on SrTiO3 Probed by Scanning Tunnelling Microscopy. *Nat Phys* (2015) 11:946–52. doi:10.1038/nphys3450
30. Zhang Y, Lee JJ, Moore RG, Li W, Yi M, Hashimoto M, et al. Superconducting gap Anisotropy in Monolayer FeSe Thin Film. *Phys Rev Lett* (2016) 117: 117001. doi:10.1103/PhysRevLett.117.117001
31. Miyata Y, Nakayama K, Sugawara K, Sato T, Takahashi T. High-temperature Superconductivity in Potassium-Coated Multilayer FeSe Thin Films. *Nat Mater* (2015) 14:775–9. doi:10.1038/nmat4302
32. Shimojima T, Suzuki Y, Sonobe T, Nakamura A, Sakano M, Omachi J, et al. Lifting of *Xz/yz* Orbital Degeneracy at the Structural Transition in Detwinned FeSe. *Phys Rev B* (2014) 90:121111(R). doi:10.1103/physrevb.90.121111
33. Nakayama K, Miyata Y, Phan GN, Sato T, Tanabe Y, Urata T, et al. Reconstruction of Band Structure Induced by Electronic Nematicity in an FeSe Superconductor. *Phys Rev Lett* (2014) 113:237001. doi:10.1103/physrevlett.113.237001
34. Suzuki Y, Shimojima T, Sonobe T, Nakamura A, Sakano M, Tsuji H, et al. Momentum-dependent Sign Inversion of Orbital Order in Superconducting FeSe. *Phys Rev B* (2015) 92:205117. doi:10.1103/PhysRevB.92.205117
35. Zhang Y, Yi M, Liu ZK, Li W, Lee JJ, Moore RG, et al. Distinctive Orbital Anisotropy Observed in the Nematic State of a FeSe Thin Film. *Phys Rev B* (2016) 94:115153. doi:10.1103/PhysRevB.94.115153
36. Yi M, Pfau H, Zhang Y, He Y, Wu H, Chen T, et al. Nematic Energy Scale and the Missing Electron Pocket in FeSe. *Phys Rev X* (2019) 9:041049. doi:10.1103/PhysRevX.9.041049
37. Xing RQ, Classen L, Chubukov AV. Orbital Order in FeSe: The Case for Vertex Renormalization. *Phys Rev B* (2018) 98:041108(R). doi:10.1103/PhysRevB.98.041108
38. Chubukov AV, Khodas M, Fernandes RM. Magnetism, Superconductivity, and Spontaneous Orbital Order in Iron-Based Superconductors: Which Comes First and Why? *Phys Rev X* (2016) 6:041045. doi:10.1103/PhysRevX.6.041045
39. Kawaguchi K, Yamakawa Y, Tsuchiizu M, Kontani H. Competing Unconventional Charge-Density-Wave States in Cuprate Superconductors: Spin-Fluctuation-Driven Mechanism. *J Phys Soc Jpn* (2017) 86:063707. doi:10.7566/jpsj.86.063707
40. Yamakawa Y, Kontani H. Spin-Fluctuation-Driven Nematic Charge-Density Wave in Cuprate Superconductors: Impact of Aslamazov-Larkin Vertex Corrections. *Phys Rev Lett* (2015) 114:257001. doi:10.1103/PhysRevLett.114.257001
41. Tsuchiizu M, Kawaguchi K, Yamakawa Y, Kontani H. Multistage Electronic Nematic Transitions in Cuprate Superconductors: A Functional-Renormalization-Group Analysis. *Phys Rev B* (2018) 97:165131. doi:10.1103/physrevb.97.165131
42. Onari S, Kontani H. SU(4) Valley+Spin Fluctuation Interference Mechanism for Nematic Order in Magic-Angle Twisted Bilayer Graphene: The Impact of Vertex Corrections. *Phys Rev Lett* (2022) 128:066401. doi:10.1103/PhysRevLett.128.066401
43. Hirata T, Yamakawa Y, Onari S, Kontani H. Unconventional Orbital Charge Density Wave Mechanism in the Transition Metal Dichalcogenide 1T−TaS2. *Phys Rev Res* (2021) 3:L032053. doi:10.1103/physrevresearch.3.l032053
44. Tazai R, Yamakawa Y, Onari S, Kontani H. Mechanism of Exotic Density-Wave and Beyond-Migdal Unconventional Superconductivity in Kagome Metal AV 3 Sb 5 (A = K, Rb, Cs). *Sci Adv* (2022) 8:eabl4108. doi:10.1126/sciadv.abl4108
45. Licciardello S, Buhot J, Lu J, Ayres J, Kasahara S, Matsuda Y, et al. Electrical Resistivity across a Nematic Quantum Critical point. *Nature* (2019) 567:213–7. doi:10.1038/s41586-019-0923-y
46. Coldea AI, Blake SF, Kasahara S, Haghighirad AA, Watson MD, Knafo W, et al. Evolution of the Low-Temperature Fermi Surface of Superconducting FeSe1−xSx across a Nematic Phase Transition. *Npj Quant Mater* (2019) 4:2. doi:10.1038/s41535-018-0141-0
47. Huang WK, Hosoi S, Čulo M, Kasahara S, Sato Y, Matsuura K, et al. Magnetization Switching Driven by Current-Induced Torque from Weakly Spin-Orbit Coupled Zr. *Phys Rev Res* (2020) 2:033367. doi:10.1103/PhysRevResearch.2.033367
48. Huang WK, Hosoi S, Čulo M, Kasahara S, Sato Y, Matsuura K, et al. Non-Fermi Liquid Transport in the Vicinity of the Nematic Quantum Critical point of Superconducting FeSe1−xSx. *Phys Rev Res* (2020) 2:033367. doi:10.1103/PhysRevResearch.2.033367
49. Mukasa K, Matsuura K, Qiu M, Saito M, Sugimura Y, Ishida K, et al. High-pressure Phase Diagrams of FeSe1−xTex: Correlation between Suppressed Nematicity and Enhanced Superconductivity. *Nat Commun* (2021) 12:381. doi:10.1038/s41467-020-20621-2
50. Mukasa K, Ishida K, Imajo S, Qiu MW, Saito M, Matsuura K, et al. Enhanced Superconducting Pairing Strength Near a Nonmagnetic Nematic Quantum Critical point. *ArXiv* (2022) 2202:11657. doi:10.48550/arXiv.2202.11657
51. Ishida K, Onishi Y, Tsujii M, Mukasa K, Qiu M, Saito M, et al. Pure Nematic Quantum Critical point Accompanied by a Superconducting Dome. *ArXiv* (2022) 2202:11674. doi:10.1073/pnas.2110501119
52. Kasahara S, Shi HJ, Hashimoto K, Tonegawa S, Mizukami Y, Shibauchi T, et al. Electronic Nematicity above the Structural and Superconducting Transition in BaFe2(As1−xP X)2. *Nature* (2012) 486:382–5. doi:10.1038/nature11178
53. Kim YK, Jung WS, Han GR, Choi KY, Chen CC, Devereaux TP, et al. Existence of Orbital Order and its Fluctuation in SuperconductingBa(Fe1−xCox)2As2Single Crystals Revealed by X-ray Absorption Spectroscopy. *Phys Rev Lett* (2013) 111:217001. doi:10.1103/physrevlett.111.217001
54. Thewalt E, Hayes IM, Hinton JP, Little A, Patankar S, Wu L, et al. Imaging Anomalous Nematic Order and Strain in Optimally Doped BaFe$_2$(As,P)$_2$. *Phys Rev Lett* (2018) 121:027001. doi:10.1103/physrevlett.121.027001
55. Shimojima T, Motoyui Y, Taniuchi T, Bareille C, Onari S, Kontani H, et al. Discovery of Mesoscopic Nematicity Wave in Iron-Based Superconductors. *Science* (2021) 373:1122–5. doi:10.1126/science.abd6701
56. Chu JH, Analytis JG, De Greve K, McMahon PL, Islam Z, Yamamoto Y, et al. In-Plane Resistivity Anisotropy in an Underdoped Iron Arsenide Superconductor. *Science* (2010) 329:824–6. doi:10.1126/science.1190482
57. Ren X, Duan L, Hu Y, Li J, Zhang R, Luo H, et al. Nematic Crossover inBaFe2As2under Uniaxial Stress. *Phys Rev Lett* (2015) 115:197002. doi:10.1103/PhysRevLett.115.197002
58. Man H, Zhang R, Park JT, Lu X, Kulda J, Ivanov A, et al. Direct Observation of Spin Excitation Anisotropy in the Paramagnetic Orthorhombic State of BaFe2−xNixAs2. *Phys Rev B* (2018) 97:060507(R). doi:10.1103/PhysRevB.97.060507
59. Wiecki P, Zhou R, Julien MH, Böhmer AE, Schmalian J. Edwards-Anderson Parameter and Local Ising Nematicity in FeSe Revealed via NMR Spectral Broadening. *Phys Rev B* (2021) 104:125134. doi:10.1103/PhysRevB.104.125134
60. Lahiri A, Klein A, Fernandes RM. Defect-induced Electronic Smectic State at the Surface of Nematic Materials. *ArXiv* (2021) 2111:00541. doi:10.48550/arXiv.2111.00541
61. Li J, Zhao D, Wu YP, Li SJ, Song DW, Zheng LX, et al. Reemergeing Electronic Nematicity in Heavily Hole-Doped Fe-Based Superconductors. *ArXiv* (2021) 1611:04694. doi:10.48550/arXiv.1611.04694
62. Liu X, Tao R, Ren M, Chen W, Yao Q, Wolf T, et al. Evidence of Nematic Order and Nodal Superconducting gap along [110] Direction in RbFe2As2. *Nat Commun* (2019) 10:1039. doi:10.1038/s41467-019-08962-z
63. Moroni M, Prando G, Aswartham S, Morozov I, Bukowski Z, Büchner B, et al. Charge and Nematic Orders in AFe2As2(A=Rb,Cs) Superconductors. *Phys Rev B* (2019) 99:235147. doi:10.1103/physrevb.99.235147
64. Ishida K, Tsujii M, Hosoi S, Mizukami Y, Ishida S, Iyo A, et al. Novel Electronic Nematicity in Heavily Hole-Doped Iron Pnictide Superconductors. *Proc Natl Acad Sci U.S.A* (2020) 117:6424–9. doi:10.1073/pnas.1909172117
65. Wiecki P, Haghighirad AA, Weber F, Merz M, Heid R, Böhmer AE. Dominant In-Plane Symmetric Elastoresistance in CsFe2As2. *Phys Rev Lett* (2020) 125: 187001. doi:10.1103/PhysRevLett.125.187001
66. Wiecki P, Frachet M, Haghighirad AA, Wolf T, Meingast C, Heid R, et al. Emerging Symmetric Strain Response and Weakening Nematic Fluctuations in Strongly Hole-Doped Iron-Based Superconductors. *Nat Commun* (2021) 12:4824. doi:10.1038/s41467-021-25121-5
67. Borisov V, Fernandes RM, Valentí R. Evolution from B2g Nematics to B1g Nematics in Heavily Hole-Doped Iron-Based Superconductors. *Phys Rev Lett* (2019) 123:146402. doi:10.1103/PhysRevLett.123.146402
68. Wu YP, Zhao D, Wang AF, Wang NZ, Xiang ZJ, Luo XG, et al. Emergent Kondo Lattice Behavior in Iron-Based SuperconductorsAFe2As2(A=K, Rb, Cs). *Phys Rev Lett* (2016) 116:147001. doi:10.1103/PhysRevLett.116.147001
69. Civardi E, Moroni M, Babij M, Bukowski Z, Carretta P. Superconductivity Emerging from an Electronic Phase Separation in the Charge Ordered Phase of RbFe2As2. *Phys Rev Lett* (2016) 117:217001. doi:10.1103/PhysRevLett.117.217001

70. Baym G, Kadanoff LP. Conservation Laws and Correlation Functions. *Phys Rev* (1961) 124:287–99. doi:10.1103/physrev.124.287
71. Allen S, Tremblay AMS, Vilk YM. *Theoretical Methods for Strongly Correlated Electrons*. New-York: Springer-Verlag (2004).
72. Blaha P, Schwarz K, Tran F, Laskowski R, Madsen GKH, Marks LD. WIEN2k: An APW+lo Program for Calculating the Properties of Solids. *J Chem Phys* (2020) 152:074101. doi:10.1063/1.5143061
73. Mostofi AA, Yates JR, Pizzi G, Lee YS, Souza I, Vanderbilt D, et al. An Updated Version of Wannier90: A Tool for Obtaining Maximally-Localised Wannier Functions. *Comput Phys Commun* (2014) 185:2309–10. doi:10.1016/j.cpc.2014.05.003
74. Miyake T, Nakamura K, Arita R, Imada M. Comparison of Ab Initio Low-Energy Models for LaFePO, LaFeAsO, BaFe2As2, LiFeAs, FeSe, and FeTe: Electron Correlation and Covalency. *J Phys Soc Jpn* (2010) 79:044705. doi:10.1143/JPSJ.79.044705
75. Bickers NE, White SR. Conserving Approximations for Strongly Fluctuating Electron Systems. II. Numerical Results and Parquet Extension. *Phys Rev B* (1911) 43:8044–64. doi:10.1103/PhysRevB.43.8044
76. Kontani H, Yamakawa Y, Tazai R, Onari S. Odd-parity Spin-Loop-Current Order Mediated by Transverse Spin Fluctuations in Cuprates and Related Electron Systems. *Phys Rev Res* (2021) 3:013127. doi:10.1103/PhysRevResearch.3.013127
77. Nakayama K, Tsubono R, Phan GN, Nabeshima F, Shikama N, Ishikawa T, et al. Orbital Mixing at the Onset of High-Temperature Superconductivity in FeSe1−xTex/CaF2. *Phys Rev Res* (2021) 3:L012007. doi:10.1103/PhysRevResearch.3.L012007
78. Zhang P, Wang Z, Wu X, Yaji K, Ishida Y, Kohama Y, et al. Multiple Topological States in Iron-Based Superconductors. *Nat Phys* (2019) 15:41–7. doi:10.1038/s41567-018-0280-z
79. Wang Z, Zhang P, Xu G, Zeng LK, Miao H, Xu X, et al. Topological Nature of theFeSe0.5Te0.5superconductor. *Phys Rev B* (2015) 92:115119. doi:10.1103/PhysRevB.92.115119
80. Lohani H, Hazra T, Ribak A, Nitzav Y, Fu H, Yan B, et al. Band Inversion and Topology of the Bulk Electronic Structure in FeSe0.45Te0.55. *Phys Rev B* (2020) 101:245146. doi:10.1103/PhysRevB.101.245146
81. Yin ZP, Haule K, Kotliar G. Kinetic Frustration and the Nature of the Magnetic and Paramagnetic States in Iron Pnictides and Iron Chalcogenides. *Nat Mater* (2011) 10:932–5. doi:10.1038/nmat3120
82. Yamasaki A, Matsui Y, Imada S, Takase K, Azuma H, Muro T, et al. Electron Correlation in the FeSe Superconductor Studied by Bulk-Sensitive Photoemission Spectroscopy. *Phys Rev B* (2010) 82:184511. doi:10.1103/PhysRevB.82.184511
83. Watson MD, Haghighirad AA, Rhodes LC, Hoesch M, Kim TK. Electronic Anisotropies Revealed by Detwinned Angle-Resolved Photo-Emission Spectroscopy Measurements of Fese. *New J Phys* (2017) 19:103021. doi:10.1088/1367-2630/aa8a04
84. Yi M, Pfau H, Zhang Y, He Y, Wu H, Chen T, et al. Nematic Energy Scale and the Missing Electron Pocket in FeSe. *Phys Rev X* (2019) 9:041049. doi:10.1103/PhysRevX.9.041049
85. Huh SS, Seo JJ, Kim BS, Cho SH, Jung JK, Kim S, et al. Absence of Y-Pocket in 1-Fe Brillouin Zone and Reversed Orbital Occupation Imbalance in FeSe. *Commun Phys* (2020) 3:52. doi:10.1038/s42005-020-0319-1
86. Rhodes LC, Boker J, Muller MA, Eschrig M, Eremin IM. Non-local D_{xy} Nematicity and the Missing Electron Pocket in FeSe. *npj Quan Mater* (2021) 6:45. doi:10.1038/s41535-021-00341-6
87. Tazai R, Matsubara S, Yamakawa Y, Onari S, Kontani H. A Rigorous Formalism of Unconventional Symmetry Breaking in Fermi Liquid Theory and its Application to Nematicity in FeSe. *ArXiv* (2022) 2205:02280. doi:10.48550/arXiv.2205.02280
88. Moon SJ, Schafgans AA, Kasahara S, Shibauchi T, Terashima T, Matsuda Y, et al. Infrared Measurement of the Pseudogap of P-Doped and Co-doped High-TemperatureBaFe2As2Superconductors. *Phys Rev Lett* (2012) 109:027006. doi:10.1103/PhysRevLett.109.027006
89. Shimojima T, Sonobe T, Malaeb W, Shinada K, Chainani A, Shin S, et al. Pseudogap Formation above the Superconducting Dome in Iron Pnictides. *Phys Rev B* (2014) 89:045101. doi:10.1103/PhysRevB.89.045101
90. Shimojima T, Malaeb W, Nakamura A, Kondo T, Kihou K, Lee CH, et al. Antiferroic Electronic Structure in the Nonmagnetic Superconducting State of the Iron-Based Superconductors. *Sci Adv* (2017) 3:e1700466. doi:10.1126/sciadv.1700466
91. Yi M, Lu D, Chu JH, Analytis JG, Sorini AP, Kemper AF, et al. Symmetry-breaking Orbital Anisotropy Observed for Detwinned Ba(Fe 1- X Co X) 2 as 2 above the Spin Density Wave Transition. *Proc Natl Acad Sci U.S.A* (2011) 108:6878–83. doi:10.1073/pnas.1015572108
92. Zhou R, Xing LY, Wang XC, Jin CQ, Zheng GQ. Orbital Order and Spin Nematicity in the Tetragonal Phase of the Electron-Doped Iron pnictidesNaFe1−xCoxAs. *Phys Rev B* (2016) 93:060502(R). doi:10.1103/PhysRevB.93.060502
93. Mizukami Y, Tanaka O, Ishida K, Tsujii M, Mitsui T, Kitao S, et al. Thermodynamic Signatures of Diagonal Nematicity in $RbFe_2As_2$ Superconductor. *ArXiv* (2021) 2108:13081. doi:10.48550/arXiv.2108.13081
94. Tsuchiizu M, Ohno Y, Onari S, Kontani H. Orbital Nematic Instability in the Two-Orbital Hubbard Model: Renormalization-Group + Constrained RPA Analysis. *Phys Rev Lett* (2013) 111:057003. doi:10.1103/PhysRevLett.111.057003
95. Yamakawa Y, Onari S, Kontani H (2022). Unpublished.

Conflict of Interest: The authors declare that the research was conducted in the absence of any commercial or financial relationships that could be construed as a potential conflict of interest.

Frontiers in
Physics

Investigates complex questions in physics to understand the nature of the physical world

Addresses the biggest questions in physics, from macro to micro, and from theoretical to experimental and applied physics.

Discover the latest Research Topics

See more →

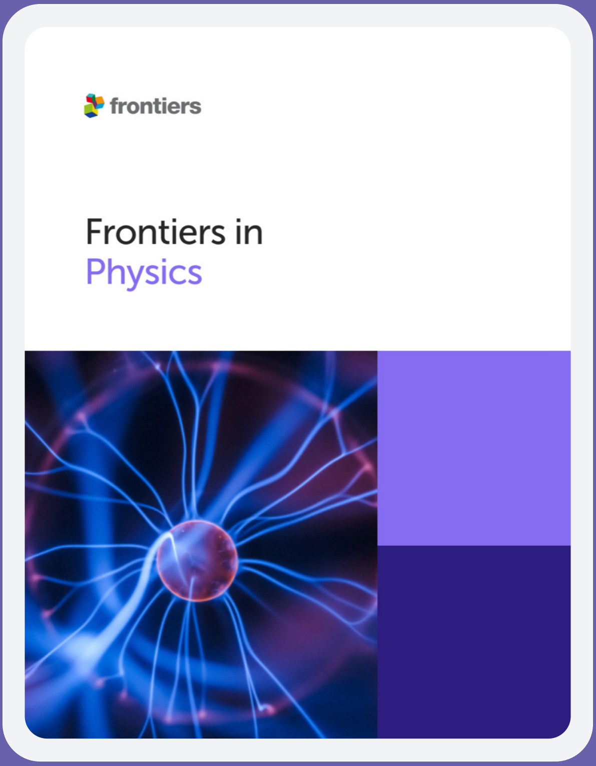

frontiers

Frontiers in
Physics

Frontiers

Avenue du Tribunal-Fédéral 34
1005 Lausanne, Switzerland
frontiersin.org

Contact us

+41 (0)21 510 17 00
frontiersin.org/about/contact